Electronic, optical and magnetic properties of self-assembled quantum dots containing magnetic ions

Anna Trojnar

Thesis submitted to the
Faculty of Graduate and Postdoctoral Studies
in partial fulfilment of requirements for the Degree of

Doctor of Philosophy in Physics

Ottawa-Carleton Institute of Physics
Department of Physics
Faculty of Science

University of Ottawa

I would like to dedicate this thesis to my Mother, who always believed in me and supported me the best she could, and never discouraged me to pursue any of my ideas.

Acknowledgements

First of all, I would like to thank Professor Pawel Hawrylak, who was my supervisor. Thank you very much for always finding time to talk to me about the progress of the projects and to discuss their future directions during the four years of my PhD. Thank you for always trying to keep me on the "right track". Furthermore, I would like to thank you for creating a very friendly atmosphere in the group, which allowed all group members to exchange ideas freely and to learn from each other. Thank you for caring about our work/life balance by organizing social activities.

I would also like to thank my co-worker and great friend Marek Korkusinski, who helped me greatly while I was settling down in Ottawa and was my guide through the research projects. I learned so much from you. Thank you for your infinite patience with explaining the details of the scientific ideas, as well as giving me life advice.

Many thanks to my Mother, who was amazingly supportive during the whole process of the PhD, starting from the application for the program, through the move to a different continent, to the moment of writing the Thesis. Particularly I would like to thank you for your understanding when I was not able to come home for Christmas this year.

I cannot underappreciate the support from my loving fiance Chris Hall, who was absolutely amazing during the writing stages of the Thesis. Thank you for taking care of me, our little puppy, and the household. Thank you for not taking me to the psychologist on account of talking to myself while writing or in my sleep.

Thesis Advisor: Dr. Pawel Hawrylak
Author: Anna Trojnar

Electronic, optical and magnetic properties of self-assembled quantum dots containing magnetic ions

Abstract

There is currently interest in developing control over the spin of a single Manganese (Mn) ion, the atomic limit of magnetic memory, in semiconductor quantum dots (QDs). In this work we present theoretical results showing how one can manipulate the spin of Mn ion with light in a QD by engineering Mn-multi-exciton interactions through quantum interference, design of exciton and bi-exciton states and application of the magnetic field.

We develop a fully microscopic model of correlated exciton and bi-exciton interacting with the Mn ion. The electrons and heavy holes, confined in the QD, approximated as a two-dimensional harmonic oscillator (HO), interact via direct and short- and long-range exchange Coulomb interactions. The matrix elements of the exchange interaction are computed for the first time in the harmonic oscillator basis and for arbitrary magnetic fields. The exciton and bi-exciton energies and states are computed using the configuration interaction method. The interaction between carriers and the Mn spin is accounted for by the Heisenberg electron-Mn and Ising hole-Mn exchange interactions.

For a single exciton confined in a magnetic dot, a novel quantum interference (QI) effect between the electron-hole Coulomb scattering and the scattering by Mn ion is obtained. The QI significantly affects the exciton-Mn coupling, modifying the splitting of the emission/absorption lines from the exciton-Mn complex depending on the degree of electronic correlations in the exciton state. The second signature of the QI are the nonuniform energy gaps between the consecutive emission peaks due to the scattering of carriers by Mn among single-particle orbitals.

Magneto-photoluminescence experiments show that the coupling between the exciton and Mn ion does not change in the magnetic field. We report that electron-hole correlations counteract the magnetic

squeezing of the single-particle wave functions strengthening the carrier-Mn interactions. As a result, the rate of change of the magneto-photoluminescence spectra with magnetic field is reduced as observed in the experiment.

We develop here for the first time a microscopic theory of bi-exciton-Mn complex, and report the presence of the fine structure of bi-exciton-Mn complex, even though as a spin-singlet it is expected to decouple from the localized spin. Theoretical results are compared with experiments in Grenoble and Warsaw.

Contents

List of Figures

Statement of Originality

All the calculations and their analysis were performed under the supervision of Dr. Pawel Hawrylak, the Group Leader of the Quantum Theory Group in Security and Disruptive Technologies, Emerging Technologies Division, National Research Council Canada in Ottawa. These results were obtained by me, however with cooperation with following co-workers and colleagues:

- Dr. Pawel Hawrylak, the Group Leader of the Quantum Theory Group in Security and Disruptive Technologies, Emerging Technologies Division, National Research Council Canada - who directed the research.
- Dr. Marek Korkusinski, a Associate Research Officer at the Quantum Theory Group at NRC, who carried out parts of the calculations in parallel to make sure of their numerical correctness, and was involved in analysis of obtained results.
- Dr. Eugene S. Kadantsev, a Research Associate at the Quantum Theory Group at NRC, who was involved in the calculations of the electron-hole exchange interaction.
- Isil Ozfian, a Ph.D Student at University of Ottawa, under a supervision of Dr. Pawel Hawrylak, with whom I shared a project on the quadrupole quantum dots.
- Udson C. Mendez, a Ph.D Student at the Institute of Physics "Gleb Wataghin"-DFMC, State University of Campinas, Campinas-SP, Brazil, who was an exchange student at the Quantum Theory Group at NRC. He participated in the calculations of the bi-exciton-Manganese ion interaction.

- Ramin M. Abolfath, Research Associate at the University of Texas, Dallas, Texas.

- Experimental collaborators: Marek Potemski, Piotr Kossacki, Piotr Wojnar, Mateusz Goryca, Tomasz Smolenski, Tomasz Kazimierczuk, Maciej Koperski from Laboratoire National des Champs Magntiques Intenses, CNRS, Grenoble, France, and Institute of Experimental Physics, Faculty of Physics, University of Warsaw, Poland.

Most of our original results have already been published in refereed jurnals, while other manuscripts are still under the consideration of the editors and referees. The full list of the papers is given below:

1. A. H. Trojnar, M. Korkusinski, E. S. Kadantsev, P. Hawrylak, M. Goryca, T. Kazimierczuk, P. Kossacki, P. Wojnar, and M. Potemski *Quantum Interference in Exciton-Mn Spin Interactions in a CdTe Semiconductor Quantum Dot*, Phys. Rev. Lett. **107**, 207403 (2011) - Published November 11, 2011

2. A. H. Trojnar, E. S. Kadantsev, M. Korkusinski, and P. Hawrylak *Theory of fine structure of correlated exciton states in self-assembled semiconductor quantum dots in a magnetic field*, Phys. Rev. B **84**, 245314 (2011) - Published December 19, 2011

3. A. H. Trojnar, M. Korkusinski, M. Potemski, and P. Hawrylak *Theory of optical properties of II-VI semiconductor quantum dots containing a single magnetic ion in a strong magnetic field*, Phys. Rev. B **85**, 165415 (2012) - Published April 6, 2012

4. A. H. Trojnar, M. Korkusinski, M. Goryca, M. Koperski, T. Smolenski, P. Kossacki, and P. Hawrylak *Fine structure of a biexciton in a single quantum dot with a magnetic impurity*, Phys. Rev. B **87**, 205311 (2013) - Published May 28, 2013

5. I. Ozfidan, A. H. Trojnar, M. Korkusinski, and P. Hawrylak *Geometry, Chirality and Electron-Electron Interactions in the Quadrupole Quantum Dot Molecule*, Submitted to Sol. St. Comm. 2013

6. R. M. Abolfath, A. H. Trojnar, B. Roostaei, T. Brabec, and P. Hawrylak *Dynamical Magnetic and Nuclear Polarization in Complex Spin Systems: Semi-magnetic II-VI Quantum Dots*, New Journal of Physics (in press) (2013), arXiv:1202.5352

7. U. C. Mendes, M. Korkusinski, A. H. Trojnar, and P. Hawrylak *Optical Properties of Charged Quantum Dots Doped with a Single Magnetic Impurity*, Manuscript in the preparation

8. A. H. Trojnar, M. Korkusinski, M. Potemski, and P. Hawrylak *Spin polarized bi-excitons in optical properties of self-assembled quantum dots with magnetic impurity*, Manuscript in the preparation

I declare that I have contributed to the entire content of purely theoretical manuscripts 2-5 collaborating with my co-workers as described above. The manuscripts 1 and 6 contain both theoretical and experimental results. The experiments were carried out by our collaborators named in the list of autors, while I took part in the theoretical calculations and analysis.

Chapter 1

Introduction

In conventional hard drives, information is stored in the form of a magnetization of domains of the ferromagnetic material. Information is written to and read from the storage medium as it moves past devices called read-and-write heads that operate very close (often tens of nanometers) over the magnetic surface. The write head magnetizes a domain region by generating a strong local magnetic field. The read head detects the magnetization of the region by measuring the change of the electrical resistance induced by the local magnetic field. The discovery of the "giant" magnetoresistance effect (GMR) [1, 2] allowed for fabrication of magnetic storage systems with much smaller magnetic domains. Despite this, in a regular hard drive one still requires about half a billion atoms to store each bit of information.

If one wants to manipulate the information stored on the hard drive, one needs to read it and then send it as an electric current through a wire to the system of semiconductor transistors, which perform a desired operation. All of the components of such a complex system are macroscopic.

An alternative direction, called semiconductor spintronics [3–12], involves putting magnetic ions directly into semiconductor [13–18]. Thanks to their expected long spin coherence time, and taking into account the fact that they constitute the ultimate limit of miniaturization of the information storage, magnetic atoms in a semiconductor host hold a promise to store quantum information in the solid state [19, 20]. In a bulk semiconductor, these localized spins interact

weakly with their environment, and they are difficult to control by electrical or optical methods.

In the last few years it has been shown that by introducing few Manganese atoms into the quantum dots, the control of a single atomic spin in a solid state environment is possible [21–24]. In particular, the state of the Mn atom can be changed by the injection of carriers into the dot. The carriers can be introduced into the QDs by optical excitation, which allows *optical control* of the spin state of the Mn ion, that is, an all-optical way of writing, reading and manipulating the information.

To be able to achieve this goal, one needs to understand the interaction between optically excited excitons and the magnetic ion. The purpose of this thesis is to explore all aspects of these interactions based on a microscopic model and to describe ways of engineering the carrier-spin coupling by tailoring the structural properties of the magnetic quantum dot.

Chapter 2

Short overview of quantum dots

2.1 Introduction: importance, fabrication

In the bulk crystalline solids, both metallic and semiconducting, the motion of the carriers is free in all three dimensions. In systems such as atoms, on the other hand, the carriers are fully confined and their energy spectra form discrete levels. Interest in artificially created confined systems dates back to the early 1970's, when it has become technologically possible to constrain the motion of the electrons to two dimmensions. This was achieved by fabricating a "sandwich" structure called a *quantum well* [25–27]. In the quantum well the external layers are made out of a semiconductor material with the energy gap greater than that of the thin layer in-between. The motion of electrons in such structures is constrained to the internal quasi-two-dimensional layer of the low-gap material.

The quasi-zero-dimensional structure called a *quantum dot* (QD) [28–33] confines the motion of electrons in all three dimensions. The first approach to fabricate such structures was reported in 1986. This attempt involved lithographic etching of the pillars in the quantum well material [34–37]. In such structures, the restriction of the motion of electrons in all three dimensions leads to the formation of discrete electronic energy levels. In a quantum dot with a circular or spherical symmetry, these energy levels form a degenerate shell structure similar to the energy shells in the atoms. The important difference between QDs and atoms, however, is the difference in their size. Quantum dots are much larger than atoms as they are built of thousands to millions of atoms, depending on their type. This

leads to the difference in the quantization energies for the electrons - in the QDs the energy gaps between electronic levels are of the order of tens to hundreds of meV, while in the atom the levels are a few eV apart. An interesting property of the QDs is the possibility of designing their electronic properties by changing the size, shape, type of constituent materials, as well as the number of confined electrons.

This work is focused mainly on the self-assembled quantum dots (SADs), since these QDs can confine both electrons and valence holes, and therefore can be addressed by optical means. This makes them good candidates for entangled photon emitters (where a cascade decay of the bi- and mono-exciton creates phase correlated photon pairs) [38–44] or far infrared detectors [45–48].

The SADs are also good candidates for quantum computing elements due to their unique optical properties [39, 41, 42, 44, 49]. The electron spin in a single-electron quantum dot can be used as a computational qubit [7], the QD coupled to a photonic crystal waveguide can be used as a single photon gun [50], or can be used as an active laser medium in quantum dot lasers [51].

In Chapter 4 we also discuss briefly the lateral gated QDs. For that reason, both the self-assembled and the lateral gated QDs will be desciribed here.

2.1.1 Fabrication of the QDs

Historically, one of the earliest methods of fabricating QDs was selective lithographic etching of semiconductor heterostructures containing a single or multiple quantum wells [34–37]. This process is used to fabricate pillars containing the parts of the quantum well in which the electrons were confined. The lateral dimensions of the confinement obtained in this way was of the order of a few hundreds of nm [37]. The density of carriers in the structure could be changed by doping the semiconductors, while applying voltage to the metal electrodes deposited on the surface of the pillars allowed to tune the number of electrons confined in the QD.

The electronic motion can also be confined to a small area by creating a non-uniform electric field [29, 33, 56]. Modulation of the electric field can be obtained in several ways. The simplest and most commonly used method is lithographic

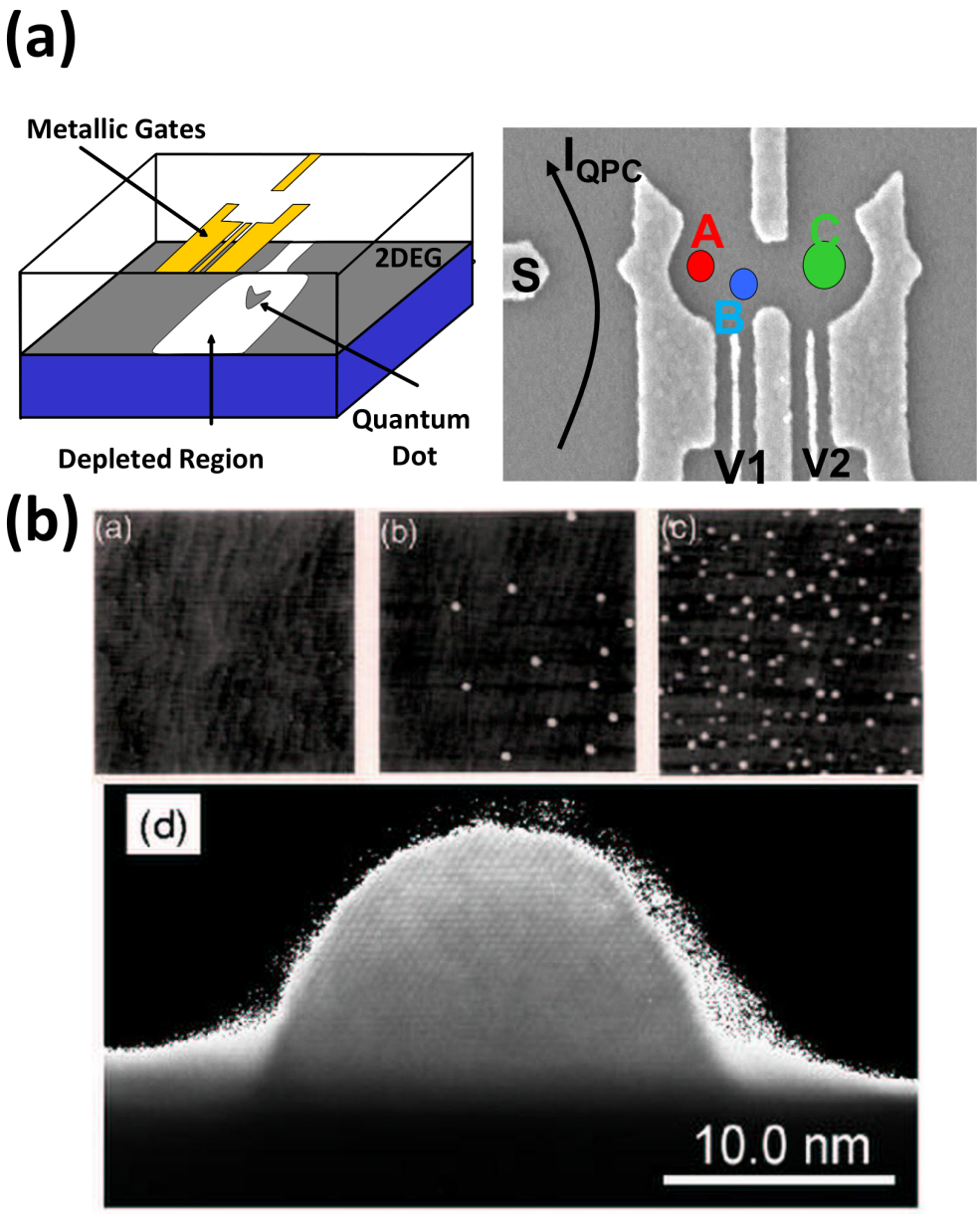

Figure 2.1: (a) An example design of metalic electrodes creating a triple QD in the 2DEG underneath it. The areas where the electrons are confined are marked by the color circles. (b, top) Atomic force microscopy photographs presenting the evolution of the QD islands during the growth of InAs on the surface of GaAs, (b,bottom) transmission electron micrograph (TEM) of an InAs SAD. The figure (a) has been adapted from Ref. [52] with permission granted by authors (Copyright (2006) by The American Physical Society), while figure (b) is adapted with permission granted by author from Ref. [53], with the original pictures from Refs. [54] (Copyright (1994), with permission from Elsevier) and Ref.[55] (Copyright (2003), with permission from Springer.)

fabrication of metal electrodes on the surface of the sample composed of an epitaxially grown heterojunction of AlGaAs/GaAs semiconductor materials, on top of which the n-doped barrier material (AlGaAs) is deposited (Fig. 2.1 (a,b)). Some of the donor atoms in the barrier material become ionized, which creates a triangular quantum well formed by the band offset of the materials and the Coulomb potential of the donors. The excess electrons are confined in this quantum well, which lies below the surface of the sample. The density of the two-dimensional electron gas (2DEG) created in this geometry is further locally modulated by the electrostatic field from the surface gates. With a precisely chosen negative gate voltage, the area directly underneath is depleted of electrons, while the surface area between the gates translates into a shallow local potential minimum (Fig. 2.1 (a)). This local minimum of the potential can be populated by electrons tunneling from the edges of the 2DEG, and can be tuned to control the number of the confined electrons.

A single [11, 57–60], double, [61–63] and triple [52, 64–68] lateral gated quantum dot molecule in a GaAlAs/GaAs heterojunction with one electron each has been demonstrated experimentally and extensively studied theoretically [68–73]. In Chapter 4 it is shown that by tuning the voltage on the electrodes one can create an artificial magnetic moment in the system of four lateral quantum dots called a quadruple quantum dot molecule.

The most important experimental techniques used for characterizing the lateral gated quantum dots are tunneling spectroscopy [11, 74, 75] and charge sensing [57, 76–79]. In the tunneling spectroscopy the gated QD is connected to two metallic leads. One of them, the source, supplies the electrons, while the other, the drain, removes the electrons from the system. The measurement is carried out by applying a voltage between the source and the gate and tuning the energy of the QD by applying a voltage on one of the gates constituting the QD. The source-drain voltage as well as the coupling of the QD to leads are chosen so that only one electron at a time can be transported through the device.

From the measurement of the intensity of the tunneling current as a function of the gate voltage one can extract information about the charging energy of the QD - the energy that is needed to add $N + 1$ electron to a dot confining N electrons. Indeed, the tunneling current is detected only if the difference in

electrochemical potentials of the dot with $N+1$ and N electrons, $\mu(N+1)-\mu(N)$, is equal to the electrochemical potential of the leads, which is typically taken as a reference energy. As a result, measuring the tunneling current as a function of the gate voltage one expects a series of peaks, separated by gaps, which contain information about the spacing of single-particle energies and about the Coulomb interactions between carriers. On the other hand, from the measurement of the changes of the tunneling current as a function of the gate voltage when the bias between the source and the drain is larger, one can obtain the information about the energies of the ground and excited states of the $N+1$-electron QD.

Another tool, very useful in investigating coupled QDs off-resonance (i.e., when no tunneling current can be detected), is charge sensing. Indeed, the conditions necessary for the tunneling current to be detected are much more stringent in coupled QDs than in single QDs. In the low source-drain bias regime, the alignment of electrochemical potentials has to exist not only between the dots and the leads, but between each tunnel-coupled pair of dots. The charge-sensing spectroscopy is not subjected to these conditions and can detect internal charge redistribution in the system even if it is not tunnel-coupled to the leads. There were several implementations of electrometers coupled to a quantum dot, however the most commonly used is a quantum point contact (QPC) [76, 78, 79]. The quantum point contact is a narrow channel in the 2DEG defined by additional metalic electrodes deposited in the vicinity of the QDs (as shown in Fig. 2.1 (b)). Since the conductance of the QPC depends strongly on the charge configurations of the nearby QDs, by measuring the current flowing through the QPC one can indeed learn about the transitions in charge distribution in the system.

A relatively simple method of producing an array of quantum potentials in which *electrons and holes* are confined in discrete quasi-atomic (or zero-dimensional) energy states, are epitaxial growth of self-assembled QDs (SAD) [54, 80–83]. Self-assembled QDs are spontaneously formed when a few monolayers of a semiconductor material are deposited on a substrate with a lattice mismatch between 1-10%. The first deposited layers of the new material crystallize on the substrate in the form of strongly strained epitaxial layers, with the lattice constant equal to the lattice constant of the substrate. The strain in the deposited material grows with the increase of its thicknes. After reaching a certain critical thickness (of

the order of a few monolayers), the additional material forms *small, randomly distributed islands* to reduce the strain in the structure. This phase transition is called *Stranski-Krastanov* [84] transition. If the growth of the new semiconducting material is continued after the critical point, the diameter and height of islands continue to grow (Fig. 2.1 (b)). Additionally, the size and shape of the self-organized islands depends on the magnitude of the strain in the material (depending on the lattice mismatch between the substrate and new deposited material) and the temperature during the growth. If the growth of the new material is stopped right after the phase transition, the islands evolve to the shape minimizing the surface energy: a lens on top of a thin *wetting layer* (Fig. 2.1 (b)). After the deposition of a thin layer of the substrate material on top of the suface of the array of islands, one obtains a sample with randomly distributed droplets of one semiconductor embedded in the other semiconducting material. The SADs fabricated this way have a diameter of tens of nanometers, while their hight is of the order of a few nanometers. By varying the materials involved, the growth conditions, and by vertically stacking layers of nanostructures, a rich variety of materials can be produced for the study of the fundamental properties of strongly confined systems, and for the development of electronic and photonic devices.

However, the main problem associated with this method is the size non-uniformity and the lack of the control of the position of the QD grown in such a way. There were many approaches to control the dimensions and position of the self-assembled QDs [85–88]. One of the methods is the nano-template technique, in which the growth of the QDs is constrained by deposition of a mask on the substrate, in which the small openings are etched [87, 89]. The growth of deposited material on a substrate prepared in this way takes place only in pre-defined openings in the mask, leading to a formation of 3D pyramids. If the first deposited material is the material of the substrate, and this proces is stoped before the growth of the pyramid is completed, a small plateau is formed on the top of the pyramid structure (Fig. 2.2 (b)). The QD material is deposited at this stage, it continues the growth of the pyramid. Depending on the size of this plateau, one or more QDs are formed once the Stranski-Krastanov phase transition is reached. As previously, a thin layer of the substrate material is then deposited. To tune

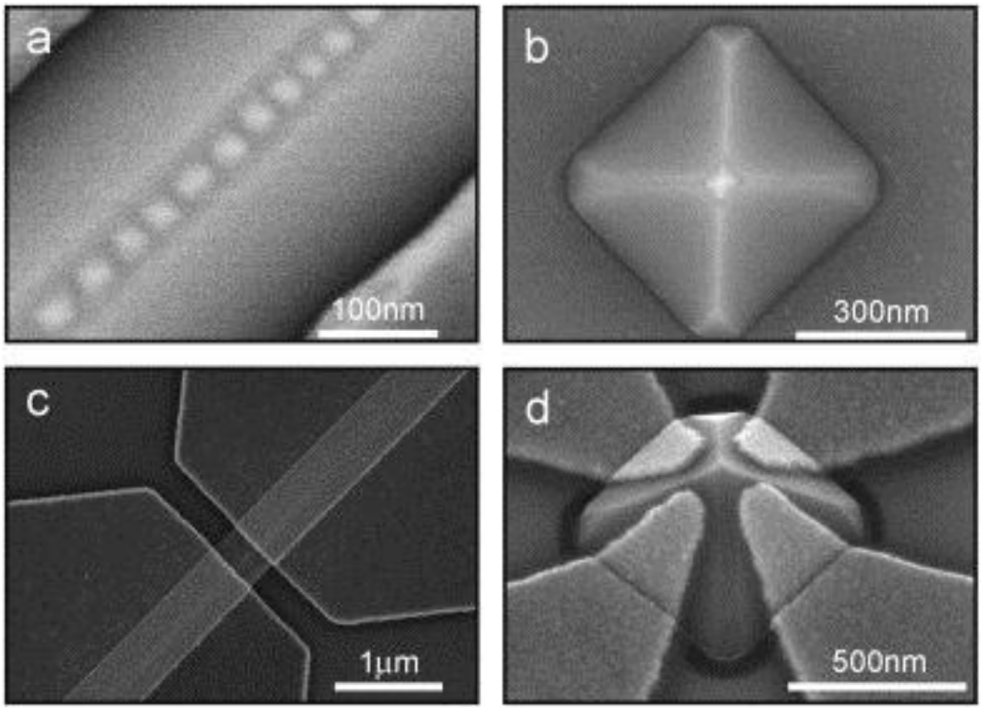

Figure 2.2: SEM micrographs of: (a) an uncappped "stripe geometry" ridge. A linear array of InAs QDs is seen at the apex of the ridge. (b) A single QD at the apex of a square based pyramidal nanotemplate. (c) A gated ridge. The InAs QDs in (a) are capped prior to gate deposition. (d) A gated pyramid with a buried individual QD. Figures are reprinted from Ref. [87], Copyright (2008), with permission from Elsevier.

the properties of the QDs like inter-shell spacing, or a number of confined carriers, one can deposit metalic gates on the sides of the pyramid (Fig. 2.2 (d)). The creation of the long chains of QDs on the elongated rectangular pyramids has been also reported in Refs. [86, 87, 89] (Fig. 2.2 (a))

The advantage of the self-assembled QDs over the lateral gated QDs is the fact that one can use optical methods to probe their electronic properties, since they confine both electrons and valence holes. A widely used technique is photoluminescence (PL) spectroscopy [30, 55, 83], in which the barrier material is excited by laser light to create excitons. The excitons migrate from the barrier to the QD in which they become confined. The radiative lifetime of the excitons

in the QD is longer than their relaxation time. This is why, after reaching the QD material, the excitons relax into their ground state and then recombine with a simultaneous emission of a photon. The emitted photons have an energy equal to that of the electron-hole pair existing prior to recombination. If there are N excitons in the QD prior to the recombination, after recombination there are $N-1$ excitons in either ground or excited state. The energies of the emitted photons provide information about the difference betwen the ground state energy of the N-exciton complex, and the energies of the ground and excited states of the $N-1$ exciton complex.

2.2 Approximation of the QD confining potential

The wave functions of carriers confined in SADs extend over the volume of the semiconductor containing typically a few milion atoms. For such a system *ab initio* methods cannot be used to calculate the electronic and optical properties. However, with the development of computational power in the recent years, it became possible to model the QD structures using an atomistic tight-binding aproach [91–94]. In this method, the QD of a chosen shape as well as barrier material are constructed atom by atom. The positions of all atoms are adjusted to minimize the total elastic energy, which arises from the mismatch of lattice constants of the constituent materials. Having obtained the equllibrium positions of all the atoms, one can start the calculations of the single-particle energies and wave functions of electrons and/or holes confined in the QD. In this calculation typically a basis of ten electron orbitals per atom is taken, and the tight-binding Hamiltonian is built out of terms describing the energies of these orbitals and terms describing the coupling (hopping) between different orbitals on different atoms. The shapes of SADs most commonly realized experimentally are the lens or the disk, and their models are shown in Fig. 2.3 (a). The result of the atomistic tight-binding calculation of the single-particle energy spectrum for these SADs is shown in Fig. 2.3 (b), where the single-particle energies of the electron are marked in blue, and those of the hole are in red [94]. The single-particle states

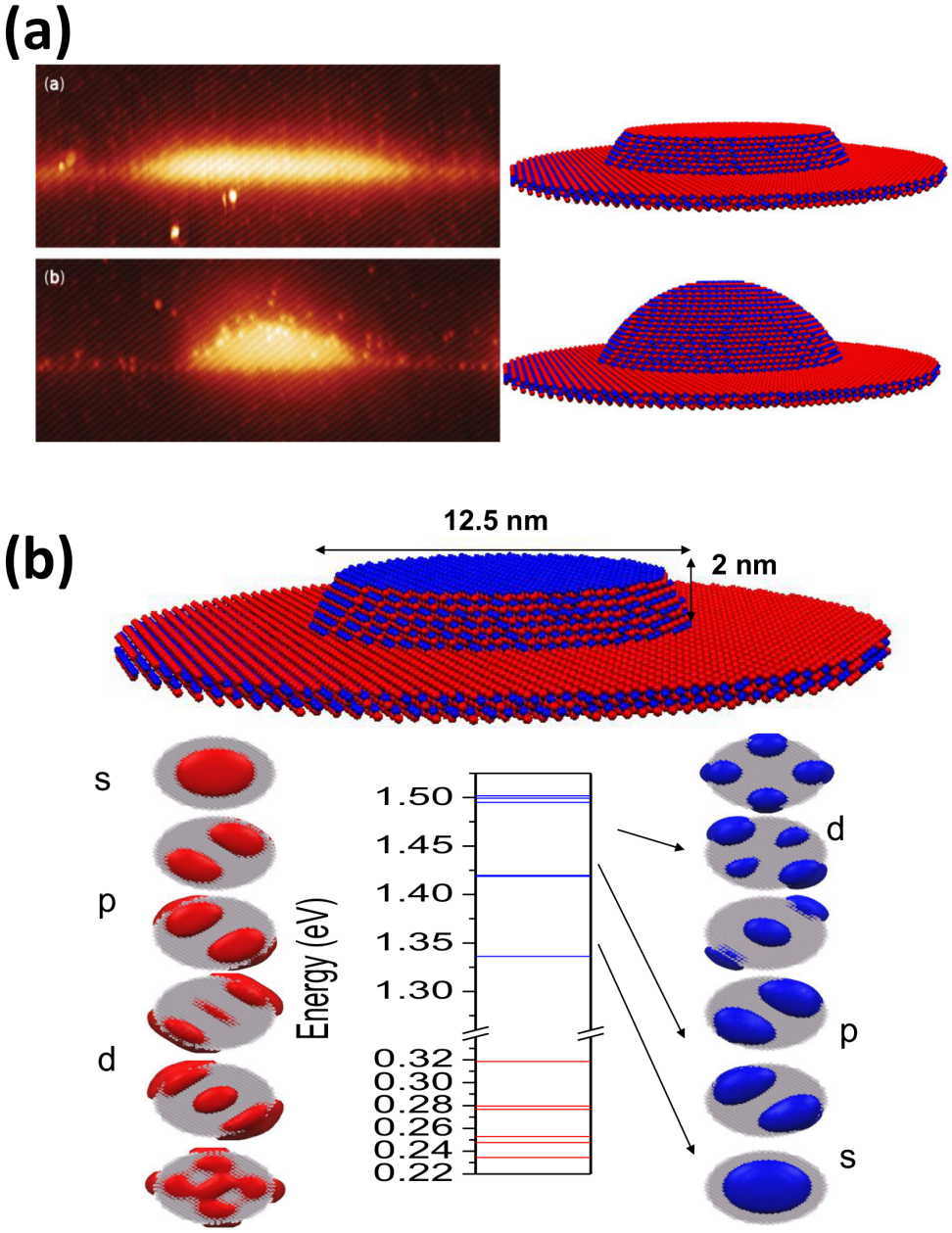

Figure 2.3: (a,left) X-STM images of a lens and disk shaped QDs reprinted with permission from Ref. [90] Copyright (2011), American Institute of Physics. Model images (a, right and (b)) by courtesy of Drs. M. Korkusinki and M. Zielinski from NRC

for both carriers have a shell structure, with the lowest energy state of the s-type symmetry (non-degenerate), second doubly-degenerate shell with the p-type symmetry, and third shell with three almost degenerate states of the d-symmetry.

Another method of finding the single-particle states of the electron and hole confined in the QD is through solving the Schrödinger equation in the effective mass approximation [95–97], with the confining potential of the QD approximated by a smooth analyticaly solvable potential (like a square, a parabola, a gaussian).

The most commonly used model confining potential of the QD is a quasi-2D parabolic potential. The single-particle shell structure in such potential very closely resembles the shell structure obtained by computationaly expensive atomistic calculations, while it has the advantage of having an analytical solution for the wave functions, as well as closed-form expressions for Coulomb interaction matrix elements. It was succesfully used in modeling of gated dot devices [9, 98, 99] as well as lens-shaped self-assembled QDs [100–104].

Additionaly, far-infrared absorption measurements [105, 106], high excitation photoluminescence [9], capacitance spectroscopy [60], compared with numerical calculations [95, 101], and measurements of the evolution of the single-particle states in the magnetic field [107] confirm that in lens-shaped quasi-two-dimensional SADs the bound states of both electrons and valence-band holes can be well understood assuming an effective quasi-2D parabolic confinement.

For that reason we study a quasi-2D parabolic quantum dot (QD) [60, 104] in the effective-mass approximation (EMA) (Appendix A.1). The confining potential is divided into the isotropic parabolic part and the anisotropic correction. The influence of the anisotropy on the electronic and optical properties of the QD is revealed, e.g., in the exciton fine structure [108] and the splitting of the p-shell [109].

The Hamiltonian of a single electron with mass m_e^*, confined by a two-dimensional parabolic potential with the characteristic frequency ω_0^e, in the presence of an external magnetic field B perpendicular to the dot plane, has the following form [60, 95, 104]:

$$\hat{H} = \frac{1}{2m_e^*}\left(\hat{\mathbf{p}} + \frac{e}{c}\mathbf{A}\right)^2 + \frac{1}{2}m_e^*\omega_0^{e2}r^2 + g_e\mu_B B\sigma, \tag{2.1}$$

where e is the electron charge, c is the velocity of light and $\mathbf{A}$ is the vector potential, which is taken in the symmetric gauge $\mathbf{A} = [-By/2, Bx/2, 0]$. The last term of this Hamiltonian is the electron Zeeman term, with g_e being the electron Lande factor, μ_B - the Bohr magneton, and $\sigma = \pm\frac{1}{2}$ $(\downarrow, \uparrow)$ - the z component of the spin of the electron.

Using the effective Rydberg ($Ry^* = m^* e^4/2\varepsilon^2\hbar^2$) as the energy unit, and the effective Bohr radius ($a_B = \varepsilon\hbar^2/m_e^* e^2$) as the unit of length (ε is the dielectric constant of the material and $\hbar$ is the reduced Planck constant), the Hamiltonian 2.1 can be rewritten as:

$$\begin{aligned} \hat{H} = & - \left(\frac{\partial^2}{\partial x_{aB}^2} + \frac{\partial^2}{\partial y_{aB}^2}\right) + \frac{1}{4}\Omega_h^{e\,2}\left(x_{aB}^2 + y_{aB}^2\right) \\ & - \frac{i}{2}\Omega_c^e\left(x_{aB}\frac{\partial}{\partial y_{aB}} - y_{aB}\frac{\partial}{\partial x_{aB}}\right) + g_e\mu_B B\sigma. \end{aligned} \tag{2.2}$$

Ω_h^e is the *hybrid frequency* defined as $\Omega_h^{e\,2} = \Omega_0^{e\,2} + \frac{1}{4}\Omega_c^e$, the x_{aB} and y_{aB} are the coordinates describing the position of the electron expressed in units of the Bohr radius, and $\Omega_c^e = \frac{eB}{m_e^* c}/Ry^*$ is the cyclotron energy expressed in Rydbergs.

The eigenstates of the Hamiltonian 2.2 are called the Fock-Darwin states [110, 111], and can be written in an analytical form:

$$\Psi_{n_r,m}(r,\phi) = \frac{1}{l_h^e}\sqrt{\frac{n_r!}{(n_r+|m|)!}}e^{\frac{r^2}{4l_h^{e\,2}}}\left(\frac{r}{\sqrt{2}l_h^e}\right)^{|m|} L_{n_r}^{|M|}\left(\frac{r^2}{2l_h^{e\,2}}\right)\frac{1}{\sqrt{2\pi}}e^{im\phi}, \tag{2.3}$$

where

$$L_{n_r}^{|m|}(x) = \sum_{k=0}^{n_r}(-1)^k\begin{pmatrix} n_r+|m| \\ n_r-k \end{pmatrix}\frac{x^k}{k!} \tag{2.4}$$

are Laguerre polynomials. In this formula, n_r is given by $n_r = \frac{n-|m|}{2}$, where n is the shell number and $m = -n, -n+2 \ldots n-2, n$ defines the angular momentum of the state.

It is useful to introduce the inter-Landau-level lowering and rising operators a, a^+, as well as the intra-Landau-level lowering and raising operators b and b^+

[60], defined as:

$$\begin{array}{ll} a = \frac{1}{2}\left(\frac{1}{\sqrt{2}}\frac{z}{l_h^e} + \sqrt{2}l_h^e\partial_z^*\right) & a^+ = \frac{1}{2}\left(\frac{1}{\sqrt{2}}\frac{z*}{l_h^e} - \sqrt{2}l_h^e\partial_z\right) \\ b = \frac{1}{2}\left(\frac{1}{\sqrt{2}}\frac{z*}{l_h^e} + \sqrt{2}l_h^e\partial_z\right) & b^+ = \frac{1}{2}\left(\frac{1}{\sqrt{2}}\frac{z}{l_h^e} - \sqrt{2}l_h^e\partial_z^*\right), \end{array} \tag{2.5}$$

where the complex variables z and z^* are defined by:

$$\begin{array}{ll} z = x - iy & z* = x + iy \\ \partial_z = \partial_x + i\partial_y & \partial_z^* = \partial_x - i\partial_y, \end{array} \tag{2.6}$$

with the hybrid length $l_h^e = \frac{1}{\sqrt{\Omega_h^e}}$ in the units of the effective Bohr radius a_B.

The harmonic-oscillator operators a, a^+ and b, b^+ fulfill the bosonic commutation relations: $[a, a^+] = 1, [b, b^+] = 1$, while any commutator of a (a^+) with b (b^+) is zero. This means that the operators a and a^+ are independent from operators b and b^+, which ensures independence of the excitations of the 2D harmonic oscillator in z and z^* direction.

The Hamiltonian given by Eq. 2.2 can now be rewritten in the form of the 2D harmonic oscillator (HO) with the eigenfrequences $\Omega_\pm^e = \Omega_h^e \pm \frac{1}{2}\Omega_c^e$ [60]:

$$\hat{H} = \Omega_+^e\left(a^+a + \frac{1}{2}\right) + \Omega_-^e\left(b^+b + \frac{1}{2}\right), \tag{2.7}$$

The eigenstates of the Hamiltonian, Eq. 2.7, can be expressed in the following form:

$$|n_+^e, n_-^e, \sigma\rangle = \frac{1}{\sqrt{n_+^e! n_-^e!}}(a^+)^{n_+^e}(b^+)^{n_-^e}|00\rangle\chi(\sigma)\,. \tag{2.8}$$

where $n_+^e = a^+a$, and $n_-^e = b^+b$ are the quantum numbers describing this state. The $|n_+^e, n_-^e, \sigma\rangle$ state corresponds to the eigenenergy [60, 107]:

$$\varepsilon_{n_+^e, n_-^e} = \hbar\Omega_+^e(n_+^e + \frac{1}{2}) + \hbar\Omega_-^e(n_-^e + \frac{1}{2}) + g_e\mu_B B\sigma. \tag{2.9}$$

Quantum numbers (n_+^e, n_-^e) are related to quantum numbers (n_r, m) by relations: $n = n_-^e + n_+^e$, $m = n_-^e - n_+^e$.

Each of the single-particle states has the angular momentum L_e given by: $L_e = n_-^e - n_+^e$. One can create the excitations from the HO state $|n_+, n_-, \sigma\rangle$ by

applying the ladder operators on HO states in the following way:

$$\begin{aligned} a^+|n_+,n_-,\sigma\rangle &= \sqrt{n_+ + 1}|n_+ + 1, n_-, \sigma\rangle, \\ a|n_+,n_-,\sigma\rangle &= \sqrt{n_+}|n_+ - 1, n_-, \sigma\rangle, \\ b^+|n_+,n_-,\sigma\rangle &= \sqrt{n_- + 1}|n_+, n_- + 1, \sigma\rangle, \\ b|n_+,n_-,\sigma\rangle &= \sqrt{n_-}|n_+, n_- - 1, \sigma\rangle. \end{aligned} \tag{2.10}$$

Since the angular momentum of the electron in the state $|n_+^e, n_-^e, \sigma\rangle$ is defined as $L_e = n_+^e - n_-^e$, the operator $a^+(b^+)$ creates an excitation of the electron with the angular momentum increased (decreased) by one unit.

In the absence of the magnetic field the eigenstates form shells with energy $E_{B=0} = \hbar\Omega_0^e(n_+^e + n_-^e + 1)$, since $\Omega_+^e = \Omega_-^e = \Omega_0^e$. Degeneracy of shells grows with the shell number and is given by $g_s = 2(n_+^e + n_-^e + 1)$. The first shell - s, with $(n_+^e, n_-^e) = (0, 0)$, has only one level with angular momentum $L_e = 0$. The p shell is doubly degenerate where one state is characterized by $(n_+^e, n_-^e) = (0, 1)$ with angular momentum $L_e = 1$ and the second: $(n_+^e, n_-^e) = (1, 0)$ with angular momentum $L_e = -1$ - as shown in Fig. 2.4 (a).

For flat self-assembled QDs with a relatively weak confinement, the strain present in the QD lifts the degeneracy of the heavy-hole (hh) and light-hole (lh) states at the top of the valence band [112]. This hh-lh splitting is significant enough to justify the approximation in which the hh-lh mixing can be neglected. This allows us to consider only the heavy hole states.

The single-heavy-hole Hamiltonian can be written in the form analogous to Eq. 2.2, scaled with the heavy-hole effective mass m_h^*, positive charge $(+e)$, and the hole characteristic frequency Ω_0^h:

$$\begin{aligned} \hat{H} = &- \frac{m_e^*}{m_h^*}\left(\frac{\partial^2}{\partial x_{aB}^2} + \frac{\partial^2}{\partial y_{aB}^2}\right) + \frac{1}{4}\frac{m_h^*}{m_e^*}\Omega_h^{h\,2}\left(x_{aB}^2 + y_{aB}^2\right) \\ &+ \frac{i}{2}\Omega_c^h\left(x_{aB}\frac{\partial}{\partial y_{aB}} - y_{aB}\frac{\partial}{\partial x_{aB}}\right) + g_h\mu_B B\tau. \end{aligned} \tag{2.11}$$

As previously, energies are expressed in electronic Rydbergs, and lengths in electronic Bohr radii. Single-hole states are labeled by $|n_+^h, n_-^h, \tau\rangle$, where $\tau = \pm\frac{3}{2}\,(\Downarrow, \Uparrow)$.

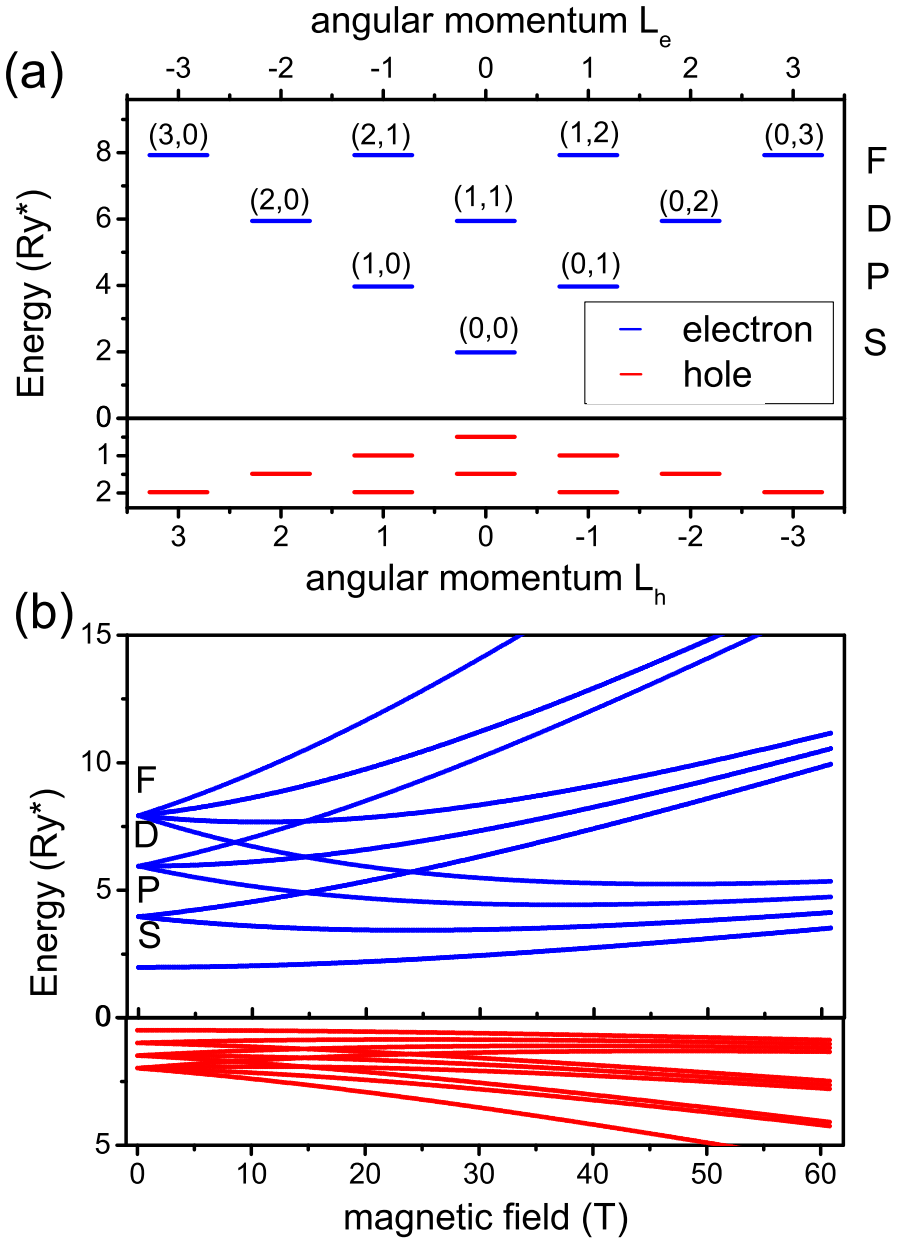

Figure 2.4: The energy spectrum of an electron (blue) and a hole (red) in a two-dimensional parabolic potential (a) as a function of angular momentum L for $B = 0$, (b) as a function of the magnetic field B. The first four of the single-particle shells are shown.

The energies corresponding to these states are given by $\varepsilon_{n_+^h,n_-^h} = \hbar\Omega_+^h(n_+^h + \frac{1}{2}) + \hbar\Omega_-^h(n_-^h + \frac{1}{2}) + g_h\mu_B B\tau$. In the absence of the magnetic field these energies also form shells: $\varepsilon^{B=0}_{n_+^h,n_-^h} = \hbar\Omega_0^h(n_+^h + n_-^h + 1)$ (Fig. 2.4 (a)). The operators $n_+^h = c^+c$ and $n_-^h = d^+d$ are defined with the bosonic operators for the hole:

$$\begin{array}{ll} d = \frac{1}{2}\left(\frac{1}{\sqrt{2}}\frac{z}{l_h^h} + \sqrt{2}l_h^h\partial_z^*\right) & d^+ = \frac{1}{2}\left(\frac{1}{\sqrt{2}}\frac{z^*}{l_h^h} - \sqrt{2}l_h^h\partial_z\right) \\ c = \frac{1}{2}\left(\frac{1}{\sqrt{2}}\frac{z^*}{l_h^h} + \sqrt{2}l_h^h\partial_z\right) & c^+ = \frac{1}{2}\left(\frac{1}{\sqrt{2}}\frac{z}{l_h^h} - \sqrt{2}l_h^h\partial_z^*\right), \end{array} \tag{2.12}$$

The HO length for hole in the electronic Bohr radius units is $l_h^h = \sqrt{\frac{m_e^*}{m_h^*\Omega_h^h}}$.

Since we define the angular momentum of the hole occupying the state $|n_+^h, n_-^h, \tau\rangle$ by $L_h = n_-^h - n_+^h$, the operator $c^+(d^+)$ creates an excitation of the hole with the angular momentum decreased (increased) by one unit.

The shell structure of the single-particle levels of an electron and a hole, confined in the potential of the two-dimensional harmonic oscillator in the absence of the magnetic field, is shown in Fig. 2.4 (a). To show the increasing degeneracy of the levels, they are presented for each of the angular momentum $L = n_+ - n_-$ separately. The quantum numbers (n_+^e, n_-^e) have been assigned to each of the single-particle levels of the electron. Since the angular momentum of the hole is decreasing from left to right, one can assign the quantum numbers to the single-particle levels of the hole in the same way as it is done to electronic states (mirroring them). In the energy spectra presented in such a way, the optical transitions are vertical. The harmonic oscillator frequencies used in the calculation of the single-particle energies are $\Omega_e = 24$ meV and $\Omega_h = 6$ meV. Magnetic field calculations were done with Lande factors choosen to be $g_e = g_h = 0$ to show only the magnetic field dependence of the single-particle levels of the harmonic oscillator.

If $m_e\Omega_0^e = m_h\Omega_0^h$, the Hamiltonian for the hole can be expressed by the Hamiltonian of the electron: $H_h = \frac{m_e}{m_h}(H_e)^*$. In this symmetric case, the following relations between the electron and the hole eigenenergies and wavefunctions exist: $E_h = E_e\frac{m_e}{m_h}$ and $H_h(r) = F_e^*(r)$. In this case the HO lengths for the electron and the hole are equal: $l_h^h = \sqrt{\frac{m_e^*}{m_h^*\Omega_h^h}} = \sqrt{\frac{1}{\Omega_h^e}} = l_h^e$.

2.3 Anisotropy correction to the symmetric 2DHO potential

In this section a small anisotropy of the confining potential will be introduced. It is assumed here that the single-particle lateral confinement of the dot is elliptical, and can be described by two characteristic frequencies, Ω_x and Ω_y. The Hamiltonian of the electron can be divided into two terms:

$$\begin{aligned} \hat{H}^e_{anis} &= \frac{1}{4}\Omega^2_{x,e}x^2 + \frac{1}{4}\Omega^2_{y,e}y^2 \\ &= \frac{1}{4}\left(\frac{\Omega^2_{x,e}+\Omega^2_{y,e}}{2}\left(x^2+y^2\right) + \frac{\Omega^2_{x,e}-\Omega^2_{y,e}}{2}\left(x^2-y^2\right)\right) \\ &= \frac{1}{4}\Omega^2_{0,e}r^2 + \frac{1}{4}\Omega^2_{0,e}\gamma_e\left(x^2-y^2\right), \end{aligned} \tag{2.13}$$

where the first term describes a cylindrically symmetric component of the parabolic confinement, with the characteristic frequency being the geometrical average of the two confinement frequencies Ω_x and Ω_y, $\Omega^2_{0,e} = \frac{1}{2}\left(\Omega^2_{x,e}+\Omega^2_{y,e}\right)$. The second term is the anisotropic correction to this potential and it is proportional to the anisotropy parameter defined as $\gamma_e = \left(\Omega^2_{x,e}-\Omega^2_{y,e}\right)/\left(\Omega^2_{x,e}+\Omega^2_{y,e}\right)$ [113]. The characteristic frequency in the above equations is expressed in effective Rydbergs, while the x^2 and y^2 are in the effective Bohr radius units. The same transformation can be done for the Hamiltonian of the hole, and the characteristic frequency $\Omega_{0,h}$ as well as the anisotropy parameter for hole γ_h can be obtained. If $\gamma_{e(h)} = 0$ then the potential is symmetric.

The x^2 and y^2 operators can be expressed in terms of the HO raising and lowering operators (Eqs. 2.5 and 2.12):

$$\begin{aligned} x_e &= \frac{l^e_h}{\sqrt{2}}\left(a + a^+ + b + b^+\right), \\ y_e &= \frac{l^e_h}{\sqrt{2}}\left(a - a^+ - b + b^+\right), \\ x_h &= \frac{l^h_h}{\sqrt{2}}\left(c + c^+ + d + d^+\right), \\ y_h &= \frac{l^h_h}{\sqrt{2}}\left(-c + c^+ + d - d^+\right). \end{aligned} \tag{2.14}$$

The anisotropic Hamiltonian $\delta\hat{H}^{e(h)}_{anis} = \frac{1}{4}\Omega^2_{0,e(h)}\gamma_{e(h)}\left(x^2_{e(h)} - y^2_{e(h)}\right)$ for the electron (hole) can now be written in terms of the HO operators as well. For example, for the electron anisotropy Hamiltonian:

$$\begin{aligned}\delta\hat{H}^{e}_{anis} &= \frac{1}{4}\Omega^2_{0,e}\gamma_e\left(x^2_e - y^2_e\right) \\ &= \frac{1}{4}\Omega^2_{0,e}\gamma_e l^{e\,2}_h\left(aa + a^+a^+ + bb + b^+b^+ + 2a^+b + 2ab^+\right) \end{aligned} \quad (2.15)$$

where the commutation relations between operators $a(a^+)$ and $b(b^+)$ have been used. The matrix elements of this Hamiltonian between single-particle states $\langle L| = \langle i(n_+, n_-)|$ and $|R\rangle = |j(k_+, k_-)\rangle$ can be now evaluated:

$$\begin{aligned}&\langle i(n_+,n_-)|\delta\hat{H}^{e(h)}_{anis}|j(k_+,k_-)\rangle \quad (2.16)\\ =\ &\frac{1}{4}\Omega^2_{0,e}\gamma_e l^{e\,2}_h\langle i(n_+,n_-)\left(aa + a^+a^+ + bb + b^+b^+ + 2a^+b + 2ab^+\right)|j(k_+,k_-)\rangle \\ =\ &\frac{\Omega^2_{0,e}}{4\Omega^e_h}\gamma_e\Big[\sqrt{k_+\left(k_+-1\right)}\delta_{n_-,k_+-2}\delta_{n_+k_-} + \sqrt{\left(k_++1\right)\left(k_++2\right)}\delta_{n_-,k_++2}\delta_{n_+k_-} \\ +\ &\sqrt{k_-\left(k_--1\right)}\delta_{n_-k_+}\delta_{n_+,k_--2} + \sqrt{\left(k_-+1\right)\left(k_-+2\right)}\delta_{n_-}\delta_{n_+,k_-+2} \\ +\ &2\sqrt{\left(k_++1\right)k_-}\delta_{n_-,k_++1}\delta_{n_+,k_--1} + 2\sqrt{k_+\left(k_-+1\right)}\delta_{n_-,k_+-1}\delta_{n_+,k_-+1}\Big].\end{aligned}$$

The anisotropic correction to the confining potential for holes has the same form. These corrections break the rotational symmetry of the quantum dot and mix those single-particle states with angular momenta which differ by two.

The anisotropy parameters $\gamma_{e(h)}$ are related to the more commonly used ratio:

$$\frac{\Omega_{y,e(h)}}{\Omega_{x,e(h)}} = \sqrt{\frac{1-\gamma_{e(h)}}{1+\gamma_{e(h)}}} \quad (2.17)$$

2.4 The problem of many interacting particles in a QD

In the previous section the discussion of the problem of a single particle - electron or hole, confined in the parabolic potential of the quantum dot was presented. Now, the single-particle orbitals are populated with several interacting

carriers. In the simplest approach one can construct the many-body states as Slater determinants of occupied orbitals. These determinants will be referred to as *configurations*. The energies of such configurations are built out of the single-particle energies of occupied orbitals, as well as the direct and exchange Coulomb interactions between carriers. However, in what follows it will be shown that the configurations are not eigenstates of the Hamiltonian of the interacting particles. In fact, the eigenstates will be sought in the form of *correlated states*, constructed as *linear combinations* of configurations. This is the essence of the configuration-interaction approach, whose details will be presented in the following.

2.4.1 Many body Hamiltonian

The Hamiltonian of the interacting N_e electrons and N_h holes confined in the general single-particle potential $U(\mathbf{r})$ in the presence of the external magnetic field has the form:

$$\begin{aligned}\hat{H}_{eh} &= \sum_i^{N_e}\left[\frac{1}{2m_e^*}\left(\hat{\mathbf{p}}_\mathbf{i}+\frac{e}{c}\mathbf{A}_\mathbf{i}\right)^2+U_e(\mathbf{r}_i)+g_e\mu_B B\sigma_i\right]\\ &+ \sum_i^{N_h}\left[\frac{1}{2m_h^*}\left(\hat{\mathbf{p}}_\mathbf{i}-\frac{e}{c}\mathbf{A}_\mathbf{i}\right)^2+U_h(\mathbf{r}_i)+g_h\mu_B B\tau_i\right]\\ &+ \frac{1}{2}\sum_{i\neq j}^{N_e}\frac{e^2}{\varepsilon(\mathbf{r}_i-\mathbf{r}_j)}+\frac{1}{2}\sum_{i\neq j}^{N_h}\frac{e^2}{\varepsilon(\mathbf{r}_i-\mathbf{r}_j)}-\sum_{i,j}^{N_e,N_h}\frac{e^2}{\varepsilon(\mathbf{r}_i-\mathbf{r}_j)},\end{aligned} \tag{2.18}$$

where the notation is the same as used in Section 2.2. The first two terms correspond to the single-particle spectrum of N_e electrons and N_h holes.The remaining terms introduce the Coulomb interactions between electrons, between holes, and between electrons with holes.

In this work the confining potential is the two-dimensional harmonic oscillator, and the solution of the single-particle part of the Hamiltonian, Eqs. 2.2 and 2.11, has been described in Section 2.2. One can introduce two sets of creation and anihilation operators: $c_{i\sigma}^+$ ($c_{i\sigma}$) and $h_{i\tau}^+$ ($h_{i\tau}$), which create (anihilate) an electron (with the spin σ) or a hole (with a spin τ), on the single-particle orbital i with the energy ε_i. The creation and annihilation operators obey the anticommutaion

rules:

$$\begin{array}{ll} \{c_{i\sigma}, c^+_{j\sigma'}\} = \delta_{ij}\delta_{\sigma\sigma'} & \{c^+_{i\sigma}, c^+_{j\sigma}\} = \{c_{i\sigma}, c_{j\sigma}\} = 0, \\ \{h_{i\tau}, h^+_{j\tau'}\} = \delta_{ij}\delta\tau\tau' & \{h^+_{i\tau}, h^+_{j\tau}\} = \{h_{i\tau}, h_{j\tau}\} = 0, \end{array} \tag{2.19}$$

to fulfill the Fermi statistics.

Using these operators, one can introduce field operators for electrons and holes expanded in the basis of the single-particle wave functions $\phi^i_{c\sigma}$ and $\phi^i_{v\tau}$, Eq. 4:

$$\begin{array}{ll} \psi_e(\mathbf{r}) = \sum_{i\sigma} \phi^i_{c\sigma}(\mathbf{r})\, c_{i\sigma} & \psi^+_e(\mathbf{r}) = \sum_{i\sigma} {\phi^i_{c\sigma}}^*(\mathbf{r})\, c^+_{i\sigma} \\ \psi_h(\mathbf{r}) = \sum_{i\tau} \phi^i_{v\tau}(\mathbf{r})\, h_{i\tau} & \psi^+_h(\mathbf{r}) = \sum_{i\tau} {\phi^i_{v\tau}}^*(\mathbf{r})\, h^+_{i\tau} \end{array}. \tag{2.20}$$

The second quantzation form of the Hamiltonian $\hat{H}_{eh}$ of interacting electrons and holes can be derived by calculation of the matrix elements of all terms of the Hamiltonian, Eq. 2.18, between the field operators, Eq. 2.20. For example, the electron single-particle part of the Hamiltonian takes the form:

$$\begin{aligned} & \langle\psi_e| \left[\frac{1}{2m^*_e}\left(\hat{\mathbf{p}}_\mathbf{i} + \frac{e}{c}\mathbf{A}_\mathbf{i}\right)^2 + U_e(\mathbf{r}_i) + g_e\mu_B B\sigma_i\right] |\psi_e\rangle \qquad (2.21) \\ = & \sum_{j\sigma,k\sigma'} \int d\mathbf{r} {\phi^j_{c\sigma}}^*(\mathbf{r}) \left[\frac{1}{2m^*_e}\left(\hat{\mathbf{p}}_\mathbf{i} + \frac{e}{c}\mathbf{A}_\mathbf{i}\right)^2 + U_e(\mathbf{r}_i) + g_e\mu_B B\sigma_i\right] \phi^k_{c\sigma'}(\mathbf{r})\, c^+_{j\sigma} c_{k\sigma'}, \\ = & \sum_{i\sigma} \varepsilon^e_{i\sigma} c^+_{i\sigma} c_{i\sigma}, \end{aligned}$$

since the wave functions $\phi^k_{c\sigma}(\mathbf{r})$ are the eigenfunctions of this part of the Hamiltonian.

The electron-electron Coulomb interaction matrix element:

$$\langle\psi_e| \frac{e^2}{\varepsilon(\mathbf{r}_i - \mathbf{r}_j)} |\psi_e\rangle = \sum_{ijkl} \sum_{\sigma,\sigma',\sigma'',\sigma'''} V_{ee}(i\sigma, j\sigma'|k\sigma'', l\sigma''') c^+_{i\sigma} c^+_{j\sigma'} c_{k\sigma''} c_{l\sigma'''}, \tag{2.22}$$

where in general the matrix element $V_{ee}(i\sigma, j\sigma'|k\sigma'', l\sigma''')$ is defined as (in Ry^*):

$$V_{ee}(i\sigma, j\sigma'|k\sigma'', l\sigma''') = \int\int d\mathbf{r}_1 d\mathbf{r}_2 \phi^+_{i\sigma}(\mathbf{r}_1)\phi^+_{j\sigma'}(\mathbf{r}_2) \frac{2}{|\mathbf{r}_1 - \mathbf{r}_2|} \phi_{k\sigma''}(\mathbf{r}_2)\phi_{l\sigma'''}(\mathbf{r}_1), \tag{2.23}$$

The electron wave functions $\phi_{i\sigma}(\mathbf{r})$ are products of the envelope function $F^j_c(\mathbf{r})$- slowly warying with $\mathbf{r}$, and the periodic part of the Bloch function $u_{c\sigma}(\mathbf{r})$, as

defined by Eq. A4 in the Appendix A.1. This integral can be approximated by:

$$V_{ee}(i\sigma, j\sigma'|k\sigma'', l\sigma''') \tag{2.24}$$
$$= \delta_{\sigma,\sigma'''}\delta_{\sigma',\sigma''} \int\int d\mathbf{r}_1 d\mathbf{r}_2 F^+_{i\sigma}(\mathbf{r}_1) F^+_{j\sigma'}(\mathbf{r}_2) \frac{2}{|\mathbf{r}_1 - \mathbf{r}_2|} F_{k\sigma''}(\mathbf{r}_2) F_{l\sigma'''}(\mathbf{r}_1),$$

where $F_{i\sigma}(\mathbf{r})$ is the ith single-particle wave function of an electron with the spin σ confined in the parabolic potential of the QD (the conduction band symbol 'c' has been droped here) and the integration over the microscopic part has been carried out. This matrix element has a non-zero value only if the spin of the orbital i - σ (j - σ') is the same as the spin of the orbital l -σ''' (k - σ''), however the spin of the orbital i can be different than that of the orbital j. Using that information, the integral takes the form:

$$V_{ee}(i\sigma, j\sigma'|k\sigma', l\sigma) = \int\int d\mathbf{r}_1 d\mathbf{r}_2 F^+_{i\sigma}(\mathbf{r}_1) F^+_{j\sigma'}(\mathbf{r}_2) \frac{2}{|\mathbf{r}_1 - \mathbf{r}_2|} F_{k\sigma'}(\mathbf{r}_2) F_{l\sigma}(\mathbf{r}_1). \tag{2.25}$$

The electron-electron Coulomb matrix elements in the harmonic oscillator basis have an analytical form [114] and will be discussed in the next section.

The full Hamiltonian $\hat{H}_{eh}$ of interacting electrons and holes in the second quantized notation, written using these operators, takes the form:

$$\begin{aligned}
\hat{H}_{eh} &= \sum_{i\sigma} \varepsilon^e_{i\sigma} c^+_{i\sigma} c_{i\sigma} + \sum_{i\tau} \varepsilon^h_{i\tau} h^+_{i\tau} h_{i\tau} \\
&+ \frac{1}{2} \sum_{ijkl} \sum_{\sigma,\sigma'} V_{ee}(i\sigma, j\sigma'|k\sigma', l\sigma) c^+_{i\sigma} c^+_{j\sigma'} c_{k\sigma'} c_{l\sigma} \\
&+ \frac{1}{2} \sum_{ijkl} \sum_{\tau\tau'} V_{hh}(i\tau, j\tau'|k\tau', l\tau) h^+_{i\tau} h^+_{j\tau'} h_{k\tau'} h_{l\tau} \\
&- \sum_{ijkl} \sum_{\sigma\tau} V_{eh}(i\sigma, j\tau|k\tau, l\sigma) c^+_{i\sigma} h^+_{j\tau} h_{k\tau} c_{l\sigma} + \hat{H}_{EHX}.
\end{aligned} \tag{2.26}$$

where the sums over i, j, k, l go over all single-particle orbitals, while the sums over σ, σ', $\tau\tau'$ and $\sigma\tau$ go over all possible spins of the particles.

The first two terms are single-particle electron and hole energies. The next two terms correspond to two-particle Coulomb electron-electron and hole-hole interactions. The last two terms are responsible for electron-hole direct- and

exchange-interactions. The electron-hole exchange interaction is described in details in Chapter 3.

When two electrons (holes) have parallel spin, they interact not only with the direct but also the exchange Coulomb interaction. The Hamiltonian $\hat{H}_{eh}$, Eq. 2.26, can be rewritten in a form in which both types of Coulomb interactions will be clearly seen:

$$\begin{aligned}\hat{H} &= \sum_i \sum_\sigma \varepsilon^e_{i\sigma} c^+_{i\sigma} c_{i\sigma} + \sum_{i\tau} \varepsilon^h_{i\tau} h^+_{i\tau} h_{i\tau} \\ &+ \sum_{i>j,k<l} \sum_{\sigma,\sigma'} \left(V_{ee}|(i\sigma, j\sigma'|k\sigma', l\sigma) - V_{ee}(i\sigma, j\sigma'|l\sigma k\sigma')\delta_{\sigma\sigma'}\right) c^+_{i\sigma} c^+_{j\sigma'} c_{k\sigma'} c_{l\sigma} \\ &+ \sum_{i>j,k<l} \sum_{\tau\tau'} \left(V_{hh}(i\tau, j\tau'|k\tau', l\tau) - V_{hh}(i\tau, j\tau'|l\tau, k\tau')\delta_{\tau\tau'}\right) h^+_{i\tau} h^+_{j\tau'} h_{k\tau'} h_{l\tau} \\ &- \sum_{ijkl} \sum_{ijkl} \sum_{\sigma\tau} V_{eh}(i\sigma, j\tau|k\tau, l\sigma) c^+_{i\sigma} h^+_{j\tau} h_{k\tau} c_{l\sigma} + \hat{H}_{EHX}. \end{aligned} \tag{2.27}$$

The states describing many particles, having the form of the Slater determinants in real space, can be written in the language of the creation operators. For example, a configuration of the N_e electrons distributed on M single-particle orbitals can be written as:

$$|n_{1\downarrow}, n_{2\downarrow}, \ldots, n_{M\downarrow}; n_{1\uparrow}, n_{2\uparrow}, \ldots, n_{M\uparrow}\rangle = \prod_{i=1}^{M} \left(c^+_{i\downarrow}\right)^{n_{i\downarrow}} \prod_{j=1}^{M} \left(c^+_{j\uparrow}\right)^{n_{j\uparrow}} |0\rangle, \tag{2.28}$$

where $|0\rangle$ denotes the vacuum, $n_{i\downarrow}$ ($n_{j\uparrow}$), taking a value of 0 or 1, denotes the number of electrons in the orbital i (j) with the spin $\downarrow$ ($\uparrow$), and $N_e = \sum_i n_{i\downarrow} + n_{i\uparrow}$. The antisymmetry of this state is guaranteed by the Fermionic anticommutation rules of the operators c_i and c^+_i, Eq. 2.19. The state of N_h holes distributed on M single-particle levels can be written analogously, while the state of N_h holes and N_e electrons is a product of the two states.

As already mentioned, many-body states constructed in this way are not eigenstates of the Hamilonian Eq. 2.26, since the Coulomb interaction can scatter particles among the single-particle orbitals. However, the eigenstates of the interacting system can be written as linear combinations of such configurations.

2.4.2 Direct Coulomb interaction in HO basis

The electron-electron Coulomb matrix elements in the two-dimensional harmonic oscillator basis have an analytical form [114] and used later on in Refs. [101, 107]. The main points of this derivation (Ref. [53, 115]) are presented in the Appendix B.2.

The Coulomb interaction matrix element $V_{ee}(i\sigma, j\sigma'|k\sigma', l\sigma)$ (given by Eq. 2.25) between the single-particle envelope wave functions: $F^{+}_{i\sigma}(\mathbf{r}_1)$,$F^{+}_{j\sigma'}(\mathbf{r}_2)$, $F_{k\sigma'}(\mathbf{r}_2)$ and $F_{l\sigma}(\mathbf{r}_1)$ of the HO, with the composite indices i, j, k and l : $i = (n^{1i}_{+}, n^{1i}_{-})$, $j = (n^{2j}_{+}, n^{2j}_{-})$, $k = (n^{2k}_{+}, n^{2k}_{+})$, and $l = (n^{1l}_{+}, n^{1l}_{-})$ has a form:

$$
\begin{aligned}
V_{ee}(i\sigma, j\sigma'|k\sigma', l\sigma) = \frac{1}{l^e_h}\delta_{L_L,L_R}\frac{(-1)^{n^{2j}_{+}+n^{2j}_{-}+n^{2k}_{+}+n^{2k}_{-}}}{\sqrt{n^{1i}_{+}!n^{1i}_{-}!n^{1l}_{+}!n^{1l}_{-}!n^{2j}_{+}!n^{2j}_{-}!n^{2k}_{+}!n^{2k}_{-}!}} \\
\times \sum_{p1=0}^{min(n^{1i}_{+},n^{1l}_{+})} p_1! \binom{n^{1i}_{+}}{p_1}\binom{n^{1l}_{+}}{p_1} \sum_{p2=0}^{min(n^{1i}_{-},n^{1l}_{-})} p_2! \binom{n^{1i}_{-}}{p_2}\binom{n^{1l}_{-}}{p_2} \\
\times \sum_{p3=0}^{min(n^{2j}_{+},n^{2k}_{+})} p_3! \binom{n^{2j}_{+}}{p_3}\binom{n^{2k}_{+}}{p_3} \sum_{p4=0}^{min(n^{2j}_{-},n^{2k}_{-})} p_4! \binom{n^{2j}_{-}}{p_4}\binom{n^{2k}_{-}}{p_4} \left(-\frac{1}{2}\right)^{p} \Gamma\left(p+\frac{1}{2}\right)
\end{aligned}
\tag{2.29}
$$

The Coulomb matrix element with the largest magnitude is the one with all orbital indices from the s-shell of the HO: $i = j = k = l = (0, 0)$: $V_{ee}(i\sigma, j\sigma'|k\sigma', l\sigma) = \frac{\sqrt{\pi}}{l} = V_0$. All other Coulomb matrix elements can be expressed in terms of V_0 and are its fractions. It is important to notice that the magnetic field dependence of the Coulomb matrix elements enters only through the length l^e_h. This allows for the calculation of these elements only for one magnetic field ($B = 0$) and then scaling them with the oscillator length l^e_h appropriate for a specific magnetic field.

If electrons and holes are confined by an identical effective confining potential (i.e,. when $m^*_e\Omega^e_0 = m^*_h\Omega^h_0$), the electron-electron (e-e), hole-hole (h-h), and electron-hole (e-h) Coulomb matrix elements involving the same HO orbitals are equal.

By identical effective confining potentials one understands that the difference between the electron and hole confinement compensates the effect of different effective masses. The corresponding Fock-Darwin orbitals of the electron and

the hole are the same. In such symmetric cases, h-h and e-h interactions can be obtained directly from e-e Coulomb matrix elements: $V_{hh}(i\tau, j\tau'|k\tau', l\tau) = V_{ee}(i\sigma, j\sigma'|k\sigma', l\sigma)$ and $V_{hh}(i\tau, j\tau'|k\tau', l\tau) = -V_{ee}(i\sigma, k\sigma'|j\sigma', l\sigma)$. In a more general case the e-h Coulomb interaction matrix elements have to be calculated separately [116]:

$$V_{eh}(i\sigma, k\sigma'|j\sigma', l\sigma) = -\frac{\sqrt{2}}{l_h^e}\delta_{L_L,L_R}\frac{(-1)^{n_+^{2j}+n_-^{2j}+n_+^{2k}+n_-^{2k}}}{\sqrt{n_+^{1i}!n_-^{1i}!n_+^{1l}!n_-^{1l}!n_+^{2j}!n_-^{2j}!n_+^{2k}!n_-^{2k}!}} \tag{2.30}$$
$$\times \left(\frac{l_h^h}{l_h^e}\right)^{n_+^{2j}+n_-^{2j}+n_+^{2k}+n_-^{2k}} \sum_{p1=0}^{min(n_+^{1i},n_+^{1l})} p_1! \binom{n_+^{1i}}{p_1}\binom{n_+^{1l}}{p_1} \sum_{p2=0}^{min(n_-^{1i},n_-^{1l})} p_2! \binom{n_-^{1i}}{p_2}\binom{n_-^{1l}}{p_2}$$
$$\times \sum_{p3=0}^{min(n_+^{2j},n_+^{2k})} p_3! \binom{n_+^{2j}}{p_3}\binom{n_+^{2k}}{p_3} \sum_{p4=0}^{min(n_-^{2j},n_-^{2k})} p_4! \binom{n_-^{2j}}{p_4}\binom{n_-^{2k}}{p_4}$$
$$\times (-1)^p \left(\frac{1}{1+\left(\frac{l_h^h}{l_h^e}\right)^2}\right)^{p+\frac{1}{2}} \left(\frac{l_h^h}{l_h^e}\right)^{-2p_3-2p_4} \Gamma\left(p+\frac{1}{2}\right),$$

where l_h^h (l_h^e) is the HO length for holes (electrons), and angular momentum: L_L and L_R denote the angular momentum of the electron-hole pairs. The e-h Coulomb matrix element for the symmetric case can be obtained from this formula by putting $l_h^h = l_h^e$. This electron-hole interaction matrix element $V_{eh}(i\sigma, k\sigma'|j\sigma', l\sigma)$ has the same absolute value as the electron-electron element (with proper indices Eq. B23).

2.5 Calculation of optical properties of the QDs

Having obtained the eigenenergies and eigenfunctions of the systems of N and $N-1$ electron-hole pairs, one can calculate the emission spectra from the Fermi's Golden Rule, which in the dipole approximation can be written as:

$$I_\varepsilon^-(\omega) = \sum_i \sum_f P_i |\langle f, N-1|\hat{P}_\varepsilon^-|i, N, \rangle|^2 \delta(E_i - E_f - \omega). \tag{2.31}$$

Here $|i, N\rangle$ denotes the initial state of the N electron-hole piars with the corresponding energy E_i. $|f, N-1\rangle$ is the final state of the $N-1$ electron-hole pairs, which remains after the recombination of one electron-hole pair. The final state has the energy E_f.

The interband polarization operator:

$$\hat{P}_{\varepsilon}^{-} = \sum_{i,\sigma} c_{i,\sigma} h_{i,-\sigma} \tag{2.32}$$

annihilates one electron-hole pair from the initial state with a simultaneous emission of one photon. The oscillator strength - the matrix element of the polarization operator between initial and final states - is then multiplied by the probability of occupation of the initial state: $P_i = \exp\{-\frac{E_i}{kT}\}/P_{SUM}$, with $P_{SUM} = \sum_i \exp\{-\frac{E_i}{kT}\}$, where k is the Boltzman constant and T is the temperature.

Depending on the spin of removed particles, emitted photons have circular σ_+ ($\hat{P}_+ = \sum_i c_{i\downarrow} h_{i\Uparrow}$), σ_- ($\hat{P}_- = \sum_i c_{i\uparrow} h_{i\Downarrow}$) or linear: X ($\hat{P}_X = \sum_i c_{i\downarrow} h_{i\Uparrow} + \sum_i c_{i\uparrow} h_{i\Downarrow}$), Y ($\hat{P}_Y = \sum_i c_{i\downarrow} h_{i\Uparrow} - \sum_i c_{i\uparrow} h_{i\Downarrow}$), polarisation. Due to the delta function in the above formula, the energy $\hbar\omega$ of the emitted photon (the position of the PL peak on the energy axis) is equal to the energy difference between the initial and final states.

The absorption spectra can be calculated in a similar way, using the expression:

$$I_{\varepsilon}^{+}(\omega) = \sum_i \sum_f P_i |\langle f, N+1 | \hat{P}_{\varepsilon}^{+} | i, N \rangle|^2 \delta(E_i - E_f - \omega). \tag{2.33}$$

The interband polarization operator $\hat{P}_{\varepsilon}^{+} = \sum_{i,\sigma} c_{i,\sigma}^{+} h_{i,-\sigma}^{+}$ creates one electron-hole pair on top of the existing N pairs in the initial state, with simultaneous absorption of the photon.

In the calculations of the emission and absorption spectra, Eqs. 2.31, 2.33, it is assumed that the temperature is much lower than the bandgap of the QD material, which assures that the conduction and valence band are empty of carriers in the absence of optical excitation. This implies that if one calculates the emission spectra of $N = 1$ electron-hole pair, the initial states $|i\rangle$ are the states of the interacting photo-excited electron and hole thermally populated with probability

P_i. In the final state $|f\rangle$ there is an emitted photon and a QD with no carriers in the conduction and valence band due to the low temperature.

On the other hand, in the calculations of the absorption spectra in the case of $N = 0$, the initial state is an empty QD. The final states are the ground and all excited states of the interacting electron-hole pair.

2.6 Exciton confined in the QD

The exciton is a correlated state of an electron in the conduction band and a hole in the valence band. The recombination of the exciton leads to the emission of the photon with well defined energy - that is the energy of the recombining exciton. This energy depends on many factors like the semiconducting material in which excitons were created, as well as the size and shape of the quantum dot [108, 117–119].
Detailed theory of an exciton as a collective state of an electron and a hole in a symmetric parabolic quantum dot has been developed in Ref. [103], while the effects of quantum dot anisotropy on the exciton p-shell have been discussed, e.g., in Ref. [109].

2.6.1 Exciton in Jacobi coordinates

Since the main subject of this work is the analysis of optical properties of QDs with magnetic impurities, it is important to understand the behaviour of the exciton in the non-magnetic quantum dots first. Some of the concepts introduced by Hawrylak et al. in Ref. [103] will be revisited here.

The confining potential of the QD is chosen to be the two-dimensional isotropic harmonic oscillator, whose single-particle states were described in Section 2.2. Here it will be assumed that the quantum dot can confine two (SP) or three (SPD) single-particle shells. The basis for calculations of the exciton is constructed out of the single-particle states for the electron and hole by populating them with one electron and one hole with all possible spin configurations.

Since in the exciton there is only one electron and only one hole, the Hamiltonian of many interacting electrons and holes (Eq. 2.26) can be simplified to:

$$\begin{aligned}\hat{H}_X &= \sum_{i\sigma} \varepsilon^e_{i\sigma} c^+_{i\sigma} c_{i\sigma} + \sum_{i\tau} \varepsilon^h_{i\tau} h^+_{i\tau} h_{i\tau} \\ &- \sum_{ijkl}\sum_{\sigma\tau} V_{eh}(i\sigma, j\tau|k\tau, l\sigma) c^+_{i\sigma} h^+_{j\tau} h_{k\tau} c_{l\sigma}. \end{aligned} \tag{2.34}$$

The electron-hole exchange term $\hat{H}_{EHX}$ [108, 120–124] has been neglected here, and will be discussed in Chapter 3. The Hamiltonian $\hat{H}_X$ commutes with both the exciton angular momentum $L = L_e + L_h = n^e_+ - n^e_- + n^h_- - n^h_+$ and the spin operators, since the kinetic energy operators of the electron and hole are diagonal, and the electron-hole direct Coulomb interaction conserves the angular momentum of the pair as well as the spin of the electron and the hole separately, Eqs. B.23 and 2.30.

In this case, the electron-hole basis can be divided into subspaces with different angular momentum L of the electron-hole pair, and with different spin configurations of the pair. There are four possible spin configurations for the electron and hole: $|\Uparrow\downarrow\rangle, |\Uparrow\uparrow\rangle, |\Downarrow\downarrow\rangle, |\Downarrow\uparrow\rangle$. The construction of the basis set as well as the calculations are the same for each of the spin configurations. For the subspace with angular momentum L, the spin of the hole τ, and the spin of the electron σ, the basis is created in the form: $|L; ij\rangle|\tau\sigma\rangle = h^+_{i\tau} c^+_{j\sigma}|0\rangle$ (or $|L; (n^h_+, n^h_-), (n^e_+, n^e_-)\rangle|\tau\sigma\rangle = h^+_{n^h_+, n^h_-\tau} c^+_{n^e_+, n^e_-\sigma}|0\rangle$). The important electron-hole configurations with angular momentum $L = 0$ and a chosen spin projection are presented in Fig. 2.5 (a).

The first of the configurations shown in Fig. 2.5, $|a\rangle = h^+_{00\Uparrow} c^+_{00\downarrow}|0\rangle$, is the configuration with the lowest possible kinetic energy. It consists of the electron and the hole occupying their s-shell. The configurations $|b\rangle = h^+_{10\Uparrow} c^+_{10\downarrow}|0\rangle$ and $|c\rangle = h^+_{01\Uparrow} c^+_{01\downarrow}|0\rangle$ are the so-called PP configurations, where both the electron and the hole are on one of the p-shell levels, in such a way that the angular momentum of the pair is zero (the other configurations would have $L = \pm 2$ respectively). If the harmonic oscillator frequencies of the electron and hole are equal ($\Omega_e = \Omega_h$), the $SD - DS$ configurations $|g\rangle = h^+_{11\Uparrow} c^+_{00\downarrow}|0\rangle$ and $|h\rangle = h^+_{00\Uparrow} c^+_{11\downarrow}|0\rangle$ have the same kinetic energy as the PP configurations ($|b\rangle$ and $|c\rangle$). The $|g\rangle$ ($|h\rangle$) configuration

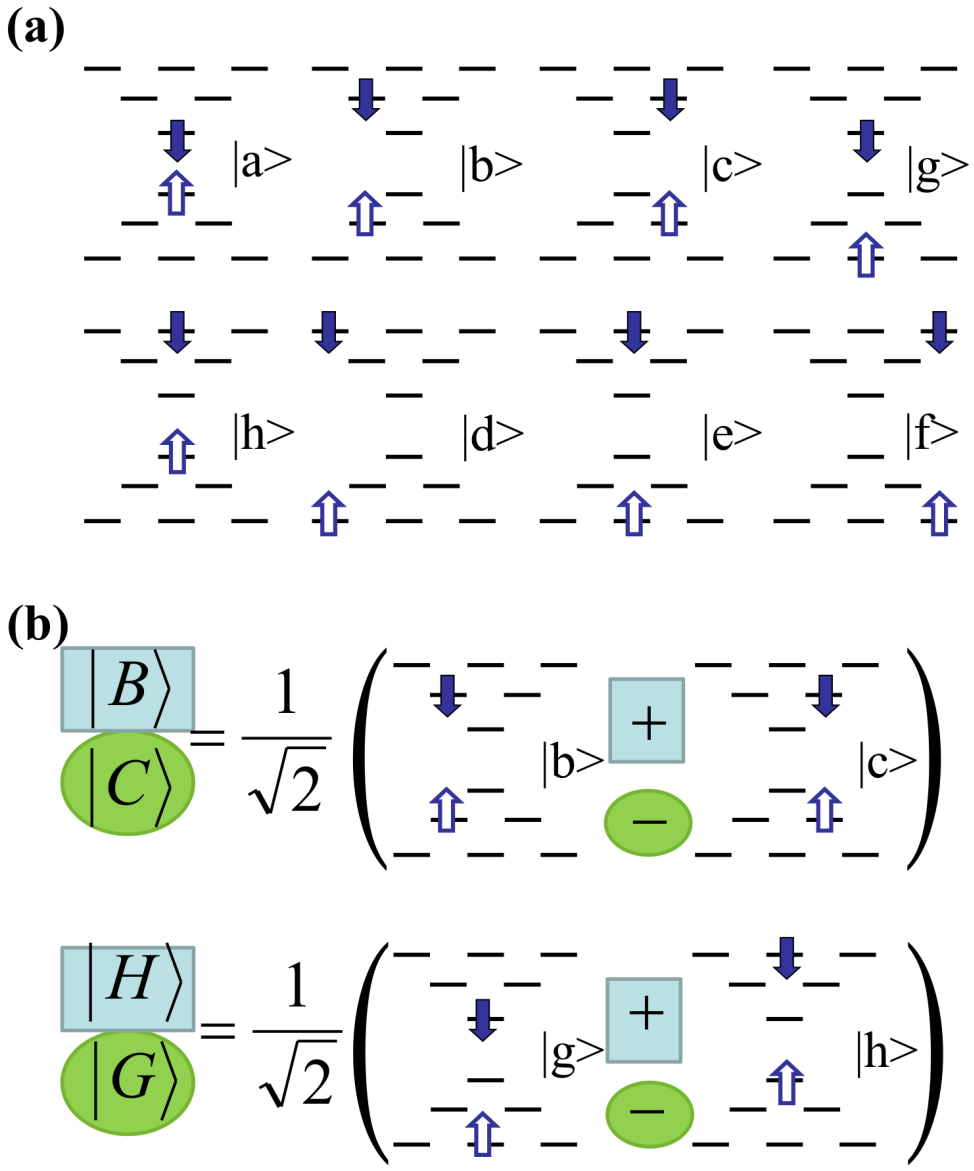

Figure 2.5: (a) The basic electron-hole configurations with the angular momentum $L = 0$. Electron (hole) is marked by the solid (empty) arrow. (b) The construction of the important Jacobi coordinates in the p-shell.

consists of the electron (hole) on the s-shell while the hole (electron) is on the zero angular momentum state of the d-shell for which $(n_+^{h(e)}, n_-^{h(e)}) = (1,1)$. The other three configurations, $|d\rangle$, $|e\rangle$ and $|f\rangle$, are the high kinetic energy DD-configurations, with both carriers on their respective d-shell levels.

Since the polarization operator $P^{+(-)}$ creates (anihilates) an electron-hole pair with opposite spins, all of the configurations $|a\rangle - |h\rangle$ belong to the *bright* spin subspace. This means that the spin part of the wave function fulfils the optical spin selection rules. The spin configurations $|\Uparrow\downarrow\rangle$ with the spin angular momentun of $+1$ ($j_z + S_z = 3/2 - 1/2$) emit a photon with the angular momentum of $+1$ (σ_+ polarization), while configurations $|\Downarrow\uparrow\rangle$ with the spin angular momentun of -1 ($j_z + S_z = -3/2 + 1/2$) emit a photon with the angular momentum of -1 (σ_- polarization). The other two types of spin configurations are considered *dark*. The second selection rule is related to the orbital part of the wave function - the created (anihilated) particles need to occupy the same single-particle orbital i. According to this rule, the configurations $|g\rangle$ and $|h\rangle$ are considered orbitaly *dark*, while the rest of the configurations is *bright*.

However, it is useful to create a different exciton representation in which one can immediately decide which states are optically active [103]. This can be done by a transformation of the basis into the Jacobi-like coordinates. Starting from the lowest energy configuration, this transformation reads [103]:

$$\begin{aligned}
|A\rangle &= |a\rangle \\
|B\rangle &= \frac{1}{\sqrt{2}}\left(|b\rangle + |c\rangle\right) \\
|C\rangle &= \frac{1}{\sqrt{2}}\left(|b\rangle - |c\rangle\right) \\
|G\rangle &= \frac{1}{\sqrt{2}}\left(|g\rangle - |h\rangle\right) \\
|H\rangle &= \frac{1}{\sqrt{2}}\left(|g\rangle + |h\rangle\right) \\
|D\rangle &= \frac{1}{\sqrt{3}}\left(|d\rangle + |e\rangle + |f\rangle\right)
\end{aligned} \tag{2.35}$$

$$
\begin{aligned}
|E\rangle &= \frac{1}{\sqrt{2}}\left(|d\rangle - |e\rangle\right) \\
|F\rangle &= \frac{1}{\sqrt{6}}\left(|d\rangle + |e\rangle - 2|f\rangle\right)
\end{aligned}
$$

In particular, the construction of the degenerate states in the p-shell is important. To illustrate it, a schematic picture has been shown in Fig. 2.5. The density of states for an exciton in the two-dimensional, symmetric QD has been presented in Fig. 2.6. There is one configuration $|A\rangle$ in the s-shell, four configurations in the p-shell, and three configurations in the d-shell. The polarization operator can be now expanded in the new basis:

$$\hat{P}^{-} = |A\rangle\langle A| + \sqrt{2}|B\rangle\langle B| + \sqrt{3}|D\rangle\langle D|. \tag{2.36}$$

From this form of the polarization operator it can be seen immediately that only one configuration from each of the shells is optically active: $|A\rangle$ from the s-shell, $|B\rangle$ from the p-shell and $|D\rangle$ from the d-shell. In Fig. 2.6 (a), the bright Jacobi coordinates are highlighted in yellow.

The Coulomb interaction between the electron and hole has been neglected so far. The inclusion of this interaction causes a coupling between the Jacobi coordinates and leads to an increased number of emission lines. Calculation of the absorption spectra of the exciton confined in the QD with two and three single-particle shells is shown in Fig. 2.6 (b), and it will be discussed in more details below. For the symmetric QD when $\omega_e/\omega_h = 1$, the Jacobi basis is particularily useful for the analysis of an exciton. In this case one can immediately see which states are coupled to the bright configurations through the Coulomb interactions ($|A\rangle$,$|B\rangle$,$|D\rangle$) and become optically active. The antisymmetric superpositions of the electron-hole configurations, $|C\rangle$, $|E\rangle$ and $|G\rangle$, do not couple to the remaining symmetric states. However, the other five states are coupled with each other. One needs to write the Hamiltonian $\hat{H}_X$ of the interacting electron and hole (Eq. 2.34) in this basis and diagonalise it numerically. The resulting eigenstates of the exciton are in the form of a linear combination of the Jacobi coordinates

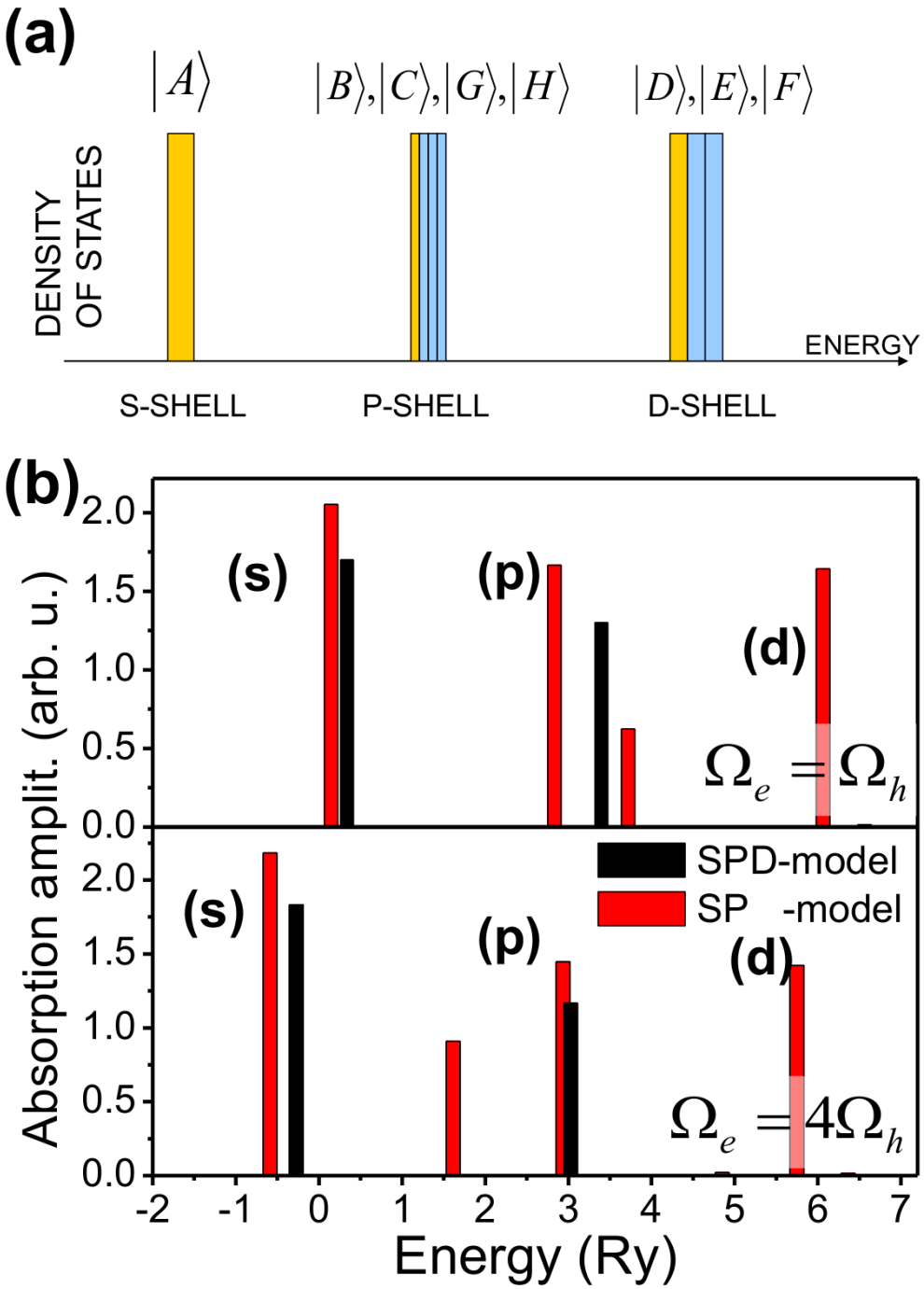

Figure 2.6: (a) The density of states of an exciton confined in the QD with three single-particle shells SPD. The dark (bright) states are presented by the blue (yellow) bars. All the states in the p- and d-shells are degenerated. (b) Calculated absorption spectra of a CdTe isotropic quantum dot without electron-hole exchange. Upper spectra are for the QD with $\omega_e/\omega_h = 1$, while the lower are for $\omega_e/\omega_h = 4$. The spectra were calculated for a QD confining two (SP - black bars), and three (SPD - red bars) single-particle shells.

$|A\rangle$, $|B\rangle$, $|H\rangle$, $|D\rangle$, and $|F\rangle$:

$$|X_i\rangle|\Uparrow\downarrow\rangle = \left(A_A^{(i)}|A\rangle + A_B^{(i)}|B\rangle + A_H^{(i)}|H\rangle + A_D^{(i)}|D\rangle + A_F^{(i)}|F\rangle\right)|\Uparrow\downarrow\rangle \tag{2.37}$$

where $i = 1\ldots5$ denotes exciton state number and $A_{A\ldots F}^{(i)}$ are the amplitudes of $|A\rangle\ldots|F\rangle$ configurations in the excitonic state with the number i. The ground state of the exciton in the symmetric case ($\omega_e/\omega_h = 1$) can be approximated by the linear combination of only three configurations (neglecting high-energy configurations that do not contribute significantly to the ground state):

$$|X_{GS}\rangle|\Uparrow\downarrow\rangle = \left(|A_A^{(1)}||A\rangle + |A_B^{(1)}||B\rangle - |A_H^{(1)}||H\rangle\right)|\Uparrow\downarrow\rangle. \tag{2.38}$$

The fact that the sign of $A_H^{(1)}$ is opposite to that of the other amplitudes has been written explicitely. The different sign of the $A_H^{(1)}$ amplitude is a result of a different sign of the Coulomb matrix element coupling the configuration $|A\rangle$ with $|B\rangle$ and $|A\rangle$ with $|H\rangle$. Later on the absolute value symbols will be dropped. Now, because the configuration $|A\rangle$ has the lowest kinetic energy, the amplitude $A_A^{(1)}$ in the state $|X_{GS}\rangle$ is the greatest.

The first excited state is in the form:

$$|X_{ES}\rangle|\Uparrow\downarrow\rangle = \left(A_A^{(2)}|A\rangle + A_B^{(2)}|B\rangle + A_H^{(2)}|H\rangle\right)|\Uparrow\downarrow\rangle, \tag{2.39}$$

with a very similar contribution from $|B\rangle$ and $|H\rangle$ ($A_B^{(2)} \approx A_h^{(2)}$) and a much smaller contribution from the $|A\rangle$ configuration. The second excited state is:

$$|X_3\rangle|\Uparrow\downarrow\rangle = \left(A_A^{(3)}|A\rangle - A_B^{(3)}|B\rangle + A_H^{(3)}|H\rangle\right)|\Uparrow\downarrow\rangle, \tag{2.40}$$

with the most even distribution of the probability of occupation of any of the configurations of the electron-hole pair.

The situation is slightly changed if the ratio ($\omega_e/\omega_h \neq 1$). The configuration $|G\rangle$ is not completely decoupled from the bright configurations, however its coupling to the excitonic ground-state is relatively small. The ground state of the exciton can be still approximated by the expression Eq. 2.38 although the amplitudes are changed. A much greater change due to the un-even shell spacing

for electrons and holes appears in the excited states of the exciton. In this asymmetric case the configuration $|g\rangle$ has a significantly lower energy than the PP configurations ($|b\rangle$ and $|c\rangle$), since it is energeticaly preferable to excite a hole to the d-shell orbital leaving the electron on the s-shell than to excite both particles to the p-shell. This results in the mixing between $|H\rangle$ and $|G\rangle$ configurations that in turn leads to the following form of the exciton wave function:

$$|X_{ES}\rangle|\Uparrow\downarrow\rangle = \left(A_A^{(2)}|A\rangle + A_B^{(2)}|B\rangle + A_H^{(2)}|H\rangle + A_G^{(2)}|G\rangle\right)|\Uparrow\downarrow\rangle, \tag{2.41}$$

for the first excited state of the exciton, where the greatest amplitude is $A_H^{(2)}$ followed by $A_G^{(2)}$. The second excited state will have now an admixture of the $|G\rangle$ configuration as well as $|D\rangle$:

$$|X_3\rangle|\Uparrow\downarrow\rangle = \left(A_A^{(3)}|A\rangle - A_B^{(3)}|B\rangle - A_D^{(3)}|D\rangle + A_G^{(3)}|G\rangle + A_H^{(3)}|H\rangle\right)|\Uparrow\downarrow\rangle. \tag{2.42}$$

This state is built predominantly out of the $|B\rangle$ configuration with significant contribution from the $|G\rangle$ state, which is a big change as compared to the symmetric case (Eq. 2.40).

It was shown in Ref. [103] that the calculated absorption spectrum of QD confining three single-particle shells consists of five peaks: one from the state $|A\rangle$ in the s shell, two from the states $|B\rangle$ and $|H\rangle$ from the p shell and two from states $|D\rangle$ and $|F\rangle$ in the d shell. The results of similar calculations are shown in Fig. 2.6 (b).

The calculations of the presented absorption spectra of a CdTe isotropic quantum dot were done for the single-particle energies $\omega_e + \omega_h = 30$ meV with the ratio between them $\omega_e/\omega_h = 1$ for the upper panel and $\omega_e/\omega_h = 4$ for lower panel. For the QD confining two single-particle shells (black spectra) there is one absorption line in the s shell and one in the p shell. Their energies are renormalized by the Coulomb interaction, and are of the different value for both ratios (in the absence of the Coulomb scattering, both spectra would be identical). The situation changes dramaticaly for the QD that confines the third - d shell (red spectra). In that case, the absorption to the d shell and the splitting in the p shell due to the presence of the d shell is visible. This splitting appears due to the

interaction between the degenerate $|B\rangle$ and $|H\rangle$ configurations, which repel each other (the energy splitting) and exchange the oscillator strength (the previously dark $|H\rangle$ configuration becomes optically active). The splitting between the lines as well as their oscillator strength depend on the QD parameters, although it is important to remember that it originates from the Coulomb interaction coupling between PP and SD configurations and it is absent in the QD with only s and p shells.

2.6.2 Anisotropy

The effects of the quantum dot anisotropy on the exciton p-shell structure have been discussed in Ref. [109] on the example of a three-exciton complex confined in the QD with only two single-particle shells (the s-shell was completely full). In this work, it has been shown that the p shell is split due to the presence of the deformation potential, and that the oscillator strength of the p-shell state, which is the sole bright exciton state for the isotropic parabolic confinement, is distributed over two optically active states, whose energy splitting depends on the dot deformation.

Calculations of the absorption spectra of an exciton in the two-dimmesional parabolic potential with increasing anisotropy is presented in the Fig. 2.7. The QD for which the calculations were made confines three single-particle states SPD, with the shell spacing $\omega_e + \omega_h = 30$ meV, and ratio $\omega_e/\omega_h = 4$. As it was discussed above, even in the absence of the anisotropy, the p-shell absorption consists of two peaks corresponding to $|X_{ES}\rangle$ and $|X_3\rangle$ excitonic states (given by the Eqs. 2.41 and 2.42). The anisotropy causes mixing between the single-particle states whose angular momentum differs by 2 as described in Section 2.3. This mixing causes a further splitting of each of the p-shell emission lines into two, each with a different oscillator strength.

The first bright excited state of the exciton, $|X_{ES}\rangle$, is coupled with the two other excitonic states with $L = L_e + L_h = 2$ and $L = -2$. They are built mostly out of configurations $|1\rangle$ and $|2\rangle$, shown in Fig. 2.8. The coupling between them is mostly through the anisotropic correction of the hole confining potential which scatters the hole from the s-shell (the state (00)) in the $|X_{ES}\rangle$ to (02)

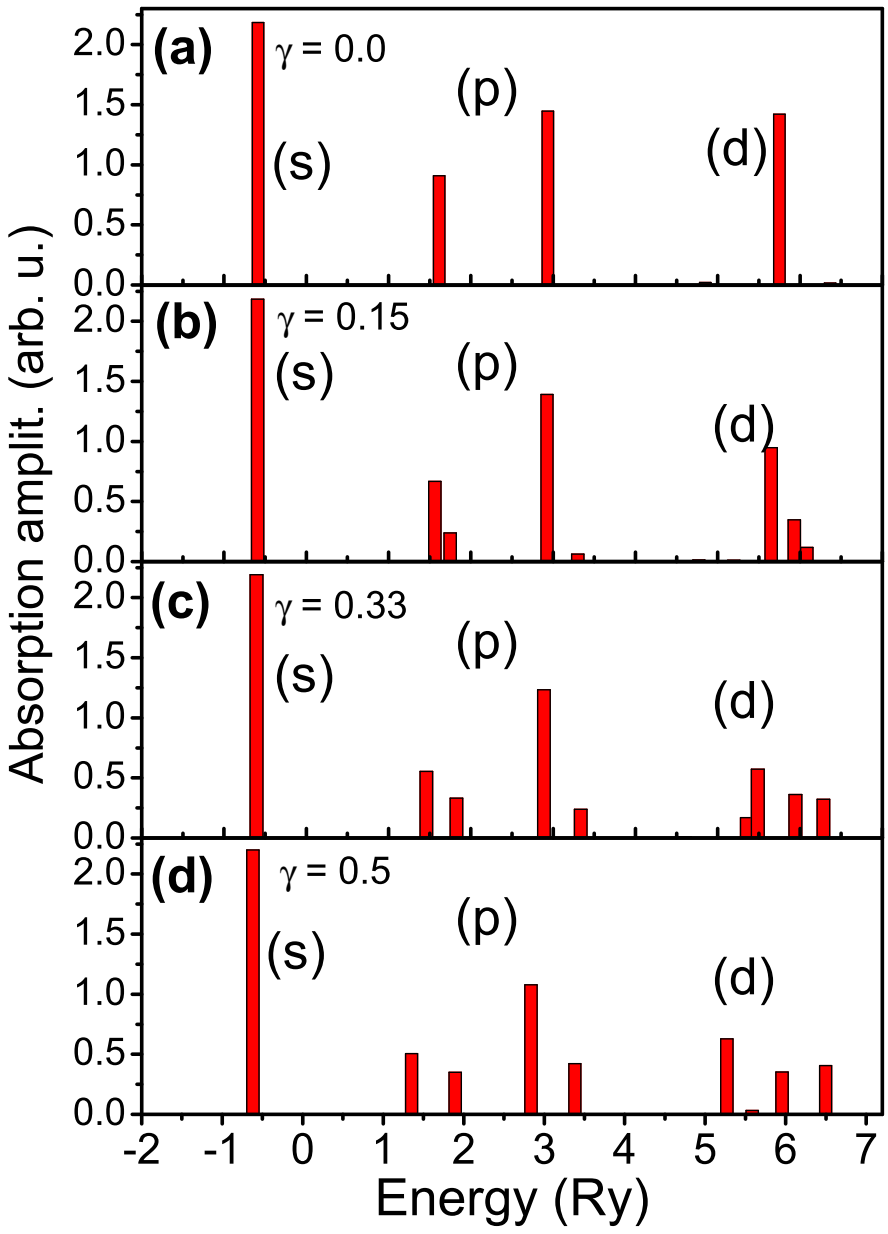

Figure 2.7: Calculated absorption spectra of a CdTe QD without an electron-hole exchange, with different anisotropies: (a) $\gamma = 0$ (QD is isotropic), (b) $\gamma = 0.15$, (c) $\gamma = 0.33$ and (d) $\gamma = 0.5$.

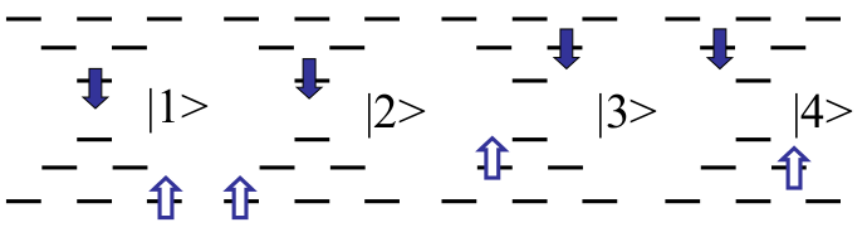

Figure 2.8: The important electron-hole configurations coupled to the $L = 0$ bright configurations in the p-shell.

in the $|1\rangle$ configuration or (20) in the $|2\rangle$ configuration (leaving the electron on the s-shell (00) level). As a result, in the presence of anisotropy, the lower-lying absorption peak corresponds to the linear combination of the form: $|X_{ES}\rangle - \alpha\left(|02,00\rangle + |20,00\rangle\right)$ while the higher peak: $|X_{ES}\rangle + \alpha\left(|02,00\rangle + |20,00\rangle\right)$.

In the isotropic QD, the third peak in the absorption spectra corresponds to the second bright excited state of an exciton $|X_3\rangle$, which is built mostly out of the $|B\rangle$ Jacobi coordinate ($|B\rangle = 1/\sqrt{2}\left(|01,01\rangle + |10,10\rangle\right)$). This state is coupled with the two other excitonic states with the $L = 2$ and $L = -2$ which are built mostly out of the configurations $|3\rangle$ and $|4\rangle$, as shown in Fig. 2.8. This time, the coupling between them is through the anisotropic correction of the hole and electron confining potential. As a result, in the presence of the anisotropy, the lower lying absorption peak corresponds to the linear combination of the form: $|X_3\rangle + \alpha\left(|01,10\rangle + |10,01\rangle\right)$ while the higher peak: $|X_3\rangle - \alpha\left(|01,10\rangle + |10,01\rangle\right)$. The splitting as well as the oscillator strength of the peaks depend on the strength of the coupling between $L = 0$ and $L = \pm 2$ states - namely the anisotropy parameter $\gamma_{e(h)}$.

2.7 Multi-exciton complexes in the QD

In the high excitation power regime, when the electron-hole pairs are excited faster than they can recombine, the existence of multiexciton complexes has been reported [117, 125, 126], and extensively studied theoreticaly [94, 102, 127–129]. The emission of (a) InAs (figure adapted from Ref. [125]) and (b) CdTe, neutral

QD as a function of energy and excitation power is shown in Fig. 2.9.

In the charge-neutral QD, in the low excitation power regime, the emission from the lowest single-particle s shell is visible (Fig. 2.9 (a, left) and Fig. 2.9 (b), green spectrum). In this regime there is only one electron-hole pair occupying predominantly the s-shell. With increasing excitation power, the number of electron-hole pairs increases and the multi-exciton complexes are created, starting with the biexciton - XX or X_2 (a bound state of two electron-hole pairs), up until the six-exciton complex X_6, when six electron-hole pairs exist simultaneously in the QD (Fig. 2.9 (a, right)). In Fig. 2.9 (a) the emission from the s shell as well as the p shell for multi-exciton complexes is visible, while the high excitation power spectra in Fig. 2.9 (b) show the emission from the d-shell as well (black spectra).

In this work we focus on the QDs in which exciton (X) and biexciton (XX) complexes are present at the same time. The exciton was described in the previous Section, while the bi-exciton will be briefly discussed here.

As it was mentioned, the biexciton is a complex that consists of two electron-hole pairs (two excitons, hence bi-exciton). The s shell of the QD can be occupied by maximum of two electron-hole pairs. Due to the Pauli exclusion principle, the electrons (holes) occupying the same QD level need to have opposite spins and form a spin singlet state. Therefore, the ground state of the biexciton is an electron and hole spin singlet state, as shown in Fig. 2.10 (a).

As an example, a higher-energy singlet-singlet $XX(j_z, s_z)$=$XXSS$(0,0) configuration of the biexciton is shown in Fig. 2.10 (b). In this configuration one electron-hole pair occupies the s shell of the QD, while the second one is in the p shell. Since the spin z projection of both electrons (s_z) and holes (j_z) is zero, while the carriers of the same type are on different orbitals, the eight possible electron-hole configurations are properly symmetrized to create a configuration with a well-defined total spin of electrons $S = 0$ and holes $j = 0$. Since the Coulomb interaction scatters the electron-hole pair from the s to the p shell without changing either the total spin or the z projection of the spin of either particle, the s-shell configuration (Fig. 2.10 (a)) and sp $XXSS$(0,0) (Fig. 2.10 (b)) are coupled. This means that the GS of the XX, similar to the GS of the previously described exciton, is a linear combination of these configurations and higher lying $XXSS$ configurations [102].

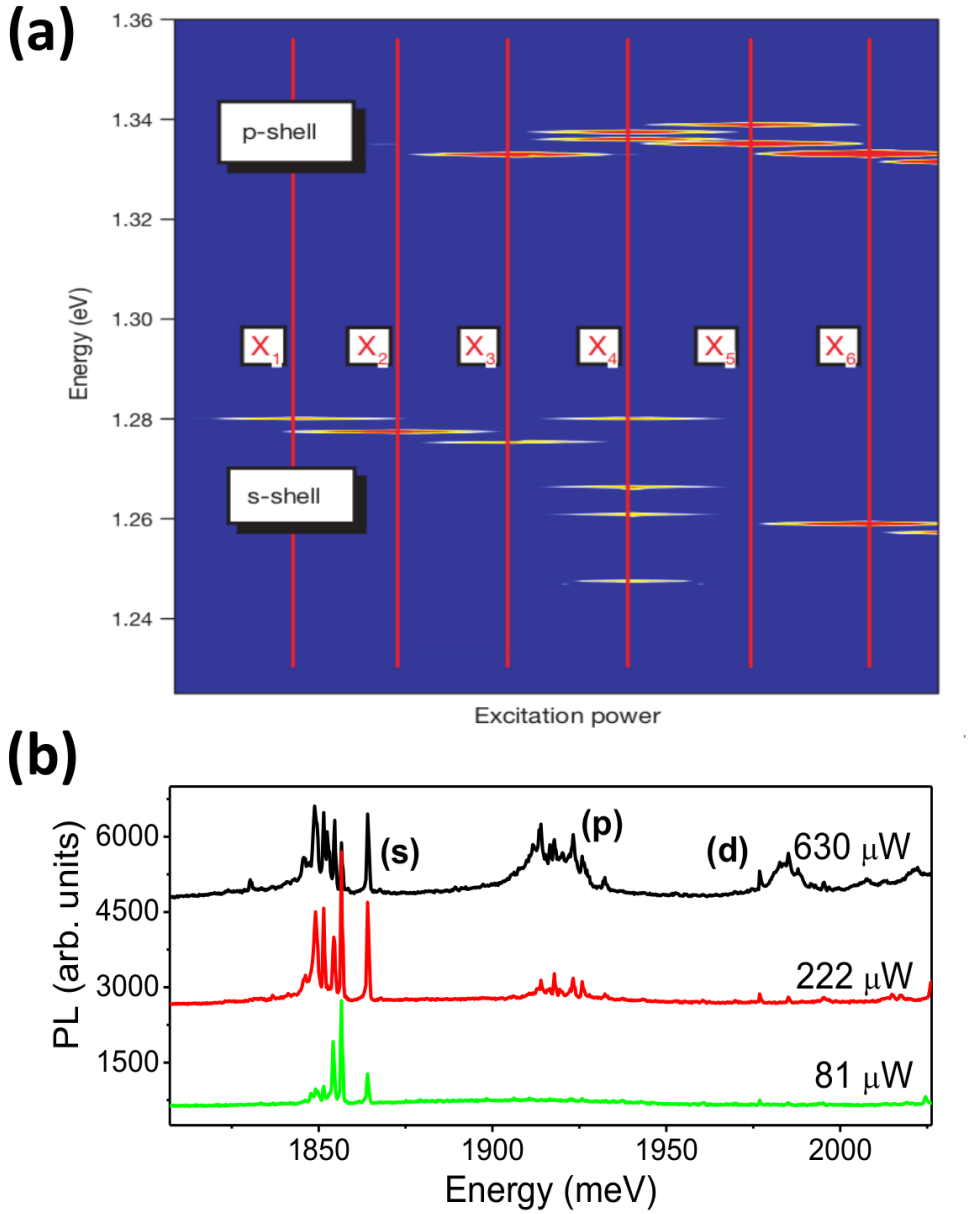

Figure 2.9: (a) The change of the emission of an $In_{0.60}Ga_{0.40}As$ single quantum dot with excitation power and with energy. Bright regions indicate strong emission intensities, blue regions low intensities. Figure is reprinted by permission from Macmillan Publishers Ltd: Nature from Ref. [125], Copyright (2000). (b) Measured emission spectra from s, p, and d shells of a single CdTe quantum dot, populated with an increasing number of electron-hole pairs, with increasing excitation power.

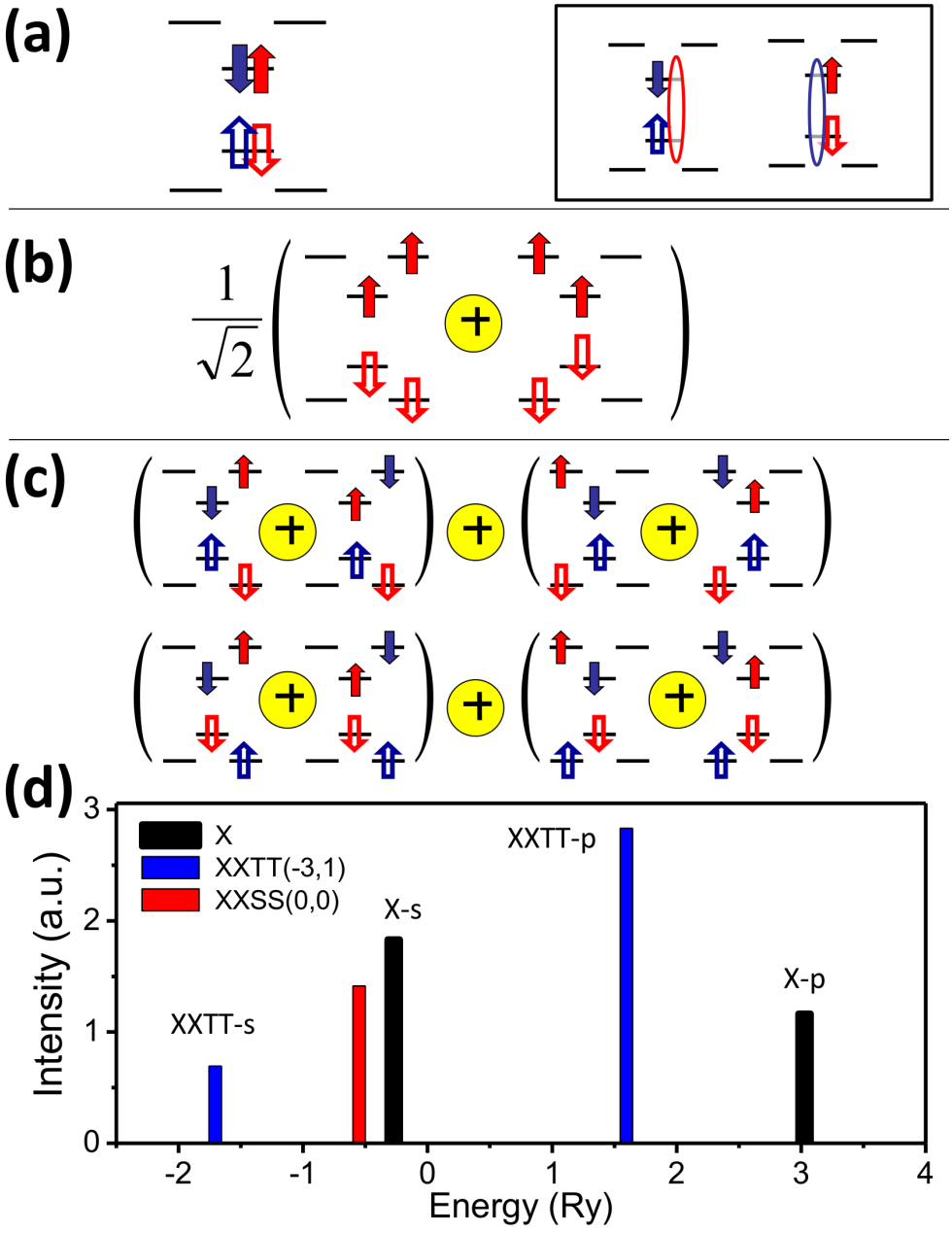

Figure 2.10: (a) The lowest XX configuration, where all carriers occupy their s shell, (b) the properly symmetrized (not normalized) configuration of s- and p electron-hole pairs creating an $XXSS(0,0)$ configuration, (c) the lowest energy configuration of $XXTT(-3,1)$, (d) the oscillator strength of the exciton (black) and biexciton (red -$XXSS$, blue $XXTT(-3,1)$) optical transitions, as a function of energy, calculated for a QD confining s and p single-particle shells.

The final state of the recombination from the XX ground state is the ground state of the exciton, whose main configurations are shown in the inset of the Fig. 2.10 (a). The recombination of the XX can happen in one of the two channels, with the emission of the σ_+ photon: recombination of the hole spin-up and electron down, $\Uparrow\downarrow$ - blue pair, with the final state being the "red" electron-hole $\Downarrow\uparrow$ pair (on the left), or with the emission of the σ_- photon, when the other electron-hole pair recombines, leaving the exciton in the spin state $\Uparrow\downarrow$ (blue pair on the right of the inset).

The energy of the GS of the correlated XX is lower than the sum of the energies of two excitons. This lowering of the energy is caused by the correlations in the system, and it results in the redshift of the $XXSS$ emission/absorption line as compared to the emission/absorption from the X GS (Fig. 2.10 (d)).

From the configurations of two electron-hole paris with the $(j_z, s_z) = (0, 0)$ one can also construct linear combinations in which the total spin of electrons or holes, or both, is non-zero: $XXST$(0,0) (singlet-triplet), when holes are in a singlet and electrons in a triplet state, $XXTS$(0,0) (triplet-singlet), when holes are in a triplet and electrons in a singlet, or $XXTT$(0,0), when both carriers are in a triplet state. This is however not the only way to create an XX state with non-zero total spin of electrons and holes. There are also spin polarized state of the biexciton as shown in Fig. 2.10 (c) (Refs. [102, 128]).

The polarized carriers cannot both occupy the s-shell, due to the Pauli exclusion principle. For that reason, the configuration shown in Fig. 2.10 (c), is a configuration of the spin-polarized triplet bi-exciton $XXTT$(-3,1) with the lowest kinetic energy. This complex can only exist in a QD, and it provides a useful tool for measuring the single-exciton spectrum without resorting to the difficult absorption experiment (Fig. 2.10 (d)). The recombination from the $XXTT$(-3,1) happens with the emission of the photon with the energy from the s-shell energy range when the final state of the recombination is the excited exciton state in the p-shell, or with the p-shell energy range when the remaining exciton is in its GS. Naturally, there are higher kinetic energy configurations of the polarized $XXTT$(-3,1) complex, which interact via the direct Coulomb interaction with this configuration, and have non-zero contribution to the $XXTT$(-3,1) ground state [102].

Chapter 3

Electron-Hole exchange, derivation and analysis

3.1 Introduction

In the previous chapter it was shown that each exciton state is a linear combination of electron-hole configurations. Each electron-hole configuration is a product of orbital and spin wave functions. With the electron spin $S_z = \pm 1/2$ and the heavy hole spin $\tau = \pm 3/2$ each configuration is fourfold degenerate due to four possible spin configurations of carriers. With only the direct Coulomb interaction between carriers accounted for, each exciton level is also fourfold degenerate. As shown experimentally by, e.g., Gammon and co-workers [130–132] and Bayer and co-workers [133, 134], the four exciton states are split into a low-energy dark multiplet and a bright multiplet at a higher energy. The bright multiplet, which describes the two bright exciton states corresponding to left and right circularly polarized photons, is further split by the long-range electron-hole exchange interaction. This long-range exchange interaction (LRE) removes the degeneracy of bright exciton states, and leads to a linear polarization of emitted photons. Hence it is important to understand the fine structure of exciton levels in self-assembled semiconductor quantum dots before one proceeds to describe the exciton confined in the magnetic QD and interacting with a magnetic impurity.

The fine structure of the exciton in bulk semiconductors was investigated almost 40 years ago [135–137]. In semiconductor self-assembled quantum dots

the fine structure and exchange interaction are significantly enhanced due to the exciton confinement. This motivated studies of the electron-hole exchange interaction in low-dimensionality systems within the framework of the envelope function approximation by, e.g. Ivchenko and co-workers [138, 139], Takagahara [120, 121], as well as others [140, 141]. Zunger and co-workers investigated the exciton fine structure using the empirical atomistic pseudopotential approach [142–144] and Goupalov and Ivchenko[122] and Korkusinski et al. [94] using atomistic tight-binding approximation [122]. It was shown that the strength of the bright exciton splitting depends on the QD in-plane anisotropy [120, 134, 139]. Several groups demonstrated tuning of the exciton fine structure by the application of the lateral and vertical electric field [86, 145], or vertical and in plane magnetic field [134, 146–148]. In both cases the splitting of bright exciton states was suppressed by an external field.

In an external magnetic field perpendicular to the plane of the quantum dot the fine structure splitting of the multiplet is caused by two contributions: the exchange interaction, which couples the spins of the electron and the hole, and their Zeeman interaction with the magnetic field. With the increasing Zeeman interaction, the two exciton states evolve from linear to circular polarization [117, 134]. The exchange interaction depends on the exciton wave function which depends on modification of the direct Coulomb scattering and the single-particle energy levels by the magnetic field.

The key result presented here, and extending the theory from Ref. [123], is the derivation of the short and long-range electron-hole exchange interaction matrix elements expressed in terms of known electron-electron exchange matrix elements. This allows for a simultaneous evaluation of the direct Coulomb, short- and long-range electron-hole exchange interaction matrix elements, and matrix elements of the anisotropic confining potential in the HO and spin basis for a perpendicular magnetic field of arbitrary magnitude.

Such a formulation of the interacting exciton Hamiltonian allows for a detailed numerical and analytical study of the effect of the electron-hole exchange, direct Coulomb interaction, anisotropy of the confining potential, quantum dot shell structure, and the magnetic field on the fine structure of correlated exciton states. The fine structure of ground and excited correlated exciton states is obtained

using exact diagonalization techniques and shows a significant effect of electron-hole correlations.

While effective mass calculations do not include details of the atomistic structure, [94, 142–144, 149], they are significantly less computationally expensive. This computational tool can help in guiding design of quantum dots with a desired exciton fine structure.

3.2 Electron-hole exchange matrix elements in a special case of the two-dimensional QD with a parabolic confining potential

Motivated by experimental demonstrations of the two-dimensional parabolic potential as a good approximation for the self-assembled QDs, [95, 104, 107] we derive the electron-hole exchange matrix elements in the the HO basis. Unlike the direct Coulomb matrix element, which has been calculated previously, [30, 116] the electron-hole exchange matrix elements, which depend on spin indices, have not been reported in this basis.

The envelope functions $F_{l\sigma}(\mathbf{r})\,(H_{j\tau}(\mathbf{r}))$ are single-particle states of the electron (hole) in an isotropic parabolic confining potential with a characteristic frequency $\Omega_0^{e(h)}$, in the presence of a perpendicular magnetic field. The single-particle Hamiltonians of the electron and hole are given by the equations Eqs. 2.2 and 2.11. The index l (j) by the electron (hole) envelope wave function denotes the full set of the orbital quantum numbers which describe the state, in this case: $l = \left(n_+^{le}, n_-^{le},\right)$ $(j = \left(n_+^{jh}, n_-^{jh},\right))$. The electron-hole exchange matrix written in the basis of elecron with spin $\sigma = \frac{1}{2}\,(\alpha)$ and $\sigma = -\frac{1}{2}\,(\beta)$ and a heavy hole with spin $\tau = \pm\frac{3}{2}$, has the form (derived in the Appendix C.3, C.4, C.5):

$$V_{eh}^{X}(ci\sigma, vj\tau|cl\sigma', vk\tau') = \tag{3.1}$$

$$\left(\begin{array}{c|cccc} |vk\tau' cl\sigma'\rangle \rightarrow & & & & \\ \langle ci\sigma vj\tau| \downarrow & |\alpha-\frac{3}{2}\rangle & |\alpha+\frac{3}{2}\rangle & |\beta-\frac{3}{2}\rangle & |\beta+\frac{3}{2}\rangle \\ \hline \langle\alpha-\frac{3}{2}| & (\delta_0^{SL}+\delta^L) & 0 & 0 & \delta_{21} \\ \langle\alpha+\frac{3}{2}| & 0 & 0 & 0 & 0 \\ \langle\beta-\frac{3}{2}| & 0 & 0 & 0 & 0 \\ \langle\beta+\frac{3}{2}| & \delta_{12} & 0 & 0 & (\delta_0^{SL}+\delta^L) \end{array}\right)$$

with:

$$\delta_0^{SL}{}_{ij}^{kl} = \delta_0^{SRE}{}_{ij}^{kl} + \delta_0^{LRE}{}_{ij}^{kl} \tag{3.2}$$

$$\delta_0^{SRE}{}_{ij}^{kl} = \frac{2E_{SR}}{V_{WS}} \int_{BvK} d\mathbf{r}_1 F_{ci}^{+}(\mathbf{r}_1) H_{vj}^{+}(\mathbf{r}_1) H_{vk}(\mathbf{r}_1) F_{cl}(\mathbf{r}_1) \tag{3.3}$$

$$\delta_0^{LRE}{}_{ij}^{kl} = -\frac{16\pi\mu^2}{3V_{WS}^2} \int_{BvK} d\mathbf{r}_1 F_{ci}^{+}(\mathbf{r}_1) H_{vj}^{+}(\mathbf{r}_1) H_{vk}(\mathbf{r}_1) F_{cl}(\mathbf{r}_1) \tag{3.4}$$

$$\delta^{L}{}_{ij}^{kl} = -\frac{\mu^2}{V_{WS}^2} \left(R_{xx}^{ijkl} + R_{yy}^{ijkl}\right) \tag{3.5}$$

$$\delta_{12}{}_{ij}^{kl} = \frac{\mu^2}{V_{WS}^2} \left(R_{xx}^{ijkl} - R_{yy}^{ijkl} - 2iR_{xy}^{ijkl}\right) \tag{3.6}$$

$$\delta_{21}{}_{ij}^{kl} = \frac{\mu^2}{V_{WS}^2} \left(R_{xx}^{ijkl} - R_{yy}^{ijkl} + 2iR_{xy}^{ijkl}\right) \tag{3.7}$$

where:

$$R_{\lambda\eta}^{ijkl} = \iint_{BvK} d\mathbf{r}_1 d\mathbf{r}_2 \left(\frac{\partial^2}{\partial \mathbf{r}_1^{\lambda} \partial \mathbf{r}_1^{\eta}} F_{ci}^{+}(\mathbf{r}_1) H_{vj}^{+}(\mathbf{r}_1)\right) \frac{2}{|\mathbf{r}_1 - \mathbf{r}_2|} H_{vk}(\mathbf{r}_2) F_{cl}(\mathbf{r}_2),$$

parameter E_{SR} is the radial part of the short-range exchange misroscopic integral given by Eq. C.33 [123], μ^2 is a numerical constant (Eq. C.40) parametrizing the long-range exchange interaction [123], V_{WS} is volume of the individual unit cell (Wigner-Seitz cell), while the integration region BvK (Born-von Karman cell) expands on the QD domain.

The exchange matrix elements $V_{eh}^{X}(ci\sigma, vj\tau|cl\sigma', vk\tau')$ can be divided into two groups according to their effect on the excitonic levels: diagonal in spin subspace [123], which causes the splitting between bright ($|\Downarrow\uparrow\rangle, |\Uparrow\downarrow\rangle$) and dark ($|\Downarrow\downarrow\rangle, |\Uparrow\uparrow\rangle$) doublets, and off-diagonal in spin subspace, responsible for the bright doublet splitting by coupling states with the spin angular momentum $\pm$ 1.

In what follows, the electron-hole exchange matrix elements $V_{eh}^{X}(ci\sigma, vj\tau|cl\sigma', vk\tau')$ will be refered to as $\langle ci\sigma, vj\tau|V_{eh}^{X}|vk\tau', cl\sigma'\rangle$. The new notation allows for easier visualisation of the position of the matrix element in the full Hamiltonian matrix.

3.2.1 Electron-hole exchange mixing bright exciton states

The electron-hole long-range exchange matrix elements, responsible for the bright exciton doublet splitting, have been derived in Ref. [123] (with the full derivation shown in the Appendix C.3, C.4, C.5) and expressed in terms of electron and hole envelope wave functions (Eq. 3.6):

$$\langle i\downarrow, j\Uparrow|V_{eh}^{X}|k\Downarrow, l\uparrow\rangle \;=\; \delta_{12}{}_{ij}^{kl} = \frac{\mu^2}{V_{WS}^2}\left(R_{xx}^{ijkl} - R_{yy}^{ijkl} - 2iR_{xy}^{ijkl}\right). \tag{3.8}$$

Using the definition of R_{xx}, R_{yy} and R_{xy} (Eq. 3.8), this matrix element can be written as:

$$\begin{aligned}
&\langle i\downarrow, j\Uparrow|V_{eh}^{X}|k\Downarrow, l\uparrow\rangle \\
&= \mu^2 \int\int_{BvK} d\mathbf{r}_1 d\mathbf{r}_2 \left(\left\{\frac{\partial^2}{\partial x_1 \partial x_1} - \frac{\partial^2}{\partial y_1 \partial y_1} - 2i\frac{\partial^2}{\partial x_1 \partial y_1}\right\} F_{ci}^{+}(\mathbf{r}_1) H_{vj}^{+}(\mathbf{r}_1)\right) \\
&\times \frac{2}{|\mathbf{r}_1 - \mathbf{r}_2|} H_{vk}(\mathbf{r}_2) F_{cl}(\mathbf{r}_2) \\
&= \mu^2 \int\int d\mathbf{r}_1 d\mathbf{r}_2 \left\{\left(\frac{\partial}{\partial x_1} - i\frac{\partial}{\partial y_1}\right)^2 F_i^{+}(\mathbf{r}_1) H_j^{+}(\mathbf{r}_1)\right\} \frac{2}{|\mathbf{r}_1 - \mathbf{r}_2|} \left(H_k(\mathbf{r}_2) F_l(\mathbf{r}_2)\right),
\end{aligned} \tag{3.9}$$

where $\frac{\mu^2}{V_{WS}^2}$ has been defined by μ'^2 and the prim was dropped. The band indices were dropped, since the electron and hole envelope functions are differentiated by different letters. The matrix element $\langle i\uparrow, j\Downarrow|V_{eh}^{X}|k\Uparrow, l\downarrow\rangle$ is the hermitian conjugate of $\langle i\downarrow, j\Uparrow|V_{eh}^{X}|k\Downarrow, l\uparrow\rangle$. Note that these matrix elements are not simply matrix elements of the Coulomb interaction $\frac{2}{|\mathbf{r}_1 - \mathbf{r}_2|}$. The long-range exchange interaction involves interaction of dipoles created by two different electron-hole pairs: (i,j) and (k,l) (Eq. C27) [120–123]. The interaction of dipoles has been translated into the Coulomb interaction of the charges (k,l) with derivatives of the charges (i,j).

The differentiation operators in Eq. 3.9, acting on a product of the electron and hole wave function, can be expressed in terms of differential operators acting on either the electron or hole wave function:

$$\begin{aligned}
&\left(\frac{\partial^2}{\partial x_1^2}-\frac{\partial^2}{\partial y_1^2}-2i\frac{\partial^2}{\partial x_1\partial y_1}\right)F_i^+(\mathbf{r}_1)H_j^+(\mathbf{r}_1) \qquad (3.10)\\
=&\left\{\left(\frac{\partial}{\partial x_1}-i\frac{\partial}{\partial y_1}\right)^2F_i^+(\mathbf{r}_1)\right\}H_j^+(\mathbf{r}_1)+F_i^+(\mathbf{r}_1)\left\{\left(\frac{\partial}{\partial x_1}-i\frac{\partial}{\partial y_1}\right)^2H_j^+(\mathbf{r}_1)\right\}\\
+&\;2\left\{\left(\frac{\partial}{\partial x_1}-i\frac{\partial}{\partial y_1}\right)F_i^+(\mathbf{r}_1)\right\}\left\{\left(\frac{\partial}{\partial x_1}-i\frac{\partial}{\partial y_1}\right)H_j^+(\mathbf{r}_1)\right\}.
\end{aligned}$$

The differential operators can be then related to the boson creation and anihilation operators of the electron (introduced in Chapter 2 by equation Eq. 2.5):

$$\begin{aligned}
a-b^+ &= \frac{1}{2}\left(\frac{1}{\sqrt{2}}\frac{z}{l_h^e}+\sqrt{2}l_h^e\partial_z^*\right)-\frac{1}{2}\left(\frac{1}{\sqrt{2}}\frac{z}{l_h^e}-\sqrt{2}l_h^e\partial_z^*\right)\\
a-b^+ &= \sqrt{2}l_h^e\partial_z^*=\sqrt{2}l_h^e\left(\frac{\partial}{\partial x}-i\frac{\partial}{\partial y}\right). \qquad (3.11)
\end{aligned}$$

A similar expression can be derived for the differential operators acting on the hole wave function using harmonic oscillator operators of the hole (Eq. 2.12). The expression, Eq. 3.10, takes now the form:

$$\begin{aligned}
&\left(\frac{\partial^2}{\partial x_1^2}-\frac{\partial^2}{\partial y_1^2}-2i\frac{\partial^2}{\partial x_1\partial y_1}\right)F_i^+(\mathbf{r}_1)H_j^+(\mathbf{r}_1) \qquad (3.12)\\
=&\left\{\left(\frac{1}{\sqrt{2}l_h^e}\left(a-b^+\right)\right)^2F_i^+(\mathbf{r}_1)\right\}H_j^+(\mathbf{r}_1)+F_i^+(\mathbf{r}_1)\left\{\left(\frac{1}{\sqrt{2}l_h^h}\left(d-c^+\right)\right)^2H_j^+(\mathbf{r}_1)\right\}\\
+&\;2\left\{\left(\frac{1}{\sqrt{2}l_h^e}\left(a-b^+\right)\right)F_i^+(\mathbf{r}_1)\right\}\left\{\left(\frac{1}{\sqrt{2}l_h^h}\left(d-c^+\right)\right)H_j^+(\mathbf{r}_1)\right\}.
\end{aligned}$$

After applying the ladder operators to the electron envelope function, the first

term in the above equation (Eq. 3.12) takes the form:

$$\left\{\left(\frac{1}{\sqrt{2}l_h^e}\left(a-b^+\right)\right)^2 F_i^+(\mathbf{r}_1)\right\} H_j^+(\mathbf{r}_1) = \tag{3.13}$$

$$= \frac{1}{2l_h^{e\,2}}\left\{\left(a^2-b^{+2}-2ab^+\right)F^+_{(n_+^{ie},n_-^{ie})}(\mathbf{r}_1)\right\} H^+_{(n_+^{jh},n_-^{jh})}(\mathbf{r}_1)$$

$$= \frac{1}{2l_h^{e\,2}}\left\{\sqrt{n_-^e\left(n_-^e-1\right)}F^+_{(n_+^{ie},n_-^{ie}-2)}(\mathbf{r}_1)+\sqrt{\left(n_+^{ie}+1\right)\left(n_+^{ie}+2\right)}F^+_{(n_+^{ie}+2,n_-^{ie})}(\mathbf{r}_1)\right.$$

$$\left. - 2\sqrt{\left(n_+^{ie}+1\right)n_-^{ie}}F^+_{(n_+^{ie}+1,n_-^{ie}-1)}(\mathbf{r}_1)\right\} H^+_{(n_+^{jh},n_-^{jh})}(\mathbf{r}_1)$$

After proceeding in the same way with two other terms, the electron-hole long-range exchange matrix elements can be expressed in terms of the electron-hole Coulomb matrix elements V_{eh}^{EX}:

$$\begin{aligned}
\langle i\left(n_+^{ie},n_-^{ie}\right)\downarrow; j\left(n_+^{jh},n_-^{jh}\right)\Uparrow| \quad & V_{eh}^X \quad |k\left(n_+^{kh'},n_-^{kh'}\right)\Downarrow, l\left(n_+^{le'},n_-^{le'}\right)\uparrow;\rangle = \\
-\mu^2\left\{\frac{1}{2l_h^{e\,2}}\left[\sqrt{n_-^{ie}\left(n_-^{ie}-1\right)}\right.\right. & V_{eh}^{EX} \quad \left(n_+^{ie},n_-^{ie}-2;n_+^{jh},n_-^{jh}|n_+^{kh'},n_-^{kh'};n_+^{le'},n_-^{le'}\right) \\
+\sqrt{\left(n_+^e+1\right)\left(n_+^e+2\right)} & V_{eh}^{EX} \quad \left(n_+^{ie}+2,n_-^{ie};n_+^{jh},n_-^{jh}|n_+^{kh'},n_-^{kh'};n_+^{le'},n_-^{le'}\right) \\
-2\sqrt{n_-^{ie}\left(n_+^{ie}+1\right)} & V_{eh}^{EX} \quad \left.\left(n_+^{ie}+1,n_-^{ie}-1;n_+^{jh},n_-^{jh}|n_+^{kh'},n_-^{k\,\prime};n_+^{le'},n_-^{le'}\right)\right] \\
+\frac{1}{2l_h^{h\,2}}\left[\sqrt{n_+^{jh}\left(n_+^{jh}-1\right)}\right. & V_{eh}^{EX} \quad \left(n_+^e,n_-^e;n_+^{jh}-2,n_-^{jh}|n_+^{kh'},n_-^{kh'};n_+^{le'},n_-^{le'}\right) \\
+\sqrt{\left(n_-^{jh}+1\right)\left(n_-^{jh}+2\right)} & V_{eh}^{EX} \quad \left(n_+^e,n_-^e;n_+^{jh},n_-^{jh}+2|n_+^{kh'},n_-^{kh'};n_+^{le'},n_-^{le'}\right) \\
-2\sqrt{n_+^{jh}\left(n_-^{jh}+1\right)} & V_{eh}^{EX} \quad \left.\left(n_+^e,n_-^e;n_+^{jh}-1,n_-^{jh}+1|n_+^{kh'},n_-^{kh'};n_+^{le'},n_-^{le'}\right)\right] \\
+\frac{1}{l_h^e l_h^h}\left[\sqrt{n_-^{ie}n_+^{jh}}\right. & V_{eh}^{EX} \quad \left(n_+^{ie},n_-^{ie}-1;n_+^{jh}-1,n_-^{jh}|n_+^{kh'},n_-^{kh'};n_+^{le'},n_-^{le'}\right) \\
-\sqrt{n_-^{ie}\left(n_-^{jh}+1\right)} & V_{eh}^{EX} \quad \left(n_+^{ie},n_-^{ie}-1;n_+^{jh},n_-^{jh}+1|n_+^{kh'},n_-^{kh'};n_+^{le'},n_-^{le'}\right) \\
-\sqrt{n_+^{jh}\left(n_+^{ie}+1\right)} & V_{eh}^{EX} \quad \left(n_+^{ie}+1,n_-^{ie};n_+^{jh}-1,n_-^{jh}|n_+^{kh'},n_-^{kh'};n_+^{le'},n_-^{le'}\right) \\
+\sqrt{\left(n_+^{ie}+1\right)\left(n_-^{jh}+1\right)} & V_{eh}^{EX} \quad \left.\left.\left(n_+^{ie}+1,n_-^{ie};n_+^{jh},n_-^{jh}+1|n_+^{kh'},n_-^{kh'};n_+^{le'},n_-^{le'}\right)\right]\right\},
\end{aligned} \tag{3.14}$$

where:

$$V_{eh}^{EX}\left(n_+^{ie},n_-^{ie};n_+^{jh},n_-^{jh}|n_+^{kh'},n_-^{kh'};n_+^{le'},n_-^{le'}\right) \tag{3.15}$$
$$=\int\int d\mathbf{r}_1 d\mathbf{r}_2 F^+_{i\left(n_+^{ie},n_-^{ie}\right)}(\mathbf{r}_1)H^+_{j\left(n_+^{jh},n_-^{jh}\right)}(\mathbf{r}_1)\frac{2}{|\mathbf{r}_1-\mathbf{r}_2|}H_{k\left(n_+^{kh'},n_-^{kh'}\right)}(\mathbf{r}_2)F_{l\left(n_+^{le'},n_-^{le'}\right)}(\mathbf{r}_2).$$

In general, the above expression has to be evaluated numerically, however in the case of $l_h^e = l_h^h$ the hole envelope wave function is a hermitian conjugate of the electron envelope function: $H_{j\left(n_+^{jh},n_-^{jh}\right)}(\mathbf{r}) = F^+_{j\left(n_+^{jh},n_-^{jh}\right)}(\mathbf{r})$. This condition is fulfilled when $m_e^*\Omega_h^e = m_h^*\Omega_h^h$. In this case, the integrals in expressions (3.14) and (3.15) can be identified as the electron-electron exchange elements:

$$V_{eh}^{EX}\left(n_+^{ie},n_-^{ie};n_+^{jh},n_-^{jh}|n_+^{kh'},n_-^{kh'};n_+^{le'},n_-^{le'}\right) = V_{ee}^{EX}\left(n_+^{ie},n_-^{ie};n_+^{kh'},n_-^{kh'}|n_+^{le'},n_-^{le'};n_+^{jh},n_-^{jh}\right).$$

These matrix elements can be computed analytically [114, 116] as shown in Chapter 2 (Eq. 2.29). The quantum numbers corresponding to the envelopes of the hole changed places due to the hermitian conjugation of the hole wave function as shown above, and the conventionally chosen order of the wave functions in the element V_{ee}^{EX}:

$$V_{ee}^{EX}\left(n_+^{ie},n_-^{ie};n_+^{kh'},n_-^{kh'}|n_+^{le'},n_-^{le'};n_+^{jh},n_-^{jh}\right) = \tag{3.16}$$
$$\int\int d\mathbf{r}_1 d\mathbf{r}_2 F^+_{i\left(n_+^{ie},n_-^{ie}\right)}(\mathbf{r}_1)F^+_{k\left(n_+^{kh'},n_-^{kh'}\right)}(\mathbf{r}_2)\frac{2}{|\mathbf{r}_1-\mathbf{r}_2|}F_{l\left(n_+^{le'},n_-^{le'}\right)}(\mathbf{r}_2)F_{j\left(n_+^{jh},n_-^{jh}\right)}(\mathbf{r}_1).$$

The orbital angular momentum conservation rules for electron-electron Coulomb integrals stipulate that the z projection of the total orbital angular momentum of a pair on the right and that on the left have to be equal, otherwise the integral is equal to zero. Knowing that, as well as the expression for the orbital angular momentum of the electron-electron pair $L^{ee} = \left(n_+^{(1e)} - n_-^{(1e)}\right) + \left(n_+^{(2e)} - n_-^{(2e)}\right)$ and for the electron-hole pair $L^{eh} = \left(n_+^{(1e)} - n_-^{(1e)}\right) - \left(n_+^{(2h)} - n_-^{(2h)}\right)$, the conservation rules for the matrix elements:
$\langle i\left(n_+^{ie},n_-^{ie}\right)\downarrow; j\left(n_+^{jh},n_-^{jh}\right)\Uparrow|V_{eh}^X|k\left(n_+^{kh'},n_-^{kh'}\right)\Downarrow; l\left(n_+^{le'},n_-^{le'}\right)\uparrow\rangle$ can be derived. If one denotes $\mathcal{L}_L = \left(n_+^{ie} - n_-^{ie}\right) - \left(n_+^{jh} - n_-^{jh}\right)$ as the angular momentum of the electron-hole pair on the left, and $\mathcal{L}_R = \left(n_+^{le'} - n_-^{le'}\right) - \left(n_+^{kh'} - n_-^{kh'}\right)$ as that of

the pair on the right of the matrix element (Eq. 3.14), then the orbital angular momentum conservation rule for this matrix element is:

$$\mathcal{L}_L = \mathcal{L}_R - 2. \tag{3.17}$$

At the same time the above matrix element is non-zero only for one specific set of spin quantum numbers: $(\tau, \sigma) = (+3/2, -1/2)$ and $(\tau', \sigma') = (-3/2, +1/2)$, for which the electron-hole pair spin conservation rule is:

$$\mathcal{S}_L = \mathcal{S}_R + 2. \tag{3.18}$$

Hence the total angular momentum of a pair (a sum of the orbital and spin angular momenta) is conserved:

$$\mathcal{J}_L = \mathcal{L}_L + \mathcal{S}_L = \mathcal{L}_R + \mathcal{S}_R = \mathcal{J}_R. \tag{3.19}$$

The long-range electron-hole exchange can flip the spin of the carriers with simultaneous transfer of at least one particle to a different single-particle orbital, so that the total angular momentum conservation rule is fulfilled.

3.2.2 Electron-hole exchange responsible for the bright-dark exciton splitting

In the previous section the analysis of the bright exciton splitting was provided. Here we analyze the splitting between the bright and dark exciton states, typically attributed to just the short-range exchange.

The electron-hole exchange matrix elements $\langle i\uparrow, j\Downarrow|V_{eh}^X|k\Downarrow, l\uparrow\rangle = \langle i\uparrow, j\Downarrow|\delta_0^{SL}|k\Downarrow, l\uparrow\rangle + \langle i\uparrow, j\Downarrow|\delta^L|k\Downarrow, l\uparrow\rangle$, which are diagonal in the spin subspace, are a sum of the local short- and long-range exchange ${\delta_0^{SL}}_{ij}^{kl}$ (Eqs. 3.2, 3.3 and 3.4) proportional to the overlap between the two electron-hole pairs, and a non-local term ${\delta^L}_{ij}^{kl}$, Eq. 3.5, which involves differential operators applied to electron-hole pair envelopes [123]. At the same time: $\langle i\downarrow, j\Uparrow|V_{eh}^X|k\Uparrow, l\downarrow\rangle = \langle i\uparrow, j\Downarrow|V_{eh}^X|k\Downarrow, l\uparrow\rangle$.

First, the non-local long-range contribution to the diagonal terms will be described:

$$\begin{aligned}\langle i\uparrow, j\Downarrow|\quad \delta^L \quad |k\Downarrow, l\uparrow\rangle &= -\mu^2\left(R_{xx}{}^{ijkl} + R_{yy}{}^{ijkl}\right) \\ &= -\mu^2\int\int d\mathbf{r}_1 d\mathbf{r}_2 \left\{\left(\frac{\partial^2}{\partial x_1^2}+\frac{\partial^2}{\partial y_1^2}\right)F_i^+(\mathbf{r}_1)H_j^+(\mathbf{r}_1)\right\}\frac{2}{|\mathbf{r}_1-\mathbf{r}_2|}H_k(\mathbf{r}_2)F_l(\mathbf{r}_2).\end{aligned} \tag{3.20}$$

As previously, the differential operator can be expressed in terms of the electron or hole ladder operators depending on the type of envelope it is acting upon:

$$\begin{aligned}\left(\frac{\partial^2}{\partial x_1^2}+\frac{\partial^2}{\partial y_1^2}\right)F_i^+(\mathbf{r}_1)H_j^+(\mathbf{r}_1) &= \frac{1}{2{l_h^e}^2}\left\{\left(b-a^+\right)\left(a-b^+\right)F_i^+(\mathbf{r}_1)\right\}H_j^+(\mathbf{r}_1) \\ &+ \frac{1}{2l_h^e l_h^h}\left\{\left(a-b^+\right)F_i^+(\mathbf{r}_1)\right\}\left\{\left(c-d^+\right)H_j^+(\mathbf{r}_1)\right\} \\ &+ \frac{1}{2l_h^e l_h^h}\left\{\left(b-a^+\right)F_i^+(\mathbf{r}_1)\right\}\left\{\left(d-c^+\right)H_j^+(\mathbf{r}_1)\right\} \\ &+ \frac{1}{2{l_h^h}^2}F_i^+(\mathbf{r}_1)\left\{\left(c-d^+\right)\left(d-c^+\right)H_j^+(\mathbf{r}_1)\right\}\end{aligned} \tag{3.21}$$

After applying the ladder operators to the envelope functions and inserting this expression into Eq. 3.20, the matrix element $\delta^{L}{}_{ij}^{kl}$ can be written as a sum of

electron-hole Coulomb matrix elements V_{eh}^{EX}:

$$
\begin{aligned}
\langle i\left(n_+^{ie},n_-^{ie}\right)\uparrow; j\left(n_+^{jh},n_-^{jh}\right)\Downarrow| \quad \delta^L \quad |k\left(n_+^{kh\prime},n_-^{kh\prime}\right)\Downarrow; l\left(n_+^{le\prime},n_-^{le\prime}\right)\uparrow\rangle = \qquad (3.22)\\
-\mu^2\Bigg\{\frac{1}{2{l_h^e}^2}\Bigg[\sqrt{n_+^{ie}n_-^{ie}} \quad V_{eh}^{EX} \quad \left(n_+^{ie}-1,n_-^{ie}-1;n_+^{jh},n_-^{jh}|n_+^{kh\prime},n_-^{kh\prime};n_+^{le\prime},n_-^{le\prime}\right)\\
+\sqrt{\left(n_+^{ie}+1\right)\left(n_-^{ie}+1\right)} \quad V_{eh}^{EX} \quad \left(n_+^{ie}+1,n_-^{ie}+1;n_+^{jh},n_-^{jh}|n_+^{kh\prime},n_-^{kh\prime};n_+^{le\prime},n_-^{le\prime}\right)\\
-\left(n_+^{ie}+n_-^{ie}+1\right) \quad V_{eh}^{EX} \quad \left(n_+^{ie},n_-^{ie};n_+^{jh},n_-^{jh}|n_+^{kh\prime},n_-^{kh\prime};n_+^{le\prime},n_-^{le\prime}\right)\Bigg]\\
+\frac{1}{2l_h^{h\,2}}\Bigg[\sqrt{n_+^{jh}n_-^{jh}} \quad V_{eh}^{EX} \quad \left(n_+^{ie},n_-^{ie};n_+^{jh}-1,n_-^{jh}-1|n_+^{kh\prime},n_-^{kh\prime};n_+^{le\prime},n_-^{le\prime}\right)\\
+\sqrt{\left(n_+^{jh}+1\right)\left(n_-^{jh}+1\right)} \quad V_{eh}^{EX} \quad \left(n_+^{ie},n_-^{ie};n_+^{jh}+1,n_-^{jh}+1|n_+^{kh\prime},n_-^{kh\prime};n_+^{le\prime},n_-^{le\prime}\right)\\
-\left(n_+^{jh}+n_-^{jh}+1\right) \quad V_{eh}^{EX} \quad \left(n_+^{ie},n_-^{ie};n_+^{jh},n_-^{jh}|n_+^{kh\prime},n_-^{kh\prime};n_+^{le\prime},n_-^{le\prime}\right)\Bigg]\\
+\frac{1}{2l_h^e l_h^h}\Bigg[\sqrt{n_+^{ie}n_+^{jh}} \quad V_{eh}^{EX} \quad \left(n_+^{ie}-1,n_-^{ie};n_+^{jh}-1,n_-^{jh}|n_+^{kh\prime},n_-^{kh\prime};n_+^{le\prime},n_-^{le\prime}\right)\\
-\sqrt{n_+^{ie}\left(n_-^{jh}+1\right)} \quad V_{eh}^{EX} \quad \left(n_+^{ie}-1,n_-^{ie};n_+^{jh},n_-^{jh}+1|n_+^{kh\prime},n_-^{kh\prime};n_+^{le\prime},n_-^{le\prime}\right)\\
-\sqrt{n_+^{jh}\left(n_-^{ie}+1\right)} \quad V_{eh}^{EX} \quad \left(n_+^{ie},n_-^{ie}+1;n_+^{jh}-1,n_-^{jh}|n_+^{kh\prime},n_-^{kh\prime};n_+^{le\prime},n_-^{le\prime}\right)\\
+\sqrt{\left(n_-^{ie}+1\right)\left(n_-^{jh}+1\right)} \quad V_{eh}^{EX} \quad \left(n_+^{ie},n_-^{ie}+1;n_+^{jh},n_-^{jh}+1|n_+^{kh\prime},n_-^{kh\prime};n_+^{le\prime},n_-^{le\prime}\right)\\
+\sqrt{n_-^{ie}n_-^{jh}} \quad V_{eh}^{EX} \quad \left(n_+^{ie},n_-^{ie}-1,n_+^{kh\prime},n_-^{kh\prime}|n_+^{le\prime},n_-^{le\prime},n_+^{jh},n_-^{jh}-1\right)\\
-\sqrt{n_+^{ie}\left(n_+^{ie}+1\right)} \quad V_{eh}^{EX} \quad \left(n_+^{ie},n_-^{ie}-1;n_+^{jh}+1,n_-^{jh}|n_+^{kh\prime},n_-^{kh\prime};n_+^{le\prime},n_-^{le\prime}\right)\\
-\sqrt{n_-^{jh}\left(n_+^{ie}+1\right)} \quad V_{eh}^{EX} \quad \left(n_+^{ie}+1,n_-^{ie};n_+^{jh},n_-^{jh}-1|n_+^{kh\prime},n_-^{kh\prime};n_+^{le\prime},n_-^{le\prime}\right)\\
+\sqrt{\left(n_+^{ie}+1\right)\left(n_+^{jh}+1\right)} \quad V_{eh}^{EX} \quad \left(n_+^{ie}+1,n_-^{ie};n_+^{jh}+1,n_-^{jh}|n_+^{kh\prime},n_-^{kh\prime};n_+^{le\prime},n_-^{le\prime}\right)\Bigg]\Bigg\},
\end{aligned}
$$

with the following orbital and spin angular momentum conservation rules: $\mathcal{L}_L = \mathcal{L}_R$ and $\mathcal{S}_L = \mathcal{S}_R$.

The remaining part of the electron-hole exchange, which is a sum of the short-range exchange and the local part of the long-range exchange, Eq. 3.2, is proportional to the overlap between the envelopes of both electron-hole pairs,

Eqs. 3.3, 3.4:

$$\begin{aligned}\langle i\uparrow, j\Downarrow|\quad \delta_0^{SL}\quad |k\Downarrow, l\uparrow\rangle &= \delta_0^{SRE}{}_{ij}^{kl} + \delta_0^{LRE}{}_{ij}^{kl} \\ &= \left(2E_{SR} - \frac{16\pi\mu^2}{3}\right)\int_{BvK} d\mathbf{r}_1 F_i^+(\mathbf{r}_1)H_j^+(\mathbf{r}_1)H_k(\mathbf{r}_1)F_l(\mathbf{r}_1).\end{aligned} \tag{3.23}$$

The integral in the Eq. 3.23 can be calculated by introducing the delta function $\delta(\mathbf{r}_1 - \mathbf{r}_2)$:

$$\begin{aligned}&\int_{BvK} d\mathbf{r}_1 F_i^+(\mathbf{r}_1)H_j^+(\mathbf{r}_1)H_k(\mathbf{r}_1)F_l(\mathbf{r}_1) \\ &= \int_{BvK}\int_{BvK} d\mathbf{r}_1 d\mathbf{r}_2 F_i^+(\mathbf{r}_1)F_l(\mathbf{r}_1)\delta(\mathbf{r}_1 - \mathbf{r}_2)H_j^+(\mathbf{r}_2)H_k(\mathbf{r}_2).\end{aligned} \tag{3.24}$$

Similarly to the electron-electron direct Coulomb interaction matrix element, where the function $v(\mathbf{r}_1 - \mathbf{r}_2) = \frac{2}{|\mathbf{r}_1 - \mathbf{r}_2|}$ was expressed in terms of the plane waves, the function $v(\mathbf{r}_1 - \mathbf{r}_2) = \delta(\mathbf{r}_1 - \mathbf{r}_2)$ has the following expansion in the plane waves:

$$\delta(\mathbf{r}_1 - \mathbf{r}_2) = \frac{1}{4\pi^2}\int d\mathbf{q}\exp\left(i\mathbf{q}(\mathbf{r}_1 - \mathbf{r}_2)\right) \tag{3.25}$$

The integral, Eq. 3.24, can be now written as:

$$\begin{aligned}&\int_{BvK} d\mathbf{r}_1 F_i^+(\mathbf{r}_1)H_j^+(\mathbf{r}_1)H_k(\mathbf{r}_1)F_l(\mathbf{r}_1) \\ &= \frac{1}{4\pi^2}\int d\mathbf{q}\int d\mathbf{r}_1 F_i^+(\mathbf{r}_1)\exp\left(i\mathbf{q}\mathbf{r}_1\right)F_l(\mathbf{r}_1)\int d\mathbf{r}_2 H_j^+(\mathbf{r}_2)H_k(\mathbf{r}_2)\exp\left(-i\mathbf{q}\mathbf{r}_2\right) \\ &= \frac{1}{4\pi^2}\int d\mathbf{q}\langle i|\exp\left(i\mathbf{q}\mathbf{r}_1\right)|l\rangle\langle j|\exp\left(-i\mathbf{q}\mathbf{r}_2\right)|k\rangle \\ &= \frac{1}{4\pi^2}\int d\mathbf{q} M_1^e M_2^h\end{aligned} \tag{3.26}$$

The analogy with the derivation of the electron-electron Coulomb interaction $V_{ee}(i\sigma, j\sigma'|k\sigma', l\sigma)$ has been used. The matrix element M_1^e is given by Eq. B16, while the element M_2^h is calculated anologously.

Writing explicitly the HO quantum numbers for each single-particle state

i, j, k, l, the integral, Eq. 3.26, can be written as:

$$\begin{aligned}
&\int d\mathbf{r}_1 F^{+}_{i\left(n^{ie}_{+},n^{ie}_{-}\right)}(\mathbf{r}_1) H^{+}_{j\left(n^{jh}_{+},n^{jh}_{-}\right)}(\mathbf{r}_1) H_{k\left(n^{kh\prime}_{+},n^{kh\prime}_{-}\right)}(\mathbf{r}_1) F_{l\left(n^{le\prime}_{+},n^{le\prime}_{-}\right)}(\mathbf{r}_1) \\
&= \frac{1}{4\pi^2} \frac{(-1)^{n^{kh}_{+}+n^{kh}_{-}+n_{+}jh+n^{jh}_{-}}}{\sqrt{n^{ie}_{+}!n^{ie}_{-}!n^{le}_{+}!n^{le}_{-}!n^{kh}_{+}!n^{kh}_{-}!n^{jh}_{+}!n^{jh}_{-}!}} \sum_{p_1=0}^{min(n^{le}_{+},n^{ie}_{+})} \binom{n^{ie}_{+}}{p_1}\binom{n^{le}_{+}}{p_1} \\
&\times \sum_{p_2=0}^{min(n^{le}_{-},n^{ie}_{-})} \binom{n^{ie}_{-}}{p_2}\binom{n^{le}_{-}}{p_2} \sum_{p_3=0}^{min(n^{kh}_{+},n^{jh}_{+})} \binom{n^{kh}_{+}}{p_3}\binom{n^{jh}_{+}}{p_3} \sum_{p_4=0}^{min(n^{kh}_{-},n^{jh}_{-})} \binom{n^{kh}_{-}}{p_4}\binom{n^{jh}_{-}}{p_4} \\
&\times p_1!p_2!p_3!p_4! \times I_{p_1p_2p_3p_4}
\end{aligned} \tag{3.27}$$

where:

$$\begin{aligned}
I_{p_1p_2p_3p_4} &= \int_0^{\infty} qdq \int_0^{2\pi} \phi_q e^{-|Q_e|^2-|Q_h|^2} \left(iQ^*_e\right)^{n^{ie}_{+}-p_1} \left(iQ_e\right)^{n^{ie}_{-}-p_2} \left(iQ_e\right)^{n^{le}_{+}-p_1} \\
&\times \left(iQ^*_e\right)^{n^{le}_{-}-p_2} \left(-iQ^*_h\right)^{n^{jh}_{+}-p_3} \left(-iQ_h\right)^{n^{jh}_{-}-p_4} \left(-iQ_h\right)^{n^{kh}_{+}-p_3} \left(-iQ^*_h\right)^{n^{kh}_{-}-p_4},
\end{aligned} \tag{3.28}$$

and

$$Q_h = \frac{l^h_h}{l^e_h} Q_e. \tag{3.29}$$

The difference between this integral and the analogous integral given by Eq. B18 is the power of the variable q, as well as the fact that there are now two different variables Q_e and Q_h. By inserting the relation between Q_e and Q_h (Eq. 3.29) into the formula for the $I_{p_1p_2p_3p_4}$ (Eq. 3.28) one obtains:

$$\begin{aligned}
I_{p_1p_2p_3p_4} &= \int_0^{\infty} qdq \int_0^{2\pi} \phi_q e^{-|Q_e|^2\left(1+\frac{l^h_h}{l^e_h}\right)} \left(iQ^*_e\right)^{n^{ie}_{+}+n^{le}_{-}-p_2-p_1} \left(iQ_e\right)^{n^{ie}_{-}+n^{le}_{+}-p_1-p_2} \\
&\times \left(-iQ^*_h\right)^{n^{jh}_{+}+n^{kh}_{-}-p_4-p_3} \left(-iQ_h\right)^{n^{jh}_{-}+n^{kh}_{+}-p_3-p_4} \left(\frac{l^h_h}{l^e_h}\right)^{n^{kh}_{+}+n^{kh}_{-}+n^{jh}_{+}+n^{jh}_{-}-2p_3-2p_4}
\end{aligned} \tag{3.30}$$

Changing variables in the same fashion as in the derivation of the direct electron-electron Coulomb matrix elements, the evaluation of the integrals over the wavevec-

tor q gives the final form of $I_{p_1p_2p_3p_4}$:

$$I_{p_1p_2p_3p_4} = \left(\frac{l_h^h}{l_h^e}\right)^{n_+^{kh}+n_-^{kh}+n_+^{jh}+n_-^{je}-2p_3-2p_4} \frac{2\pi}{{l_h^e}^2}\delta_{L_L,L_R}(-1)^p \left(1+\left(\frac{l_h^h}{l_h^e}\right)^2\right)^{-(p+1)} \Gamma(p+1). \tag{3.31}$$

The Eqs. 3.23, 3.27, and 3.31 are the final expressions for the short-range exchange contribution.

3.3 Exciton in a high magnetic field. Application and analysis of electron-hole exchange matrix elements

The derived expressions of long- and short-range exchange Coulomb matrix elements in the HO basis, Eqs. 3.14, 3.23, 3.22, for an arbitrary magnetic field can now be included in the exciton Hamiltonian and combined with the direct Coulomb interaction, anisotropy, and magnetic field. This methodology allows to introduce and understand the influence of electron-hole correlations and their modification by the magnetic field on the exciton fine structure.

In order to understand the effect of electron-hole correlations, the exciton fine structure is studied as a function of the number of confined electron and hole electronic shells for a fixed shell energy spacing. The more electronic shells present, the stronger the electronic correlations. For a very deep quantum dot with a large number of confined shells, such analysis is equivalent to the analysis of convergence. In reality, dots with a different number of confined shells can be grown. Understanding the role of different shells, *s*,*p*,*d*,.. on the exciton fine structure might allow to design the exciton fine structure by designing quantum dot shells.

The exciton Hamiltonian $\hat{H'}_X$ (Eq. 2.34) has now four terms:

$$\hat{H'}_X = \hat{H}_X + \delta\hat{H}^e_{anis} + \delta\hat{H}^h_{anis} + \hat{H}_{EHX}. \tag{3.32}$$

The first term is the exciton Hamiltonian of the isotropic parabolic quantum dot (Section 2.6) including the single-particle HO energies $\varepsilon_{i,\tau}^{e(h)}$ of the electron (hole) HO and the direct Coulomb interaction between them. The next two terms in the Hamiltonian, Eq. 3.32, introduce the anisotropic correction of the confining potential of electrons and holes, Eq. 2.15. The third term in the Hamiltonian, Eq. 3.32, is the electron-hole exchange term, which for ease of use can be written in the following compact form:

$$\hat{H}_{EHX} = \sum_{ijkl\sigma\sigma'\tau\tau'} \langle i\sigma, j\tau | V_{eh}^{X} | k\tau', l\sigma' \rangle c_{i\sigma}^{+} h_{j\tau}^{+} h_{k\tau'} c_{l\sigma'}. \tag{3.33}$$

The Hamiltonian of the exciton in a QD with an isotropic confining potential without the electron-hole exchange interaction $\hat{H}_X$ conserves both the electron and hole spin and the angular momentum of the electron-hole pair. The Hamiltonian matrix $\hat{H}_X$ was built and diagonalized in each of the L, σ, τ subspaces separately. The presence of anisotropy in the QD, as well as the electron-hole exchange interaction, mixes different angular momenta and spin subspaces. The complete Hamiltonian matrix has to be built using all electron-hole configurations in the form $|i\tau j\sigma\rangle = h_{i\tau}^{+} c_{j\sigma}^{+} |0\rangle$, where i, j denote the HO single-particle levels. From diagonalization of the exciton Hamiltonian matrix one obtains the set of eigenstates in the form of linear combinations of basis configurations: $|X_k\rangle = \sum_{ij\sigma\tau}^{N} A_{ij\sigma\tau}^{(k)} |i\tau j\sigma\rangle$ with energy E_k, where $k = 1, ..., N$, N is the size of the basis, and $A_{ij\sigma\tau}^{(k)}$ is the amplitude of the configuration $|i\tau j\sigma\rangle$ in the state $|X_k\rangle$. Coefficients $A_{ij\sigma\tau}^{(k)}$ as well as the exciton energies depend on the magnetic field B and are evaluated for each magnetic field separately.

Having obtained the eigenenergies and eigenfunctions of the electron-hole pair, one can calculate the emission and absorption spectra from Fermi's Golden Rule, Eqs. 2.31 and 2.33, respectively.

The model isotropic quantum dot discussed below has the electron shell spacing $\Omega_e = 24$ meV and the hole shell spacing $\Omega_h = 6$ meV. The dielectric constant $\varepsilon = 10.6$, the effective mass of the electron $m_e^* = 0.1 m_0$ and the hole $m_h^* = 0.4 m_0$, and Lande factors $g_e = -0.7$, $g_h = 0.38$ [19, 150–152]. With these parameters, the effective Rydberg is $Ry = 12.11$ meV, the effective Bohr radius $a_B = 5.61$ nm, and $\Omega_e = 4 \cdot \Omega_h$. The anisotropy of the quantum dot is given by the ratio

Ω_y/Ω_x or the anisotropy parameter γ. Results for the exciton fine structure will be illustrated for the anisotropy of $\Omega_y/\Omega_x = 0.72$ ($\gamma = 0.32$ as defined in Section 2.3).

The exciton Zeeman energy in a high magnetic field dominates over the exchange splitting of the two exciton bright states. To bring out the magnetic field evolution of this splitting due to the exchange interaction, the Zeeman energy is not included in the calculations presented in what follows.

First, the dependence of several important electron-hole exchange matrix elements, involving the s, p and d shells, $\langle 00\uparrow; 00\Downarrow|V_{eh}^{X}|20\Uparrow; 00\downarrow\rangle$, $\langle 00\uparrow; 00\Downarrow|\delta^{SL}|00\Downarrow; 00\uparrow\rangle$, $\langle 00\uparrow; 00\Downarrow|\delta^{L}|00\Downarrow; 00\uparrow\rangle$ and $\langle 00\uparrow; 00\Downarrow|\delta^{SL}+\delta^{L}|00\Downarrow; 00\uparrow\rangle$ on the magnetic field in the symmetric electron-hole case, where $l_h^h = l_h^e$, will be analyzed. Their dependence on the magnetic field is shown in Fig. 3.1.

Since the electron-hole exchange elements are expressed as a linear combination of the direct Coulomb interaction elements, they are proportional to the parameter V_0: $V_{eh}^{EX} \sim \sqrt{\pi\omega_h} = \frac{\sqrt{\pi}}{l_h}$, Ref. [104]). The matrix element $\langle 00\uparrow; 00\Downarrow|V_{eh}^{X}|20\Uparrow; 00\downarrow\rangle$, which mixes bright excitonic configurations, Eq. 3.14, evolves as l_h^{-3}, while the magnetic-field dependence of the diagonal matrix element $\langle 00\uparrow; 00\Downarrow|\delta^{SL}+\delta^{L}|00\Downarrow; 00\uparrow\rangle$, Fig. 3.1 (d), is more complicated due to the interplay between the l_h^{-2} dependence of δ^{SL}(b) and the l_h^{-3} dependence of δ^{L}(c).

Now the electron-hole exchange matrix elements will be used in the calculations of the correlated exciton states. It will be analyzed here how the bright exciton level splitting depends on the number of electron and hole single-particle energy shells, anisotropy of the confining potential and the magnetic field. Following previous publications [108], the bright exciton level splitting is denoted by the Δ_2. Fig. 3.2 (right inset) shows the exciton emission spectrum calculated for s, p, d confined single-particle shells in an anisotropic QD. There are two emission peaks corresponding to the two bright exciton states.

Fig. 3.2 (left inset) shows the energy of the two lowest bright exciton states for a different number of confined single-particle shells in an anisotropic QD. As expected, the more HO shells that are confined in the QD, the lower the exciton energy, due to the direct Coulomb scattering. Due to the fact that the basis used is that of the isotropic HO, one does not observe any electron-hole exchange

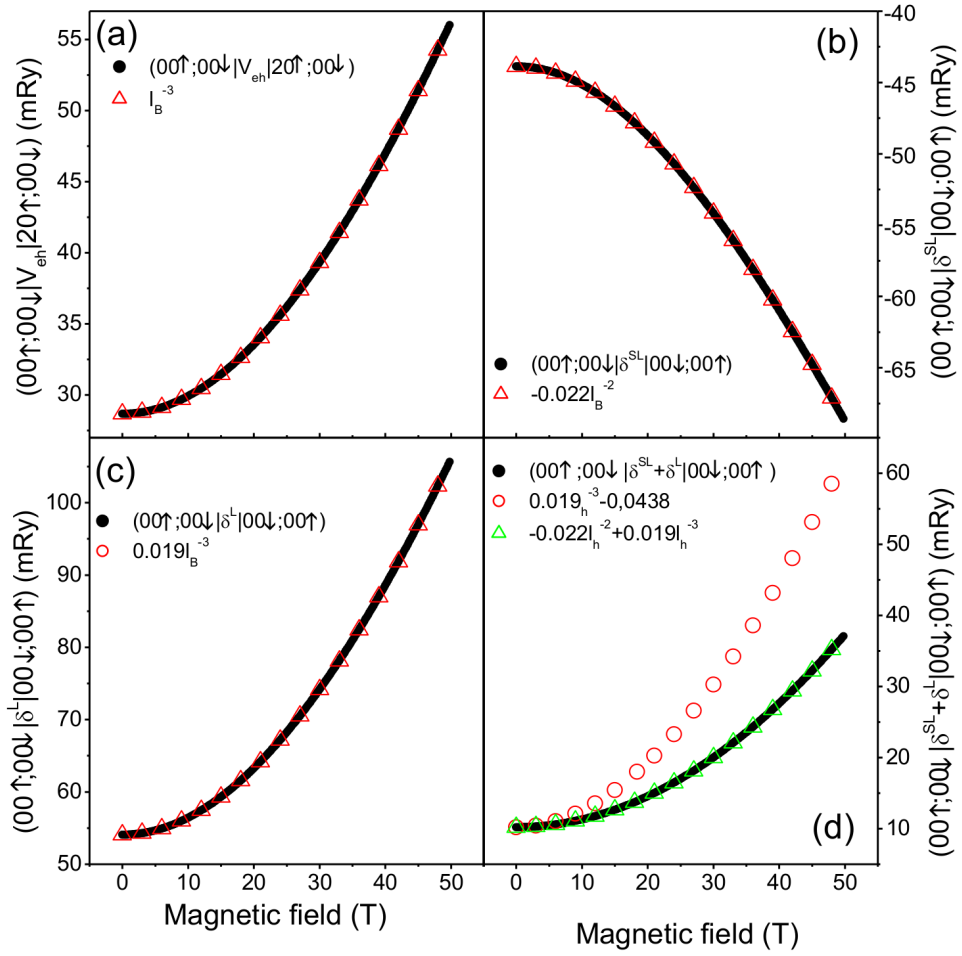

Figure 3.1: Magnetic-field evolution of the selected electron-hole exchange matrix elements, namely: (a) $\langle 00\uparrow;00\Downarrow|V_{eh}^{X}|00\Uparrow;20\downarrow\rangle$, (b) the local part of the $\langle 00\uparrow;00\Downarrow|V_{eh}^{X}|00\Downarrow;00\uparrow\rangle$ matrix element, (c) the non-local part of the $\langle 00\uparrow;00\Downarrow|V_{eh}^{X}|00\Downarrow;00\uparrow\rangle$ matrix element, and (d) the full $\langle 00\uparrow;00\Downarrow|V_{eh}^{X}|00\Downarrow;00\uparrow\rangle$ matrix element.

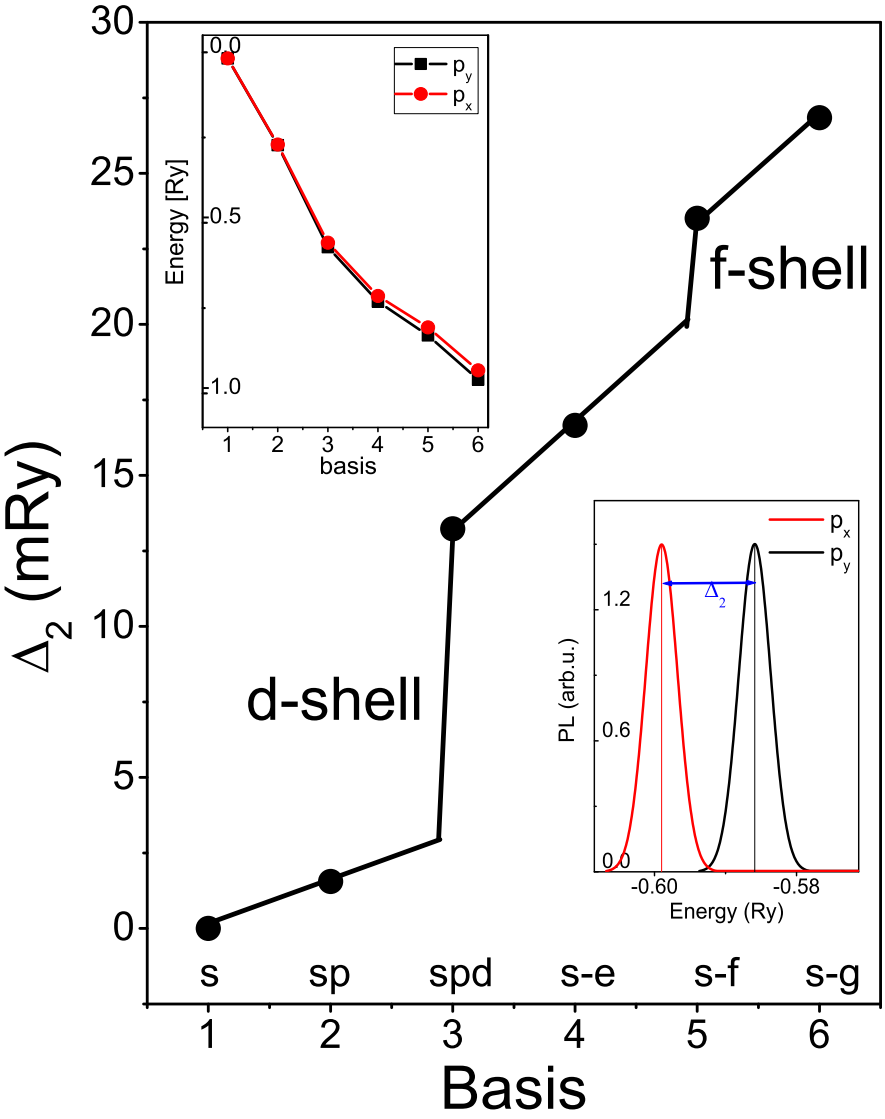

Figure 3.2: The bright exciton state splitting Δ_2 for QDs with a different number of confined shells, and with an anisotropy parameter $\gamma = 0.32$. (Left inset) The energies of bright exciton states for QDs with a different number of confined shells. (Right inset) The exciton emission spectrum from an anisotropic QD confining s, p and d single-particle shells.

splitting, Fig. 3.2, when the QD confines only the s shell for electrons and holes. As explained in Section 3.2.2, the electron-hole exchange matrix elements are nonzero only between pairs of states for which the orbital angular momentum differs by two. For this reason we observe a strong increase in the electron-hole exchange splitting Δ_2 when the shells with angular momenta $2, 4, ..,$ (d- and f-shells) are added. There is no significant change in the splitting when an odd shell is added (p, e, g-shell).

To understand why the anisotropy in the confining potential of the QD is necessary to observe the electron-hole exchange splitting of the bright states Δ_2, an anisotropic QD in the absence of the long-range electron-hole exchange will be analyzed. The wave function of the bright state with the spin angular momentum $\tau + \sigma = 1$ in the presence of the anisotropy has the form:

$$\begin{aligned} |GS\Uparrow\downarrow\rangle &= A_{00,00}|00\Uparrow,00\downarrow\rangle - A_{00,11}|00\Uparrow,11\downarrow\rangle - A_{11,00}|11\Uparrow,00\downarrow\rangle \\ &+ A_{01,01}\left(|01\Uparrow,01\downarrow\rangle + |10\Uparrow,10\downarrow\rangle\right) + A_{11,11}|11\Uparrow,11\downarrow\rangle \\ &- A_{20,00}\left(|02\Uparrow,00\downarrow\rangle + |20\Uparrow,00\downarrow\rangle\right) \\ &- A_{00,02}\left(|00\Uparrow,20\downarrow\rangle + |00\Uparrow,02\downarrow\rangle\right) \\ &- A_{10,01}\left(|01\Uparrow,10\downarrow\rangle + |10\Uparrow,01\downarrow\rangle\right). \end{aligned} \tag{3.34}$$

A similar expression can be written for the second bright state with the spin angular momentum equal to $\tau + \sigma = -1$. Now, the coupling between these states due to the long-range exchange interaction is given by the sum:

$$\begin{aligned} \langle GS\uparrow\Downarrow|V_{eh}^X|GS\Uparrow\downarrow\rangle = -2(\quad & A_{00,00}A_{20,00}\langle 00\uparrow,00\Downarrow|V_{eh}^X|20\Uparrow,00\downarrow\rangle \\ + \; & A_{00,00}A_{10,01}\langle 00\uparrow,00\Downarrow|V_{eh}^X|10\Uparrow,01\downarrow\rangle \\ + \; & A_{00,00}A_{00,02}\langle 00\uparrow,00\Downarrow|V_{eh}^X|00\Uparrow,02\downarrow\rangle \\ + \; & A_{11,00}A_{20,00}\langle 00\uparrow,11\Downarrow|V_{eh}^X|20\Uparrow,00\downarrow\rangle \\ + \; & A_{11,00}A_{10,01}\langle 00\uparrow,11\Downarrow|V_{eh}^X|10\Uparrow,01\downarrow\rangle \\ + \; & A_{11,00}A_{00,02}\langle 00\uparrow,11\Downarrow|V_{eh}^X|00\Uparrow,02\downarrow\rangle \\ + \; & \ldots). \end{aligned} \tag{3.35}$$

Because all of the $\langle i\uparrow, j\Downarrow|V_{eh}^X|k\Uparrow, l\downarrow\rangle$ matrix elements are of the same order, the

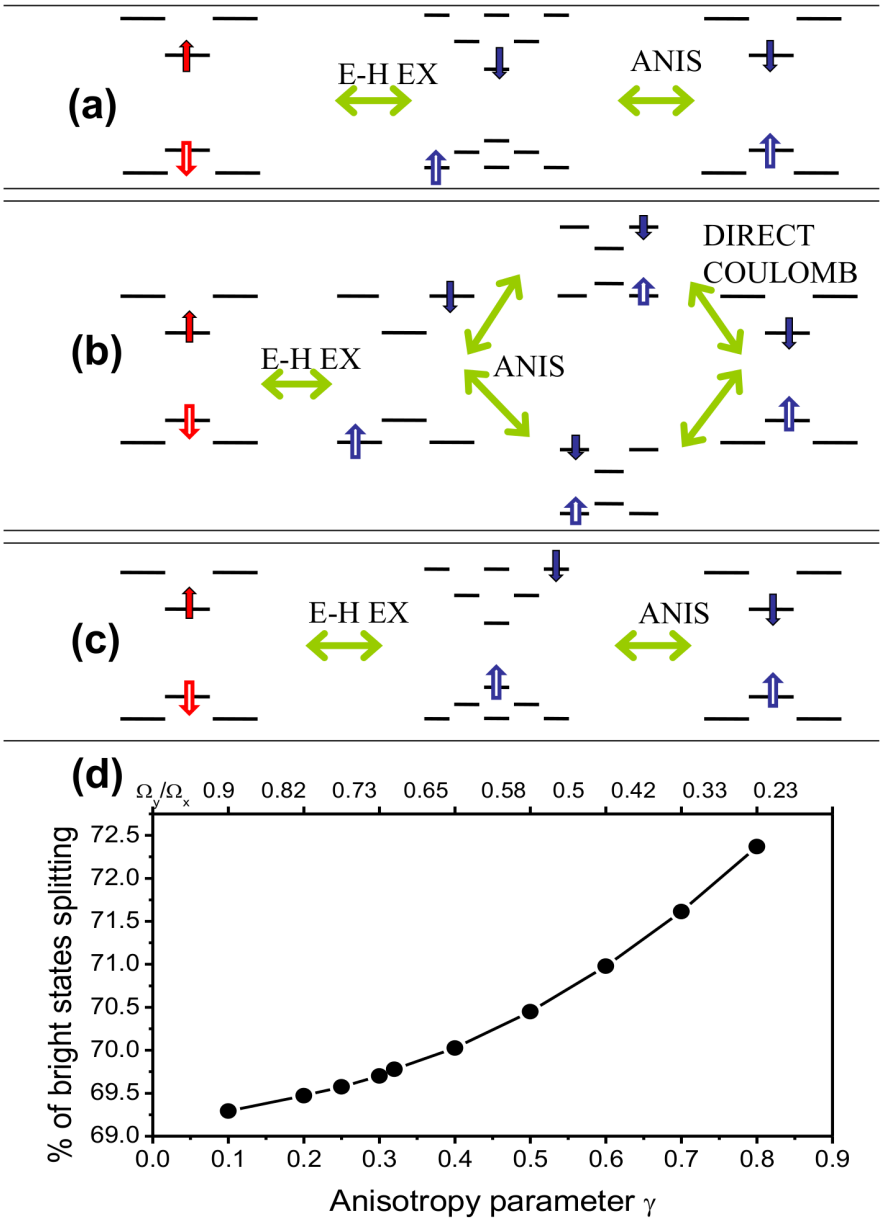

Figure 3.3: The three most important paths of coupling between two bright excitonic states $|GS \Downarrow\uparrow\rangle$ and $|GS \Uparrow\downarrow\rangle$ involving e-h matrix elements: $\langle 00\uparrow, 00\Downarrow |V_{eh}^{X}| 20\Uparrow, 00\downarrow\rangle$ (a) ,$\langle 00\uparrow, 00\Downarrow |V_{eh}^{X}| 10\Uparrow, 01\downarrow\rangle$ (b) and $\langle 00\uparrow, 00\Downarrow |V_{eh}^{X}| 00\Uparrow, 02\downarrow\rangle$ (c). (d) The percentage of the long-range exchange matrix element covered by the three first terms of Eq. (3.35).

contribution of the terms in Eq. 3.35 is largely determined by the magnitude of the product of the coefficients A_{ij}, A_{kl} in the exciton wavefunctions. Since the lowest-energy single-particle state is $|00,00\rangle$, the coefficient $A_{00,00}$ is the biggest. The first three terms of the sum, Eq. 3.35, correspond to the most important coupling mechanisms between the two bright excitonic states $|GS \Downarrow\uparrow\rangle$ and $|GS \Uparrow\downarrow\rangle$, involving electron-hole exchange matrix elements: (a) $\langle 00\uparrow, 00\Downarrow|V_{eh}^{X}|20\Uparrow, 00\downarrow\rangle$, (b) $\langle 00\uparrow, 00\Downarrow|V_{eh}^{X}|10\Uparrow, 01\downarrow\rangle$ and (c) $\langle 00\uparrow, 00\Downarrow|V_{eh}^{X}|00\Uparrow, 02\downarrow\rangle$. They are shown schematically in Fig. 3.3 (a-c). The contribution of these three terms to the bright exciton exchange splitting is $\approx 70\%$ of the splitting for a broad range of values of the anisotropy parameter, as shown in Fig. 3.3 (d).

Now, the effect of the magnetic field on the exciton fine structure will be analyzed. The magnetic field changes the single-particle energy levels of both electrons and holes and increases the strength of direct Coulomb interactions [101, 107]. In Fig. 3.4 (a) the energy splitting of the two bright exciton levels Δ_2 for anisotrpic QD ($\gamma = 0.32$) is shown as a function of increasing magnetic field. The splitting Δ_2 is extracted from the energies of the exciton, obtained by exact diagonalization of the exciton Hamiltonian, Eq. (3.32), for different numbers of confined electronic shells. Alternatively, one can think of different dots, each confining a different number of electronic shells.

In Fig. 3.4 (a) the splitting increases with the increasing magnetic field, and its dependence on the magnetic field changes with the number of confined single-particle shells. While the splitting changes little with the magnetic field for shallow quantum dots with s, p shells, with increasing number of shells it becomes a nonlinear function of the magnetic field. Since the exciton Zeeman energy is a linear function of the magnetic field, the measurement of the exciton fine structure splitting in a magnetic field should allow the extraction of the nonlinear part and hence of the magnetic-field dependence of the electron-hole exchange. According to the results presented here, this dependence should correlate with the number of confined electronic shells as measured in high-excitation emission spectroscopy.

The nonlinear dependence of the bright exciton splitting can be also traced to the exciton fine structure of isotropic QDs. For isotropic QDs in the absence of the magnetic field, there is no electron-hole exchange-induced splitting as shown previously [120, 121, 123, 134, 139], however, as the field increases, the non-zero

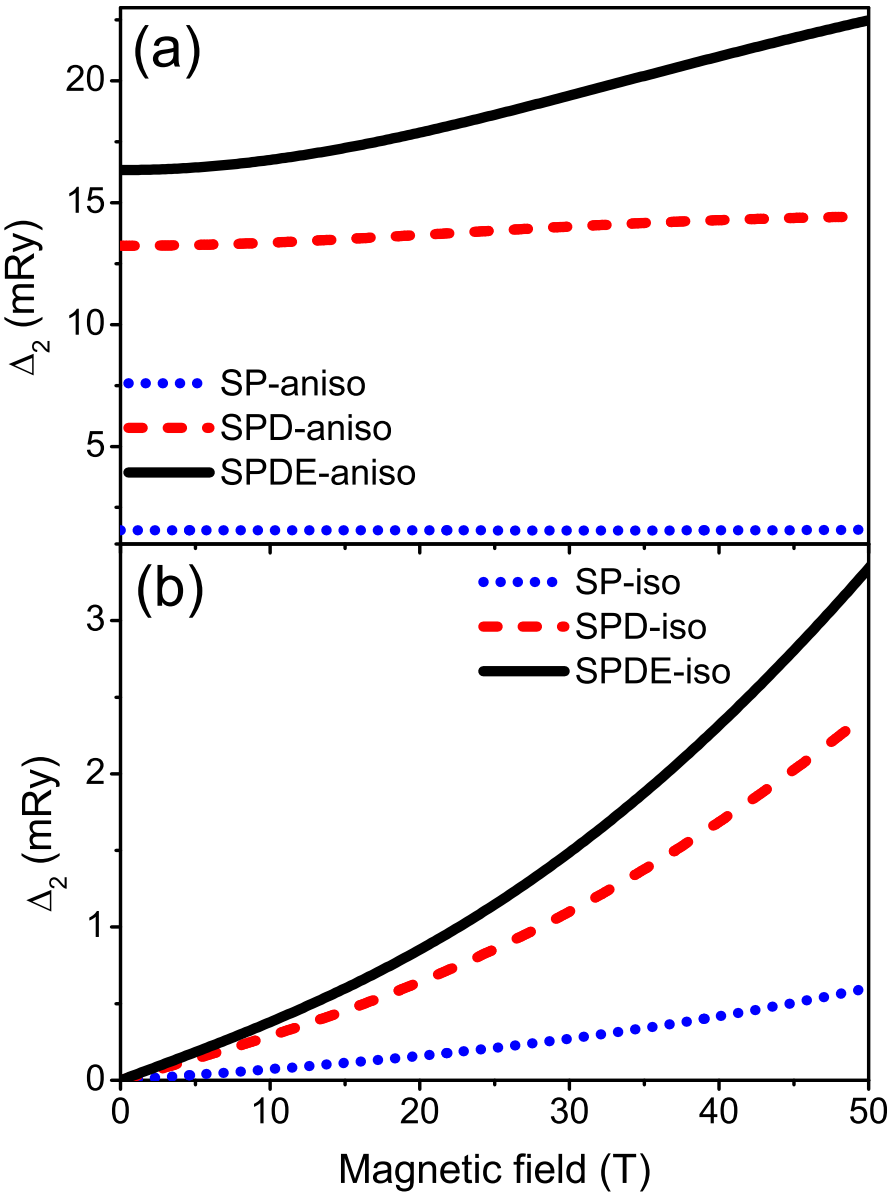

Figure 3.4: Magnetic-field evolution of the splitting of bright exciton states Δ_2, calculated for the (a) anisotropic QDs with anisotropy parameter $\gamma = 0.32$, and (b) isotropic QDs.

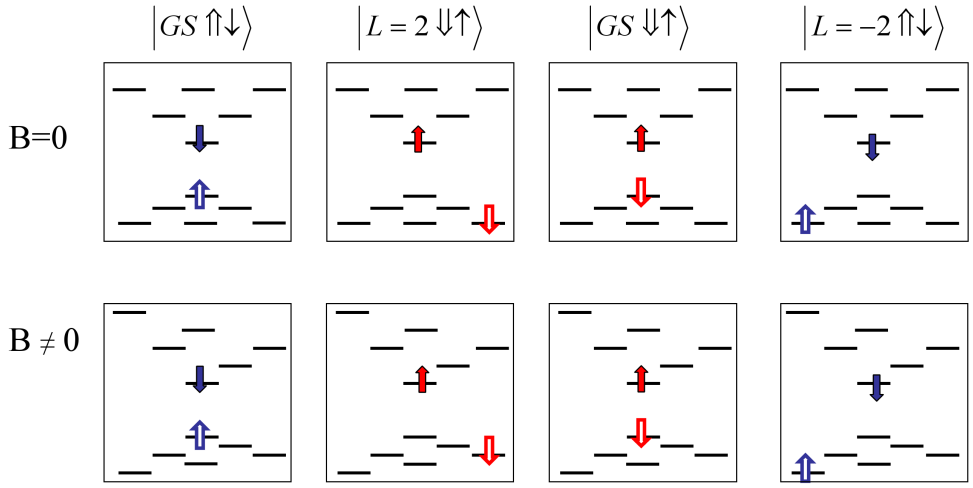

Figure 3.5: Important electron-hole configurations in the absence of the magnetic field (upper row), and at a finite magnetic field (lower row).

splitting of the bright states appears, Fig. 3.4 (b), due to symmetry breaking by the magnetic field. This can be understood on a simple example in which we consider only four electron-hole configurations, as shown in Fig. 3.5. Two of these configurations, 1 and 3, are the lowest-energy configurations with both carriers on the s-shell, and they differ only by the spin projection of the carriers. The other two configurations (2 and 4) are examples of configurations with angular momentum $L = \pm 2$, which are coupled by the electron-hole exchange interaction with the lowest-energy configurations (1-2) and (3-4). In the absence of the magnetic field, the configurations 2 and 4 from the upper row in Fig. 3.5 have the same kinetic energy. Since all diagonal and off-diagonal matrix elements are the same, the resulting eigenstates will have the same energy, leading to a lack of electron-hole exchange splitting. However, as the field increases, it shifts the single-particle levels and causes a splitting of the shells similar to the splitting induced by the anisotropy, Fig. 3.5. Since the energies of single-particle levels change in the magnetic field, the kinetic energies of the electron-hole configurations change as well so the second and third configurations in the lower row no longer have the same kinetic energy. For these reasons the non-zero electron-hole exchange splits the bright exciton levels of isotropic quantum dots in finite

magnetic fields.

Chapter 4

Magnetic moments in semiconductors

4.1 Mn ion

The properties of an electron-hole pair creating an excitonic complex in a non-magnetic QD, have been discussed in Chapters 2 and 3. Here we will consider what happens if magnetic ion (Mn^{2+}) is placed inside the QD.

4.1.1 Free Mn atom and its interaction with solid state

Manganese is a transition metal with the electronic configuration $[Ar]4s^2 3d^5$ with valence electrons corresponding to the $4s^2$ orbital. In the ground state the spins of the five $3d$ electrons are aligned to maximize their spin, following the Hund's Rule. This results in the uncompensated spin of 5/2 of the Mn ion and a total angular momentum $L = 0$, since according to the Pauli exclusion principle the electrons occupy the $3d$ shell in such a way that the angular momentum of each electron is different (ranging over five possible values from -2 to $+2$).

Diluted magnetic semiconductors (DMS, semimagnetic semidonductors) are semiconducting alloys whose lattice is made up in part of substitutional magnetic ions. The most extensively studied and understood materials of this type are the $A^{II}_{1-x}Mn_xB^{VI}$ alloys in which a fraction of the group II sublattice is replaced at random by Mn. These alloys form either a zinc-blende or a wurtzite lattice

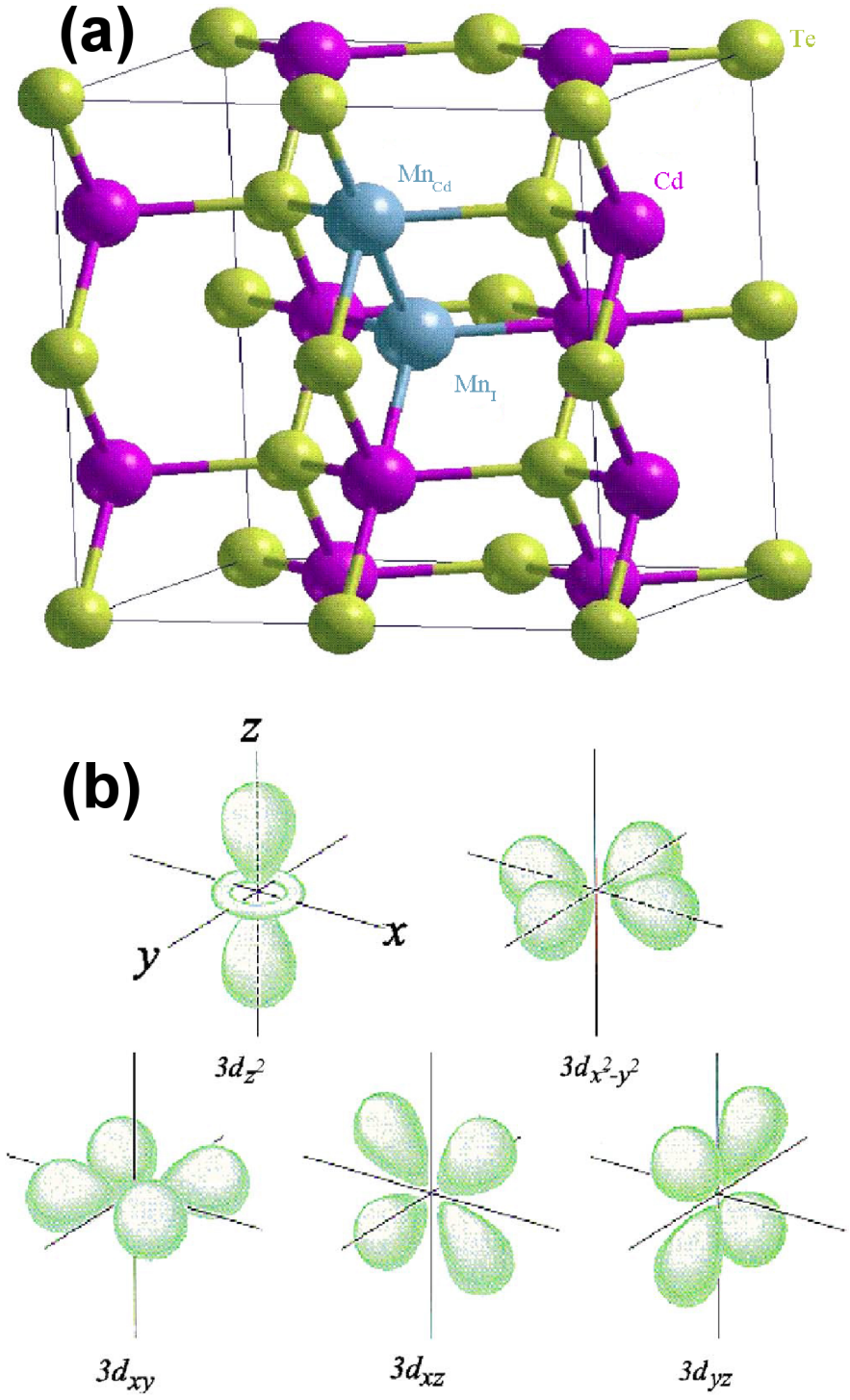

Figure 4.1: (a) CdTe zinc-blende structure with the substitutional (Mn_{Cd}) and interstitial (Mn_I) Mn impurity. (b) Two e_g and three t_{2g} $3d$ orbitals of the Mn. This figure is adapted from [17].

structure. These two types of crystal lattice are very closely related in spite of the difference in symmetry, since they are both formed with tetrahedral ($s-p^3$) bonding, which involves the two valence s electrons of the group II element, and the six valence p electrons of the group VI element. Although manganese differs from the group II elements by the fact that its $3d$ shell is only half-filled, it can contribute its $4s^2$ electrons to the $s-p^3$ bonding and can therefore substitutionally replace the group II elements in the $A^{II}B^{VI}$ tetrahedral structures. The ease with which Mn atoms substitute for the group II elements in the zinc-blende and wurzite structures results from the fact that the $3d$ orbitals of Mn are *exactly* half-filled. By Hund's Rule all five electrons have parallel spin in this orbital and it would require considerable energy (about $6-7$ eV) to add an electron with opposite spin to the $3d$ orbital of the Mn atom [153]. In this sense the $3d^5$ orbital acts as a complete shell and the Mn atom is thus more likely to resemble a group II element in its behaviour than are other transition-metal elements.

The substitutional Mn_{Cd} and less common interstitial Mn_I positions are illustrated in Fig. 4.1 (a). When the Mn atom is placed substitutionally in the cation site of a $A^{II}B^{VI}$ host lattice, it is acted upon by the crystal field. The dominant crystal field interaction arises from the four surrounding anions, and in this sense the effect of the crystal field is the same in zinc-blende and wurtzite systems. The degenerate $3d$ obitals split into two groups of orbitals: triply degenerate t_{2g} ($3d_{xy}$, $3d_{xz}$, $3d_{yz}$) and doubly degenerate e_g ($3d_{x^2-y^2}$, $3d_{z^2}$), which are shown in Fig. 4.1 (b). Since the orbitals t_{2g} hybridize strongly with the ligand s and p orbitals, they form a bonding t_b state in the valence band. The antibonding state t_a is pushed up into the band gap of the host. The e_g orbitals form a highly localized nonbonding e state due to the small $p-d$ hybridization (Fig. 4.2 (a)). If the impurity is interstitial, all orbitals can hybridize strongly with the ligand s and p orbitals, leading to a completely different level sequence (Fig. 4.2 (b)) All occupied d orbitals have the same spin orientation (as it was for a free Mn atom), and together comprise the $S=5/2$ local moment.

At the same time, since the Mn ion has two electrons on its valence orbital - the same number as the atoms from the II group - the Mn ion does not introduce an additional Coulomb potential or carriers if it is placed in a II-VI CdTe

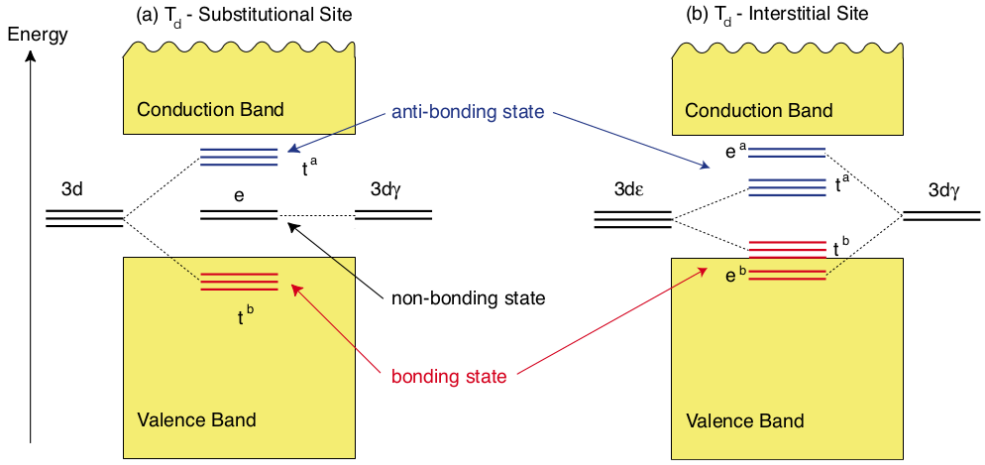

Figure 4.2: Schematic picture of the electronic structure of the $3d$ impurity in semiconductors at (a) the substitutional site, and (b) the interstitial site. This figure is adapted from [154].

semiconductor. This is a big advantage of this material since it allows to treat the Mn ion as a pure spin impurity with the angular momentum $M = \frac{5}{2}$.

4.1.2 Magnetic II-VI quantum dots

In recent years, incorpotation of the single Mn ions into the CdTe QDs grown on a ZnTe substrates [20, 22, 155, 156], as well as into InAs QDs grown on GaAs substrates [157, 158] has become possible.

Since in the absence of the magnetic field the life-time of the spin of the Mn ion has been measured to be about a few μs [159–161], there is growing interest to use the magnetic moment of Mn as a medium for information storage. For that reason, these materials have been extensively studied using optical methods [20, 22, 24, 162–165], as well as theoretically [151, 166, 167]. The initialization and readout of information with the Mn spin are possible optically [161, 164]. For example, optical pumping with σ_- photons tends to decrease the population of the spin state of the Mn $M_z = -5/2$ with simultaneous increase of the one with $M_z = +5/2$. This fact can be used to prepare the Mn ion in a state with $M_z = +5/2$. The initialization time of the Mn spin is of the order of a few

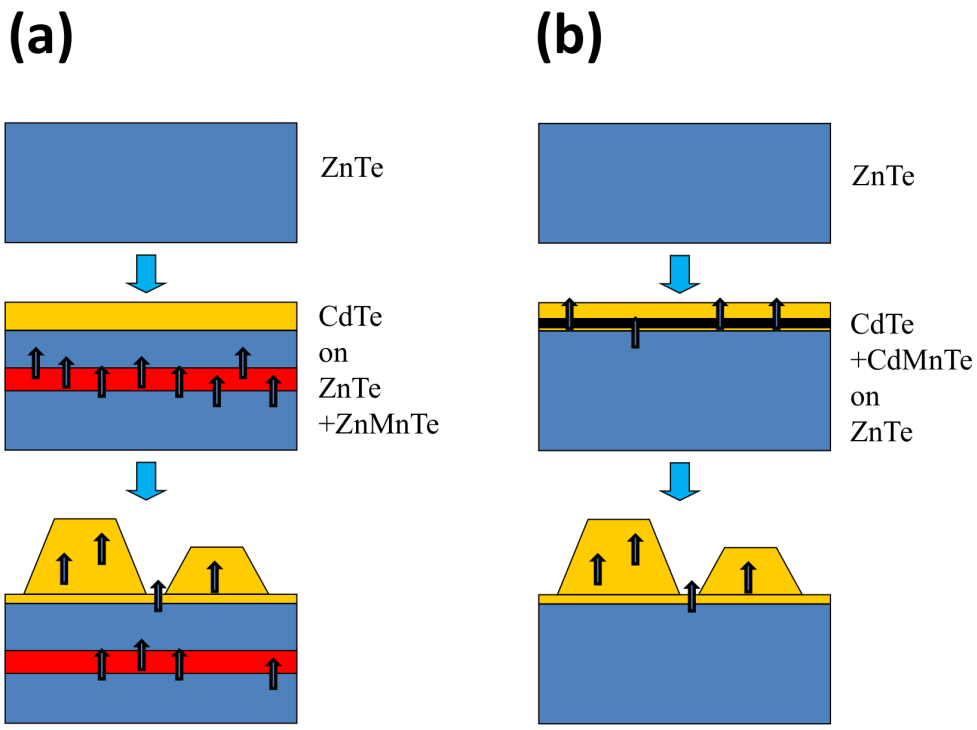

Figure 4.3: Growth of magnetic QDs using method based on (a) the diffusion of the Mn ions from the ZnMnTe layer, (b) direct injection of the Mn ions during the growth of the CdTe QDs.

nanoseconds [164].

The magnetic field evolution of the optical spectra has been studied as well, revealing a number of interesting structures [22, 156] which will be described below.

Most of the methods of introduction of the Mn ion into non-magnetic QDs use the interdiffusion of the Mn from the diluted magnetic layer [168–170], or from a remote Mn-rich layer [22, 171].

First, the method used by the Besombes et al. [22] will be described. In this method a few layers of a $Zn_{0.94}Mn_{0.06}Te$ material is deposited on the ZnTe substrate, which is followed by ten monolayers of a ZnTe spacer (Fig. 4.3 (a)). When the CdTe layer is then deposited, the growth of the QDs takes place due to the lattice mismatch between CdTe and ZnTe. During the growth of the

ZnTe spacer and the CdTe layer, the migration of the Mn ions takes place which introduces a sparse distribution of Mn ions in the QD layer. The layer of the CdTe QD is then capped with a ZnTe barrier. The composition of the $Zn_{0.94}Mn_{0.06}Te$ layer has been adjusted to introduce the same density of Mn atoms as the density of the QDs ($\approx 5 \times 10^{-9}$ cm$^{-}2$). This assures a high probability of finding many QDs with a single magnetic impurity.

The other method of growing the semimagnetic QDs is by introduction the Mn ions directly into the QDs themselves, with the intentional position of the Mn in the center [172] (Fig. 4.3 (b)). The samples are grown in a molecular beam epitaxy apparatus as well. On a GaAs substrate, a 4 μm thick CdTe buffer is first deposited, followed by 1 μm thick $Zn_{0.6}Cd_{0.4}Te$ barrier layer. The QD layer is formed from five monolayers of a large lattice constant material of which the two lower and the two uppermost monolayers are made of pure CdTe. The Mn ions are introduced during the growth of the central CdTe monolayer. The density of quantum dots in the samples grown this way is about $5 \cdot 10^{-9}$cm^{-2}. The Mn concentration during the growth of the middle CdTe layer is adjusted to obtain a significant number of QDs containing exactly one Mn ion. The QDs are finally capped with the 100 nm thick $Zn_{0.6}Cd_{0.4}Te$ barrier layer.

4.1.3 Model of e-h-Mn interaction Hamiltonian and its properties

The interaction of the N_e electrons and N_h holes with the Mn impurity is modeled by the short-range $sp-d$ exchange interaction, and its Hamiltonian in the effective mass approximation has the form:

$$\hat{H}_{e-Mn} + \hat{H}_{h-Mn} = -J^e_{c2D} \sum_{i=1}^{N_e} \hat{M} \cdot \hat{S}_i \delta\left(\mathbf{r}^e_i - \mathbf{R}\right) + J^h_{c2D} \sum_{i=1}^{N_h} \hat{M} \cdot \hat{j}_i \delta\left(\mathbf{r}^h_i - \mathbf{R}\right), \quad (4.1)$$

where $\hat{M}$ is a spin of the Mn ion, $\hat{S}_i$ is the spin of the i-th electron, and $\hat{j}_i$ is the spin of the ith hole, while $\mathbf{r}^{e(h)}$ is the electron (hole) position respectively, and $\mathbf{R}$ is the position of Mn in the QD. The interaction with Mn is ferromagnetic for electrons, while for holes it is anti-ferromagnetic, with coupling strength $J^{e(h)}_{c2D}$, respectively. Constants $J^{e(h)}_{c2D}$ for a quasi two-dimensional system are computed as

$J_{c2D}^{e(h)} = 2J_c^{e(h)}/d$, where constants $J_c^{e(h)}$ are bulk carrier-Mn exchange constants, and d is the thickness of the quantum dot.

For computational purposes it is convenient to transform the Hamiltonian, Eq. 4.1, to a second-quantization form [152] by the introduction of the quantum field operators $\hat{\Psi}$ expanded as:

$$\hat{\Psi} = \sum_{i,\sigma} \left(F_i(\mathbf{r}_e) \otimes \chi_\sigma \right) c_{i\sigma}, \tag{4.2}$$

where $F_i(\mathbf{r}_e)$ is a wave function of the electron single-particle state described by the composite index i, χ_σ is the spin part of the wavefunction, and $c_{i\sigma}$ is the anihilation operator, anihilating an electron with a spin σ from the single-particle state i. Here only the transformation for the e-Mn part of this Hamiltonian is shown, and the h-Mn part is written analogously.

$$\begin{aligned} \langle \hat{\Psi} | H_{e-Mn} | \hat{\Psi} \rangle &= -J_{c2D}^e \sum_{ij\sigma\sigma'} \int d\mathbf{r}_e F_i^*(\mathbf{r}_e) \delta(\mathbf{r}_e - \mathbf{R}) F_j(\mathbf{r}_e) \\ &\times \langle \chi_{\sigma'} | \hat{S} | \chi_\sigma \rangle \hat{M} c_{i\sigma}^+ c_{j\sigma}, \end{aligned} \tag{4.3}$$

After integrating out the position $\mathbf{r}_e$ and spin degrees of freedom, one obtains:

$$H_{e-Mn} = \sum_{ij\sigma\sigma'} J_{ij}^e(\mathbf{R}) \hat{S}_{\sigma\sigma'} \cdot \hat{M} c_{i\sigma}^+ c_{j\sigma'}, \tag{4.4}$$

where $\hat{S}_{\sigma\sigma'}$ are Pauli spin matrices, and

$$J_{ij}^e(\mathbf{R}) = J_{c2D}^e F_i^*(\mathbf{R}) F_j(\mathbf{R}) \tag{4.5}$$

are exchange matrix elements between the electron and impurity spin. The exchange matrix elements $J_{ij}^e(\mathbf{R})$ are given by the product of the wave functions of the states i and j at position $\mathbf{R}$ of the Mn ion. In what follows, the Mn position in a QD is fixed at $R = (0, 0)$ (the center of the QD). Detailed results of calculations of e-Mn interaction as a function of the position of the Mn were given by Qu et

al. [152]. An analogous expression can be derived for holes:

$$H_{h-Mn} = -\sum_{ij\tau\tau'} J^h_{ij}(\mathbf{R})\hat{j}_{\tau\tau'} \cdot \hat{M} h^+_{i\tau} h_{j\tau'}, \tag{4.6}$$

with $J^h_{ij}(\mathbf{R}) = J^h_{c2D} H^*_i(\mathbf{R}) H_j(\mathbf{R})$ (Refs. [150, 152]), where $H_j(\mathbf{R})$ is a single-particle wave function of a hole at the position $\mathbf{R}$. Explicit form of these coupling constants will be given in the Section 4.1.4.
The exchange Hamiltonian written in terms of the Mn spin rising and lowering operators M^+, M^- allows to analyze the interaction more easily:

$$H_{e-Mn} = -\frac{1}{2}\sum_{ij} J^e_{ij}(\mathbf{R}) \left(\left(c^+_{i\uparrow} c_{j\uparrow} - c^+_{i\downarrow} c_{j\downarrow} \right) M_z + c^+_{i\downarrow} c_{j\uparrow} M^+ + c^+_{i\uparrow} c_{j\downarrow} M^- \right) \tag{4.7}$$

where $\frac{1}{2}$ is the absolute value of the electron spin projection. This Hamiltonian consists of two terms - the first one acts as the local Zeeman energy, and when $i = j$, it measures the difference of the number of electrons with a spin of $+1/2$ and of $-1/2$. The second term accounts for the simultaneous flip of the electron and Manganese spins (total spin projection $S_z + M_z$ is conserved). At the same time the Mn acts as a "regular" dopant, scattering the electron between different i and j orbitals.

As was mentioned previously in Chapter 2, the light- and heavy- hole bands are split in the QDs, by around 30 meV, due to the strain and confinement [173]. Because of this splitting, in the first approximation, the Mn-hole spin flip can be neglected. The Hamiltonian describing the hole-Mn interaction has the Ising form:

$$H_{h-Mn} = \frac{3}{2}\sum_{ij} J^h_{ij}(\mathbf{R}) \left(h^+_{i\Uparrow} h_{j\Uparrow} - h^+_{i\Downarrow} h_{j\Downarrow} \right) M_z. \tag{4.8}$$

where $\frac{3}{2}$ is the heavy-hole angular momentum - *hole spin*. The spin projection of the hole j_z is conserved by this part of the Hamiltonian. Since the hole-Mn coupling constant J^h_{c2D} is around 4 times greater than the electron-Mn coupling constant J^e_{c2D}, the hole in the QD acts on the Mn ion as an *internal magnetic field*, leading to Zeeman-like splitting of Mn spin energy levels.

From the form of the e-Mn Hamiltonian (4.7) one can see that the electron-Mn interaction couples dark ($S_z + j_z = \pm 2$) and bright ($S_z + j_z = \pm 1$) heavy-hole exciton states [22]. This coupling can be observed in photoluminescence spectra [165]. Note that the electron-Mn as well as hole-Mn exchange interaction can also mix the configurations with a different total angular momentum by scattering electrons from state i to j. Thus the total angular momentum L_{tot} is no longer a good quantum number. Thus, the effect of Mn is to introduce a spin related disorder to the electron-hole complex.

The full e-h-Mn Hamiltonian in a magnetic field has now the form:

$$\begin{aligned}
\hat{H}_{ehMn} &= \sum_{i\sigma} \varepsilon^e_{i\sigma} c^+_{i\sigma} c_{i\sigma} + \sum_{i\tau} \varepsilon^h_{i\tau} h^+_{i\tau} h_{i\tau} \\
&+ \frac{1}{2} \sum_{ijkl} \sum_{\sigma,\sigma'} V_{ee}(i\sigma, j\sigma' | k\sigma', l\sigma) c^+_{i\sigma} c^+_{j\sigma'} c_{k\sigma'} c_{l\sigma} \\
&+ \frac{1}{2} \sum_{ijkl} \sum_{\tau\tau'} V_{hh}(i\tau, j\tau' | k\tau', l\tau) h^+_{i\tau} h^+_{j\tau'} h_{k\tau'} h_{l\tau} \\
&- \sum_{ijkl} \sum_{\sigma\tau} V_{eh}(i\sigma, j\tau | k\tau, l\sigma) c^+_{i\sigma} h^+_{j\tau} h_{k\tau} c_{l\sigma} \\
&+ \sum_{ij\sigma} t^e_{ij} c^+_{i\sigma} c_{i\sigma} + \sum_{ij\tau} t^h_{ij} c^+_{h\tau} h_{i\tau} + \hat{H}_{EHX} \\
&+ g_{Mn} \mu_B B M_z + \sum_{ij} \frac{3 J^h_{ij}(\mathbf{R})}{2} \left(h^+_{i\Uparrow} h_{j\Uparrow} - h^+_{i\Downarrow} h_{j\Downarrow} \right) M_z \\
&- \sum_{ij} \frac{J^e_{ij}(\mathbf{R})}{2} \left(\left(c^+_{i\uparrow} c_{j\uparrow} - c^+_{i\downarrow} c_{j\downarrow} \right) M_z + c^+_{i\downarrow} c_{j\uparrow} M^+ + c^+_{i\uparrow} c_{j\downarrow} M^- \right),
\end{aligned} \tag{4.9}$$

where the first five terms of this Hamiltonian are the same as in the electron-hole Hamiltonian H_{eh} (Eq. 2.26), which was discussed in detail in Chapter 2. These terms are: single-particle energies of the electron and hole with their Zeeman energies, and all Coulomb interactions between electrons and holes. The following terms correspond to the anisotropy corrections of the confining potential (Chapter 2) of the electron and hole, and it is followed by the electron-hole exchange term (Chapter 3). Next is the Zeeman energy term of the magnetic ion with the g_{Mn} being the Lande factor of the Mn ion, and μ_B - the Bohr magneton. The last two terms describe the electron-Mn and hole-Mn interaction.

4.1.4 Electron-Mn exchange constants

The electron-Mn exchange constants are defined as:

$$J^e_{ij}(\mathbf{R}) = J^e_{c2D} F^*_i(\mathbf{R}) F_j(\mathbf{R}) = J^{e2D}_c \int d\mathbf{r}_e F^*_i(\mathbf{r}_e)\delta(\mathbf{r}_e - \mathbf{R})F_j(\mathbf{r}_e), \tag{4.10}$$

where $F_{j(i)}(\mathbf{r}_e)$ are the electron single-particle envelope functions corresponding to the HO state with the complex indices $j = (n^{je}_+, n^{je}_-)$ and $i = (n^{ie}_+, n^{ie}_-)$. This equation can be written in the form that explicitly shows that $J^e_{ij}(\mathbf{R})$ is a matrix element of the delta function between the two electron envelope wave functions:

$$J^e_{ij}(\mathbf{R}) = J^e_{c2D}\langle i|\delta(\mathbf{r}_e - \mathbf{R})|j\rangle. \tag{4.11}$$

This element can be calculated in a similar manner as the integral in the short-range electron-hole exchange matrix element, given by equation Eq. 3.23. The delta function $\delta(\mathbf{r}_e - \mathbf{R})$ can be expanded again as a sum of the plane waves:

$$\delta(\mathbf{r}_e - \mathbf{R}) = \frac{1}{4\pi^2}\int d\mathbf{q} \exp\left(i\mathbf{q}\cdot(\mathbf{r}_e - \mathbf{R})\right), \tag{4.12}$$

and the matrix element $J^h_{ij}(\mathbf{R})$ takes the form:

$$J^e_{ij}(\mathbf{R}) = J^e_{c2D}\frac{1}{4\pi^2}\int d\mathbf{q}\langle i|\exp\left(i\mathbf{q}(\mathbf{r}_e - \mathbf{R})\right)|j\rangle = J^e_{c2D}\frac{1}{4\pi^2}\int d\mathbf{q} M_1. \tag{4.13}$$

The integral M_1 has been defined while calculating the analytical form of the direct Coulomb interaction in the HO basis $V_{ee}(i\sigma, j\sigma'|k\sigma', l\sigma)$, by the equation Eq. B16. After changing variables to the cylindrical coordinates one obtains:

$$J^e_{ij}(\mathbf{R}) = J^h_{c2D}\frac{1}{4\pi^2}\int_0^\infty q dq \int_0^{2\pi} d\phi_q \cdot \exp\left(-i\mathbf{q}\cdot\mathbf{R}\right) M_1. \tag{4.14}$$

Since in this work the main focus will be on the Mn in the center of the QD,

$\mathbf{R} = (0,0)$, this expression can be simplified to:

$$\begin{aligned} J^e_{ij}(0) &= J^e_{c2D}\frac{1}{4\pi^2}\int_0^\infty qdq\int_0^{2\pi} d\phi_q M_1 \\ &= J^e_{c2D}\frac{1}{4\pi^2}\frac{1}{\sqrt{n^{ie}_+!n^{ie}_-!n^{je}_+!n^{je}_-!}}\sum_{p_1=0}^{min(n^{ie}_+,n^{je}_+)}\sum_{p_2=0}^{min(n^{ie}_-,n^{je}_-)} p_1!p_2! \\ &\times \binom{n^{ie}_+}{p_1}\binom{n^{je}_+}{p_1}\binom{n^{ie}_-}{p_2}\binom{n^{je}_-}{p_2} I_{p_1p_2}, \end{aligned} \tag{4.15}$$

where the integral $I_{p_1p_2}$ is given by:

$$I_{p_1p_2} = \int_0^\infty qdq\int_0^{2\pi} d\phi_q \exp\left(-|Q|^2\right)\left(iQ^*\right)^{n^{ie}_+-p_1}\left(iQ\right)^{n^{ie}_--p_2}\left(iQ\right)^{n^{je}_+-p_1}\left(iQ^*\right)^{n^{je}_--p_2}. \tag{4.16}$$

Following the same steps of calculations as in the case of the direct and short-range exchange Coulomb interactions, one finds:

- the angular integral has non-zero value only if the angular momentum of the electron on the right is equal to the angular momentum on the left $L_R = L_L$,
- if one defines the variable $p = n^{ie}_+ + n^{je}_- - p_1 - p_2$, then the integral takes the form:

$$I_{p_1p_2} = (-1)^p\frac{4\pi}{l_h^{e\,2}}\int_0^\infty dQ \exp -|Q|^2Q^{2p+1} = (-1)^p\frac{2\pi}{l_h^{e\,2}}\Gamma\left(p+1\right). \tag{4.17}$$

The final expression for the electron-Mn exchange constants takes the form:

$$\begin{aligned} J^e_{ij}(\mathbf{0}) &= \frac{1}{2\pi l_h^{e\,2}}\frac{1}{\sqrt{n^{ie}_+!n^{ie}_-!n^{je}_+!n^{je}_-!}}\sum_{p_1=0}^{min(n^{ie}_+,n^{je}_+)}\sum_{p_2=0}^{min(n^{ie}_-,n^{je}_-)} p_1!p_2!\binom{n^{ie}_+}{p_1}\binom{n^{je}_+}{p_1}\binom{n^{ie}_-}{p_2}\binom{n^{je}_-}{p_2} \\ &\times (-1)^p\Gamma\left(p+1\right), \end{aligned} \tag{4.18}$$

with $p = n^{ie}_+ + n^{je}_- - p_1 - p_2$. For the Mn in the center of the QD, its scattering abilities are supressed. Only the single-particle orbitals with the angular momentum equal to zero are interacting with Mn. The other interesting property of

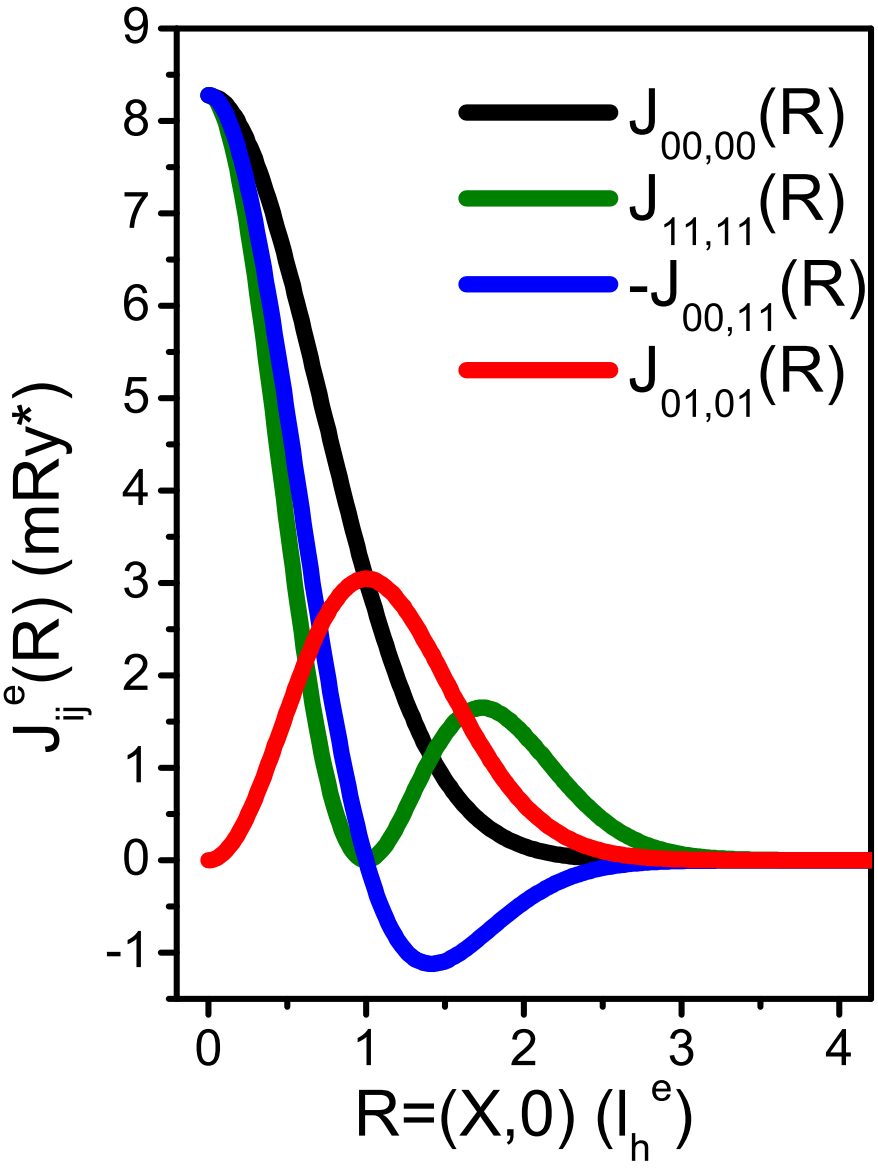

Figure 4.4: The dependence of the electron-Mn coupling constants on the position of the Mn in the QD.

such a system is that the coupling constant of the $L = 0$ orbitals have all the same absolute value, while the sign depends on the number of the shell to which the orbital belongs, for example:

$$\begin{aligned} J^e_{00,00}(0) &= \frac{J_c^{e2D}}{2\pi l_h^{e\,2}} \\ J^e_{00,11}(0) &= -\frac{J_c^{e2D}}{2\pi l_h^{e\,2}} = -J^e_{00,00}(0) \\ J^e_{11,11}(0) &= \frac{J_c^{e2D}}{2\pi l_h^{e\,2}} = J^e_{00,00}(0). \end{aligned} \tag{4.19}$$

The dependence of the coupling constants as a function of the position of the Mn ion in the QD is presented in Fig. 4.4.

The expressions describing the electron-Mn coupling constants in the situations when Mn is away from the center can be either obtained from the general equation, Eq. 4.14, or Eq. 4.10 using the analytical expressions for the Fock-Darwin wave functions, Eq. 2.3. In the second method, one needs to remember about the change of phase with respect to the z, z^* representation of the HO wavefunctions. In the calculations for Fig. 4.4 the latter method has been used. The parameters used to calculate the $J^e_{ij}(\mathbf{R})$ coupling constants are: single-particle energies $\omega_e + \omega_h = 30$ meV and $\omega_e/\omega_h = 4$, the height of the QD $d = 3$ nm, while the material constant $J^e_{c2D} = 15$ meV $\cdot$ nm^3. The effective Rydberg and the Bohr radius, are the same as used in Chapter 2 for CdTe. The coupling constants that have a non-zero value when Mn is in the center of the QD decrease with the position of the ion $\mathbf{R}$. The coupling constants of levels with angular momentum $L \neq 0$ initially increase with the $\mathbf{R}$. However, when the Mn is far away from the center of the QD, all of the coupling constants quickly decrease to zero.

4.2 Magnetic moment realised in the Quadruple Quantum Dot

Another method to introduce a magnetic moment into the semiconductor structure is through the design of artificial lateral quantum dot molecules with con-

trolled number of electrons.

The theory of electronic properties of a quadruple quantum dot molecule (QQD) [174–178] [179, 180] has been developed and presented in the Ref. [181]. The geometry of the molecule has been varied by changing the physical parameters such as inter-dot tunneling, energy bias, intra- and inter-dot Coulomb interactions, as well as a number of electrons N_e confined in the QQD.

Here it is shown that for a ring-like half-filled QQD molecule charged with either an electron or a hole, the chirality of the three(five)-electron complex leads to the appearance of a topological phase and an effective gauge field. As a result, the ground state can be tuned between a total spin of $S = 1/2$ and $S = 3/2$ by changing the strength of onsite interactions. This allows to introduce a *tunable* magnetic moment into semiconductors.

The QQD can be realized in a lateral gated AlGaAs/GaAs heterostructure [68, 179, 180]. For example, a metallic gate with four openings can be deposited on the surface of the AlGaAs/GaAs heterostructure, as shown in Fig. 4.2. Electrostatic fields due to the openings in the gate create local potential minima in the plane of the two-dimensional electron gas (2DEG), which are capable of confining electrons. The lateral confinement results in a quantized energy spectrum in each dot i. The voltage on the main metallic gate and additional gates (not shown here) can be tuned to control the number of electrons confined in the QQD as well as the geometry of the QQD without significantly altering the confinement energies E_i.

Assuming that the interactions between dots are short-range, one can go from a ring geometry to a linear quadruple quantum dot geometry (LQQD) by inserting a gate (G1 in Fig. 4.2) between dots 1 and 4. Applying a high negative voltage increases the tunneling barrier and prevents electrons from tunneling from dot 1 to dot 4. A triangular configuration, studied previously in Ref. [176] i.e., three dots arranged on the corners of an equilateral triangle that are equidistant to a central dot, can also be obtained by tuning the tunneling between the dots.

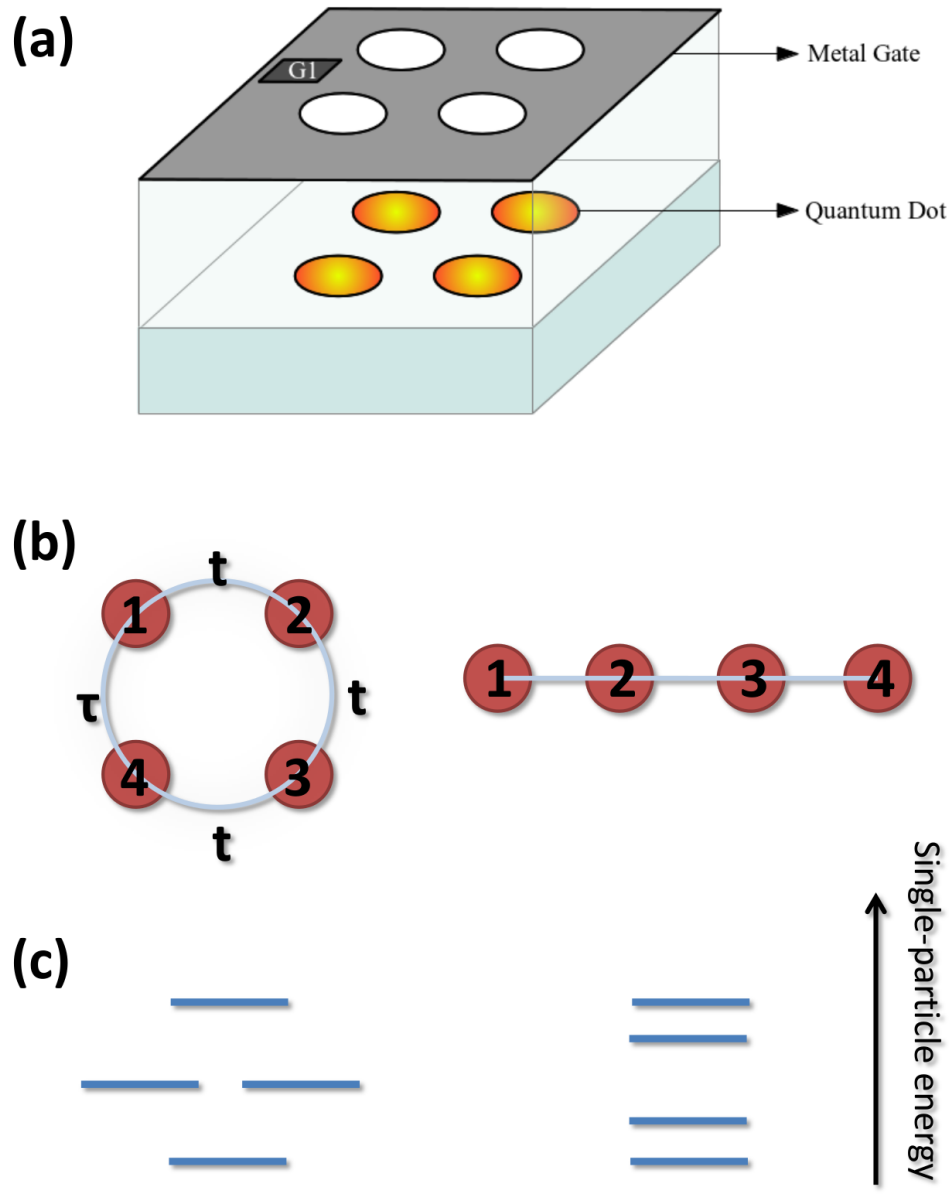

Figure 4.5: (a) A schematic cross-sectional view of the four-dot lateral gated device. The dots can be arranged in ring or linear geometry (b). The solid lines represent nearest-neighbor interactions. (c) Single-particle energy spectra of ring and linear geometries, respectively.

4.2.1 Hubbard model

Electronic properties of the QQD can be described in the Hubbard model with one spin-degenerate orbital per dot.[68, 71] In the Hubbard model, the Hamiltonian is characterized by the energy levels of the ith quantum dot E_i, the on-site Hubbard repulsion U_i, the tunneling matrix elements $t_{ij} \geq 0$, and direct Coulomb matrix elements V_{ij} between dots i and j. The Hamiltonian in site representation is written explicitly as:

$$\hat{H} = \sum_{\sigma,i=1}^{4} E_i c_{i\sigma}^{+} c_{i\sigma} - \sum_{\sigma,\langle i,j\rangle}^{4} t_{ij} c_{i\sigma}^{+} c_{j\sigma} + \sum_{i=1}^{4} U_i n_{i\downarrow} n_{i\uparrow} + \frac{1}{2} \sum_{\langle i,j\rangle} V_{ij} \varrho_i \varrho_j, \tag{4.20}$$

where $c_{i\sigma}^{+}(c_{i\sigma})$ are operators creating (annihilating) an electron with spin σ on the ith orbital $|i\rangle$ of the dot. Here, $n_{i\sigma} = c_{i\sigma}^{+} c_{i\sigma}$ and $\varrho_i = n_{i\downarrow} + n_{i\uparrow}$ are the spin and charge density on the ith dot, respectively. The summation goes over the nearest-neighbor (NN) dots $\langle i, j\rangle$ and retains the NN interactions V_{ij} and the NN tunneling matrix elements t_{ij}. With a single energy level per dot, up to $N_e = 8$ electrons can occupy the quadruple quantum dot molecule.

In Ref. [181] the electronic structure of the QQD with $N_e = 1$ to $N_e = 8$ electrons is calculated using the exact diagonalization approach. In this work, however, the main focus will be on the case of three and five electrons in the QQD. For a given number of electrons N_e one can form all possible configurations $|\alpha\rangle = \prod_{i=1}^{N_e} c_{i\sigma}^{+}|0\rangle$, where $|0\rangle$ denotes the vacuum. Since the Hamiltonian, Eq. 4.20, commutes with the total S and S_z, the matricies of this Hamiltonian can be constructed and diagonalized (numerically or analytically) separately in each of the S, S_z subspaces, to obtain the corresponding eigenenergies and eigenvectors.

When all dots are on resonance, the energy of the single state in each QD is the same, i.e., $E_1 = E_2 = E_3 = E_4 = E_0 = 0$. This resonant case resembles the situation in the Mn atom, where all five $3d$ states are degenerate. Additionally, if the tunneling matrix elements are equal, $t_{12} = t_{23} = t_{34} = t$ and $t_{14} = \tau$ (ring geometry), one-electron energy spectrum in the QQD, is symmetric around a doubly degenerate energy level $E_0 = 0$, with the ground and highest excited level energies of $\pm 2t$ as shown in Fig. 4.2 (c, right). As in the case of the triple dot [70], the degeneracy of two levels is an outcome of the geometry. In the limit of

a linear quadruple dot molecule where $\tau = 0$, the degeneracy is lifted and the energy spectrum of the molecule consists of four energy levels, $\{(1\pm\sqrt{5})t/2, (-1\pm\sqrt{5})t/2\}$, as shown in Fig. 4.2 (c, left).

4.2.2 Three electrons in a QQD

The importance of topology can be further demonstrated by the example of the three-electron system. The three-electron states can be classified according to their total spin, $S = 3/2$ or $S = 1/2$.

In the strong coupling limit, $U \gg V > t$, one can demonstrate [181] Nagaoka's ferromagnetism [182] for a QQD in a ring geometry. If the dots are on resonance, the $S = 1/2$ ground state can be perturbatively calculated from the real-space Hamiltonian as:

$$E^S_{1/2} \approx E^S_{3/2} + t(2-\sqrt{3}) - \frac{2t^2}{U+\sqrt{3}t} - \frac{3t^2}{U-2V+\sqrt{3}t}. \tag{4.21}$$

Compared to the $S = 3/2$ ground state energy $E^S_{3/2} = 2V + 3E - 2t$, the energy of this level increases by $(2-\sqrt{3})t$, but decreases with the superexchange contribution (the last two terms in Eq. 4.21). As a result, by manipulating the tunneling and on-site Hubbard repulsion, one can tune the ground state of the three-electron system between the total spin $S = 3/2$ and $S = 1/2$ states. If $\frac{2t}{U+\sqrt{3}t} + \frac{3t}{U-2V+\sqrt{3}t} > (2-\sqrt{3})$, the ground state corresponds to $S = 1/2$. By increasing the onsite repulsion U or decreasing the tunneling matrix element t, the transition between $S = 1/2$ and $S = 3/2$ can be induced as seen in the phase diagram in Fig. 4.6 (b). So as in the case of the Mn ion, the interaction between the electrons, leads to the polarization of the spin of the electrons. In the case of the QQD one can turn *on* and *off* the magnetic moment by changing the voltages applied to the gates, which might be usefull in application.

On the other hand, one finds that the ground state of the linear, topologically different QQD is always spin depolarized. Therefore it is not possible to tune the ground state of the three-electron linear QQD molecule between the $S = 1/2$ and $S = 3/2$ states by varying the strength of the Coulomb interaction or the tunneling matrix elements.

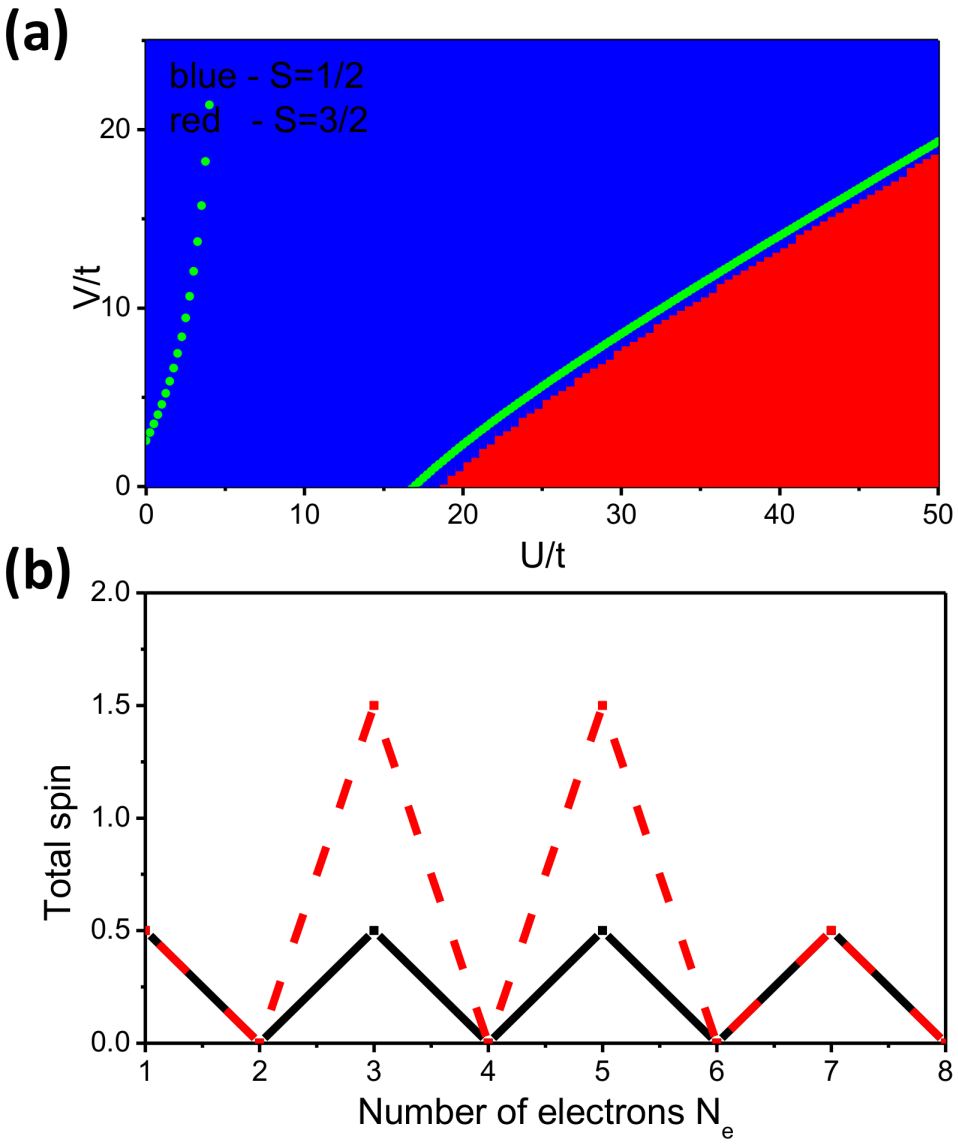

Figure 4.6: (a) Ground state phase diagram. Red corresponds to parameter space when the state with the $S = 3/2$ is the GS, while blue when the GS has $S = 1/2$. (b) Total spin of the GS as a function of the number of electrons in the system.

In Ref. [181] it was shown that since the single-particle spectrum is fully symmetric,Fig. 4.2 (c), the energy spectrum of $N_h = N$ holes is always the same as $N_e = N$ electrons, however all energy levels are shifted up in energy because of the additional terms in the diagonal elements of the Hamiltonian (the selfenergy of the holes). For that reason, the similar spin phase transition is present for the $N_e = 5$ electrons in the QQD.

The total spin of the ground state as a function of the total number of electrons in the system is shown in Fig. 4.6 (c). The total spin of the three-electron/hole ground states can be tuned between $S = 3/2$ and $S = 1/2$ by varying the onsite repulsion and tunneling matrix elements without the need of a magnetic field, as discussed above. However, it was shown in Ref. [181] that in the $S = 3/2$ regime for $N_e = 3$ and $N_e = 5$ electrons one can observe spin blockade when one tries to add an electron to a QQD. The ground state of the linear QQD also follows the black line given in Fig. 4.6 (c) as it becomes total spin-0 and spin-1/2 ground state for even and odd numbers of electrons, respectively.

Chapter 5

Computational Procedure

In this chapter the computational details of the calculations of the electronic properties of the interacting electron-hole-Mn complexes will be described. The most straight-forward, however computationaly expensive approach, is to construct the Hamiltonian of the interacting electron-hole-Mn complex, Eq. 4.10, in the basis built out of the configurations of non-interacting electrons and holes, multiplied by all states of the Mn ion $|M_z\rangle$, $M_z = \pm 5/2, \pm 3/2, \pm 1/2$. The basis states of $N_{h\Downarrow} + N_{h\Uparrow}$ holes and $N_{e\downarrow} + N_{e\uparrow}$ electrons would have the form:

$$|\Psi\rangle = |h^+_{1\Downarrow} \dots h^+_{N_{h\Downarrow}\Downarrow} h^+_{1\Uparrow} \dots h^+_{N_{h\Uparrow}\Uparrow} c^+_{1\downarrow} \dots c^+_{N_{e\downarrow}\downarrow} c^+_{1\uparrow} \dots c^+_{N_{e\uparrow}\uparrow} |0\rangle \otimes |M_z\rangle, \tag{5.1}$$

where the particles are grouped according to their spin. The Hamiltonian matrix, Eq. 4.10, built in this basis, upon numerical diagonalization, gives the eigenenergies and eigenstates of the interacting e-h-Mn complex in the form of a linear combination of the configurations defined by Eq. 5.1. However, there are two disadvantages of such an approach. First, the form of the obtained eigenstates of the e-h-Mn complex is difficult to relate to the excitonic states in the absence of the Mn. The analysis of the Mn-induced coupling between the excitonic states is difficult in this case. The second problem has a computational origin. Due to the electron-hole exchange, the presence of the anisotropy in the confining potential of the QD, as well as the scattering by Mn, none of the quantum numbers such as the angular momentum of a electron-hole pair L, z-projection of the total spin of holes j_z, electron S_z, or Mn M_z, are conserved. That means that

the size of a basis constructed in such a way cannot be reduced by dividing it according to any of the above quantum numbers. In this work, the effect of the strong magnetic field on the optical properties of the QDs will be considered. Each magnetic field requires separate computation, including diagonalization of the Hamiltonian, Eq. 4.10. Therefore, having very big sizes of the Hamiltonian matricies is not desired.

To solve the problem of big matrix sizes one can use a different approach. It will be described here in the example of the exciton-Manganese complex. The computation of the interacting e-h-Mn complex, Eq. 4.10, is broken into two separate steps.

5.1 Exciton

One can start with the Hamiltonian $\hat{H}_X$ which describes the electron-hole pair in the isotropic parabolic quantum dot with single-particle HO states i, energies $\varepsilon_{i,\tau}^{e(h)}$ and only direct Coulomb interaction matrix elements [114, 116] $V_{eh}(i\sigma, j\tau|k\tau, l\sigma)$. This Hamiltonian is given by Eq. 2.34. In this step the single particle energies $\varepsilon_{i,\tau}^{e(h)}$ do not include Zeeman energies of the electron or the hole. Since the Hamiltonian $\hat{H}_X$ commutes with both the exciton angular momentum $L = n_+^e - n_-^e + n_-^h - n_+^h$ and spin operators, one can construct the electron-hole configurations separately for each total angular momentum L and spin configuration $(\tau\sigma)$ of hole and electron. These configurations are in the form:

$$|L; ij\rangle|\tau\sigma\rangle = h_{i\tau}^{+} c_{j\sigma}^{+}|0\rangle, \tag{5.2}$$

where the composite indices i and j correspond to the HO states with the numbers: $i = (n_+^{ih}, n_-^{ih})$ and $j = (n_+^{je}, n_-^{je})$. However, the single-particle energies of the electron and hole $\varepsilon_{i,\tau}^{e(h)}$, as well as the direct Coulomb interaction between the electron and the hole do not depend on the spins of the carriers. In this case the calculations can be done in one of the four spin subspaces, and the spin indices can be dropped. The new exciton basis will have the form:

$$|L; ij\rangle = h_i^{+} c_j^{+}|0\rangle. \tag{5.3}$$

In each of the L subspaces and for each value of the magnetic field B, the $\hat{H}_X$ Hamiltonian matricies, Eq. 2.34, are built and diagonalized numerically. All of the results presented in this work were obtained using the procedure DSYEV from the numerical library LAPACK for Fortran 77. The diagonalization of the Hamiltonian matrix gives a set of eigenstates in the form of linear combinations of basis configurations:

$$|X_k^L\rangle = \sum_{(ij)}^{N_L} A_{L;ij}^{(k)} |L; ij\rangle, \tag{5.4}$$

with energy E_k^L, where $k = 1, ..., N_L$, and N_L is the size of the basis with angular momentum L, and $A_{L;ij}^{(k)}$ is the amplitude of configuration $|L; ij\rangle$ in state $|X_k^L\rangle$. Again, since the Zeeman energies of the electron and the hole are not included in the single-particle energies $\varepsilon_i^{e(h)}$, the resulting energies E_k^L are fourfold degenerate due to the four possible electron and hole spin alignments. The coefficients $A_{L;ij}^{(k)}$, as well as the exciton energies, depend on the magnetic field B and are evaluated for each B separately. The calculations are done in all of the angular momentum subspaces, since the electron-hole exchange as well as the exciton interaction with the Mn ion mixes X states with different angular momenta.

5.2 Exciton-Mn Hamiltonian

In the next step the electron-hole exchange, the quantum dot anisotropy, the Zeeman energies of the electron, hole and Mn ion, and the exchange interaction of electron (hole) with the Mn ion are included. The interacting electron-hole-Mn system is described by the Hamiltonian [150]:

$$\hat{H}_{X-Mn} = \hat{H}_X + \hat{H}_{EHX} + \hat{H}_{anis} + \hat{H}_{Zeeman} + \hat{H}_{h-Mn} + \hat{H}_{e-Mn}. \tag{5.5}$$

The first term is the electron-hole Hamiltonian $\hat{H}_X$, Eq. 2.34, discussed above. The second term is the electron-hole exchange term in the magnetic field [113] described in Chapter 3:

$$\hat{H}_{EHX} = \sum_{ijkl\sigma\sigma'\tau\tau'} \langle i\sigma, j\tau | V_{eh}^X | k\tau', l\sigma' \rangle c_{i\sigma}^+ h_{j\tau}^+ h_{k\tau'} c_{l\sigma'}. \tag{5.6}$$

The third term is the anisotropic correction, Eq. 2.16:

$$\hat{H}_{anis} = \sum_{ij\tau} t^h_{ij} h^+_{i\tau} h_{j\tau} + \sum_{ij\sigma} t^e_{ij} c^+_{i\sigma} c_{i\sigma}, \tag{5.7}$$

which breaks the cylindrical symmetry of the quantum dot and mixes the single-particle states with different angular momenta.

The fourth term is the Zeeman energy of the magnetic ion, the hole and the electron:

$$\hat{H}_{Zeeman} = g_{Mn}\mu_B B M_z + g_e \mu_B B S_z + g_h \mu_B B j_z, \tag{5.8}$$

where g_{Mn}, g_e, g_h are the Mn ion, electron and hole Lande g-factors respectively, and μ_B is the Bohr magneton. M_z, S_z and j_z are the Mn, electron, and heavy-hole spin z-projections.

The $\hat{H}_{h-Mn}$ and $\hat{H}_{e-Mn}$ are respectively the hole-Mn Hamiltonian, Eq. 4.8, and the electron-Mn Hamiltonian, Eq. 4.7, that describe the scattering of the hole and electron by the Mn ion at position $\mathbf{R}$. This scattering process depends on the state M_z of the Mn spin as well as its position $\mathbf{R}$.

Having calculated the excitonic states $|X^L_k\rangle$, one generates the X-Mn basis states by multiplying each excitonic state by the electron-hole spin wave function $|\sigma, \tau\rangle$, and by the Mn spin wave function $|M_z\rangle$. Thus, the X-Mn basis configurations are of the form:

$$|X^L_k, \tau\sigma, M_z\rangle = |X^L_k\rangle \otimes |\tau\sigma\rangle \otimes |M_z\rangle. \tag{5.9}$$

In the next step, the X-Mn basis is limited to the states that are built using the correlated exciton states with energies below the energy cut-off E^X_c. The energy cutoff is varied to assure convergence of numerical results. The results of the diagonalization of the exciton-Mn Hamiltonian with $E^x_c = 6.19\mathcal{R}^*$, the energy of the electron-hole configuration with both carriers on the d shell, are shown in Chapter 6. The total number of the basis states in that calculations is $N_c = 768$.

5.3 Construction of the exciton-Mn Hamiltonian

The matricies of the Hamiltonian H_{X-Mn}, Eq. 4.10, are built in the basis of the correlated exciton states. The non-zero elements of the e-Mn Hamiltonian, Eq. 4.7, consist of two parts: one is an Ising-like interaction leaving the electron and Mn spins unchanged, and the second, flipping the Mn spin with simultaneous flipping of the electron spin to leave $M_z + S_z$ constant.

The Ising-like terms of the electron-Mn interaction written in the basis of correlated exciton states take the form:

$$\begin{aligned}\langle X_r^L \downarrow\Uparrow, M_z|\hat{H}_{e-Mn}|X_s^{L'} \Uparrow\downarrow, M_z\rangle &= \sum_{(ij)}^{N_L}\sum_{(kl)}^{N_{L'}} A^{*r}_{L;ij}A^{s}_{L';kl}\langle ij^L \downarrow\Uparrow, M_z|\hat{H}_{e-Mn}|kl^{L'} \Uparrow\downarrow, M_z\rangle \\ &= \sum_{(ij)}^{N_L}\sum_{(kl)}^{N_{L'}} A^{*r}_{L;ij}A^{s}_{L';kl}\frac{J^e_{i,l}(\mathbf{R})}{2}M_z \\ &= \frac{1}{2}J^{e,eff}_{r,s}(\mathbf{R})M_z, \end{aligned} \tag{5.10}$$

where

$$J^{e,eff}_{r,s}(\mathbf{R}) = \sum_{(ij)}^{N_L}\sum_{(kl)}^{N_{L'}} A^{*r}_{L;ij}A^{s}_{L';kl}J^e_{i,l}(\mathbf{R}) \tag{5.11}$$

is the effective coupling constant constructed as a combination of single-particle exchange coupling constants $J^e_{i,l}(\mathbf{R})$ weighted by their probability in the exciton wave function. All elements building the effective coupling constant, the wave function coefficients $A^r_{L;ij}$ and the single-orbital coupling constants $J^e_{i,l}(\mathbf{R})$, depend on the magnetic field. The matrix element of the electron-Mn Hamiltonian, Eq. 4.7, calculated between the X-Mn basis states with the opposite spin of the electron e.g,: $\langle X_r^L \uparrow\Uparrow, M_z|$ and $|X_s^{L'} \Uparrow\uparrow, M_z\rangle$, has the same value but opposite sign to the matrix element given by Eq. 5.10.

The spin-flipping matrix elements take the form:

$$\begin{aligned}\langle X_r^L \downarrow\Uparrow, M_z|\hat{H}_{e-Mn}|X_s^{L'} \Uparrow\uparrow, M_z'\rangle &= \sum_{(ij)}^{N_L}\sum_{(kl)}^{N_{L'}} A_{L;ij}^{*r} A_{L';kl}^{s} \langle ij^L \downarrow\Uparrow, M_z|\hat{H}_{e-Mn}|kl^{L'} \Uparrow\uparrow, M_z'\rangle \\ &= -\sum_{(ij)}^{N_L}\sum_{(kl)}^{N_{L'}} A_{L;ij}^{*r} A_{L';kl}^{s} \frac{J_{i,l}^{e}(\mathbf{R})}{2} \langle M_z|M^+|M_z'\rangle \\ &= -\frac{1}{2} J_{r,s}^{e,eff}(\mathbf{R}) \langle M_z|M^+|M_z'\rangle. \end{aligned} \tag{5.12}$$

The Hamiltonian $\hat{H}_{h-Mn}$, Eq. 4.8, has only the Ising elements similar to the diagonal elements for $\hat{H}_{e-Mn}$.

5.4 Bi-exciton-Mn complex

Calculations of the electronic properties of the bi-exciton-Mn complex (XX-Mn) are done in a similar two-step process as in the case of a X-Mn.

The bi-exciton Hamiltonian $\hat{H}_{eh}$, given by the equation, Eq. 2.26, conserves the total angular momentum L of the carriers, the total spin, and spin projection of electrons (S, S_z) and holes (j, j_z). The electron-hole configurations can be divided according to these quantum numbers into subspaces denoted by $\alpha = [L, j, j_z, S, S_z]$. In the first step, one can build the matrices of the electron-hole Hamiltonian $\hat{H}_{eh}$ in the basis $|\alpha; ijkl\rangle$ of two-electron and two-hole configurations of the form:

$$|\alpha; ijkl\rangle = h_{i\tau}^{+} h_{j\tau'}^{+} c_{k\sigma}^{+} c_{l\sigma'}^{+} |0\rangle, \tag{5.13}$$

where the complex indices i, j, k, and l correspond to the HO states, while spin $S_z = \sigma + \sigma'$ and $j_z = \tau + \tau'$.

Diagonalization of this Hamiltonian in each of the basis α gives the energies E_r^{α} of N_α states of the biexciton, where $r = 1, \ldots, N_\alpha$. The corresponding eigenstates $|XX_r^{\alpha}\rangle = \sum_{ijkl}^{N_\alpha} A_{\alpha;ijkl}^{(r)} |\alpha; ijkl\rangle$ are linear combinations of two-pair configurations, in which single-particle orbitals i,j (k,l) are occupied by holes (electrons) and $A_{\alpha;ijkl}^{(r)}$ are their amplitudes.

Next, the XX-Mn basis is prepared as the tensor product $|XX_r^{\alpha}, M_z\rangle =$

$|XX_r^\alpha\rangle \otimes |M_z\rangle$ of the XX eigenstates (with energies lower than the energy cutoff) and the Mn spin wave functions with $M_z = \pm 5/2, \pm 3/2, \pm 1/2$. In this basis, the matrix of the Hamiltonian, Eq. 5.5, of the XX-Mn system [167] is built and diagonalized numerically.

The energy cut-off for the XX-Mn states is $E_c^{XX} = 5.32$ Ry*. If one introduces the notation:

$$\begin{aligned} E_{GS}^X + \epsilon &= 6.19 Ry* = E_c^X \\ E_{GS}^{XX} + \epsilon &= 5.32 Ry* = E_c^{XX}, \end{aligned}$$

then the energy cut-off E_c^{XX} for XX assures that the ϵ for the X-Mn and XX-Mn is equal. This means that we include in the basis all the states that have energies lower than $E_{GS}^X + \epsilon$ ($E_{GS}^{XX} + \epsilon$), while neglecting the ones that are higher in energy. This way the absolute number of 26136 of XX-Mn configuration in the QD with three single-particle shells is restricted to 4902, what significantly improved the computation time.

5.5 Calculations of emission spectra

Having obtained the eigenenergies and eigenfunctions of N and $N-1$ electron-hole pairs in the presence of Mn, the emission and absorption spectra can be calculated from Fermi's Golden Rule. The equations Eqs. 2.31 and 2.33 need to be slightly modified to take into consideration the presence of the Mn in the QD. The formula Eq. 2.31 takes the following form now:

$$I_\varepsilon^-(\omega) = \sum_i \sum_f P_i |\langle f, N-1, M_z | \hat{P}_\varepsilon^- | i, N, M_z \rangle|^2 \delta(E_i - E_f - \omega). \tag{5.14}$$

The $|i, N, M_z\rangle$ denotes the initial state of the N excitons with a Mn ion in state M_z, while $|f, N-1, M_z\rangle$ is the final state of $N-1$ excitons, in the presence of the same Mn state M_z, which remains unchanged after the recombination of one electron-hole pair.

Since the polarisation operator (Eq. 2.32) does not act on the spin of the Mn ion, the Mn has to be in the same M_z state in the initial and in all final states.

The absorption spectra in the presence of the Mn can be calculated as:

$$I_{\varepsilon}^{+}(\omega) = \sum_{i} \sum_{f} P_i |\langle f, N+1, M_z | \hat{P}_{\varepsilon}^{+} | i, N, M_z \rangle|^2 \delta(E_i - E_f - \omega). \tag{5.15}$$

Now, the initial state $|i, N, M_z\rangle$ has N excitons, while the final state $|f, N+1, M_z\rangle$ has one more exciton, and the state of Mn is M_z in both final and initial states.

In the absorption there are now six initial $|M_z\rangle$ states thermally populated depending on the Mn Zeeman splitting, while there is a large number of final states for each M_z visible in the absorption spectra. In the calculations of the emission spectra, on the other hand, there are six final $|M_z\rangle$ states that need to be considered. Note that the interband polarization operators anihilate/create an electron-hole pair in the initial state without changing the $|M_z\rangle$ state of the Mn. Since the Mn state does not change, the Mn Zeeman energy does not contribute to the energy of the emitted/absorbed photon.

Chapter 6

Exciton-Mn complex

It was shown recently that the coupling of the finite spin of the exciton to that of the impurity opens a way to detect and manipulate localized spins by optical means [183]. For that reason, the system of an exciton confined in a QD and coupled to a magnetic impurity, typically a Manganese (Mn) ion, was analyzed experimentally [22–24, 155, 156, 162–165, 173, 184] and theoretically [139, 150, 151, 161, 167, 185, 186]. The existence of the Mn ion with the magnetic moment $M = 5/2$ has been detected by observation of a characteristic exciton emission spectrum consisting of six emission lines related to the $2M+1 = 6$ quantum states of Mn. This emission spectrum was explained on the basis of a spin model, where the electrons and valence band holes are represented as spins interacting with the spin of the Mn ion. This spin model will be briefly discussed in Section 6.1. Here we apply the fully microscopic treatment of the exciton-Mn interaction to provide a more complete understanding of the system. The results, their analysis as a function of the model parameters, as well as a comparison of the calculated and measured optical spectra are shown in Section 6.2.

6.1 Spin model

The simplest approach to solve the X-Mn problem involves restriction of the single-particle states of the electron and the hole to the lowest energy level in the s-shell, as is frequently done for the QDs. Within this restriction there are

four possible exciton configurations due to different spin alignments of carriers as shown in Fig. 6.1.

Figure 6.1: Four possible exciton configurations in the spin model. Configurations differ in the spin allignment of the electron and the hole.

The exciton configurations $|a\rangle$ and $|c\rangle$ are *bright*. This means that excition in configuration $|a\rangle$ or $|c\rangle$ can recombine radiatively, creating a photon with polarization σ_+ or σ_-, respectively. On the other hand, exciton configurations $|b\rangle$ and $|d\rangle$ are *dark* - radiative recombination of the exciton in those configurations is not possible. More about the optical selection rules can be found in Chapter 2 (Section 2.6).

If one retains only this lowest single-particle level for the electron and the hole, then the correlated model of X-Mn system, discussed in Chapter 4 with the Hamiltonian given by Eq. 4.10, can be reduced to the simple spin model [22, 150, 165] with the following Hamiltonian:

$$\begin{aligned} \hat{H}^{ss}_{X-Mn} &= E_X\hat{1} + g_{Mn}\mu_B\vec{B}\cdot\hat{M} + g_e\mu_B\vec{B}\cdot\hat{\sigma} + g_h\mu_B B_z j_z \\ &- \frac{1}{2}J^e(\mathbf{R})\hat{\sigma}\cdot\hat{M} + \frac{3}{2}J^h(\mathbf{R})j_z M_z + H_{EHX}, \end{aligned} \tag{6.1}$$

where $\hat{M}$, $\hat{\sigma}$, j_z are the Mn, electron and hole spin operators, respectively. For electron $\hat{\sigma}$ represents Pauli matricies, while for hole $j_z = \pm 1$. E_X is the energy of the excitonic configuration, containing single-particle energies of the electron and the hole, and the direct Coulomb interaction between them, Eq. 2.34. Since this term is equal for all four configurations, it is often neglected. The Zeeman energies of the electron and the hole are typically included the single-particle energies, but here they are written explicitly. The next three terms represent the Zeeman energies of the magnetic ion, the electron, and the hole respectively, while the following two terms represent the electron-Mn and the hole-Mn interactions,

with the exchange constants $J^{e(h)}(\mathbf{R}) = J_{00}^{e(h)}(\mathbf{R})$, where the Mn ion is at the position $\mathbf{R}$. Often the coupling constants of the lowest single-particle state of the electron (hole) are replaced by phenomenological constants $J^{e(h)}$ fitted to the experimental data.

The last term of Eq. 6.1 represents the electron-hole exchange, which in the basis of exciton states (Fig. 6.1): $(|a\rangle, |c\rangle, |b\rangle, |d\rangle)$ can be written as [134]:

$$H_{EHX} = \frac{1}{2}\begin{pmatrix} \Delta_0 & \Delta_2 & 0 & 0 \\ \Delta_2 & \Delta_0 & 0 & 0 \\ 0 & 0 & -\Delta_0 & \Delta_1 \\ 0 & 0 & \Delta_1 & -\Delta_0 \end{pmatrix}. \tag{6.2}$$

This fully phenomenological model of the electron-hole exchange interaction is characterized by the parameters extracted from the experiment: bright-dark exciton splitting Δ_0, and the anisotropic exchange splitting of the bright (Δ_2), and dark (Δ_1) exciton states. The spin model of the electron-hole exchange was created to allow for a simple correction of the exciton energy levels, without using a fully microscopic model. For simple calculation it is epecially important because the application of the full electron-hole exchange model (as described in Chapter 3) in this restricted basis would lead only to the bright-dark exciton splitting, leaving each of these manifolds degenerate. It follows from the fact that the bright exciton splitting is caused by the coupling of the s-shell exciton configurations with each other through higher excitonic configurations with angular momentum $L = \pm 2$, as seen in Eq. 3.35.

It is important to notice that in the spin model described by the Hamiltonian Eq. 6.1 all of the exchange constants $J^{e(h)}(\mathbf{R})$ as well as Δ_{0-2} are parametrized at $B = 0$, and the dependence on the magnetic field enters only through the Zeeman terms.

As explained in Chapter 5, to construct the Hamiltonian matrix of the interacting exciton with Mn ion, each of the configurations (Fig. 6.1) need to be multiplied by one of the six Mn spin projections $|M_z\rangle$. The construction of this basis is schematically shown in Figs. 6.2 and 6.3. In the following, the notation $|a, M_z\rangle, |b, M_z\rangle, ...$ will be kept when talking about the spin alignments defined in Figs. 6.2 and 6.3.

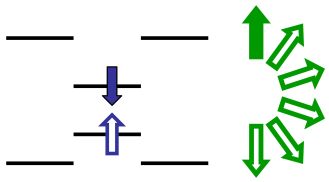

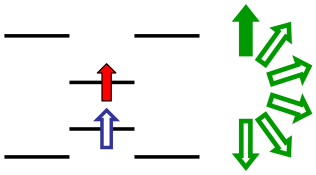

Figure 6.2: $|a, M_z\rangle = h^+_{00\Uparrow} c^+_{00\downarrow}|0\rangle \otimes |M_z\rangle$, $|b, M_z\rangle = h^+_{00\Uparrow} c^+_{00\uparrow}|0\rangle \otimes |M_z\rangle$

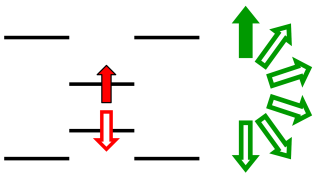

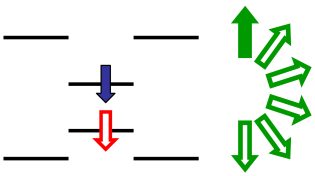

Figure 6.3: $|c, M_z\rangle = h^+_{00\Downarrow} c^+_{00\uparrow}|0\rangle\otimes)|M_z\rangle$, $|d, M_z\rangle = h^+_{00\Downarrow} c^+_{00\downarrow}|0\rangle \otimes |M_z\rangle$

Here the X-Mn spectrum in zero magnetic field in the absence of an electron-hole exchange will be analysed, starting from the pure exciton and gradually turning on the interactions between carriers and the Mn ion.

Figures 6.2 and 6.3 show the basis of X-Mn configurations $|a, M_z\rangle$, $|b, M_z\rangle$, $|c, M_z\rangle$, $|d, M_z\rangle$. In the absence of X-Mn interactions, all those 24 configurations are degenerate (Fig. 6.4).

In the presence of the hole-Mn interaction only, the second quantization form of the Hamiltonian of such a system is given by [187]:

$$\hat{H}^{ss}_{h-Mn} = \hat{E}_X \hat{1} + \frac{3J^h(\mathbf{R})}{2}\left(h^+_{00\uparrow}h_{00\uparrow} - h^+_{00\downarrow}h_{00\downarrow}\right) M_z \tag{6.3}$$

This Hamiltonian conserves the spin of all particles. Configurations with the same exciton state, for example: $|a, M_z\rangle$ and $|a, M_z\prime\rangle$ are not mixed by the Hamiltonian, Eq. 6.3, because they differ by the Mn spin projection. On the other hand, the configurations from different excitonic groups, like $|a, M_z\rangle$ and $|b, M_z\rangle$ are not coupled due to a different spin allignment of carriers. For that reason, the hole-Mn interaction has only diagonal Hamiltonian matrix elements. It leads to a splitting of the 24-fold degenerate level into six fourfold degenerate levels, see Fig. 6.4. These levels are equidistant in energy with splitting equal to $\frac{3}{2}J^h(\mathbf{R})$.

One can think about the fixed spin of the hole as a source of an *effective internal* magnetic field, which acts on Manganese spin and leads to the Zeeman splitting of its levels. The lowest X-Mn level in this case is fourfold degenerate, and corresponds to the following configurations:

$$h^+_{00\Uparrow}c^+_{00\downarrow}|0\rangle \otimes |-\frac{5}{2}\rangle, \qquad h^+_{00\Uparrow}c^+_{00\uparrow}|0\rangle \otimes |-\frac{5}{2}\rangle, \tag{6.4}$$
$$h^+_{00\Downarrow}c^+_{00\downarrow}|0\rangle \otimes |\frac{5}{2}\rangle, \qquad h^+_{00\Downarrow}c^+_{00\uparrow}|0\rangle \otimes |\frac{5}{2}\rangle.$$

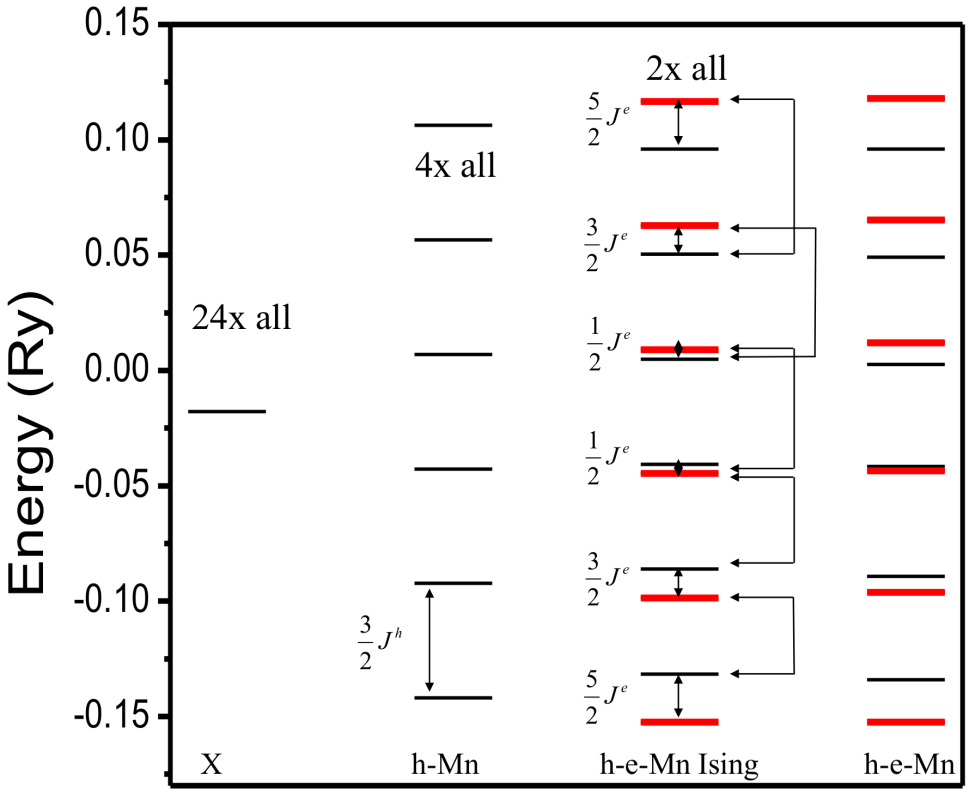

Figure 6.4: The evolution of the X-Mn energy spectra with inclusion of the interactions: first column - no X-Mn interaction, second column - h-Mn interaction, third - Ising part of the e-Mn interaction, fourth - full X-Mn interaction present. Red colour bars correspond to energies of the bright X-Mn states. Calculations done with following parameters: $Ry = 12.11$ meV, $aB = 5.61$ nm, $\omega_h + \omega_e = 30$ meV, $\omega_e/\omega_h = 4$, $J^e_c = 15$ meV $\cdot$ nm^3, $J^h_c = 60$ meV $\cdot$ nm^3, $d = 3$ nm.

The full X-Mn Hamiltonian at zero magnetic field, $\hat{H}^{ss}_{X-Mn}$, Eq. 6.1, can be expressed in second quantization as:

$$\begin{aligned}\hat{H}^{ss}_{X-Mn} &= \hat{E}_X\hat{1} + \frac{3J^h(\mathbf{R})}{2}\left(h^+_{00\Uparrow}h_{00\Uparrow} - h^+_{00\Downarrow}h_{00\Downarrow}\right)M_z \\ &- \frac{J^e(\mathbf{R})}{2}\left(\left(c^+_{00\uparrow}c_{00\uparrow} - c^+_{00\downarrow}c_{00\downarrow}\right)M_z + c^+_{00\downarrow}c_{00\uparrow}M^+ + c^+_{00\uparrow}c_{00\downarrow}M^-\right)\end{aligned} \tag{6.5}$$

From this form of the Hamiltonian one can see that the hole spin j_z is conserved, while the electron spin can be flipped with a simultaneous flip of the Manganese spin. The spin-flip process conserves the total $M_z + S_z$. From that, one can draw conclusions about mixing of X-Mn $|a, M_z\rangle$, $|b, M_z\rangle$, $|c, M_z\rangle$, $|d, M_z\rangle$ configurations.

The Ising part of the electron-Mn interaction term, as h-Mn Hamiltonian, has only diagonal non-zero matrix elements. Inclusion of this interactions leads to the splitting of the fourfold degenerate levels into two doubly degenerate levels, as shown in the third column of Fig. 6.4. For example, the previous ground state, Eq. 6.4, splits into two levels. The lowest level corresponds to the *bright* X-Mn state: $h^+_{00\Uparrow}c^+_{00\downarrow}|0\rangle \otimes |-\frac{5}{2}\rangle$, degenerate with $h^+_{00\Downarrow}c^+_{00\uparrow}|0\rangle \otimes |\frac{5}{2}\rangle$, while the first excited level: $h^+_{00\Uparrow}c^+_{00\uparrow}|0\rangle \otimes |-\frac{5}{2}\rangle$, degenerate with $h^+_{00\Downarrow}c^+_{00\downarrow}|0\rangle \otimes |\frac{5}{2}\rangle$ is *dark*. The splitting between the states due to the e-Mn interaction is not equal (Fig. 6.4), but depends on the Manganese spin projection. However, the energy distances between the *bright* X-Mn states are still equal, and equal to:

$$\delta_{Mn} = \frac{1}{2}\left(3J^h\left(\mathbf{R}\right) + J^e\left(\mathbf{R}\right)\right). \tag{6.6}$$

The second part of the e-Mn Hamiltonian involves an electron-Mn spin flip. As previously, this interaction doesn't mix states within the same exciton group, e.g., $|a, M_z\rangle$. These groups consist of *the same* orbital exciton configuration but with a different Mn spin, while the spin-flip interaction relies on a *simultaneous* electron and Manganese spin flip. On the other hand, this interaction mixes states from groups $|a, M_z\rangle$ and $|b, M_z\rangle$ ($|c, M_z\rangle$ and $|d, M_z\rangle$), which have the Manganese spin different by 1, e.g., $|a, M_z\rangle$ and $|b, M_z - 1\rangle$. There is no mixing between states from groups with different spins of holes, e.g., $|a, M_z\rangle$ and $|c, M_z\rangle$ due to

j_z conservation. In Fig. 6.4 the coupling scheme has been shown by the black arrows.

In the absence of the electron-hole exchange, the basis of all 24 configurations can be divided into the subspaces according to j_z and $M_z + S_z$. As a result one obtains ten 2×2 matricies and four configurations that are eigenstates of the $\hat{H}^{ss}_{X-Mn}$ Hamiltonian.

An example of the calculations in one of the two-dimensional subspaces, namely $M_z + S_z = -2$, is shown below. In this subspace there are two configurations $|b, -5/2\rangle$ and $|a, -3/2\rangle$. The Hamiltonian matrix in this basis has the form:

$$\hat{H} = E_X\hat{1} + \begin{bmatrix} -\frac{5}{2}\frac{1}{2}\left(-J^e + 3J^h\right) & -\sqrt{5}\frac{J^e}{2} \\ -\sqrt{5}\frac{J^e}{2} & -\frac{3}{2}\frac{1}{2}\left(J^e + 3J^h\right) \end{bmatrix}. \tag{6.7}$$

Diagonalization of this matrix leads to eigenenergies:

$$E^{X-Mn}_{+/-} = E_X + \frac{1}{4}J^e \pm \frac{3}{4}J^h\sqrt{96\left(J^e\right)^2 - 24J^eJ^h + 9\left(J^h\right)^2}, \tag{6.8}$$

and eigenvectors in the form of linear combinations of the bright configuration $|a, -3/2\rangle$ and the dark configuration $|b, -5/2\rangle$:

$$|X - Mn\rangle_+ = \alpha_+|b, -\frac{5}{2}\rangle + \beta_+|a, -\frac{3}{2}\rangle \tag{6.9}$$

$$|X - Mn\rangle_- = \alpha_-|b, -\frac{5}{2}\rangle + \beta_-|a, -\frac{3}{2}\rangle. \tag{6.10}$$

The emission spectra of the X-Mn complex confined in the anisotropic QD depend strongly on the interplay between two energy scales: the electron-hole exchange and the exciton-Mn exchange. In case of a symmetric quantum dot with Mn in the center, the spectrum is strongly dominated by the presence of the Mn ion. On the other hand, if the coupling constant $J^h(\mathbf{R})$ is smaller or comparable to the bright exciton splitting Δ_2, the spectrum is dominated by electron-hole exchange. This takes place if the QD is asymmetric or tall, or when the Mn is shifted away from the center. These two cases of the X-Mn emission spectra will be analysed.

The figures presented in this section show results of calculations using quantum dot parameters defined previously in Chapter 3 (Section 3.3). Additionally, the bulk electron-Mn exchange coupling is given by $J_c^e = 15$ meV $\cdot$ nm^3, while the hole-Mn exchange constant is $J_c^h = 60$ meV $\cdot$ nm^3 [152, 187]. The QD height is $d = 3$ nm, while the electron-hole exchange parameters, defined by Eq. 6.2, are: $\Delta_0 = 0.506$ meV, $\Delta_2 = 0.166$ meV, $\Delta_1 = 0$ meV.

Figure 6.5 shows two cases: (a) when the X-Mn interaction completely dominates electron-hole exchange, and (b) with the electron-hole exchange larger than X-Mn exchange. This results in increased spacing between consecutive emission lines in the center of the spectra. The electron-hole exchange induced opening of the central gap was first reported by Leger *et al.* [155]. The central gap can be approximated by the expression $\sqrt{\Delta_2^2 + \delta_{Mn}^2}$, where δ_{Mn} is given by the Eq. 6.6. In Ref. [155] the observed spectra, either the Mn or e-h exchange dominated, were related to the in-plane shift of the Mn ion position from the center of the QD. This shift of the position of the Mn ion causes a decrease of the hole-Mn and electron-Mn coupling constants as shown in Fig. 4.4. However, one should remember that the coupling constants depend also on the height of the quantum dot d and the s-p single-particle shell spacing.

To learn more about the X-Mn emission spectra one can extract from them the splittings between the emission lines Δ_i, where $\Delta_i = E_{i+1} - E_i$, as shown in Fig. 6.5 (a). To compare the splittings Δ_i for different QDs they are normalized by the average splitting of the spectra $\Delta_{aver} = (E_6 - E_1)/5$. The dependence of the average splitting of the emission spectra Δ_{aver} on the height d of the QD is shown in Fig. 6.6 (a), while the normalized emission line spacings Δ_i/Δ_{aver} for these dots are shown in Fig. 6.6 (b).

As was mentioned, the parameter d changes the strength of the hole-Mn and electron-Mn coupling, and as a result changes the splitting of the spectra Δ_{aver}. In figure 6.6 the paramter d was varied between 2 and 6 nm. The smaller the height of the QD, the greater the exchange coupling of the spin of the carriers to the Mn spin, and the greater average splitting (Fig. 6.6 (a)). Since the electron-hole parameters are kept unchanged, the electron-hole exchange-induced gap in the middle of the spectra becomes more pronounced with the increase of the height d (Fig. 6.6 (b)).

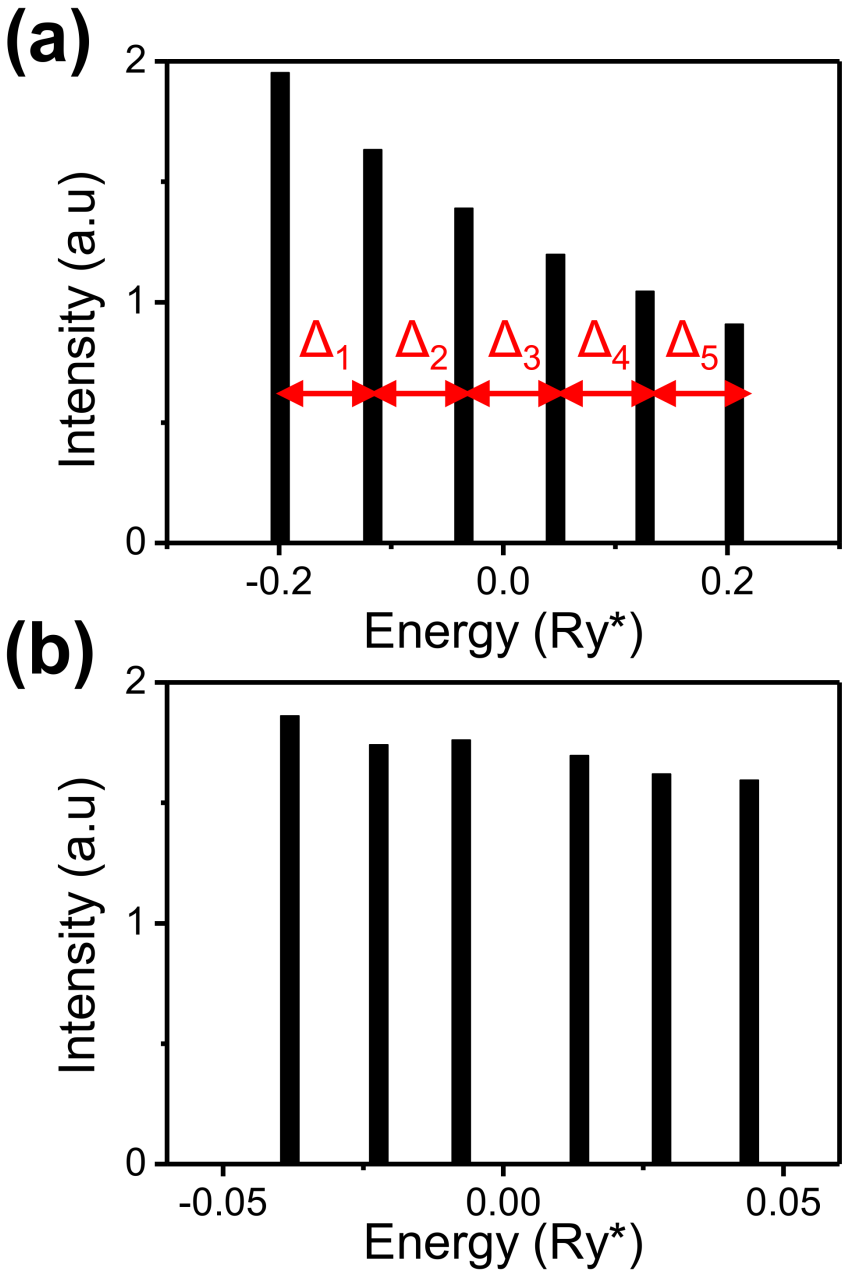

Figure 6.5: The calculated emission spectra from the QD with different hights of the QD: $d = 2$ nm (a) and $d = 10$ nm (b).

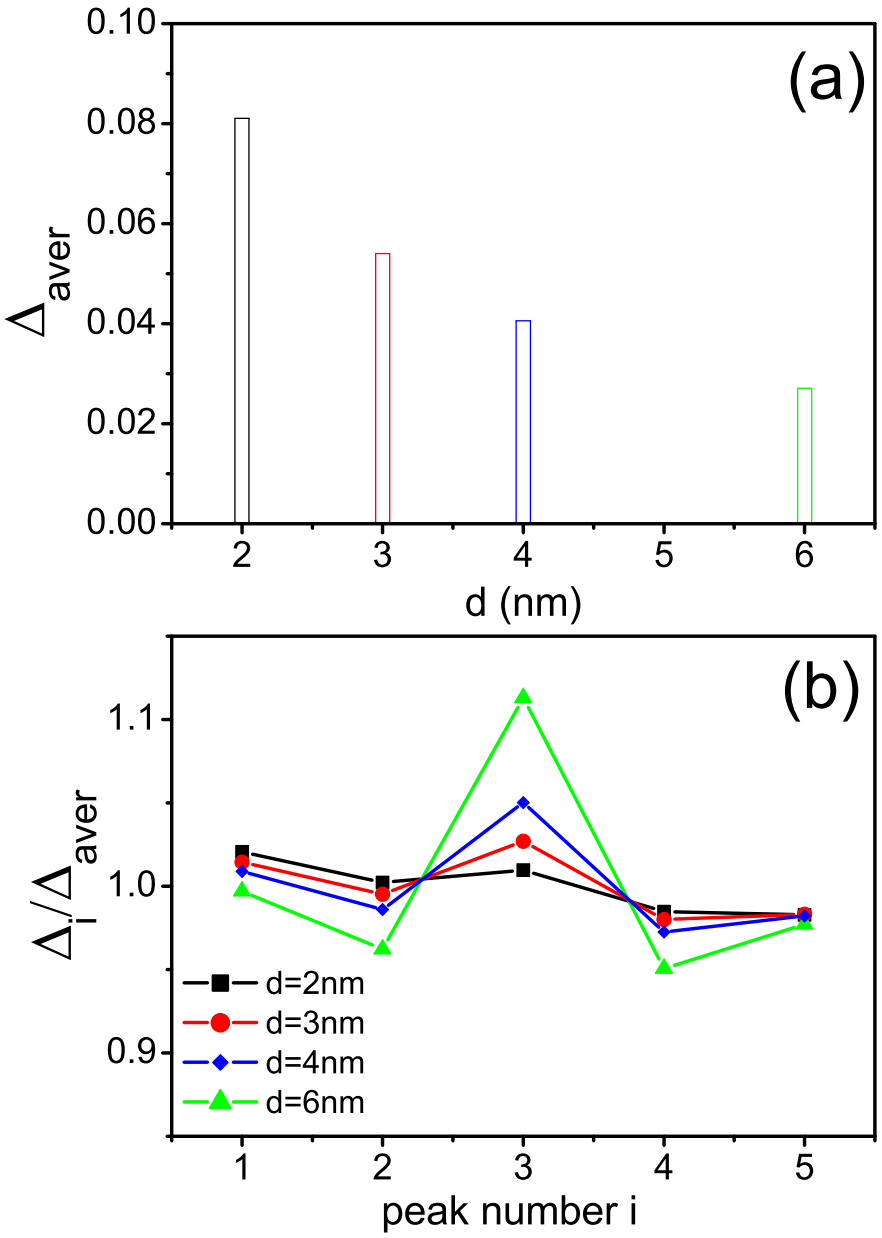

Figure 6.6: The dependence of the average splitting of the spectra (Δ_{aver})(a) and Δ_i/Δ_{aver} (b) on the height d of the QD. The height of the QD was $d = 2, 3, 4$ and 6 nm.

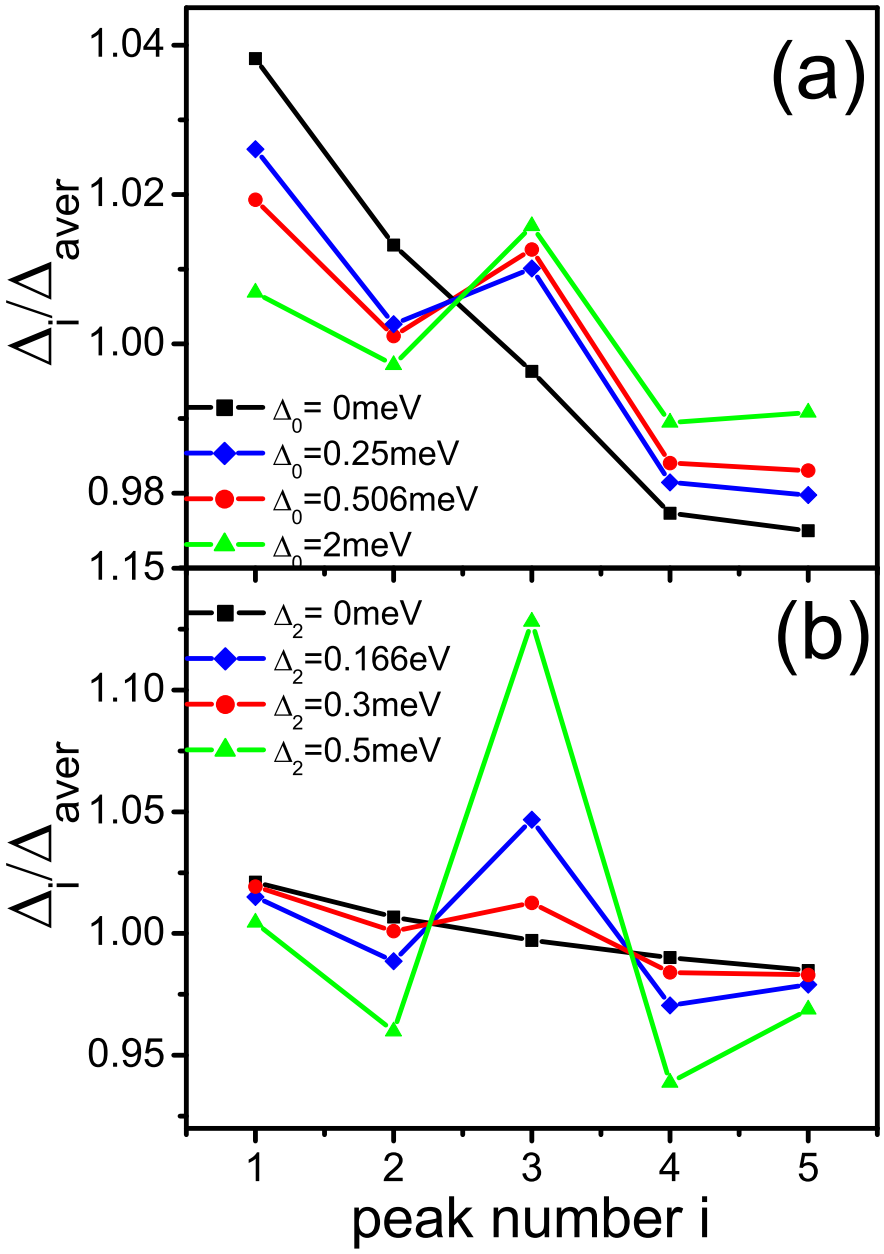

Figure 6.7: The dependence of the Δ_i/Δ_{aver} on (a) the dark-bright exciton splitting Δ_0 and (b) the bright exciton splitting Δ_2.

The other feature that one notices in Fig. 6.6 (b) is the general non-zero slope of the $\Delta_i/\Delta_{aver}(i)$ function. The dependence of this slope on the other parameters of the QD has been investigated. The greatest variation of the slope was observed when the bright-dark electron-hole exchange splitting Δ_0 was varied. This dependence has been presented in Fig. 6.7 (a). For the $\Delta_0 = 0$ meV the slope of the Δ_i/Δ_{aver} is the greatest. It decreases quickly when the value of the parameter Δ_0 is increased. In the spin model, the non-uniformity of the distribution of the X-Mn emission lines is related to the spin-flip part of the electron-Mn exchange interaction, Eq. 6.6. This interaction causes mixing between bright and dark exciton configurations which are split by the energy Δ_0. The greater the difference between the energies of the interacting bright and dark configurations of the exciton, the smaller the repulsion between them and the smaller the re-normalization of the X-Mn emission lines. For the range of the bright-dark exciton splitting observed experimentally, $\Delta_0 = 0.5 - 1$ meV, the change of the emission line splitting does not exceed 2%. A uniform splitting of the emission lines corresponds to $\Delta_i/\Delta_{aver} = 1$).

Figure 6.7 (b) shows the dependence of the normalized emission line spacing Δ_i/Δ_{aver} on the bright exciton splitting Δ_2. The parameter Δ_2 was varied between $0 - 0.5$ meV. This figure has many similarities with the Fig. 6.6 (b). They both represent the interplay between the two energy scales - carrier-Mn coupling δ_{Mn}, and long-range electron-hole exchange interaction Δ_2.

6.2 Microscopic, correlated model of the X-Mn complex

Here we move beyong the spin model of the exciton and show how one can engineer exciton-Mn interactions in a semiconductor quantum dot through design of a quantum-dot exciton [103, 125]. A novel quantum interference (QI) effect between the electron-hole Coulomb scattering and the scattering by Mn ion is shown to significantly change the exciton-Mn coupling revealed by a characteristic pattern in the emission spectrum. All the figures in this Section are obtained using quantum dot parameters defined in Chapter 3 (Section 3.3). Additionally,

the bulk electron-Mn exchange constant: $J_c^e = 15$ meV $\cdot$ nm^3, while the hole-Mn exchange constant: $J_c^h = 60$ meV $\cdot$ nm^3. The QD height is typically $d = 3$ nm. The full microscopic model of electron-hole exchange (Chapter 3) is implemented, and calculations are done with the bulk parameters $\mu^2 = 0.11$ and $E_{SR} = 0.093$. The exciton energy spectra in the non-magnetic QD with the above parameters have been calculated as well. This allowed for the extraction of the dark-bright exciton splitting $\Delta_0 = 0.506$ meV and bright exciton splitting $\Delta_2 = 0.166$ meV from energy spectra.

6.2.1 Quantum interference

6.2.1.1 Magnetic field produced by the spin of the hole

The dominant component of the exchange interaction of the correlated exciton with the Mn spin is the hole-Mn Ising-like interaction. For a qualitative description of the exciton-Mn interaction one can focus on the hole-Mn part of this interaction [150, 188]. As discussed in the previous Section, the spin of the hole plays the role of the effective magnetic field, leading to the "exchange" splitting of different M_z states. One can evaluate how the strength of this *internal magnetic field* changes due to the correlations. This can be done by calculating the expectation value of the hole-Mn Hamiltonian, Eq. 4.8, in the ground state of the exciton: $\langle H_{h-Mn}\rangle = \langle M_z|\langle\downarrow\Uparrow|\langle X_{GS}|H_{h-Mn}|X_{GS}\rangle|\Uparrow\downarrow\rangle|M_z\rangle$.

It was shown in Chapter 2 that the ground state of a correlated exciton confined in the QD with three (SPD) single-particle shells can be approximated by the linear combination of the three Jacobi coordinates: $|A\rangle$, $|B\rangle$ and $|H\rangle$ (Eq. 2.38). With p orbitals not coupled to the Mn in the center of the dot [152], the ground state of the exciton can be further simplified and written as:

$$|X_{GS}\rangle|\Uparrow\downarrow\rangle = \left(A_A^{(1)}|A\rangle - A_H^{(1)}|H\rangle\right)|\Uparrow\downarrow\rangle. \tag{6.11}$$

The expectation value of the hole-Mn interaction Hamiltonian in this state is

then:

$$\begin{aligned}
\langle H_{h-Mn}\rangle &= \langle M_z|\langle\downarrow\Uparrow|\langle X_{GS}|H_{h-Mn}|X_{GS}\rangle|\Uparrow\downarrow\rangle|M_z\rangle \\
&= {A_A^{(1)}}^2\langle M_z|\langle\downarrow\Uparrow|\langle A|H_{h-Mn}|A\rangle|\Uparrow\downarrow\rangle|M_z\rangle \\
&- 2A_A^{(1)}A_H^{(1)}\langle M_z|\langle\downarrow\Uparrow|\langle H|H_{h-Mn}|A\rangle|\Uparrow\downarrow\rangle|M_z\rangle \\
&+ {A_H^{(1)}}^2\langle M_z|\langle\downarrow\Uparrow|\langle H|H_{h-Mn}|H\rangle|\Uparrow\downarrow\rangle|M_z\rangle \\
&= \frac{3}{2}\left(\{{A_A^{(1)}}^2+{A_H^{(1)}}^2\}J_{ss}(0)-\sqrt{2}A_A^{(1)}A_H^{(1)}J_{sd}(0)\right)M_z,
\end{aligned} \tag{6.12}$$

where the example of a matrix element:

$$\begin{aligned}
\langle M_z|\langle\downarrow\Uparrow|\langle H|H_{h-Mn}|A\rangle|\Uparrow\downarrow\rangle|M_z\rangle &= \frac{1}{\sqrt{2}}\langle M_z|\langle\downarrow\Uparrow|(\langle sd|+\langle ds|)|H_{h-Mn}|ss\rangle|\Uparrow\downarrow\rangle|M_z\rangle \\
&= \frac{1}{\sqrt{2}}J_{sd}(0).
\end{aligned} \tag{6.13}$$

Equation 6.12 can be written in the compact form:

$$\langle H_{h-Mn}\rangle = \alpha M_z, \tag{6.14}$$

where the exchange splitting $\alpha = 3/2\left[{A_A^*}^2 J_{ss}-\sqrt{2}A_A^{(1)}A_H^{(1)}J_{sd}\right]$ of Mn levels is a difference of two terms. The first term, ${A_A^*}^2 J_{ss}$, is proportional to the product of the sum of probability amplitudes of the hole occupying s and d orbitals, ${A_A^*}^2 = {A_A^{(1)}}^2+{A_H^{(1)}}^2$ in the exciton GS, while the electron is on the s-shell, weighted by the exchange matrix element $J_{dd} = J_{ss}$. The renormalized amplitude ${A_A^*}^2$ is slightly smaller than 1, which is the value in front of the J_{ss} in the spin model. The second term, $-\sqrt{2}A_A^{(1)}A_H^{(1)}J_{sd}$, changes the magnitude of the hole-Mn exchange. This term is proportional to the product $A_H^{(1)}J_{sd}$, i.e., the amplitude $A_H^{(1)}$ of the $|H\rangle$ configuration in the exciton GS, and scattering matrix element J_{sd} of the hole by the Mn ion. The presence of the $|H\rangle$ configuration in the ground state of the exciton is caused by the direct Coulomb interaction between the electron and hole, while the scattering of the hole from s to $d = (1,1)$ orbital is caused by the Mn ion acting as an impurity. Hence, both the electron-hole Coulomb interactions, and the scattering by the Mn impurity must be simultaneously present to induce a change in the hole exchange field. This effect is the quantum interference (QI)

effect between these interactions. The QI is absent in shallow quantum dots with s-p shells, but takes place in quantum dots with at least three confined shells. The same conclusion holds for Mn off-center but with A_A^* renormalized by the J_{pp} coupling.

Figure 6.8 shows the results of the numerical calculations of the average spacing of Mn energy levels in the s shell as a function of the number of shells confined in the isotropic QD, with a negligible electron-hole exchange. The calculations include the electron-hole direct Coulomb interaction and electron-Mn and hole-Mn interactions, and are done for parameters typical for a CdTe quantum dot, specified at the begining of this Section. Figure 6.8 (a) shows the case when the scattering constants J_{sd} have opposite signs to the J_{ss}, $J_{sd} = -J_{ss}$, as it follows from the calculations presented in Chapter 4. Figure 6.8 (b), on the other hand, presents the results with $J_{sd} = J_{ss}$. In the first case (Fig. 6.8 (a)), there is a *constructive* quantum interference between the Coulomb and Mn scattering, which leads to the increase of the hole-Mn interaction, and the increase of the splitting of the X-Mn emission lines, when the d shell is present in the QD. The effect persists when the higher shells are introduced to the QD. If one were to develop the means to control independently the value of the coupling constants J_{ij}, the system in which $J_{sd} = J_{ss}$ could be designed. In the case when the scattering constant J_{sd} is equal to the J_{ss}, the quantum interference is *destructive* and the splitting of the emission lines decreases. In Fig. 6.8 (b), this splitting decreases by a factor of about 2, Ref. [151], when the quantum dot admits the d shell.

6.2.1.2 Effects of the excited states of the exciton

In Chapter 5 it was mentioned that the eigenstates of the exciton in the non-magnetic QD are no longer eigenstates in the presence of the Mn. The Mn ion acts as a scattering center coupling different exciton states. This coupling leads to the second signature of the quantum interference. For the simplicity of the analytical analysis the number of the excitonic states is restricted to only two: the ground state and the first excited state. The effect of the Mn ion-induced coupling between the excitonic states on the distribution of the s-shell emission lines from the X-Mn complex will be shown.

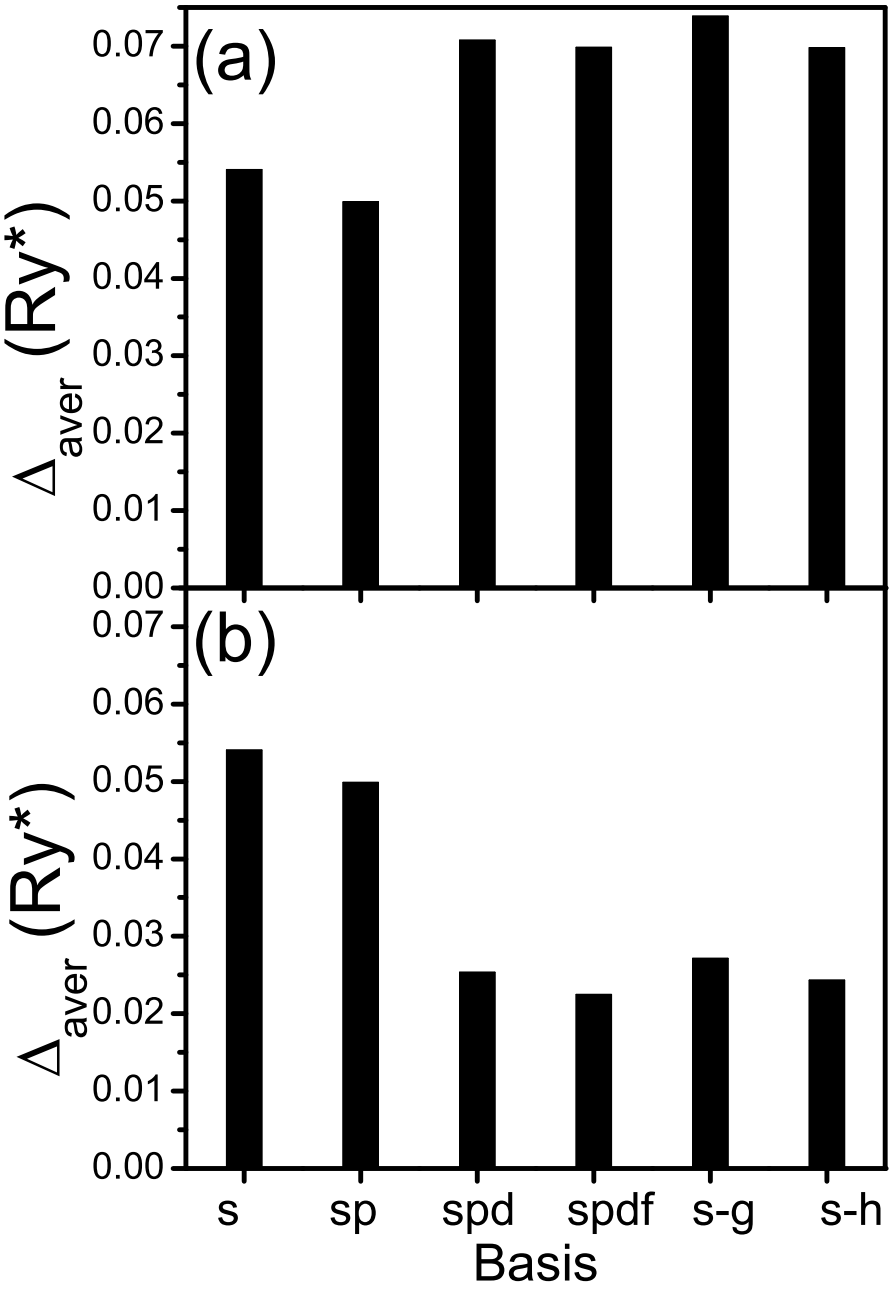

Figure 6.8: Calculated average spacing $\Delta_{aver} = (E_{-5/2} - E_{5/2})/5$ of Mn energy levels in the s-shell as a function of the number of shells of an isotropic CdTe QD with negligible electron-hole exchange. The parameters used in the calculation were specified at the begining of this section, while the scattering constants: $J_{sd} = -J_{ss}$ (a) and $J_{sd} = J_{ss}$ (b).

For CdTe QD, the shell spacing for hole is around four times smaller than that for the electron. In the case of $\Omega_e/\Omega_h = 4$, the first excited exciton orbital state is of the form (Eq. 2.41):

$$|X_{ES}\rangle|\Uparrow\downarrow\rangle = \left(A_A^{(2)}|A\rangle + A_B^{(2)}|B\rangle + A_H^{(2)}|H\rangle + A_G^{(2)}|G\rangle\right)|\Uparrow\downarrow\rangle, \tag{6.15}$$

where the greatest amplitude is $A_H^{(2)}$, followed by $A_G^{(2)}$, and then by $A_B^{(1)}$. The contribution from the $|A\rangle$ configuration is very small.

The states of the X-Mn complex built out of this bare exciton state $|X_{ES}\rangle$ interact with Mn in a similar way as the states built out of the ground state of the exciton X_{GS}. They experience a uniform splitting $\langle M_z|\langle\downarrow\Uparrow|\langle X_{ES}|H_{h-Mn}|X_{ES}\rangle|\Uparrow\downarrow\rangle|M_z\rangle = \beta M_z$, where the coefficient β is *different* from the coefficient α, describing the splitting of X_{GS}. This leads to a different magnitude of the splitting of the ground and excited states of the X-Mn complex.

The coupling between the ground $|X_{GS}\rangle|\sigma\tau\rangle|M_z\rangle$ and excited state $|X_{ES}\rangle|\sigma\tau\rangle|M_z'\rangle$ of an exciton by the hole-Mn exchange interaction is given by the matrix element: $\langle M_z|\langle\downarrow\Uparrow|\langle X_{GS}|H_{h-Mn}|X_{ES}\rangle|\Uparrow\downarrow\rangle|M_z'\rangle = \kappa M_z\delta_{M_z,M_z'}$, which turns out to be proportional to the projection of the Mn spin M_z, with the proportionality coefficient

$$\kappa = \left(A_A^{(1)}A_A^{(2)} - A_H^{(1)}A_H^{(2)}\right)J_{ss} - \left(A_A^{(1)}(A_H^{(2)} + A_G^{(2)}) - A_H^{(1)}A_A^{(2)}\right)J_{sd}. \tag{6.16}$$

The Hamiltonian matrix is then block-diagonal. For each of the M_z one can write 2×2 matricies:

$$\begin{bmatrix} E_{GS} + \alpha M_z & \kappa M_z \\ \kappa M_z & E_{ES} + \beta M_z \end{bmatrix}. \tag{6.17}$$

From this simple model one can see that the excited state renormalizes the energy of the ground state of the exciton-Mn complex:

$$E_{GS}^{M_z} = E_{GS} + \alpha M_z - \left(\frac{\kappa^2 M_z^2}{(\Delta E + (\beta - \alpha)M_z)}\right), \tag{6.18}$$

where the excited exciton state $|X_{ES}\rangle$ has energy E_{ES}, and $\Delta E = E_{ES} - E_{GS}$ [151].

The spacings between the s-shell energy levels of the X-Mn complex are now renormalized and non-uniform:

$$\begin{aligned}\Delta_{M_z} &= E_{GS}^{M_z+1} - E_{GS}^{M_z} \\ &= \left(\alpha - \frac{\kappa^2}{\Delta E} - \frac{\kappa^2(\beta-\alpha)}{\Delta E^2}\right) - \frac{2\kappa^2}{\Delta E}M_z - \frac{2\kappa^2(\beta-\alpha)}{\Delta E^2}M_z.\end{aligned} \tag{6.19}$$

The renormalization of the s-shell Mn energy levels by the excited exciton state is shown schematically in Fig. 6.9. The ground and excited exciton levels corresponding to the same M_z are coupled by Mn, with the coupling strength proportional to the magnitude of the manganese spin z-projection. The repulsion between the states with a higher $|M_z|$ is stronger, which leads to a greater shift of their energies. This in turn leads to a nonuniform spacing of levels. The differences in the magnitude of this shift are visualized in Fig. 6.9 in the form of different lengths of arrows. The solid (dashed) vertical lines represent the exciton-Mn energy levels with (without) the ground state-excited state coupling.

Usually for a QD with $J_{sd} = -J_{ss}$ the splitting of the p-shell is smaller that the splitting of the s-shell of the X-Mn complex: $\beta - \alpha < 0$. This leads to a competition between the terms in Eq. 6.19. The final result depends on the sign of the following expression:

$$-\frac{2\kappa^2}{\Delta E}M_z - \frac{2\kappa^2(\beta-\alpha)}{\Delta E^2}M_z = -\frac{2\kappa^2}{\Delta E}M_z\left(1 - \frac{|\alpha-\beta|}{\Delta E}\right). \tag{6.20}$$

If the splitting of the s and p-shell structures of the X-Mn complex is similar ($\alpha \approx \beta$), the expression for the emission line spacing Δ_{M_z}, Eq. 6.19, can be simplified [151]:

$$\Delta_{M_z} = E_{GS}^{M_z+1} - E_{GS}^{M_z} = \left(\alpha - \frac{\kappa^2}{\Delta E}\right) - \frac{2\kappa^2}{\Delta E}M_z. \tag{6.21}$$

6.2.2 Results of numerical calculations

Having obtained the eigenenergies and eigenstates of the X-Mn complex, one can calculate the emission and absorption spectra using the Fermi's Golden Rule,

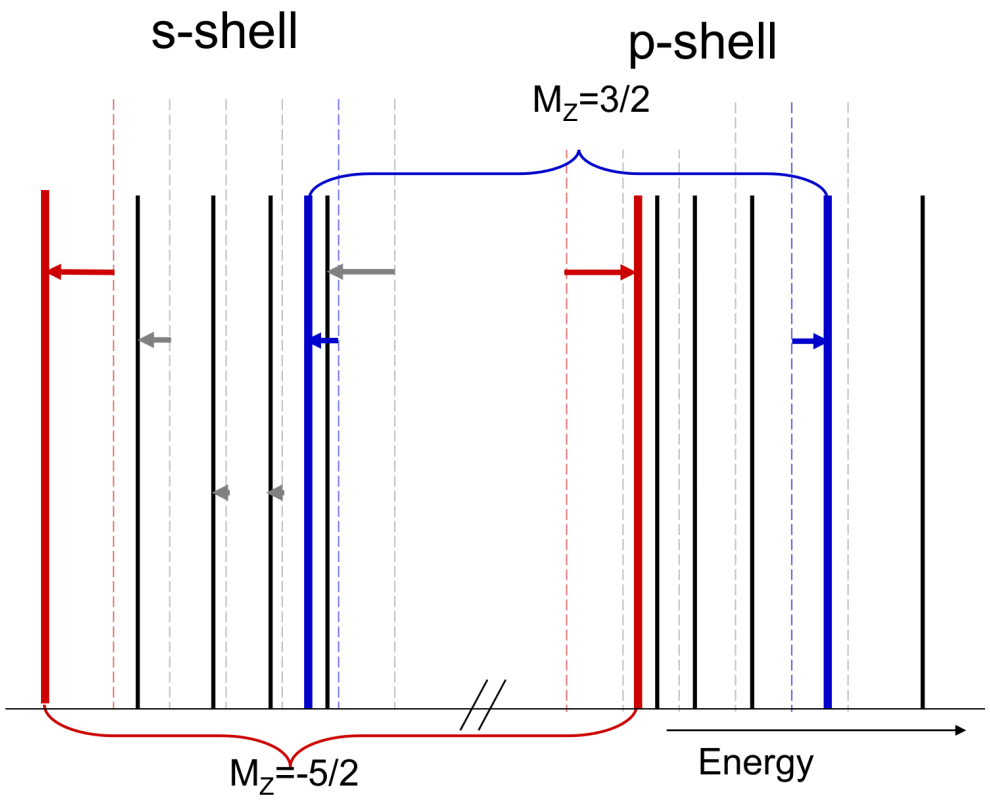

Figure 6.9: Schematic renormalization of ground $|GS\rangle$ and excited $|ES\rangle$ exciton-Mn complex energy levels by the Mn-induced interaction between them. Levels corresponding to the same Mn ion spin projection repel each other, with the strength proportional to M_z, whose magnitude is represented by the horizontal arrows. Dashed-unrenormalized (solid-renormalized) vertical lines represent the energy levels of the X-Mn system in the s-shell (six lines on the left) and the p-shell (six lines on the right) energy region.

Eqs. 5.14 and 5.15. The results of these calculations are shown in Figs. 6.10, 6.11 (emission) and Figs. 6.12, 6.13 (absorption).

The exchange constants of the hole-Mn and electron-Mn interactions used in the calculations are $J_{sd} = -J_{ss}$ (Fig. 6.10) and $J_{sd} = J_{ss}$ (Fig. 6.11). The main difference between the figures is the average splitting between emission lines - the first figure represents the case of the *constructive* quantum interference, where Δ_{M_z} are greater than δ_{Mn} as calculated in the spin model, Eq. 6.6. On the other hand, Fig. 6.11 presents the results with *destructive* quantum interference, where the average emission line spacing is smaller than the one predicted by the spin model. The height of the emission lines corresponds to the emission intensity in the polarization p_x (upper panel - red) or p_y (lower panel - black bars). The emission spectra in Fig. 6.11 have greater linear polarization. This is so because in this case the relative strength of the electron-hole exchange is greater in comparison to the Mn-induced splitting, hence the stronger linear polarization. The fact that the polarization p_x is stronger than the p_y in both Figs. 6.10 and 6.10 is related to the thermal occupation P_i of the X-Mn states $|i\rangle$. States with lower energy have greater population at low temperature. This re-normalizes the emission intensities and leads to stronger emission intensity from these states. At very high temperatures,when all of the X-Mn states are equally populated, the intensities of the lines directly correspond to the oscillator strength of that states.

Finally, Figs. 6.12 and 6.13 show the calculated absorption spectra. In these spectra one can see the s shell, the two excited exciton states associated with $|B\rangle$ and $|H\rangle$ configurations in the energy range of the p shell, and the d shell. The shells are split into a fine structure by the presence of Mn. In the same way as in the emission spectra, the different height of the peaks corresponds to the degree of linear polarization of absorbed photons, with black (red) denoting the p_y (p_x) polarization. In this spectrum one can identify two consequences of the existence of the d shell: the complex emission pattern in the p-shell range of energies, and the QI in the s shell. For the QD with the $J_{sd} = -J_{ss}$ (Fig. 6.12), where the *constructive* interference in the s-shell occurs, the splitting of the p-shell due to the presence of the Mn ion is much *smaller* than for the QD with the $J_{sd} = J_{ss}$ (Fig. 6.13), with the *destructive* interference in the s-shell. This effect can be

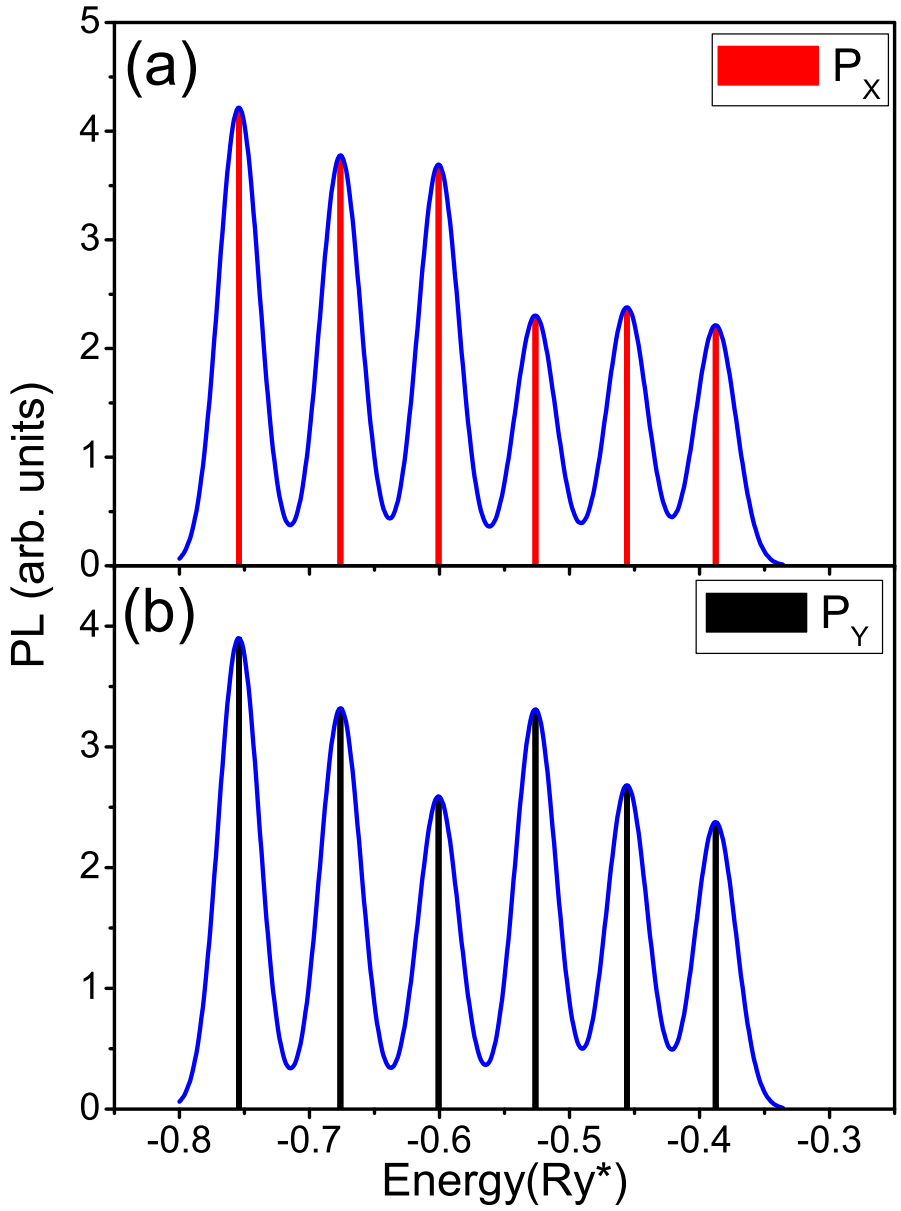

Figure 6.10: Emission spectrum calculated for a CdTe QD, with parameters as specified at the begining of this section, while the exchange constant $J_{sd} = -J_{ss}$. The top panel is calculated with p_x, bottom - with p_y polarization. The calculated emission spectra with gaussian broadening of the emission lines are shown in blue.

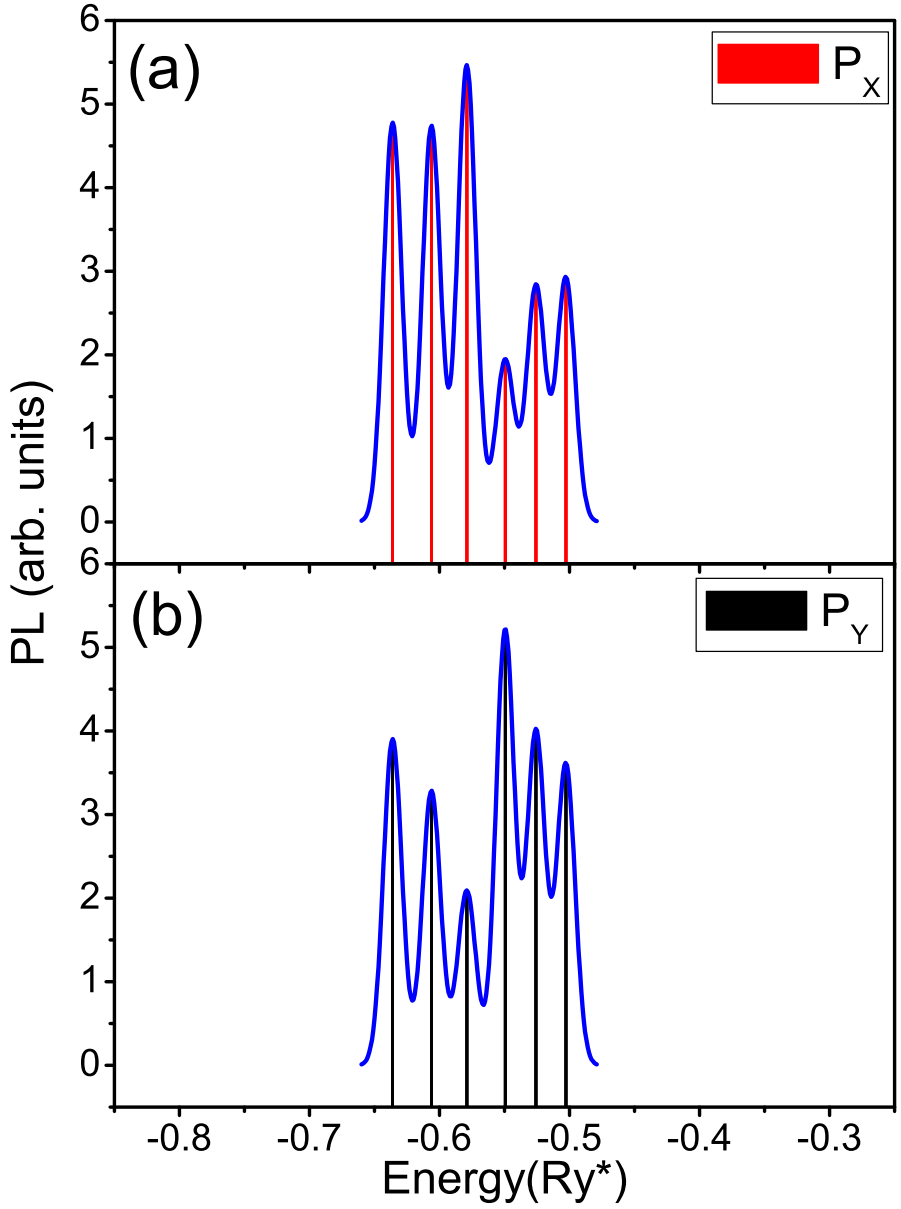

Figure 6.11: Emission spectrum calculated for a CdTe QD, with parameters as specified at the begining of this section, while the exchange constant $J_{sd} = J_{ss}$. The top panel is calculated with p_x, bottom - with p_y polarization. The calculated emission spectra with gaussian broadening of the emission lines are shown in blue.

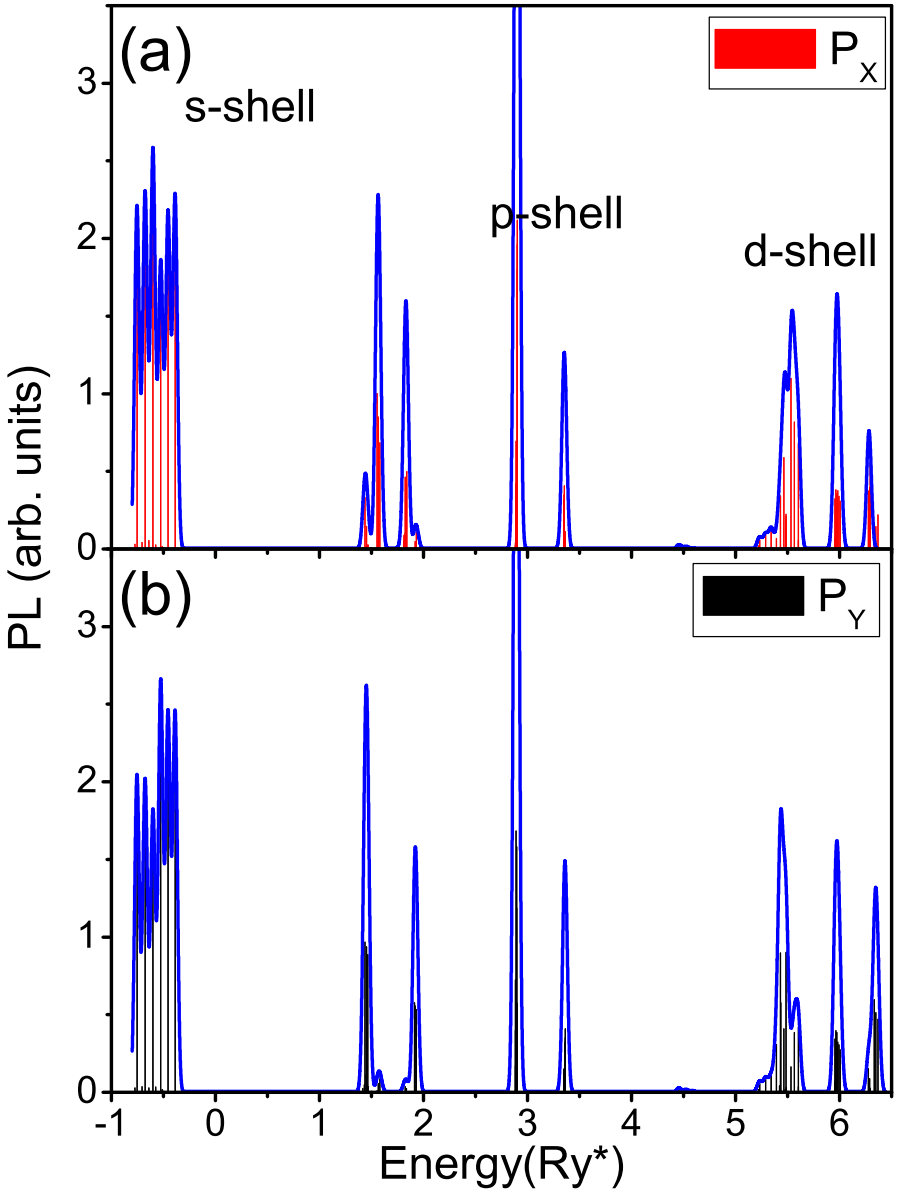

Figure 6.12: Absorption spectrum calculated for a CdTe QD, with parameters as in Fig. 6.10 (top - p_x, bottom - p_y polarization) and $J_{sd} = -J_{ss}$. The calculated absorption spectra with gaussian broadening of the absorption lines are shown in blue.

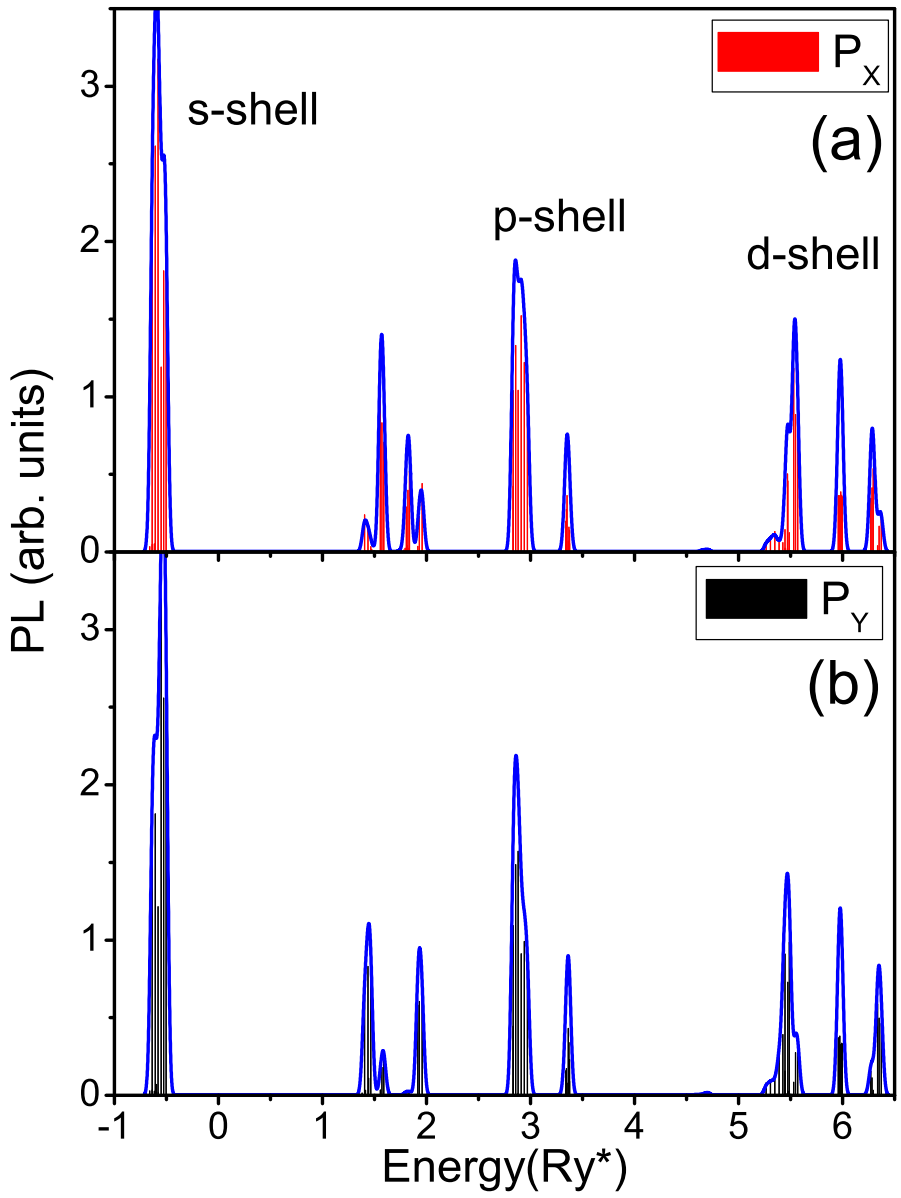

Figure 6.13: Absorption spectrum calculated for a CdTe QD, with parameters as in Fig. 6.11 (top - p_x, bottom - p_y polarization) and $J_{sd} = J_{ss}$. The calculated absorption spectra with gaussian broadening of the absorption lines are shown in blue.

easily understood by studying the form of the ground, Eq. 2.38, and excited wave function of the exciton (Eq. 2.41). The electron-hole exchange splitting of the p-shell is larger than that of the s and d shell. This leads to a much stronger linear polarization of the emission lines in the p-shell. Experiments are on the way to verify the predicted absorption spectra.

Using the notation of the emission line spacings Δ_i defined in Section 6.1 (Fig. 6.5 (a)), one can extract the values for the Δ_i from the X-Mn emission spectra calculated using the correlated model. Figure 6.14 (a) shows the comparison of the average emission line spacing Δ_{aver}, calculated using the correlated model ($J_{sd} = -J_{ss}$) (full bars), and the spin model (empty bars), for a few different heights of the QD $d = 2, 3, 4$, and 6 nm. In the correlated model the constructive quantum interference is visible, leading to the increase of the average splitting Δ_{aver} with respect to the spin model (the full bars are taller than the empty ones). At the same time, the average spacing decreases with the increase of the parameter d in the same way as in the spin model. The dependence of the normalized splittings Δ_i/Δ_{aver} on the QD height d is presented in Fig. 6.14 (a). The thick-solid lines represent the calculations done using the correlated model (SPD), while the black-dotted line shows the result of the analogous calculations using the spin model with $d = 2$ nm (as in Fig. 6.6 (b)). The data calculated using the spin model are shown here for comparison. The slope of the line $\Delta_i/\Delta_{aver}(i)$ calculated in the SPD model, with the $d = 2$ nm (black-solid line), has significanly *increased* compared to the spin model (black-dotted line). The second signature of the QI, namely the increased non-uniformity in the emission lines due to the Mn ion-induced interaction of the ground state with the excited states of an exciton is clearly visible.

As in the spin model, the slope of the $\Delta_i/\Delta_{aver}(i)$ decreases with the increase of the QD height d. This happens because the carrier-Mn exchange constants decrease with increase of the parameter d. In the correlated model this effect leads not only to a suppression of the spin-flip process between the electron and Mn ion, due to the smaller scattering constants, but also to a decreased coupling between the ground and excited exciton state. Together with the decrease of the slope, the electron-hole exchange-induced gap in the middle of the spectra increases, creating a growing "bump" on the $\Delta_i/\Delta_{aver}(i)$ function. The effect of

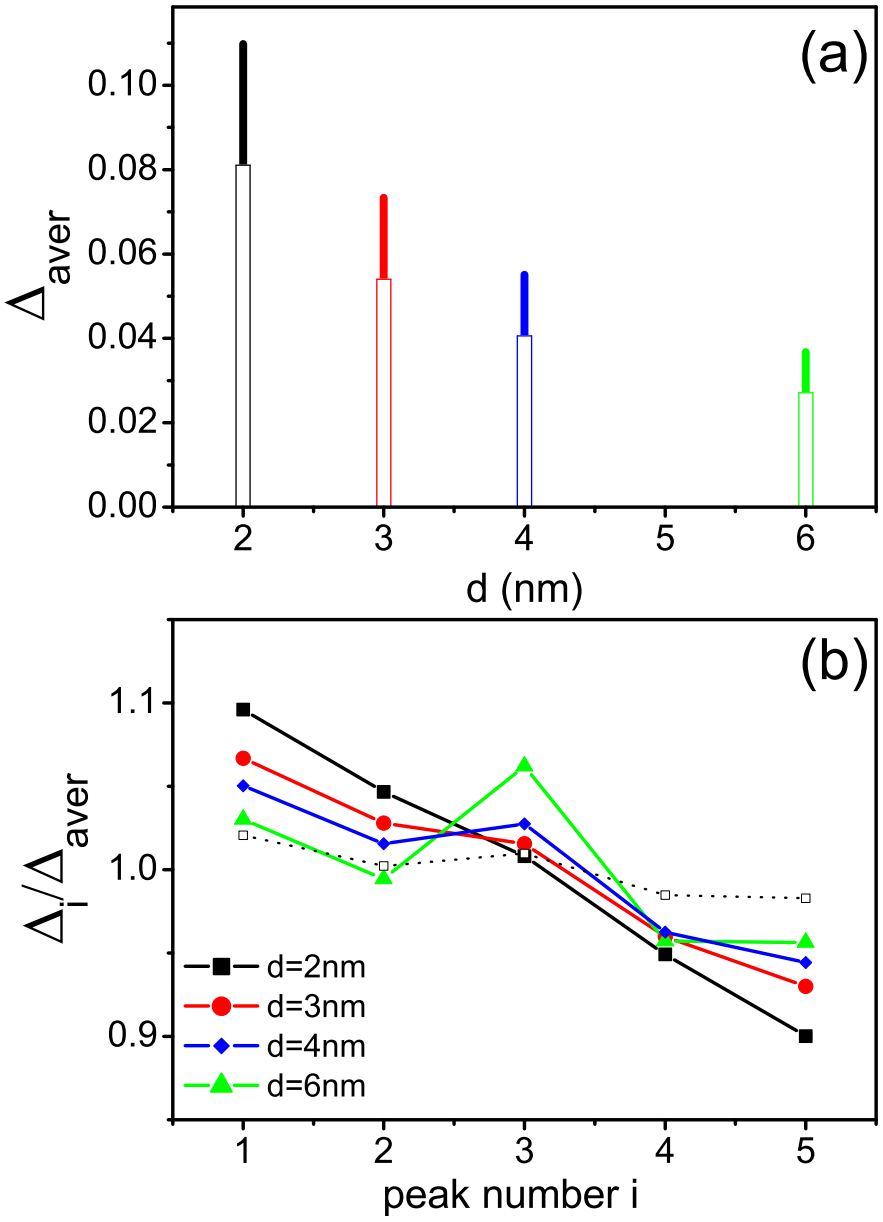

Figure 6.14: (a) The dependence of the average splitting of the spectra (Δ_{aver}) on the height of the QD d, calculated in the correlated (solid bars) and spin (empty bars) model. The parameter d changes the hole-Mn and electron-Mn coupling, and changes the splitting of the spectra. (b) The dependence of the Δ_i/Δ_{aver} on the height of the QD d. The thick solid lines show the data calculated using the correlated model, while the thin dotted lines show calculations in the spin model. Parameters used for calculations were specified at the begining of this section.

the interplay between the Mn and electron-hole exchange-induced splitting has been discussed previously in Section 6.1, which describes the spin model.

In the spin model there is a very strong dependence of the slope of the $\Delta_i/\Delta_{aver}(i)$ on the bright-dark exciton splitting Δ_0 (Fig. 6.7 (a)), since the non-uniformity in the distribution of lines in this model is caused by the spin-flip process between the electron and Mn. This proces couples the bright and dark exciton states, and is very sensitive to the energy difference between them, mainly Δ_0. In the correlated model this dependence is much weaker, as presented in Fig. 6.15 (b). The thick-solid lines correspond to the data obtained in the correlated model, with the different brigth-dark exciton splittings $\Delta_0 = 0, 0.25, 0.506$ (bulk) and 2 meV. The different Δ_0 splittings were obtained by varying the short-range exchange parameter E_{SR}. For comparison, the spin model calculations for the $\Delta_0 = 0$ and 0.506 meV, and $d = 2.2$ nm, are shown in Fig. 6.15 (b) (thin-dotted lines). The height of the QD has been changed with respect to the correlated model to compare the splittings Δ_i/Δ_{aver} of the emission spectra with same average spacing. Figure 6.15 (a) shows the comparison of the Δ_{aver} spacing in the correlated (solid bars) and spin (empty bars) models as a function of Δ_0. The Δ_{aver} does not depend on the bright-dark exciton splitting.

The comparison of the Δ_{aver} between the correlated (solid bars) and spin (empty bars) models, calculated for a few values of the bright exciton splittings Δ_2 is shown in Fig. 6.16 (a). As in the previous case, the average splitting of the X-Mn emission lines Δ_{aver} does not depend on the bright exciton splitting Δ_2. The different values of the Δ_2 were obtained by changing the strength of the long-range electron-hole exchange μ^2, leaving the dark-bright exciton splitting unchanged ($\Delta_0 = 0.506$ meV) to limit the number of varying parameters. Since both long- and short-range exchange interactions contribute to the dark-bright exciton splitting, the value of the short-range exchange parameter E_{SR} had to be adjusted accordingly.

Figure 6.16 (b) shows how the $\Delta_i/\Delta_{aver}(i)$ depends on the bright exciton splitting Δ_2. The slopes of the curves do not change, however the electron-hole exchange induced gap in the middle of the spectra becomes more pronounced with the increase of the parameter Δ_2. This behaviour is very similar to the dependence observed in Fig. 6.7 (b) for the spin model.

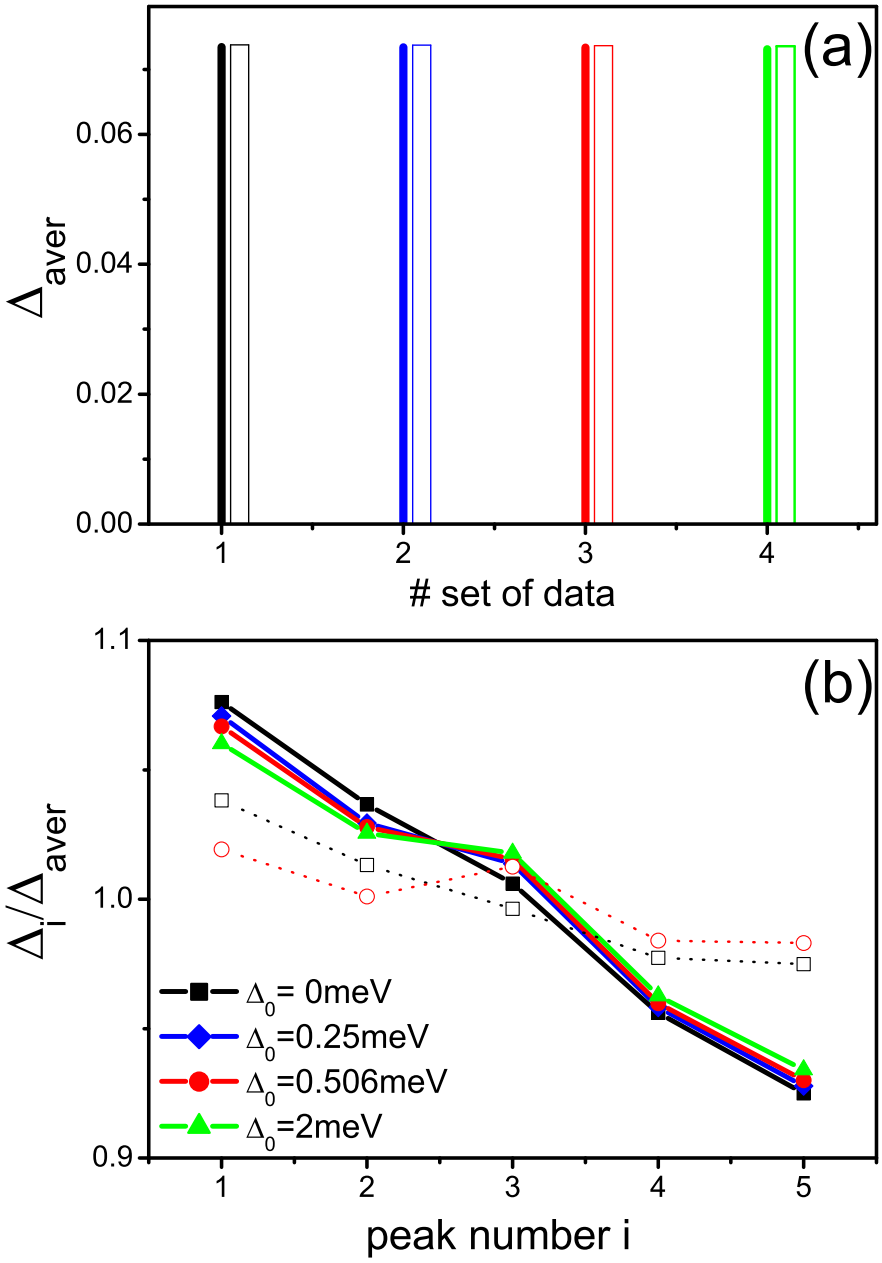

Figure 6.15: (a) The dependence of the average splitting of the spectra (Δ_{aver}) calculated using the correlated (solid bars) and spin (empty bars) model on the bright - dark exciton splitting Δ_0. To obtain the same average splitting for both model, the spin model was calculated for a dot with the $d = 2.2$ nm height, while the correlated model with $d = 3$ nm. (b) The dependence of the Δ_i/Δ_{aver} on the Δ_0 splitting. The thick-solid lines show the data calculated using the correlated model, while the thin-dotted lines show calculations in the spin model. Other parameters used here were specified at the begining of this section.

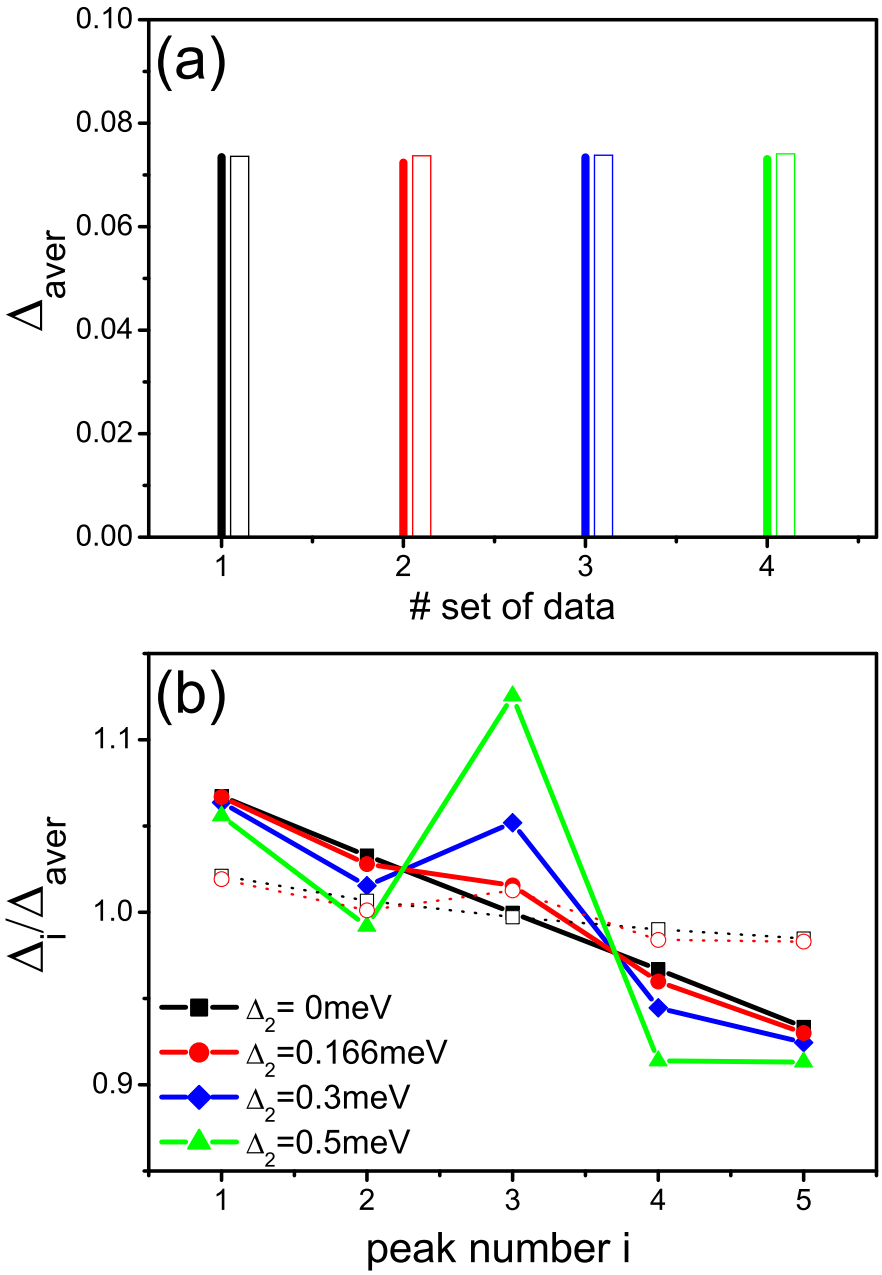

Figure 6.16: (a) The dependence of the average splitting of the spectra (Δ_{aver}) calculated using the correlated (solid bars) and spin (empty bars) model on the bright exciton splitting Δ_2. The spin model was applied to a dot with the $d = 2.2$ nm height, while the correlated model to a dot with $d = 3$ nm. (b) The dependence of the Δ_i/Δ_{aver} on the Δ_2 splitting. The thick-solid lines show the data calculated using the correlated model, while the thin-dotted lines show calculation in the spin model. Other parameters used here were specified at the begining of this section.

6.2.3 Comparison of the model calculations to the experimental emission spectra

The experimental emission spectra of the quantum dots were obtained by Kossacki *at. al* for CdTe-based heterostructures grown using molecular beam epitaxy [151, 172]. The process of the fabrication quantum dot samples has been described in Chapter 4. For the measurements, the sample was placed in a microphotoluminescence setup composed of piezo-electric $x-y-z$ stages, and a microscope objective. The system was kept at the temperature of 4.2K in a helium exchange gas. The PL of the QDs was excited either above the gap of the ZnTe barrier (at 532 nm) or using a tunable dye laser in the range $570-610$ nm. Both the exciting and the collected light were transmitted through a monomode fiber coupled directly to the microscope objective. The overall spatial resolution of the set-up was better then 1 μm which assured possibility to select different single quantum dots containing a single Mn ion. The dots without Mn ion were observed in the same samples. The PL analysis was done for the dots having emission lines in the low energy tail of the broad PL emission band [24, 172] which assured good separation from the lines related to the other dots. The characteristic PL spectra contain a neutral exciton line split into sextuplets. Lower in energy, the lines related to charged excitons (X^+ and X^-) and biexciton were observed. Higher in energy, the emission from higher shells (s, p, $d\ldots$) appear with an increasing excitation power, as is shown in Fig. 2.9 (b). From many quantum dots, those with emission spectra with six emission lines, i.e., Mn in the center of a dot [155], were selected.

Figure 6.17 (a) presents the measured and calculated s-shell emission spectrum at temperature T=75K. The QD parameters used in this calculations are the same as defined in the Chapter 3, Section 3.3, while the coupling constants between carriers and Mn ion in the bulk material were defined in Section 6.2. This calculation was done for the case when $J_{sd} = -J_{ss}$, when the constructive interference takes place. To compare this calculation to the experimental data height of the QD was taken as $d = 6.9$ nm.

The predicted peak spacing $\Delta_{i(M_z)}$, $i = 1-5$ calculated using the Eq. 6.21 and normalized by the the average line spacing Δ_{aver}, is plotted in Fig. 6.17 (b) in

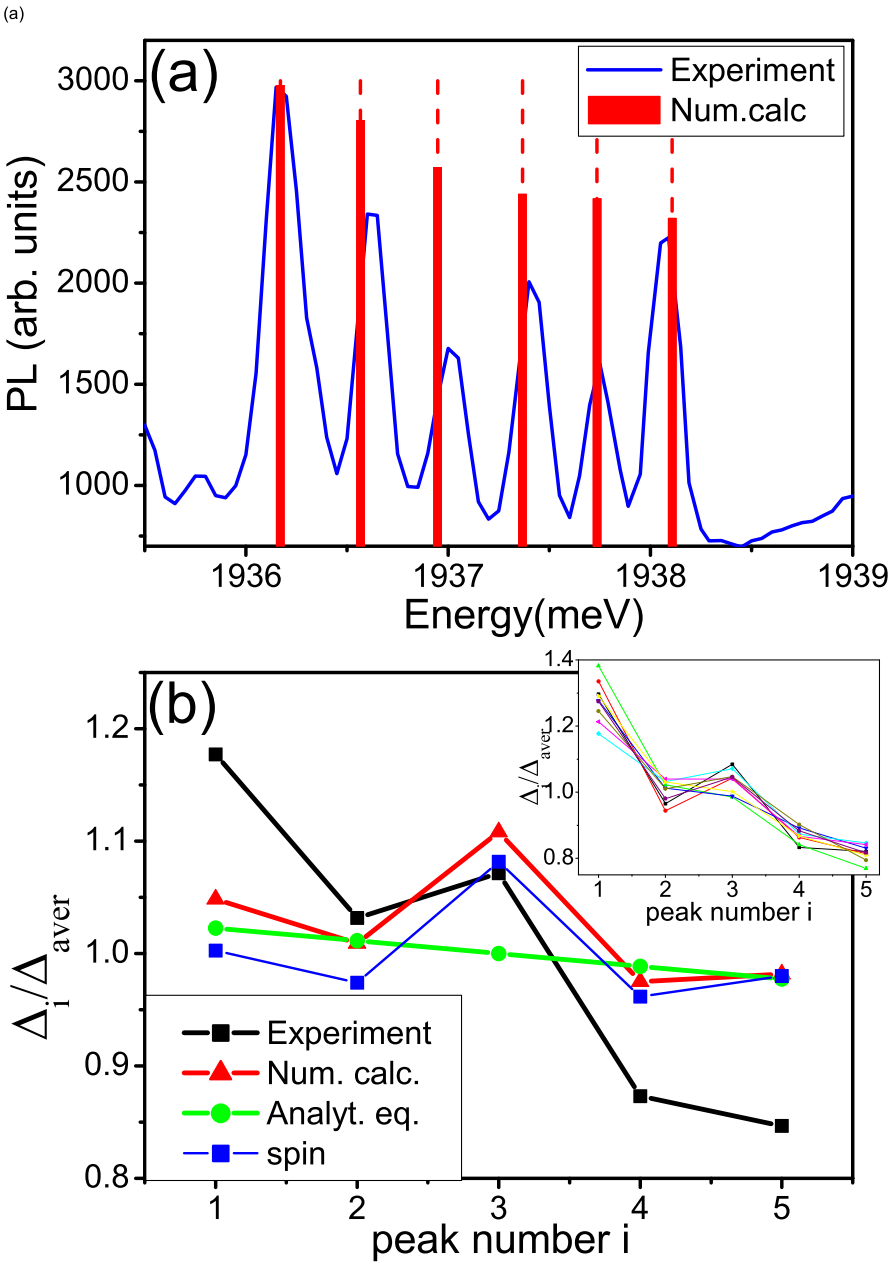

Figure 6.17: (a) Measured and calculated s-shell emission spectrum at temperature $T = 75$ K with $J_{sd} = -J_{ss}$. Parameters used in the calculation are explained in the text. (b) Comparison of the measured (black) and calculated (red) peak separation $\Delta_{i(M_z)}/\Delta_{aver}$ (Δ_{aver} being the average distance) as a function of the peak separation number i. The inset shows measured Δ_i/Δ_{aver} for ten QDs from the same wafer. The green line shows $\Delta_{i(M_z)}/\Delta_{aver}$ calculated analytically (neglects anisotropy and electron-hole exchange interaction).

green. It decreases linearly with increasing i or M_z. This decrease is reproduced by numerical calculations (red line) and the $\Delta_{i(M_z)}/\Delta_{aver}$ extracted from the experimental data (black line). Deviations from linear dependence of Δ_i are due to the electron-hole exchange interaction and anisotropy. The inset of Fig. 6.17 (b) confirms the characteristic pattern of spacings between the X-Mn emission peaks for ten different quantum dot samples.

Figure 6.18 (a) shows the same measured emission spectrum from the s-shell of the X-Mn complex as in Fig. 6.17 (a). The calculated emission spectra, however, are obtained by using the scattering constant $J_{sd} = J_{ss}$, while the other parameters are the same as used in the calculations shown in Fig. 6.17. Since in the case $J_{sd} = J_{ss}$ the destructive interference occurs, the height of the QD has been adjusted to $d = 2.56$ nm to increase Δ_{aver}. The spectrum is calculated at temperature T=75K.

Analogously to the figure 6.17 (b), Fig. 6.18 (b) shows the predicted peak spacing $\Delta_{i(M_z)}/\Delta_{aver}$ calculated using the Eq. 6.21 (green), extracted from the experiment (black), and computed numerically (red). The slopes of the calculated peak spacings are much greater for this data set. The reason for this is that the coupling between the ground and excited states, given by the parameter κ, Eq. 6.16, is significantly greater compared to the calculations with $J_{sd} = -J_{ss}$. At the same time, the average splitting of lines Δ_{aver}, defined mostly by the splitting of the ground state α, is unchanged. The average splitting is kept the same (controled by the parameter d) to compare the results with the experiment.

However, for the same height of the QD d, the parameter κ is greater when $J_{sd} = -J_{ss}$. After re-scaling of the carrier-Mn exchange constants by the parameter d to fit the experimental data, the coupling of the ground state with the excited state significantly decreases, leading to the smaller slope of the Δ_i/Δ_{aver}.

In summary, in the microscopic description of the exciton-Mn interaction, which includes correlations in the electron-valence hole complex, the short range exchange of Mn ion with the hole and the electron, the long- and short-range electron-hole exchange and the quantum dot anisotropy has been presented. A new quantum interference (QI) effect between the electron-hole Coulomb scattering and the scattering by Mn ion has been predicted and observed in the emission spectra as the increase of emission peak spacing with increasing state of

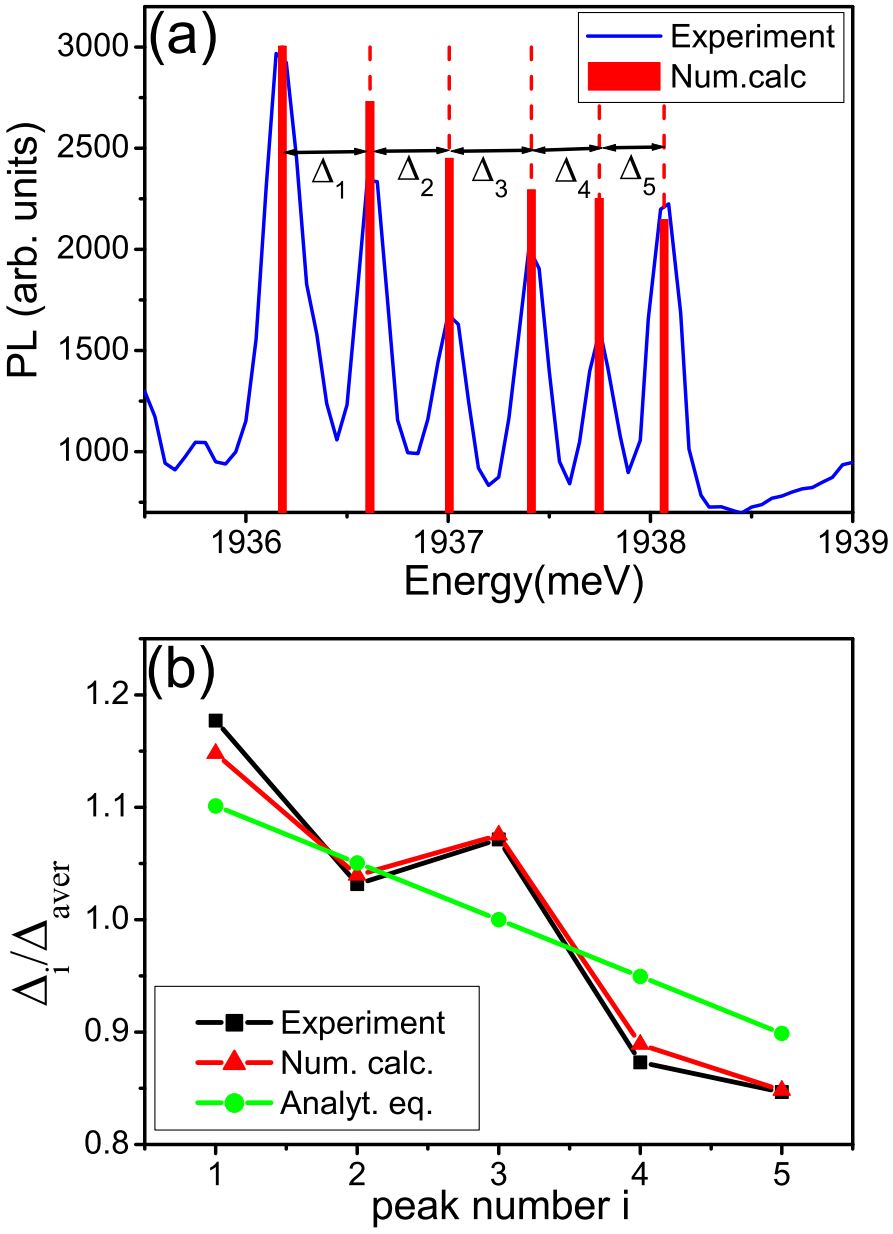

Figure 6.18: (a) Measured and calculated s-shell emission spectrum at temperature $T = 75$ K with $J_{sd} = J_{ss}$. Parameters used in the calculation are explained in the text. (b) Comparison of the measured (black) and calculated (red) peak separation $\Delta_{i(M_z)}/\Delta_{aver}$ as a function of the peak separation number i. The green line shows $\Delta_{i(M_z)}/\Delta_{aver}$ calculated analytically (neglects anisotropy and electron-hole exchange interaction).

the Mn ion. This opens the possibility of engineering exciton-Mn spin interaction in quantum dots via quantum interference for quantum memory and information processing applications.

Chapter 7

Exciton-Mn complex in a magnetic field

By applying a strong magnetic field one modifies the electron and hole energy levels and wave functions. By increasingly localizing the electron and hole wave function in the quantum dot, one expects to increase the strength of electron(hole)-Mn exchange interaction, and hence significantly modify the optical properties of semi-magnetic quantum dots. However, recent experiments [22, 155, 165] indicate that the emission properties do not change significantly with the magnetic field and can be described by a magnetic field-independent spin model, where the exchange constants between the carriers and Mn ion are parameterized at $B = 0$, from fitting the experimental data. The exchange constants do not change with the magnetic field, and the only dependence on the magnetic field is the Zeeman energy.

Here, the microscopic model of the exciton-Mn system presented previously in Chapter 6 and in Refs. [151] is extended to high magnetic fields, Ref.[167]. The impact of the magnetic field on the absorption and emission spectra of a model quantum dot with different shell structures is analyzed [167]. This allows to predict the signature of a Mn ion in the absorption spectra corresponding to excited quantum dot shells, as well as to compare the emission spectra from a correlated X-Mn complex with a spin model. In Chapter 6 it was shown that the experimental data [151] indicate that in CdTe quantum dots there are at least three confined electronic shells s, p, and d, and that the presence of these

shells leads to qualitatively different effects, such as the quantum interference in the electronic structure of the X-Mn complex at $B = 0$. Hence all calculations were performed for CdTe quantum dots with s; s, p, and s, p, d shells. The QD parameters used in the calculations presented in this chapter are the same as in Chapters 3 and 6, and are described in the details in Section 3.3 [14, 150–152]. The electron-Mn and hole-Mn bulk coupling constants are $J_{sd} = -J_{ss}$, while the height of the QD is assumed to be $d = 3$ nm, with the Manganese impurity in the center ($R = 0$). In Ref. [167] the scattering constants $J_{sd} = J_{ss}$ were used, while the height of the QD was $d = 2.56$ nm. The Lande factors are: g_e = -0.7, g_h = 0.38, g_{Mn}=2, for the electron, the hole, and the Mn respectively. The electron-hole exchange is calculated using the full microscopic model (Chapter 3) with bulk paramters μ^2 and E_{SR} as in Chapter 6. The bright-dark exciton splitting in $B = 0$, calculated for the non-magnetic QD with the same parameters, is $\Delta_0 = 0.506$ meV, while the bright exciton splitting $\Delta_1 = 0.166$ meV. The dark exciton splitting is $\Delta_2 = 0$ meV.

Figure 7.1 shows the results of calculated absorption spectra in the (a) correlated exciton-Mn model with SPD shells, and (b) the spin model. The red (blue) lines correspond to the absorption of the σ_- (σ_+) photons.

From Fig. 7.1 (a) one can see that the absorption consists of three groups of lines corresponding to the absorption into the s shell, p shell and d shell. The p-shell absorption consists of lower-energy transitions involving SD configurations ($|H\rangle$ Jacobi coordinate), activated by Coulomb interactions [103, 151], and higher-energy PP states ($|B\rangle$ Jacobi coordinate)(Chapter 2). The SD transitions correspond to zero angular momentum states and evolve in B in parallel with the emission from the s-shell states. The PP transitions are split by Coulomb interactions and anisotropy, with the upper branch crossing the transitions associated with the d-shell. All excitonic transistions are "dressed" by the electron, hole, and Mn spin states. By contrast, the absorption in the spin model covers only the s shell. The number of absorption lines in this energy range is equal to the number of absorption lines in the correlated exciton model, however the spin model predicts only a linear magnetic-field dependence through the Zeeman

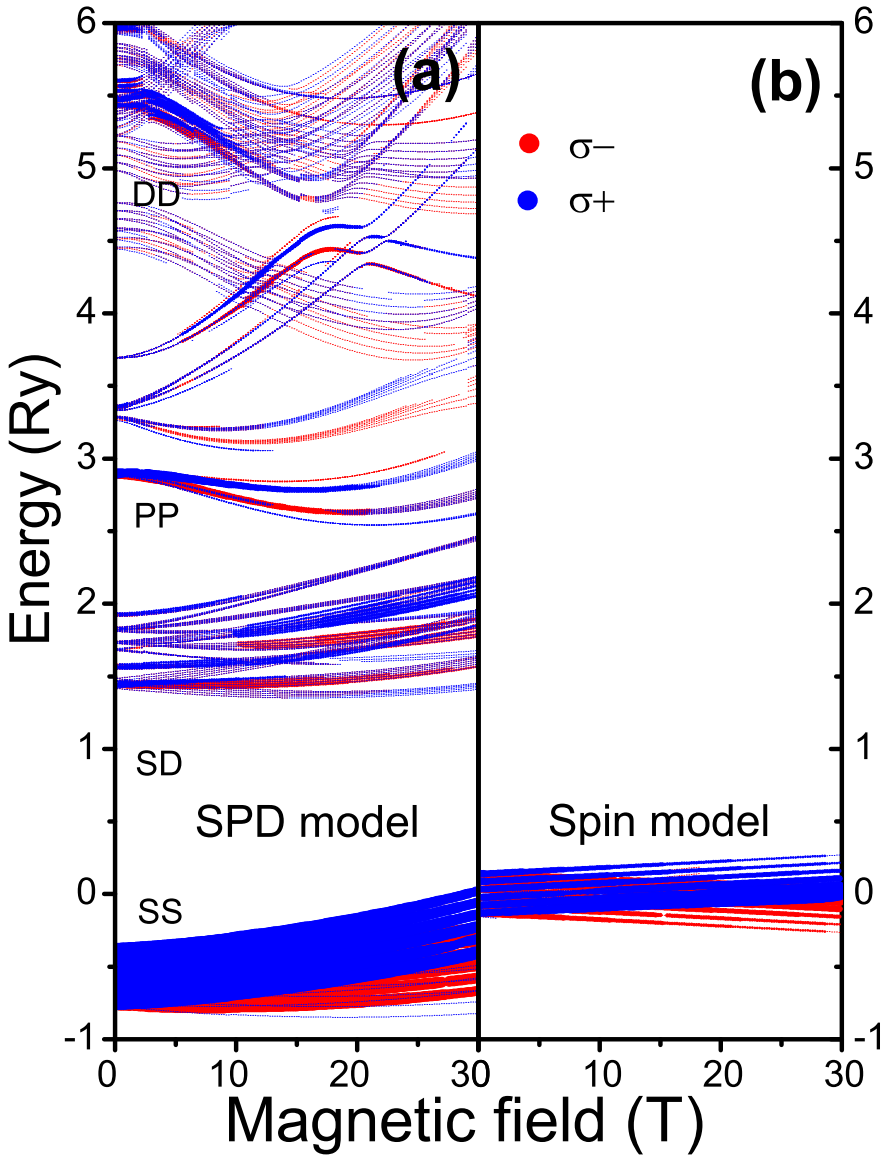

Figure 7.1: Magnetic-field evolution of the absorption spectra calculated in the spin model (a) and correlated exciton model (b) which includes s, p and d single-particle shells and a small anisotropy of the QD confining potential ($\gamma = 0.33$). Parameters used in the calculation are given at the begining of this section. Calculations correspond to the temperature of the sample of 75 K. Thickness of the lines represents the heights of the absorption peaks at a given energy.

coupling. Hence, the correlated exciton model is necessary for the description of the higher-energy part of the absorption spectra.

Since the easiest experimentally accesible optical information about the QD is its emission spectra, the main focus of this chapter will be on the discussion of the emission spectra from the s shell of the X-Mn complex [167]. Figure 7.2 compares the magnetic field evolution of the emission spectra for the two circular polarizations, calculated using different approximations. Panels show the calculated emission spectra in increasing degree of accuracy: (a) the spin model, (b) the s-shell model, with electron-hole configurations restricted to the s-shell but with a microscopic form of exciton-Mn interaction, (c) the SPD-correlated exciton model, with $|A\rangle$, $|B\rangle$ and $|H\rangle$ Jacobi configurations as described in Chapter 2, but with Mn not allowed to mix different electronic configurations ($i = j$ in the H_{e-Mn} and H_{h-Mn} part of the Hamiltonian, Eqs. 4.7 and 4.8), and (d) the SPD-correlated exciton model including scattering by Mn as a spin-dependent impurity.

The emission spectra are different for the two polarizations and vary depending on different models used. In the s shell of the X-Mn complex there are $N_c = 24$ low-energy configurations. In the spectra predicted by each model there are, however, only six dominant emission lines for each polarization. At model-specific characteristic values of the magnetic field, more features are visible due to anticrossings of emission lines.

In the spin model, the only magnetic-field dependence of emission of photon energy is linear through the Zeeman terms. The current emission experiments combine the spin model spectra as shown here with a diamagnetic term added *ad-hoc* in order to fit the experimental spectra [155, 165]. In the s-shell model, the magnetic field dependence enters through the electron and hole s-shell energy levels, their Coulomb attraction, and through the magnetic field dependence of the e-Mn and h-Mn exchange coupling constants $J^{e(h)}_{00,00}(R)$. The exchange coupling of the hole in the s shell with the Mn ion in the center [152] $J^{h}_{00,00}(0) = J^{h}_{2D}\frac{1}{2\pi}\frac{1}{l_h^{e\,2}}$ is inversely proportional to the area of the quantum dot, with explicit dependence

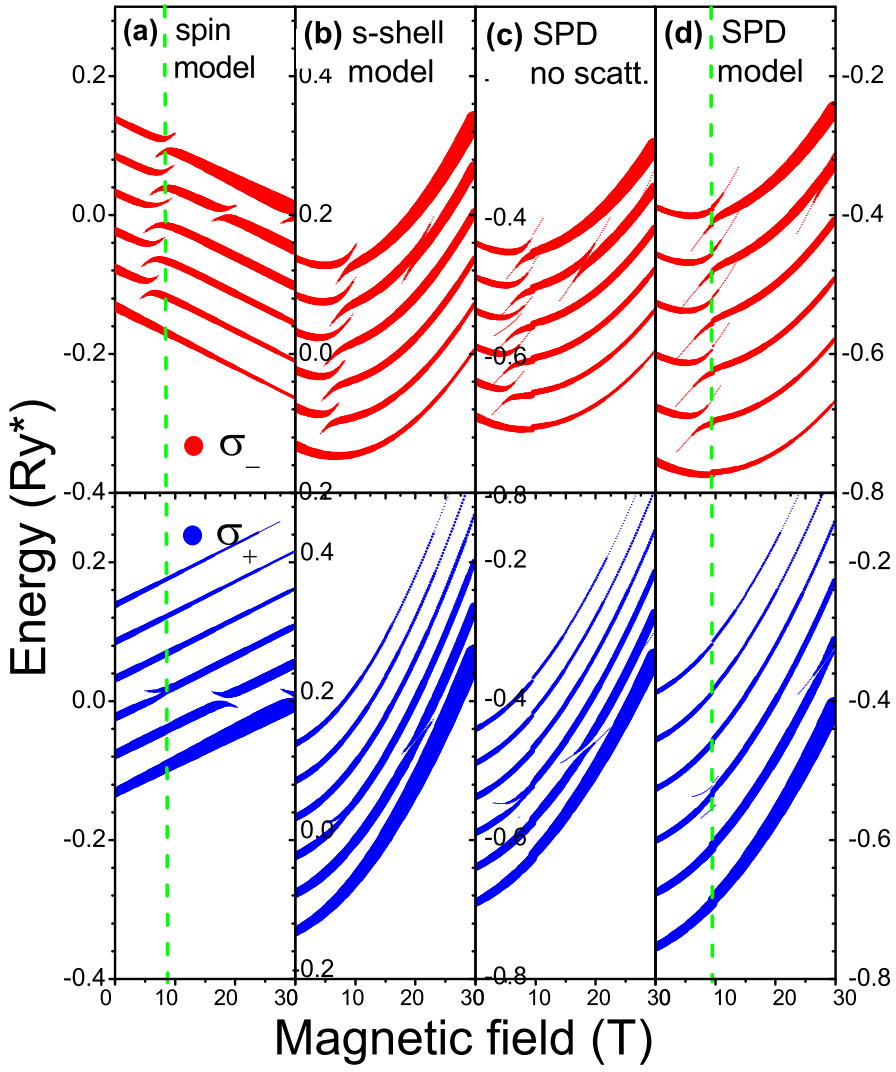

Figure 7.2: Magnetic-field evolution of the emission spectra calculated using different models: (a) spin model, (b) s-shell model, (c) SPD-correlated exciton model neglecting the scattering by Mn, and (d) full SPD correlated exciton model. Parameters of all the QDs are the same as for Fig. 7.1. The thicknes of the lines represents the heights of the emission peaks at a given energy.

on the magnetic field given by:

$$J^h_{00,00}(0) = J^h_{2D}\frac{1}{2\pi}\sqrt{\Omega_0^{e2} + \frac{1}{4}\Omega_c^{e2}}. \tag{7.1}$$

$J^{e(h)}_{00,00}$ increases with the magnetic field due to squeezing of the wave function toward the center of the QD. The rate of change with the magnetic field depends on the ratio of the hole cyclotron energy to the energy spacing of hole electronic shells.

Figure 7.2 (c) shows the calculated excitonic emission spectrum with the correlated exciton state built out of the s, p, and d shells. The interaction of the exciton with the Mn ion does not allow for the scattering by Mn impurity. The final result is a slight decrease of the splitting of the emission lines in zero magnetic field due to a decreased occupation of the lowest-energy s-shell configuration in the exciton wave function, and an increased population of p-shell orbitals which do not couple to Mn. This leads to a decrease of the $J^{h,eff}_{GS}$, Eq. 5.11, and hence the effective magnetic field produced by the spin of the valence hole. However, the inclusion of scattering by Mn, described previously in the Chapter 6 and Ref. [151], leads to the quantum interference (QI) effect. As calculated here, QI results in a significant increase of the splitting of the emission lines ($J_{sd} = -J_{ss}$) as a function of the magnetic field, as shown in Fig. 7.2 (d). The article [151] shows the results for $J_{sd} = J_{ss}$, with a decrease in the splitting of the emission lines due to the QI. As shown in Ref. [151], together with the decrease of the effective field produced by the hole, the electron-hole exchange becomes more visible in the emission spectra, since its strength becomes comparable to the exciton-Mn exchange coupling ($\Delta_1 = 0.16$ meV vs. an average splitting of emission lines in the SPD model of $\frac{1}{2}\left(J^e_{GS}(0) + 3J^h_{GS}(0)\right) = 0.38$ meV at zero magnetic field). In the calculations with $J_{sd} = -J_{ss}$ one observes opposite tendency. The electron-hole exchange becomes less visible due to the constructive QI and spectrum is dominated by the Mn induced splitting.

Details of the $\sigma+$ emission spectra in the spin model and in the correlated exciton model for two selected values of B, $B = 0$, and $B = 8.8$ T, are shown in Fig. 7.3. The magnetic field $B = 8.8$ T was chosen, because for this magnetic field most of the anticrossings take place in the emission spectra shown in Fig. 7.2 (d).

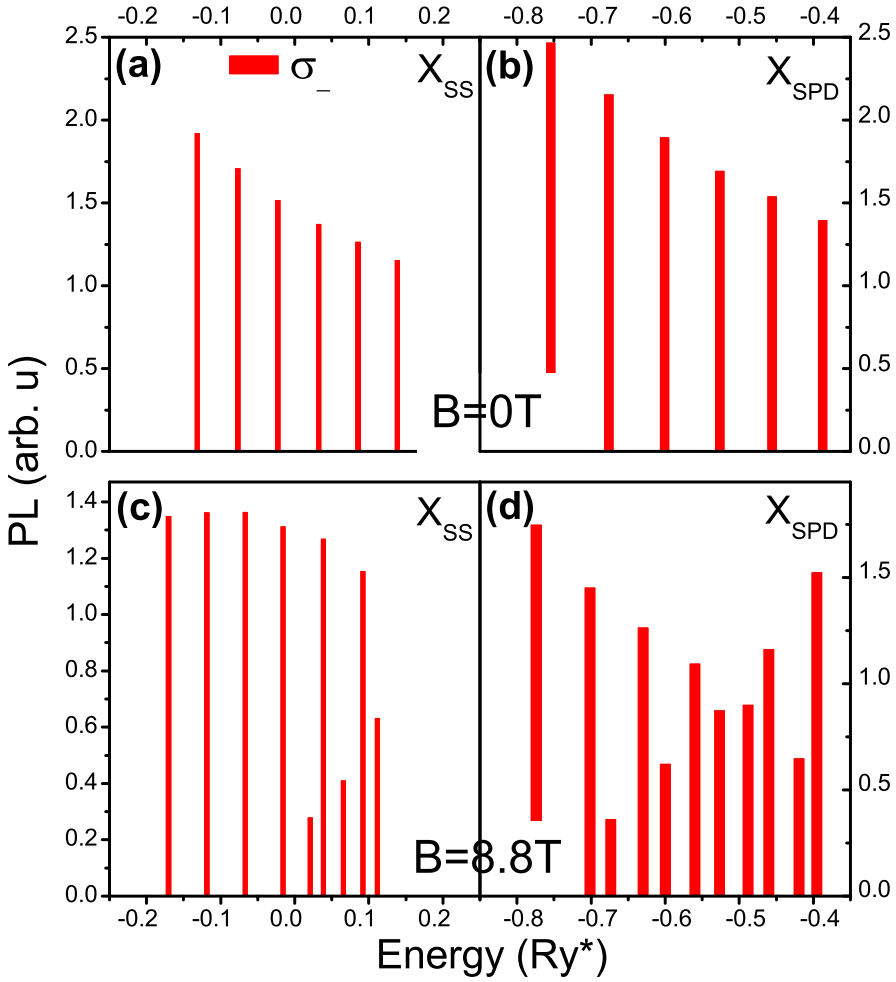

Figure 7.3: Comparison between calculated emission spectra in the spin (left) and correlated exciton model (right) for zero magnetic field (upper panel) and magnetic field $B = 8.8$ T (lower panel) with the parameters explained at the begining of this chapter. Both models predict a splitting of excitonic emission line into six X-Mn emission lines due to the interaction of the exciton with Mn, however the quantitative splitting between lines is much different in these models. In SPD model at $B = 8.8$ T there are more emission lines, since this is the magnetic field for which most of the anticrossings take place in this model.

The predicted lineshape of the correlated exciton emission spectrum at $B = 0$ is similar to the spin model spectrum. The main difference is that the spacing of emission peaks is greater than the spacing in the spin model. However, the correlated exciton spectrum at $B = 8.8$ T is different compared to the spin model. This is because the anticrossings of emission lines in the correlated model take place at a higher magnetic field, which is visible in Fig. 7.3, since the correlated exciton model leads to a greater exchange coupling with Mn. The central crossing (subspace $M_z+S_z = 0$) takes place at $B = 8.6$ T (in the Ref. [167] with $J_{sd} = -J_{ss}$ and $d = 2.56$ nm, $B = 5.25$ T) for the SPD correlated model, instead of $B = 6.6$ T ($B = 7.6$ T) in the spin model. The magnitudes of the magnetic fields at which the crossings occur are a sensitive measure of the approximate model used.

Figure 7.4 identifies different emission peaks in the σ_- polarization (upper panel) and compares the σ_- emission spectrum with the calculated σ_+ emission spectrum (lower panel) for the magnetic field $B = 8.8$ T. The σ_- polarization spectrum has a very rich structure at this magnetic field. Peaks are labeled according to the final-state Mn spin projection M_z. Since all of the anticrossings appear for that field, all of the peaks split into two, except the first peak with $M_z = 5/2$. This peak comes from the subspace with $M_z + S_z = 3$ which doesn't couple to any state through the spin-flip part of H_{e-Mn} Hamiltonian.

The σ_+ emission spectrum is much simpler due to the lack of the anticrossings between emission lines. This spectrum is also qualitatively similar to the emission spectra in the absence of the magnetic field for both polarizations with the only difference being the splitting of the $M_z = -1/2$ emission line. The state with the final $M_z = -1/2$ appears three times in the σ_+ polarization spectrum. The reason for that is the electron-hole exchange mixing between this state, $|\Uparrow\downarrow, M_z = -1/2\rangle$, visible in σ_- polarization, and state $|\Downarrow\uparrow, M_z = -1/2\rangle$ visible in σ_+ polarization. As a result both states are visible in both polarizations - the two lines with the lower intensity have the same energy as the two lines in the σ_- polarization spectrum with the $M_z = -1/2$.

The important aspect of this calculation is the discussion of the magnetic field evolution of the spacing of the peaks in the emission spectra shown in Fig. 7.2. The focus here will be on the discussion of the average splitting of emission lines in σ_+ and σ_- polarizations. The spin model assumes that the electron-Mn,

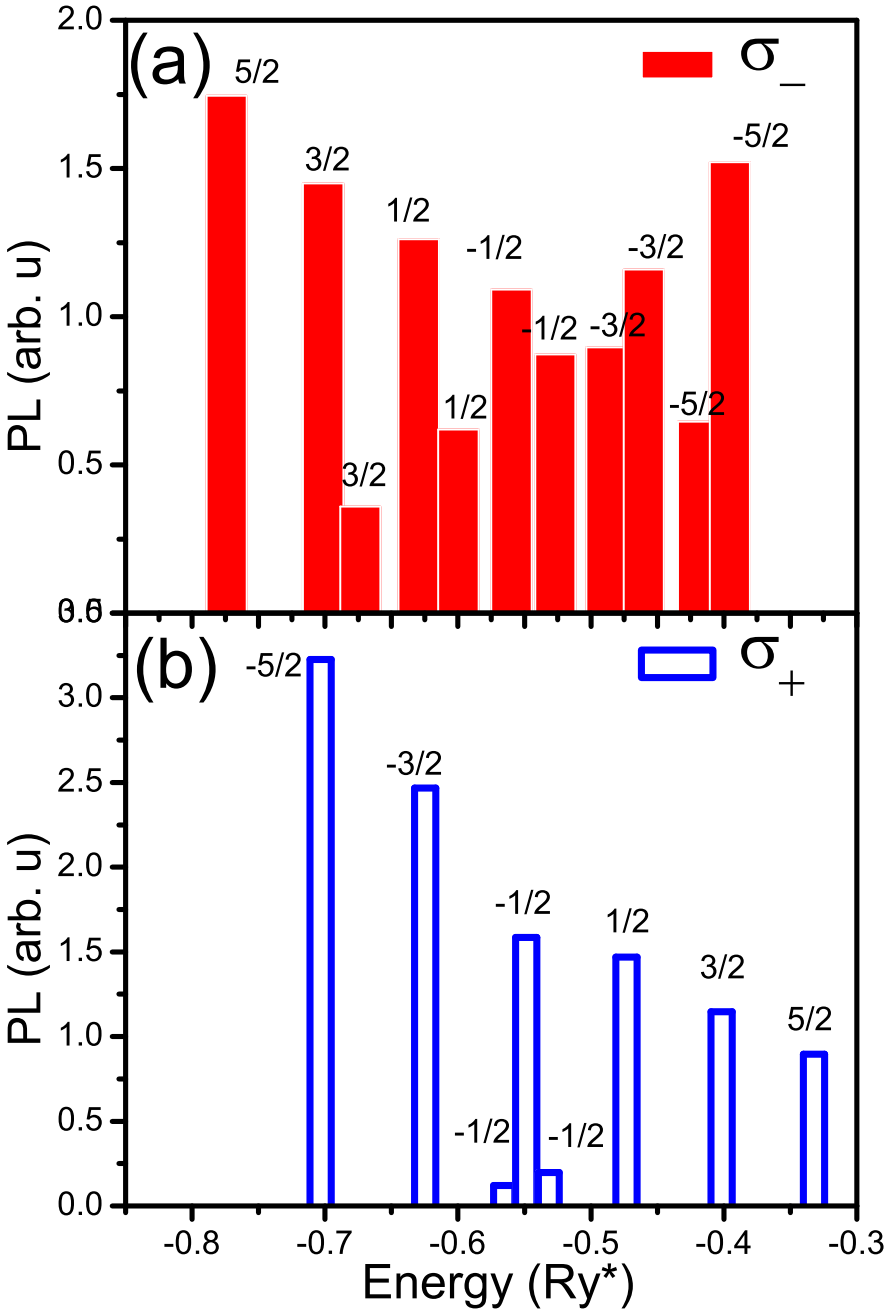

Figure 7.4: Comparison between calculated emission spectra in the correlated exciton model in σ_- (upper panel) and σ_+ (lower panel) polarization for a small magnetic field $B = 8.8$ T with the same parameters as for Figs. 7.1, 7.3.

hole-Mn and electron-hole exchange constants do not change with the magnetic field. Since in the emission process the initial and final states correspond to the same M_z state of the Mn ion, the Zeeman energy cancels out, and the spacing of the emission peaks shown in black in Fig. 7.5 , does not change with the magnetic field. However, as discussed earlier, the hole-Mn exchange coupling $J^h_{00,00}(0)$ (Eq. 7.1) increases with the magnetic field. The splitting of the emission lines is directly proportional to the hole-Mn exchange coupling. Figure 7.5 shows the magnetic-field dependence of the splitting of the emission lines, based on the analytical expression for $J^h_{00,00}(0)(B)$, and on a numerical calculation of the spacing of the emission peaks in the s-shell model (green dotted line and green empty dots respectively).

When one allows for the scattering of the electron and hole to s, p, and d shells by the Coulomb interaction, the ground state of the exciton in a magnetic field becomes a linear combination of the electron-hole configurations as described in Chapter 2 (Eq. 2.38) and Ref. [151]:

$$|X_{GS}\rangle|\Uparrow\downarrow\rangle = \left(|A^{(1)}_A||A\rangle + |A^{(1)}_B||B\rangle - |A^{(1)}_H||H\rangle\right)|\Uparrow\downarrow\rangle. \tag{7.2}$$

The configurations $|A\rangle$, $|B\rangle$, and $|H\rangle$ are Jacobi coordinates given by Eq. 2.35. The magnetic field B changes both the energies of the HO states [101, 107], as well as increases the electron-hole Coulomb interactions. This changes the probabilities $A_A(B), A_B(B), A_H(B)$ of occupation of the single-particle levels with increasing magnetic field, and modifies the strength of the exchange coupling of the electron and hole spin with the spin of the Mn ion. The Mn ion acts as an impurity and scatters carriers among single-particle states as well. With this scattering turned off, the resulting splitting of emission lines, calculated numerically, is shown in Fig. 7.5 as magenta squares.

One can see that at zero magnetic field there is a slight decrease of the emission line splitting, due to the decreased population of the lowest exciton configuration, and transfer of this probability to higher-energy configurations. The splitting increases with the magnetic field, but the correlations in the excitonic wave function lead to a decrease of the rate of increase of the peak splitting. For each magnetic field it is possible to calculate semi-analytically the effective exciton-Mn

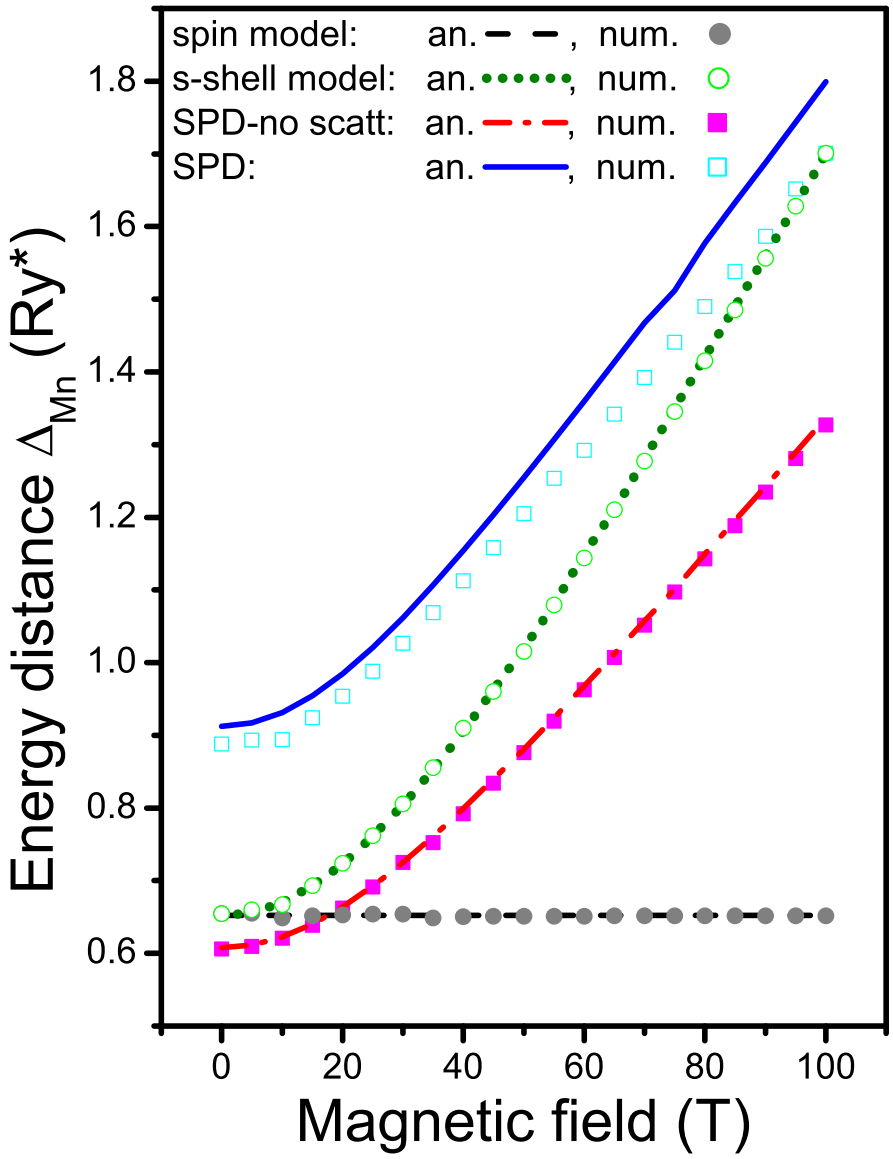

Figure 7.5: Magnetic-field evolution of the average splitting of the emission lines calculated in different models: spin model, s-shell model, and SPD with and without Mn scattering. The line spacing is calculated analytically as $\frac{1}{2}(J_{GS}^{e,eff} + 3J_{GS}^{h,eff})$ (solid, dashed or dotted lines) based on the expectation values of H_{h-Mn} and H_{e-Mn} in the exciton ground state wavefunction [151] and as an average splitting of emission lines from both $\sigma+$ and $\sigma-$ polarization calculated based on numerical emission spectra shown in Fig. 7.2 (dots).

interaction (splitting of emission lines) as $\frac{1}{2}\left(J_{GS}^{e,eff}+3J_{GS}^{h,eff}\right)$ using the exciton ground state wave function form as demostrated in Eq. 5.11. In Fig. 7.5 these calculations are shown with the red dot-dashed line which agrees very well with the emission line spacings calculated numerically.

The splitting of emission lines calculated in the SPD model accounting for the scattering by the Mn ion is shown in Fig. 7.5 as the blue solid line and light-blue empty squares (analytical and numerical calculations, respectively). The quantum interference effect causes a significant increase of the splitting of the emission lines (Chapter 6) due to the increase of the effective magnetic field produced by the hole, leading to the "exchange" splitting of different M_z states: $\langle H_{h-Mn}\rangle = \langle M_z|\langle\downarrow\Uparrow|\langle X_{GS}|H_{h-Mn}|X_{GS}\rangle|\Uparrow\downarrow\rangle|M_z\rangle$.

The result of analytical calculation of the emission line splitting $\Delta_{Mn}(B)$, shown in Fig. 7.5 with the blue solid line, exhibits only a slight deviation from the full numerical calculations. This deviation is due to the fact that the semi-analytical solution does not include the anisotropy of the QD, the electron-hole exchange or interactions with higher exciton states. However, it is instructive to see that this simplified calculation gives qualitalively the same result as the complicated numerical calculation.

Comparison between the green-dotted and blue-solid lines shows that not only the magnitude of the splitting decreases, but that the correlations lead to the decrease of the rate of growth of the splitting with increasing magnetic field.

The change in rate with which the emission line spacing grows with the magnetic field is even more visible in Fig. 7.6. In Fig. 7.6 the ratio between the spacing between $\Delta_{Mn}(B)$ (changing in magnetic field) and $\Delta_{Mn}(B=0)$ is shown. The colors and symbols used in this figure are the same as in Fig. 7.5. The rate of growth of the emission line spacing, calculated in the fully correlated model SPD (blue squares), is the lowest. This is a further confirmation that the correlations in the X-Mn complex are responsible for the slow growth of the spacings of the emission lines seen in the experiment.

Current experiments probe the emission spectrum of CdTe quantum dots in magnetic fields up to 30 T. As can be seen from Fig. 7.5, the magnetic field dependence of the splitting of the emission peaks is weak in this magnetic field range.

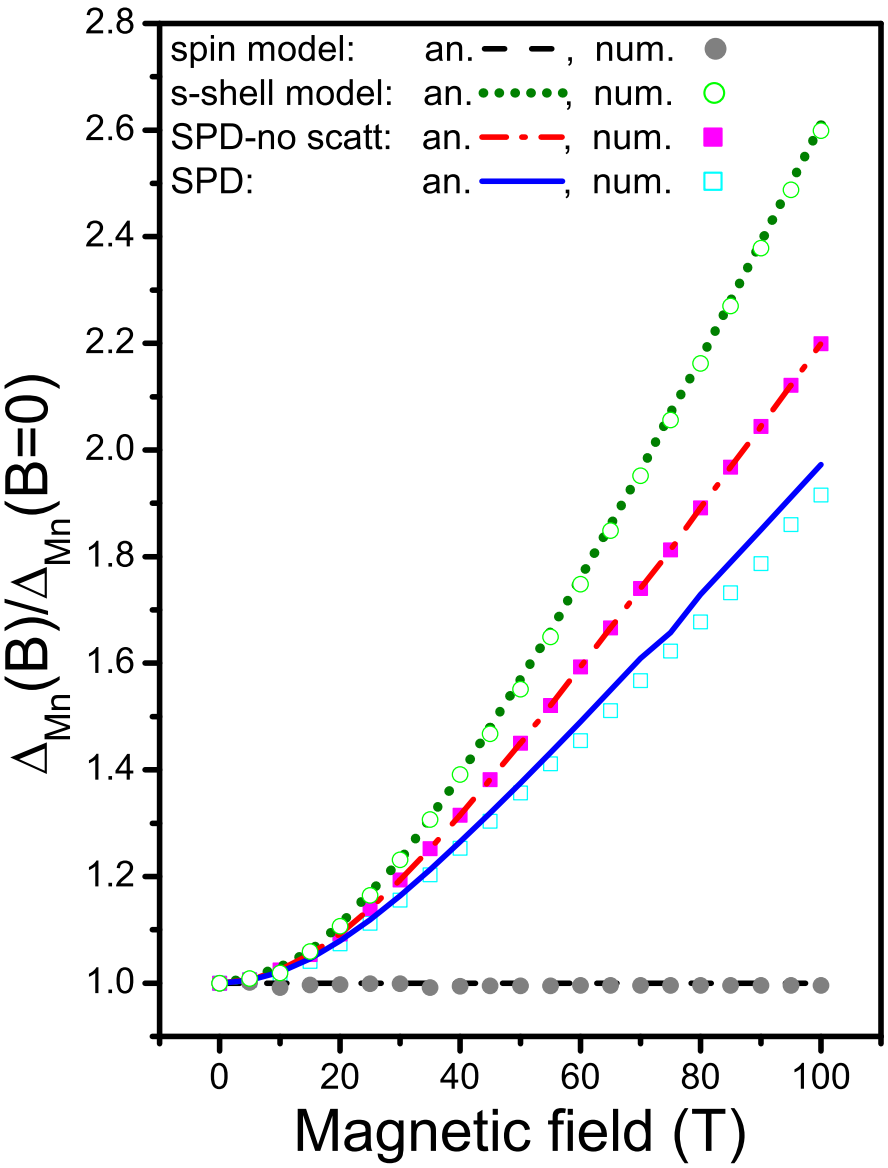

Figure 7.6: Magnetic-field evolution of ratios of the average splitting of the emission lines $\Delta_{Mn}(B)/\Delta_{Mn}(B=0)$ calculated in different models: spin model, s-shell model, and SPD with and without Mn scattering. The average distances $\Delta_{Mn}(B)$ have values as in Fig. 7.5. The notation used in this figure is the same as in Fig. 7.5.

Much higher magnetic fields, of the order of 100 T, are required to distinguish the different theoretical treatments of the emission spectrum.

Chapter 8

Bi-exciton-Mn complex

In this chapter the analysis of the optical properties of the self-assembled quantum dots with the magnetic impurity is extended to the higher excitation power. In this regime, the existence of bi-exciton (XX) in quantum dots is observed [117, 125, 126]. As was mentioned in Chapter 2, in self-assembled quantum dots the XX ground state is a spin singlet, with the carriers of the same type arranged in pairs with antiparallel spins.

In QDs with magnetic impurities each of the carriers interacts with the localized impurity spin via the contact exchange interaction (Chapter 4). Since the XX ground state is spinless (the total electron S and hole j spins in the ground state are zero), it is typically assumed to be decoupled from the impurity spin [23, 156, 163, 173, 184]. For that reason the XX-Mn complex was considered a good candidate to probe the excited states of the X-Mn complex.

It has been shown previously in Chapters 6 and 7 [151, 167] that, although the spin model for the exciton is a significant simplification of the problem (does not describe quantum interference or non-uniform emission line splitting), it is still a good tool to describe the physics of the exciton-Mn system in the range of experimentally accessible magnetic fields.

Here we are going to show that for the bi-exciton-Mn complex (XX-Mn) the spin model does not apply. We report the existence of the fine structure in the ground state of the XX-Mn due to the magnetic impurity-mediated interaction of the lowest XX singlet-singlet (XX_{SS}) state with higher XX states, like triplet-singlet XX_{TS} state [189].

Further, the dependence of this ground state splitting is analyzed as a function of the strength of the electron- and hole-Mn interaction and the quantum dot shell spacing. The XX-Mn emission spectrum is predicted as a function of photon energy, number of confined shells, and anisotropy. The signatures of the XX-Mn ground state fine structure in the emission spectra are presented and analyzed.

Our model predicts also a fundamental difference between the temperature dependence of the XX-Mn and X-Mn spectra, and provides a method of engineering of all of the above effects.

8.1 Fine structure of the ground state of the XX-Mn complex

Figure 8.1 (a-b) shows the schematic picture of the six lowest XX-Mn energy levels in the models with increasing accuracy. In the spin model there is only one possible configuration for the bi-exciton with all the carriers on the s-shell: $|XX_{spin}\rangle = h^+_{s\Downarrow}h^+_{s\Uparrow}c^+_{s\downarrow}c^+_{s\uparrow}|0\rangle$ (Fig. 8.1 (a, left)). Since the matrix elements: $\langle XX_{spin}, M_z|H_{e-Mn}|XX_{spin}, M_z\rangle = 0$ and $\langle XX_{spin}, M_z|H_{h-Mn}|XX_{spin}, M_z\rangle = 0$, XX_{spin} does not interact with Mn ion and the XX-Mn GS is sixfold degenerate (Fig. 8.1 (a, right)). In the correlated model, on the other hand, there are higher states of the bi-exciton, which due to the presence of the Mn ion interact with its ground state (similar to the X-Mn in Chapter 6). This interaction leads to the splitting of the GS manifold into three groups of doubly-degenerate levels (Fig. 8.1 (b)), each for a different Manganese spin z-projection $|M_z|$.

The signature of the XX-Mn fine structure was seen previously in the experimental emission spectra [156], however the origin of this splitting was not understood. The present work identifies the anisotropic Kondo coupling of the spin-singlet electronic system to the localised spin as responsible for the XX-Mn fine structure.

The spin-flip interaction between electron and Mn ion leads to the further splitting of these group of levels (Fig. 8.1 (c)).

To illustrate this effect on an even simpler example, the localised Mn spin $|\vec{M}| = 5/2$ interacting with a pair of holes confined in a QD can be considered.

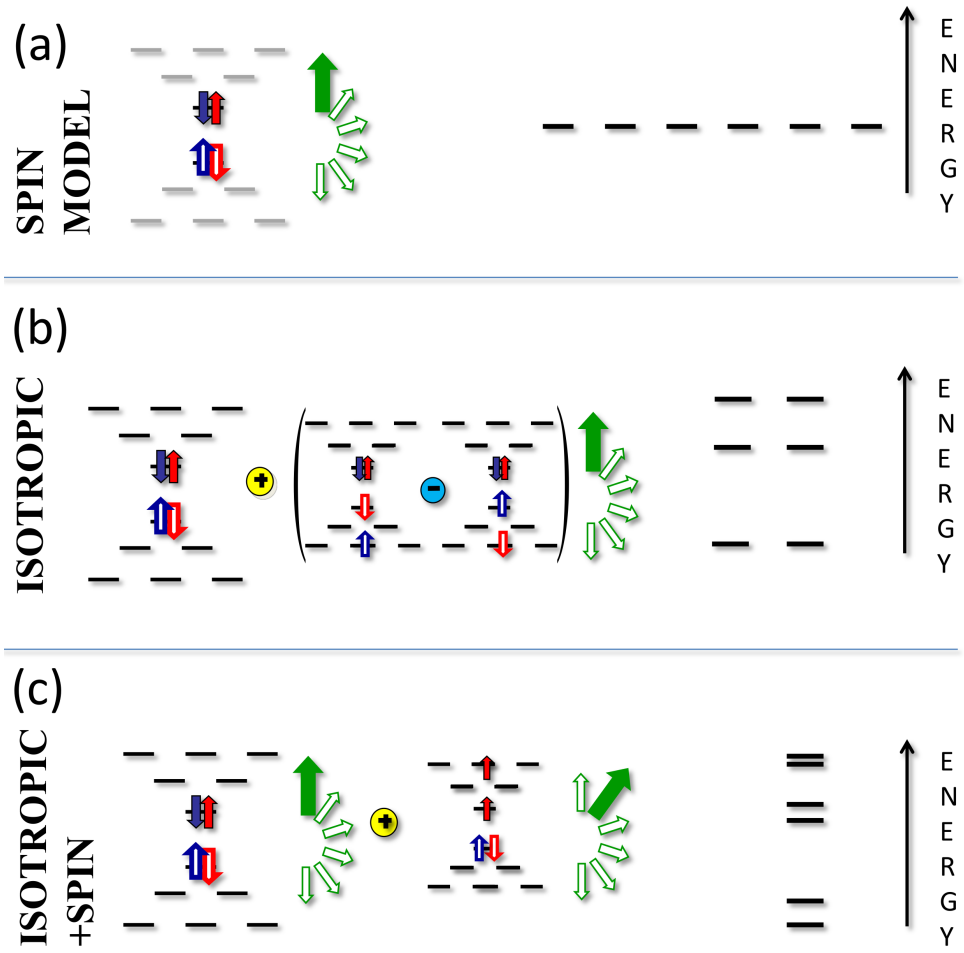

Figure 8.1: Schematic picture of the six lowest XX-Mn energy lines (left) in the spin model (a), the correlated XX model without spin-flip processes between the electron and the Mn ion (b), the full correlated model (c). The important configurations of the XX-Mn for each of the models are shown on the right.

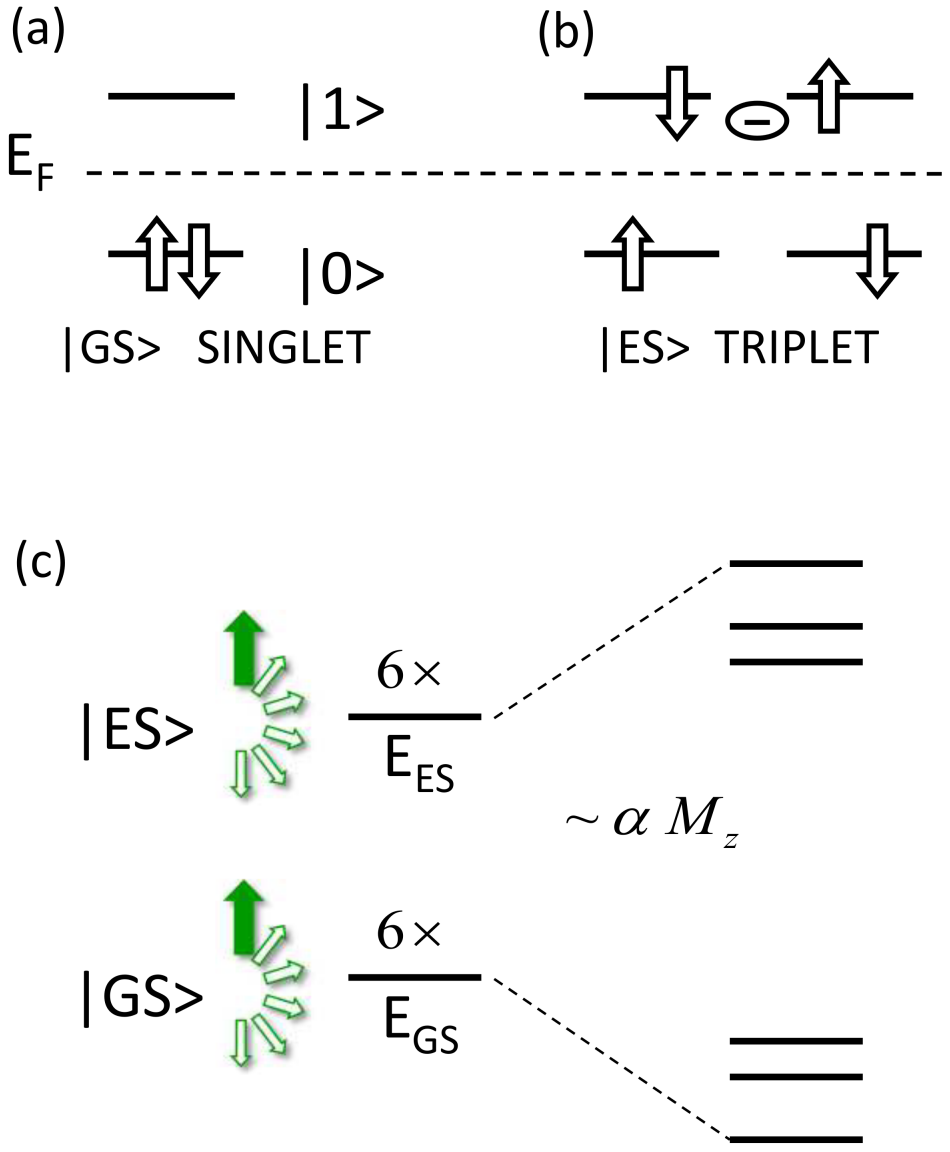

Figure 8.2: Schematic picture of the Mn ion-mediated coupling between the spin-singlet GS-Mn and the spin-triplet ES-Mn states. Panel (a) shows schematically the two-hole configuration dominant in the singlet state $|GS\rangle$, while panel (b) shows the triplet linear combination of configurations dominant in the state $|ES\rangle$. The two states do not interact with the localized spin directly, and therefore form a sixfold degenerate ground and excited manifold shown in the left-hand part of panel (c). The localized spin can, however, scatter the carriers from $|GS\rangle$ to $|ES\rangle$, resulting in the appearance of splitting of both manifolds into three pairs (right).

The ground-state configuration of two holes in a QD without the localised spin is a spin singlet $j = 0$ (Figure 8.2 (a)), and is created by placing the holes on the lowest-energy single-particle orbital $|0\rangle$:

$$|GS\rangle = h^+_{0\Uparrow} h^+_{0\Downarrow} |0\rangle. \tag{8.1}$$

The interaction of the two holes with the Mn can be described by the Ising Hamiltonian, Eq. 4.8, [187]. Clearly, the expectation value of this Hamiltonian in the ground state of the pair of holes is equal to zero:

$$\langle M_z | \langle GS | H_{h-Mn} | GS \rangle | M_z \rangle = 0, \tag{8.2}$$

for any M_z, i.e., the holes and the Mn spin are decoupled. Therefore, the state $|GS\rangle|M_z\rangle$ is sixfold degenerate with the energy E_{GS}. This is shown schematically in the lower left-hand part of Fig. 8.9 (c). As in the Kondo problem, Ref. [190], one can construct an excited triplet state by promoting a hole with either spin to the excited single-particle orbital $|1\rangle$ (Fig. 8.9 (b)):

$$|ES\rangle = \frac{1}{\sqrt{2}} \left(h^+_{1\Uparrow} h_{0\Uparrow} - h^+_{1\Downarrow} h_{0\Downarrow} \right) |GS\rangle \tag{8.3}$$

The $|ES\rangle$ is decoupled from Mn, which produces a sixfold degenerate excited manifold, with energy E_{ES} represented in the upper left-hand part of Fig. 8.9 (c).

The two degenerate manifolds are *coupled* by the *scattering* term of the hole-Mn Hamiltonian

$$H_{h-Mn} \approx J_{10} \left(h^+_{1\Uparrow} h_{0\Uparrow} - h^+_{1\Downarrow} h_{0\Downarrow} \right) M_z. \tag{8.4}$$

Here, the hole-Mn exchange interaction J_{10} scatters a hole from state $|0\rangle$ to state $|1\rangle$ in the effective magnetic field produced by the Mn spin. The minus sign in the hole-Mn Hamiltonian is going to play an important role in further calculations. The matrix element of the hole-Mn interaction $\langle M_z | \langle GS | H_{h-Mn} | ES \rangle | M_z \rangle$ between the ground and excited states for each Mn spin projection can be eval-

uated as:

$$\langle M_z|\langle GS|J_{10}\left(h^+_{1\Uparrow}h_{0\Uparrow}-h^+_{1\Downarrow}h_{0\Downarrow}\right)\hat{M}_Z \\ \times\frac{1}{\sqrt{2}}\left(h^+_{1\Uparrow}h_{0\Uparrow}-h^+_{1\Downarrow}h_{0\Downarrow}\right)|GS\rangle|M_z\rangle.$$

In this expression there are two minus signs, one in the Hamiltonian and one related to the Fermi statistics (triplet character) of the excited state. They cancel each other and lead to the constructive interference resulting in a non-zero matrix element:

$$\langle M_z|\langle GS|H_{hMn}|ES\rangle|M_z\rangle=\kappa M_z, \tag{8.5}$$

where $\kappa=\sqrt{2}J_{10}$. With these off-diagonal matrix elements, the six-fold degenerate ground-state manifold splits into three pairs of energy levels. The energy of each pair,

$$E_-(M_z)\approx E_{GS}-\frac{\kappa^2}{E_{ES}-E_{GS}}|M_z|^2, \tag{8.6}$$

acquires a correction proportional to the magnitude of $|M_z|$, as shown in the right-hand side of Fig. 8.9 (c). The excited manifold splits similarly, but with the reversed order of the gaps.

The removal of degeneracy of the ground state of two holes depends on the form of h-Mn exchange coupling - the splitting is largest for Ising and vanishes for the isotropic Heisenberg coupling [191].

The analysis of the XX-Mn ground state splitting will be done by analogy to the simple example of the two-hole-Mn complex described above. The splitting of the XX-Mn ground-state manifold occurs as a result of the Mn-mediated coupling of the XX ground (GS) and excited (ES) states. To capture the underlying physics one must therefore go beyond the spin model and construct the relevant XX states.

Using the notation introduced in Chapter 5, denoting the two-electron-hole pair subspaces by $\alpha=\{L,j,j_z,S,S_z\}$, the ground state of the bi-exciton $|XX^{GS}_{SS}\rangle$ is the state $|XX^{\alpha}_1\rangle$ with $\alpha=\{0,0,0,0,0\}$. On the other hand, one of the excited states with two holes in the triplet and two electrons in the singlet spin state $|XX_{TS}\rangle$, is the state $|XX^{\alpha'}_1\rangle$ for $\alpha'=\{0,1,0,0,0\}$. In the presence of the electron-

hole Coulomb interaction, the ground state $|XX_{SS}^{GS}\rangle$ of the bi-exciton consists of several configurations, of which the most important are:

$$\begin{aligned} |XX_{SS}^{GS}\rangle &= A_{ss-ss}^{SS}|s\Downarrow s\Uparrow, s\downarrow s\uparrow\rangle \\ &- A_{sd-ss}^{SS}\left(|s\Downarrow d\Uparrow, s\downarrow s\uparrow\rangle + |d\Downarrow s\Uparrow, s\downarrow s\uparrow\rangle\right). \end{aligned}$$

The $|XX_{TS}\rangle$ state is constructed by promoting one of the holes into the d shell and creating a properly antisymmetrized hole triplet

$$|XX_{TS}\rangle = \frac{1}{\sqrt{2}}\left(|s\Downarrow d\Uparrow, s\downarrow s\uparrow\rangle - |d\Downarrow s\Uparrow, s\downarrow s\uparrow\rangle\right).$$

In both of these states the electrons are on the s-shell, and they are playing the role of *spectators*. The expectation values of the hole-Mn and electron-Mn interaction Hamiltonian H_{h-Mn} and H_{e-Mn} (Eqs. 4.7 and 4.8) in each of the $|XX_{SS}, M_z\rangle$ and $|XX_{TS}, M_z\rangle$ states are equal to zero:

$$\begin{aligned} \langle XX_{SS}, M_z|H_{h-Mn} + H_{e-Mn}|XX_{SS}, M_z\rangle &= 0 \\ \langle XX_{TS}, M_z|H_{h-Mn} + H_{e-Mn}|XX_{TS}, M_z\rangle &= 0, \end{aligned} \tag{8.7}$$

since the spin projection of electrons, and holes (S_z and j_z) in both of those states is equal to zero, and for the Mn at the center of the QD $R = (0,0)$, $J_{ss}^h(0) = -J_{sd}^h(0) = J_{dd}^h(0)$. Thus, at this point both states of the XX-Mn complex are sixfold degenerate. However, in a similar way as in the example with two holes, the two states are coupled by an *offdiagonal matrix element* of the H_{h-Mn} Hamiltonian:

$$\langle XX_{SS}, M_z|H_{h-Mn}|XX_{TS}, M_z'\rangle = \kappa M_z \delta_{M_z, M_z'},$$

where $\kappa = \frac{3}{\sqrt{2}} A_{ss-ss}^{SS} J_{sd}^h(\mathbf{0})$. This matrix element is proportional to the Mn-ion spin projection M_z and to the hole-Mn exchange constant $J_{sd}^h(\mathbf{0})$, which scatters the hole from the s-shell to the central orbital of the d-shell. Thus, the 12×12

Hamiltonian splits into six 2×2 matrices of the form:

$$H_{h-Mn} = \begin{pmatrix} E_{SS} & \kappa M_z \\ \kappa M_z & E_{TS} \end{pmatrix}, \tag{8.8}$$

with E_{SS} and E_{TS} being the energy of bare XX_{SS} and XX_{TS}, respectively. As previously for the case of the two holes, assuming that the offdiagonal element is small, one obtains the energy of the lower state:

$$E- = E_{SS} - \frac{\kappa^2}{E_{TS} - E_{SS}} |M_z|^2. \tag{8.9}$$

Since the correction to the E_{SS} energy is proportional to the square of Mn spin projection $|M_z|^2$, the repulsion is the strongest for the states with $M_z = \pm 5/2$ and the weakest for states with $M_z = \pm 1/2$. This leads to the splitting of the sixfold degenerate E_{SS}-Mn energy level into three pairs, as shown in Fig. 8.1. Each of the levels has different $|M_z|$, and is doubly degenerate. The s-shell energies of the XX-Mn complex are denoted by E_{XXi} ($i = 1 \ldots 6$). The lowest, doubly degenerate energy level has the energy $E_{XX1} = E_{XX2}$ and the Mn spin projection $|M_z| = 5/2$, the higher, $E_{XX3} = E_{XX4}$, corresponds to $|M_z| = 3/2$, and the highest-energy $E_{XX4} = E_{XX6}$ pair has $|M_z| = 1/2$. The splitting between the states with $|M_z| = 5/2$ and $|M_z| = 3/2$ ($\delta_2 = E_{XX3} = E_{XX2} = 4\frac{\kappa^2}{E_{TS}-E_{SS}}$) is twice as big as between $|M_z| = 3/2$ and $|M_z| = 1/2$ (δ_4).

In figure 8.3 the numerical calculations of the energy level spacings of the XX-Mn ground state for two different QDs: shallow (SP-black) - confining only the s and p single-particle shells, and deeper (SPD-red), confining also a d shell, are analyzed. The inset shows the schematic picture of the XX-Mn energy levels, with the six energy levels grouped into three two-levels groups. Figure 8.3 (a) shows the distances between the XX-Mn energy levels $\delta_i = E_{XXi+1} - E_{XXi}$ as a function of its number i. The splitting of the XX-Mn levels, is much weaker in the shallow QDs. The average splitting between energy levels ($\delta_{aver} = (E_{XX6} - E_{XX1})/5$) is over an order of magnitude smaller than in the deeper QDs. The SP model does not predict the splitting between XX-Mn states with the same $|M_z|$ ($\delta_1 = \delta_3 = \delta_5 = 0$), while in the presence of the d-shell in the QD, these splittings, although still dominanted by the main splittings δ_2 and δ_4, are non-

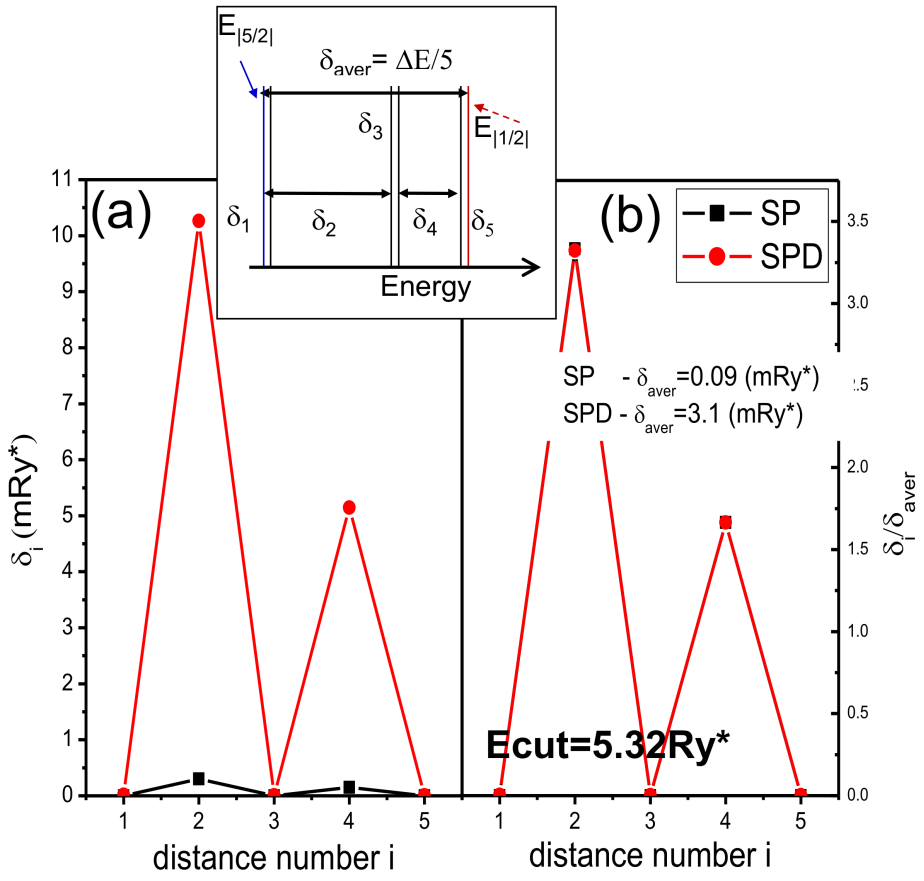

Figure 8.3: (a) Comparison of the splittings (δ_i) of the six lowest XX-Mn energy levels for the shallow (SP) and deep (SPD) quantum dots as a function of the distance number i. (b) The normalized energy level splitting (δ_i/δ_{aver}), with δ_{aver} being the average splitting of the energies of the XX-Mn complex.

zero. Figure 8.3 (b) shows the ratio between the energy level distance and the average distance between XX-Mn lines, δ_i/δ_{aver}, as a function of the distance number i. This re-scaling, leads to the alignment of the δ_i/δ_{aver} lines calculated in both models. The numerical calculations confirm simple analytical formulas discussed above, which predicted that the δ_2 spacing is twice as big as δ_4.

To explain the origin of the splitting of each of the three doubly degenerate XX-Mn levels (seen in the SPD model), corresponding to the same magnitude of the Mn spin projection $|M_z|$, the contributions from the sp-sp electron-hole pairs (with one electron-hole pair on s-shell, and the second on the p-shell) to the bi-excitonic ground state cannot be neglected (as done in the Eq. 8.7). The ground state of the bi-exciton $|XX^{GS}_{SS}\rangle$ has then the form:

$$\begin{aligned}
|XX^{GS}_{SS}\rangle &= A^{SS}_{ss-ss}|s\Downarrow s\Uparrow, s\downarrow s\uparrow\rangle - A^{SS}_{ss-sd}\left(|s\Downarrow s\Uparrow, s\downarrow d\uparrow\rangle + |s\Downarrow s\Uparrow, d\downarrow s\uparrow\rangle\right)\\
&- A^{SS}_{sd-ss}\left(|s\Downarrow d\Uparrow, s\downarrow s\uparrow\rangle + |d\Downarrow s\Uparrow, s\downarrow s\uparrow\rangle\right)\\
&+ A^{SS}_{sp-sp}|\left(s\Downarrow p1\Uparrow + p1\Downarrow s\Uparrow\right), \left(s\downarrow p1\uparrow + p1\downarrow s\uparrow\right)\rangle\\
&+ A^{SS}_{sp-sp}|\left(s\Downarrow p2\Uparrow + p2\Downarrow s\Uparrow\right), \left(s\downarrow p2\uparrow + p2\downarrow s\uparrow\right)\rangle,
\end{aligned} \tag{8.10}$$

where $p1 = (n_+, n_-) = (0,1)$ and $p2 = (1,0)$. The configurations of XX-Mn, created based on the XX ground state: $|XX^{GS}_{SS}, M_z\rangle = |XX^{GS}_{SS}\rangle \otimes |M_z\rangle$, are coupled through the spin-flip terms of the electron-Mn Hamiltonian H_{e-Mn}, Eq. 4.7, with the higher XX-Mn states. An example of the XX state coupled to the $|XX^{GS}_{SS}, M_z\rangle$ is the state in which the holes are in a spin singlet and electrons in a triplet state from the subspace $\chi = \{L, j, j_z, S, S_z\} = \{0, 0, 0, 1, -1\}$ of the form:

$$\begin{aligned}
|XX^{\chi}_{ST}, M_z+1\rangle &= \{A^{\chi}_{ss-sd}|s\Downarrow s\Uparrow, s\downarrow d\downarrow\rangle\\
&- A^{\chi}_{sp-sp}|\left(s\Downarrow p1\Uparrow + p1\Downarrow s\Uparrow\right), s\downarrow p1\downarrow\rangle\\
&+ A^{\chi}_{sp-sp}|\left(s\Downarrow p2\Uparrow + p2\Downarrow s\Uparrow\right), s\downarrow p2\downarrow\rangle\} \otimes |M_z+1\rangle.
\end{aligned} \tag{8.11}$$

In this state, both of the electrons have spin down and the z projection of Mn spin is increased by one $|M_z+1\rangle$.

There is also a coupling between the $|XX^{GS}_{SS}, M_z\rangle$ and the XX-Mn configuration, in which both electrons have spin up ($\chi' = \{L, j, j_z, S, S_z\} = \{0, 0, 0, 1, 1\}$),

and the Mn spin is lowered by one:

$$\begin{aligned} |XX^{\chi'}_{ST}, M_z - 1\rangle &= \{A^{\chi'}_{ss-sd}|s \Downarrow s \Uparrow, s \uparrow d \uparrow\rangle \\ &- A^{\chi'}_{sp-sp}|\left(s \Downarrow p1 \Uparrow + p1 \Downarrow s \Uparrow\right), s \uparrow p1 \uparrow\rangle \\ &+ A^{\chi'}_{sp-sp}|\left(s \Downarrow p2 \Uparrow + p2 \Downarrow s \Uparrow\right), s \uparrow p2 \uparrow\rangle\} \otimes |M_z - 1\rangle. \end{aligned} \tag{8.12}$$

The splitting between the states with $|M_z| = 5/2$ is the greatest, so the analysis of the splitting between the states with the same $|M_z|$ will be done using the example of these states. The interaction between the XX-Mn states $|XX^{GS}_{SS}, M_z = -5/2\rangle$ and $|XX^{\chi}_{ST}, M_z = -3/2\rangle$ is given by the matrix element:

$$\begin{aligned} &\langle XX_{SS}, -5/2|H_{e-Mn}|XX^{\chi}_{ST}, -3/2\rangle \\ = &\left(A^{SS}_{ss-ss}A^{\chi}_{ss-sd}J^{e}_{sd}(0) - 4A^{SS}_{sp-sp}A^{\chi}_{sp-sp}J^{e}_{ss}(0)\right)\langle -5/2|M^{-}| - 3/2\rangle, \end{aligned} \tag{8.13}$$

while between the XX-Mn state $|XX^{GS}_{SS}, M_z = 5/2\rangle$ and the state $|XX^{\chi'}_{ST}, M_z = 3/2\rangle$:

$$\begin{aligned} &\langle XX_{SS}, 5/2|H_{e-Mn}|XX^{\chi'}_{ST}, 3/2\rangle \\ = &\left(A^{SS}_{ss-ss}A^{\chi'}_{ss-sd}J^{e}_{sd}(0) + 4A^{SS}_{sp-sp}A^{\chi'}_{sp-sp}J^{e}_{ss}(0)\right)\langle 5/2|M^{+}|3/2\rangle. \end{aligned} \tag{8.14}$$

The matrix elements $\langle -5/2|M^{-}| - 3/2\rangle = \langle 5/2|M^{+}|3/2\rangle$, as well as the amplitudes $A^{\chi}_{ss-sd} = A^{\chi'}_{ss-sd}$ in the absence of the magnetic field. For that reason, the corresponding terms in the matrix elements given by Eqs. 8.13 and 8.14, are equal. However, these matrix elements (Eqs. 8.13 and 8.14) have different values, since one is a *difference*, while the second is a *sum* of the two terms. This results in a different magnitude of the coupling between the two pairs of states, which in turn leads to the different energies of the final XX-Mn states with $\pm 5/2$. In the SP model, the amplitude A^{χ}_{ss-sd} is equal to zero, $A^{\chi}_{ss-sd} = 0$, and the above matrix elements differ only by a sign, hence the energies of XX-Mn states with $M_z = \pm 5/2$ are the same.

8.2 The fine structure of the XX-Mn in the emission spectra

It will be explained now how the Kondo interaction of XX with the Mn ion can be observed in the emission spectrum. Figure 8.4 (a, left) shows schematically the energy alignment of the Mn, X-Mn, and XX-Mn complexes in a diagram similar to that in Refs. [156, 184]. The energy levels of the Mn, X-Mn, and XX-Mn are plotted as a function of the M_z (horizontal axis). The Mn states are a degenerate manifold. The spectrum of the X-Mn complex, built from the electron spin-down and hole spin-up states is shown in blue (opposite spin alignment in red). Emission from both X-Mn and XX-Mn occurs vertically within the same M_z channel. The polarization of the resulting maxima is denoted by colors - blue (red) for $\sigma+$ ($\sigma-$). The right-hand side of this panel shows schematically the corresponding emission spectra.

Figure 8.4 (a) shows the energy level alignment and the schematic emission spectra for the spin model. The energy levels of the X-Mn are approximatelly equally spaced and the XX-Mn energy is sixfold degenerate. The emission spectra from both complexes (Fig. 8.4 (a, right)), with equally spaced emission lines, look exactly the same.

The schematic picture of the energy levels and emission spectra resembling the one calculated in the correlated model is presented in figures 8.4 (b and c). Note the irregular distribution of the bright X-Mn levels due to the quantum interference effect [151, 167]. The splitting of the XX-Mn sixfold degenerate manifold into three pairs, due to the coupling of the XX complex with Mn, is visible in Figures 8.4 (b and c). Each pair of levels is further split due to electron-Mn spin-flips, however this effect is much smaller (Fig. 8.3) and is not shown here. Similar splitting of XX-Mn levels was observed by Besombes *et al.* [156] who found that the injection of a second exciton almost cancelled the exchange interaction of X with Mn ion. The remaining splitting was attributed either to perturbation of carrier orbital wavefunction by Mn ion or strain-induced magnetic anisotropy [184]. The suggested interpretation in terms of the strain-induced magnetic anisotropy turned out to lead to the opposite order of the XX-Mn levels [184].

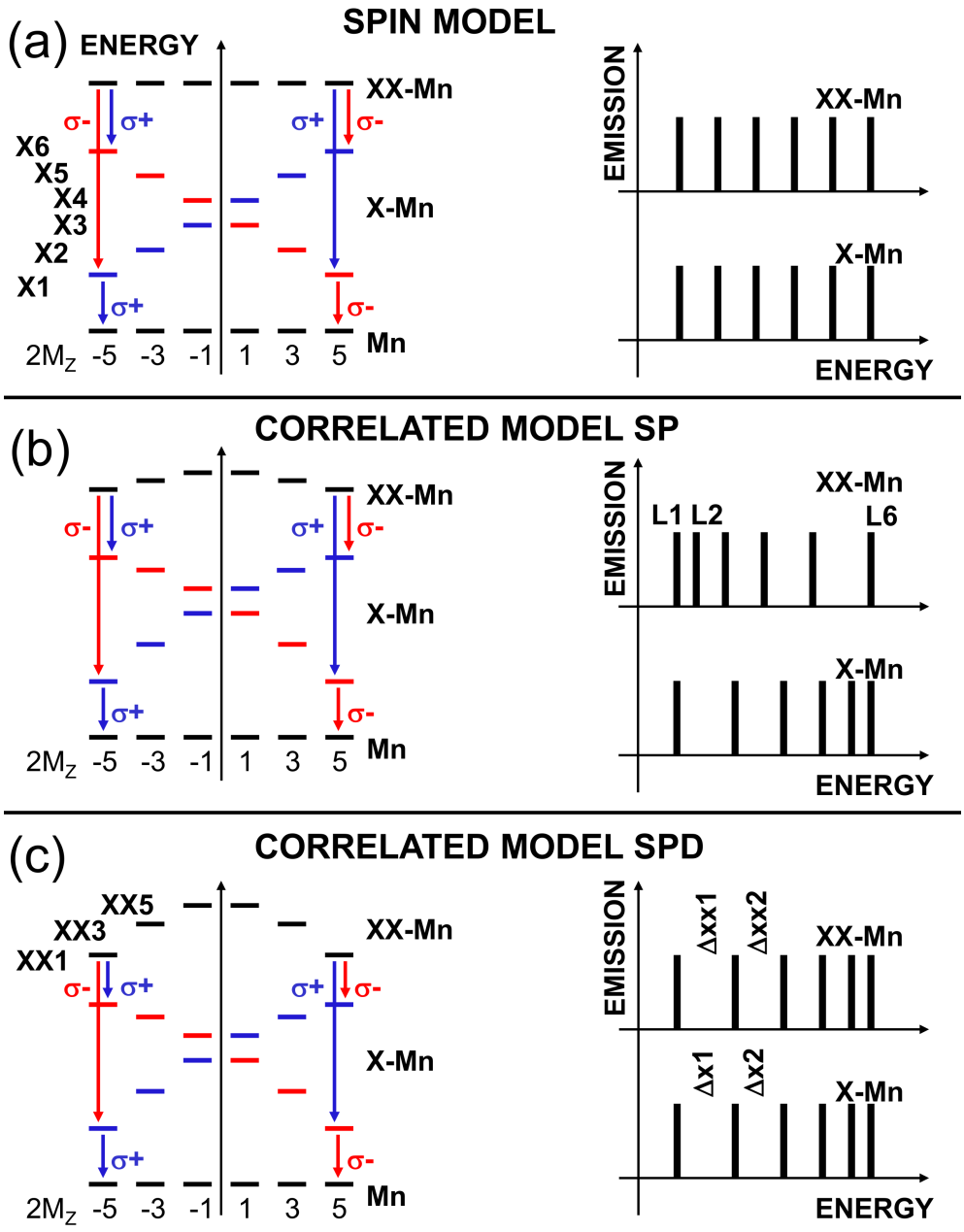

Figure 8.4: Left-hand diagrams show schematically the energies of the Mn, X-Mn (bright subspace), and XX-Mn systems in the spin model (a) and in the correlated model (b) and (c), as a function of the projection M_z of the localized spin. Right-hand diagrams show the corresponding emission spectra. Gaps between X-Mn (XX-Mn) lines are denoted as Δ_i (Δ_i^{XX}).

The figures 8.4 (b and c) differ in the magnitude of the splitting of the XX-Mn ground state. The two situations presented here lead to significantly different XX-Mn emission spectra. If the splitting of the XX-Mn ground state is small, the XX-Mn emission spectra is a mirror reflection of the X-Mn emission spectra - the XX-Mn peaks are denser on the low-energy side of the spectrum while the distribution of X-Mn peaks is opposite (Fig. 8.4 (b)).

In Fig. 8.4 (c), the splitting of energy levels of the XX-Mn complex is larger, and it inverts the XX-Mn emission spectrum: now the pattern of gaps in the XX-Mn and X-Mn spectra is the same.

Let us now discuss emission spectra resulting from this arrangement of XX-Mn levels. The notation introduced in Fig. 8.4 (b) will be used and the recombination channel with $M_z = -5/2$ will be described as an example. Here, the XX-Mn state has the lowest energy E_{XX1}. Since this state contains both $\sigma-$ and $\sigma+$ excitons, there are two recombination paths: (i) $\sigma+$ emission (blue), leaving the X-Mn in the state $|h^+_{\Downarrow}c^+_{\uparrow}|0\rangle \otimes |-5/2\rangle$, and (ii) $\sigma-$ emission (red), with the final state $|h^+_{\Uparrow}c^+_{\downarrow}|0\rangle \otimes |-5/2\rangle$. The first event produces the lowest-energy emission line with energy $L_1 = E_{XX1} - E_{X6}$, while the second one - the highest energy line $L_6 = E_{XX1} - E_{X1}$. The same photon energies, although with opposite polarizations, will be obtained in the channel $M_z = 5/2$. As a result the emission spectrum is unpolarized. The same procedure is applied to the other four XX-Mn states to obtain the emission energies L_2-L_5.

Here, in Figs. 8.5 and 8.6, the calculated emission spectra from the QD containing both X-Mn and XX-Mn charge neutral excitonic complexes for few different temperatures are shown. As discussed above (Fig. 8.4), there are six dominant emission lines from each of the X-Mn and XX-Mn complexes in each polarization, p_x and p_y, however, the polarization of the X-Mn and XX-Mn emission lines is reversed [192]. The emission spectra from XX-Mn and X-Mn behave significantly differently with increasing temperature. In the limit of very low temperature ($T = 0.1$ K, Figs. 8.5 and 8.6 (a)), the X-Mn complex is trapped in the dark-X-Mn state (due to the electron-hole exchange splitting of the excitonic states), which is the GS of this complex. For that reason there is no emission from the X-Mn complex at low temperature. On the other hand, the GS of the XX-Mn is the bright state, which results in a strong emission from the GS and

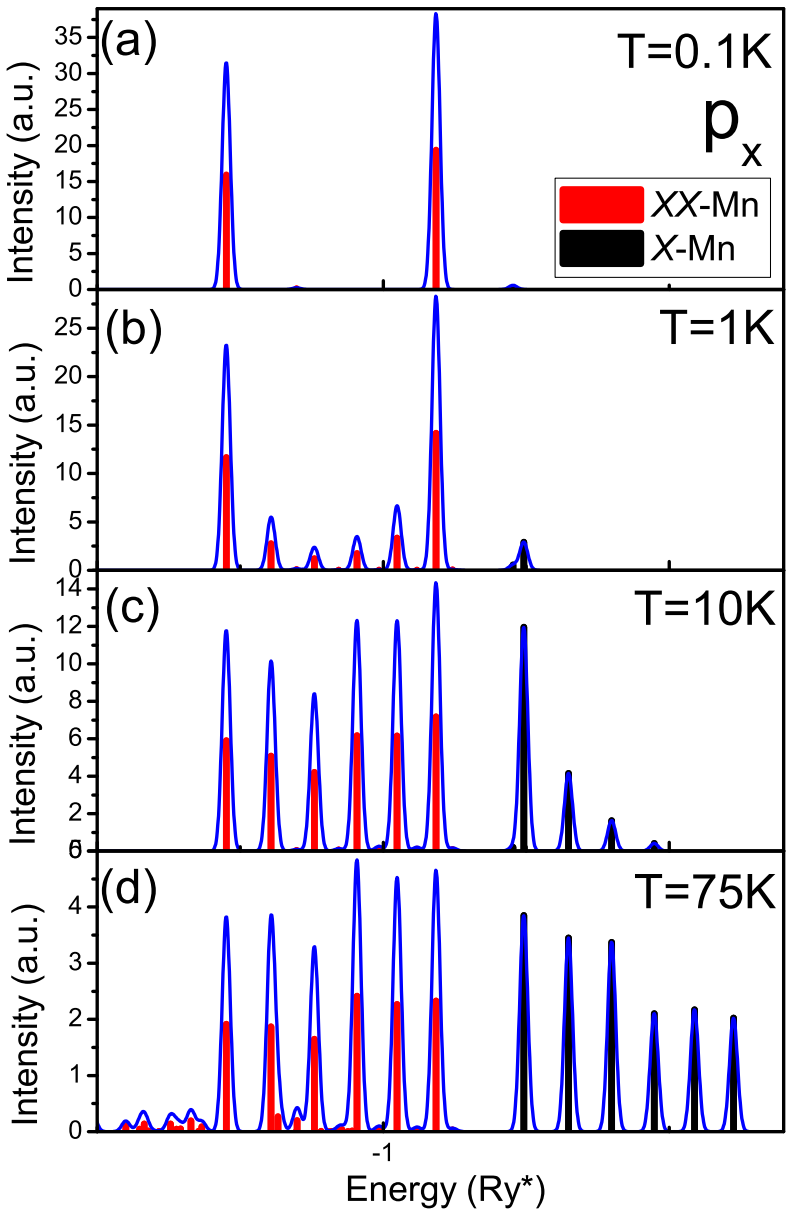

Figure 8.5: Emission spectra of the QD, with the emission from X-Mn complex (black) and XX-Mn complex (red) calculated for the range of temperatures T=$\{$0.1K, 1K, 10K, 75K$\}$. The energy spectra are calculated in p_x polarization. The calculated emission spectra with gaussian broadening of the emission lines are shown in blue.

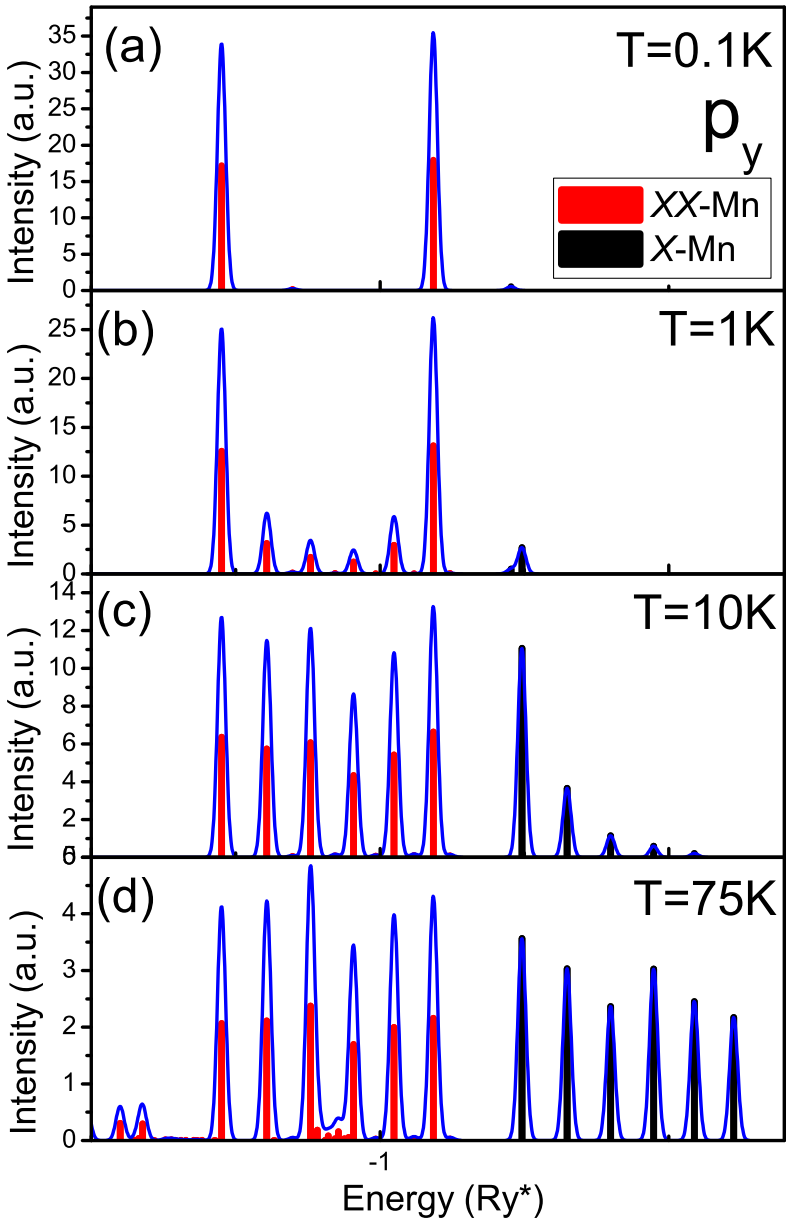

Figure 8.6: Emission spectra of the QD, with the emission from X-Mn complex (black) and XX-Mn complex (red) calculated for the range of temperatures T={0.1K, 1K, 10K, 75K}. The energy spectra are calculated in p_y polarization. The calculated emission spectra with gaussian broadening of the emission lines are shown in blue.

first excited state (almost degenerate with the GS), of the XX-Mn complex with $M_z = \pm 5/2$. The two emission channels from these states were discussed above, and as a result the emission spectra consist of two unpolarized emission lines (in fact there are line doublets, but since the splitting between these lines is of the order of the $|M_z| = 5/2$ energy level splitting (δ_1), it cannot be seen on the Figs. 8.5 and 8.6).

When the temperature is increased to $T = 1$ K (Figs. 8.5 and 8.6 (b)), the higher XX-Mn states become populated and more emission lines are visible. At the same time the lowest bright state of the X-Mn is thermally populated and one weak X-Mn emission line is present. As the temperature increases to $T = 10$ K (Figs. 8.5 and 8.6 (c)), the six lowest XX-Mn states are almost equally populated, due to small XX-Mn energy level splitting compared to the temperature, while in the X-Mn emission the emission from the lowest X-Mn level is still dominating the spectra.

The temperature of $T = 75$ K is needed to reach the limit of almost equal thermal population of the X-Mn levels (Figs. 8.5 and 8.6 (d)). In this temperature the emission from the X-Mn and XX-Mn complexes look qualitatively similar, however the emission from higher states of the bi-exciton-Mn complex is already visible.

It was mentioned previously that the form of the emission spectra from XX-Mn complex depends on the splitting of the XX-Mn ground state. Here, the three regimes of the magnitude of the XX-Mn ground state splitting, which lead to three different distributions of the XX-Mn emission lines, will be defined.

Similarily as done previously for the X-Mn complex, one can extract the splittings of emission line for both excitonic complexes Δ_i^{XX} for the XX-Mn, and Δ_i for X-Mn, and plot them as a function of the spacing number i. Figure 8.7 (a) shows schematically a dependence of the $\Delta_i^{XX}/\Delta_{aver}$ on the spacing number i, in the case when the splitting of the XX-Mn ground state δ_4 is smaller than the critical value δ_4^*. For this case the distances Δ_i^{XX} of the XX-Mn emission lines increase with the spacing number i. The XX-Mn emission lines (red) shown on the left are a mirror reflection of the analogous emission line distances of the X-Mn (black).

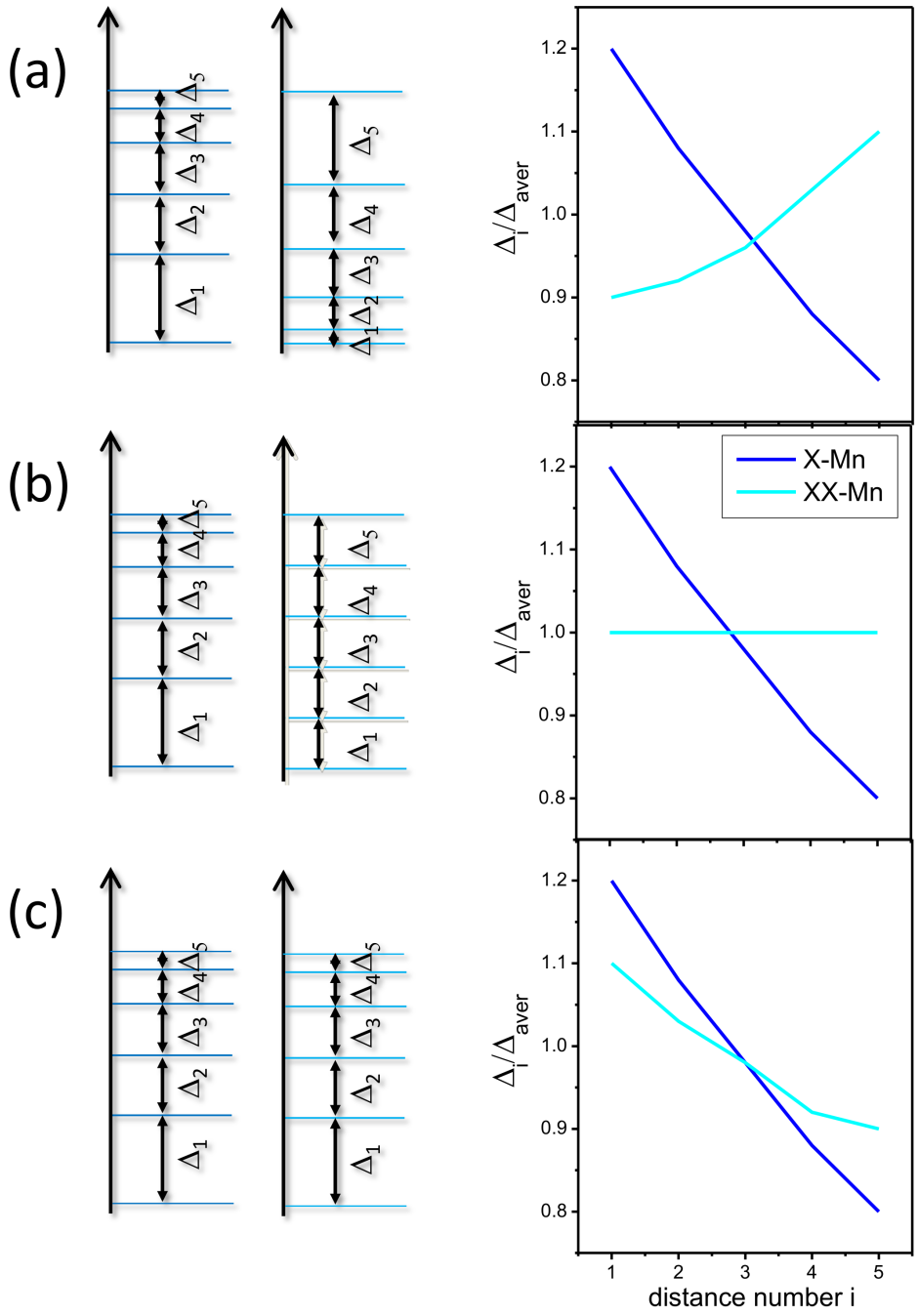

Figure 8.7: Schematic picture of the relative X-Mn and XX-Mn emission line distances for the small($\delta_4 < \delta_4^*$) (a), medium ($\delta_4 = \delta_4^*$) (b) and big ($\delta_4 > \delta_4^*$) (c) XX-Mn ground state splitting. δ_4^* is a critical XX-Mn GS splitting for which the $(\Delta_i^{XX}/\Delta_{aver})$ is constant. On the left side of the (a-c) figures the schematic picture of the ditribution of emission lines for both complexes is shown.

The magnitude of the XX-Mn splitting δ_4^* is defined as the splitting that leads to uniform distribution of the XX-Mn emission lines in Fig. 8.7 (b). In that case the distance between the two lowest-energy emission lines for the XX-Mn complex has to be equal to the distance between its two highest energy emission lines $\Delta_5^{XX} = \Delta_1^{XX}$, where $\Delta_5^{XX} = L_6 - L_5$ and $\Delta_1^{XX} = L_2 - L_1$. Using the relations between the XX-Mn emission lines energies (L_i) and the energies of the XX-Mn (E_{XXi}) and X-Mn (E_i) one obtains:

$$\Delta_5^{XX} = E_{XX1} - E_{XX3} + (E_2 - E_1) = \Delta_1 - 2\delta_4, \tag{8.15}$$

and similarly

$$\Delta_1^{XX} = 2\delta_4 + \Delta_5. \tag{8.16}$$

Critical splitting of the XX-Mn levels is then related to non-uniformity in the X-Mn emission lines:

$$\delta_4^* = (\Delta_1 - \Delta_5)/4. \tag{8.17}$$

The distribution of the emission lines from both XX-Mn and X-Mn complexes, when the splitting of the XX-Mn levels is greater than critical ($\delta_4 > \delta_4^*$), is shown in Fig. 8.7 (c). The splitting of the XX-Mn emission lines $\Delta_i^{XX}/\Delta_{aver}$ follows that of the X-Mn complex.

The results of the numerical calculations of the splittings $\Delta_i^{XX}/\Delta_{aver}$ and Δ_i/Δ_{aver} of the emission lines for XX-Mn and X-Mn complexes respectively, confined in shallow QD confining the s and p single-particle shells, are presented in Fig. 8.8 (a). This figure is qualitatively similar to Fig. 8.7 (b) when the splitting of the ground state of the XX-Mn complex is smaller than the critical value δ_4^*. In fact, in the SP model one can observe a small splitting of the XX-Mn levels (Fig. 8.3), but it is weak and it does not lead to the reversal of the emission spectra.

On the other hand, the figure 8.8 (b) shows the emission line splitting $\Delta_i^{XX}/\Delta_{aver}$ and Δ_i/Δ_{aver} computed in the SPD model. It is aparent that in this model the XX-Mn ground state splitting is big enough ($\delta_4 > \delta_4^*$) to overcompensate for the non-uniformity in X-Mn spectra and leads to the X-Mn-like distribution of the XX-Mn emission lines.

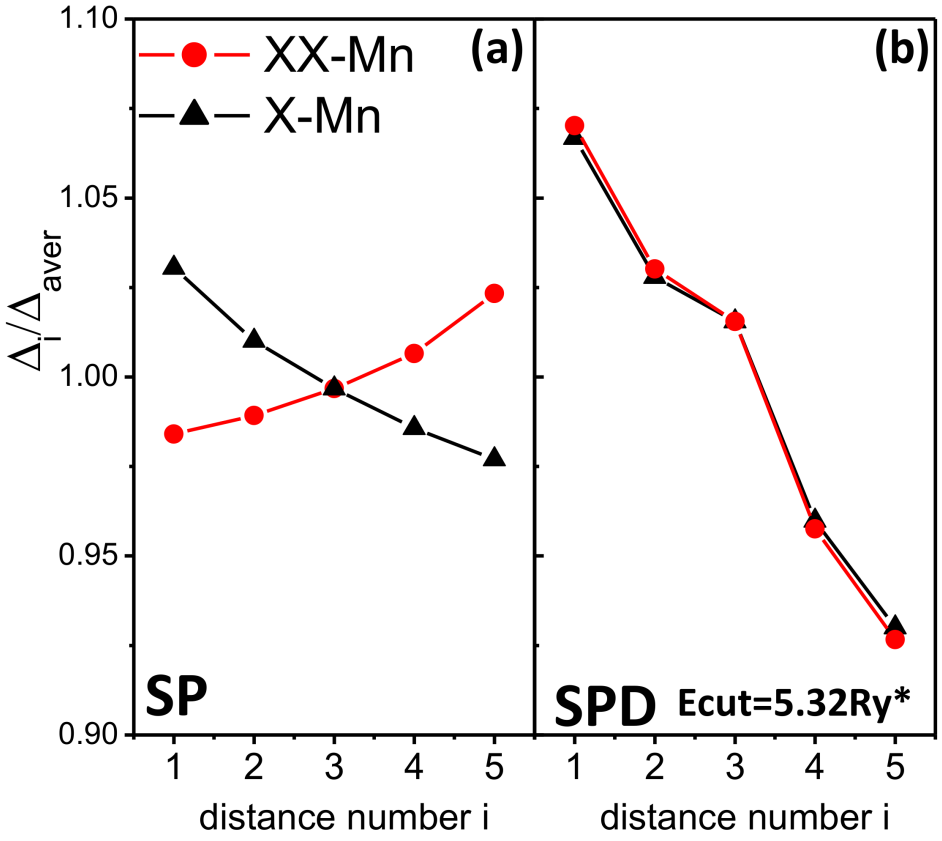

Figure 8.8: The normalized spacings of the emission lines $\Delta_i^{XX}/\Delta_{aver}$ and Δ_i/Δ_{aver} of the XX-Mn and X-Mn complex, calculated for the shallow (SP)(a) and deep quantum dot(SPD)(b). Black lines (triangles) correspond to the distances of emission lines of the X-Mn, while red lines (circles) to those of the XX-Mn complex.

However, one could potentially engineer the XX-Mn ground state splitting to exactly compensate the non-uniform distribution of X-Mn energy levels, and as a result obtain equally spaced emission from the XX-Mn complex. This effect could be achieved by changing the s-p single particle energy spacing or the anisotropy of the QD.

We now demonstrate that the gaps between XX-Mn energies δ_2 and δ_4 can be extracted from the emission data. In the X-Mn emission spectra one has direct access to all energies E_i, as well as all XX-Mn *emission maxima* L_i, as defined in Fig. 8.4 (b). The gaps between XX-Mn ground state energies are by definition: $\delta_2 = E_{XX3} - E_{XX2}$ and $\delta_4 = E_{XX5} - E_{XX4}$. From Fig. 8.4 it is evident that the position of the lowest XX-Mn emission maximum $L_1 = E_{XX2} - E_6$ (alternatively $L_1 = E_{XX2} - E_6$) while the second maximum $L_2 = E_{XX3} - E_5$. By subtracting L_1 from L_2 one gets:

$$\delta_2 \;=\; \Delta_1^{XX} - \Delta_5 = (L_2 - L_1) - (E_6 - E_5) \tag{8.18}$$

Similary one can show that:

$$\delta_4 \;=\; \Delta_2^{XX} - \Delta_4 = (L_3 - L_2) - (E_5 - E_4) \tag{8.19}$$

8.3 Fine structure of the XX-Mn as a function of the QD parameters

In this section the dependence of the XX-Mn ground state splittings (δ_{1-5}) on the size of the quantum dot and its anisotropy is investigated. The main splitting of the XX-Mn ground state δ_2 and δ_4 as a function of the s-p energy spacing $\Omega_e + \Omega_h$ is shown in Fig. 8.9 (a). The calculations were performed for four different ratio $r = \Omega_e/\Omega_h$=$\{1,2,3,4\}$, which are represented by various symbols ($r = 1$, squares, $r = 2$, stars, $r = 3$, triangles, $r = 4$, circles), and for four different s-p single-particle shell spacings $\Omega_e + \Omega_h = \{20, 30, 40, 50\}$ meV. The red-dashed lines showing the δ_4 splitting (multiplied by factor of 2), and the black-solid lines corresponding to the δ_2 splitting, are overlapping and have a linear dependence on the s-p energy spacing for each of the ratio $r = \Omega_e/\Omega_h$.

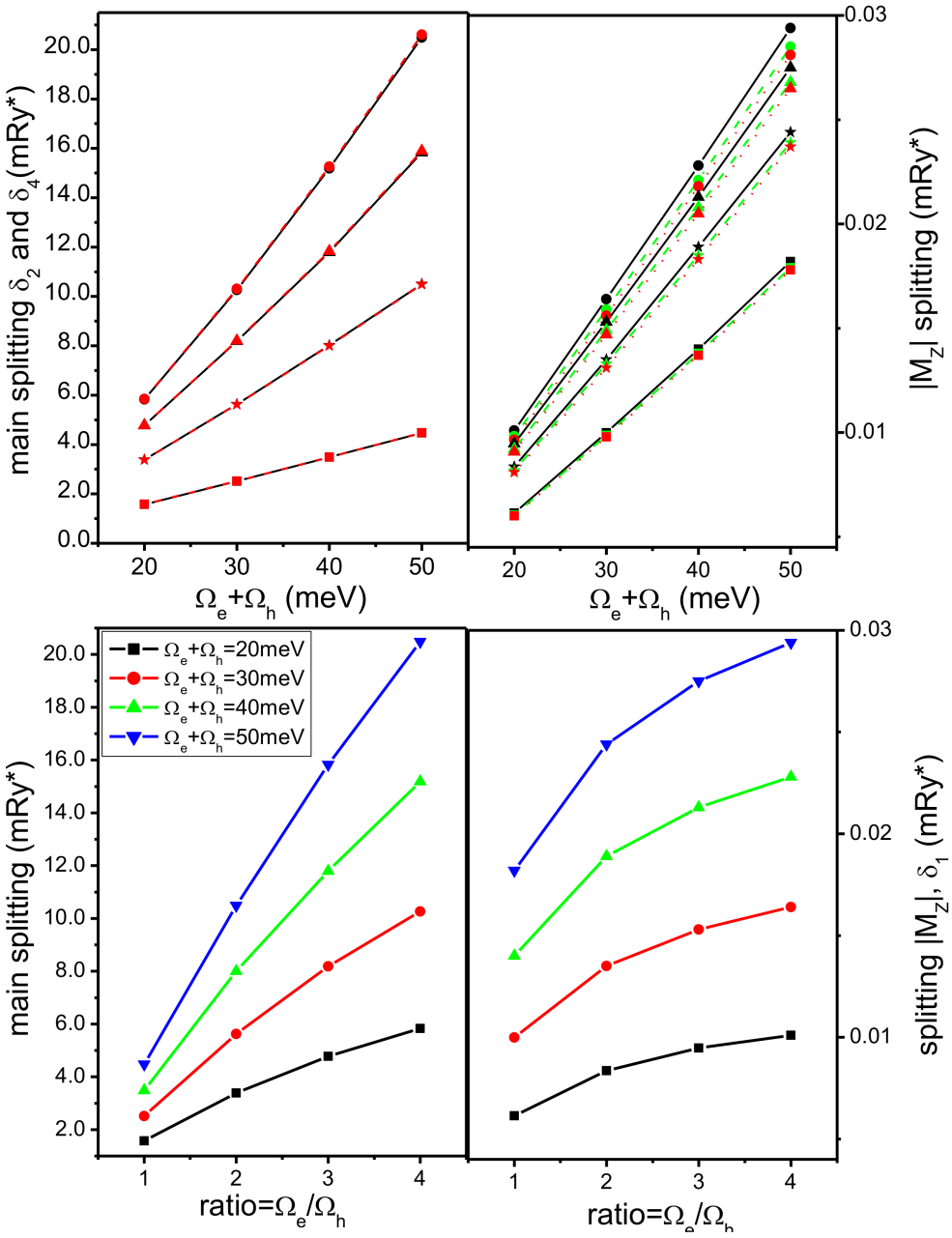

Figure 8.9: The splittings of the XX-Mn GS as as a function of the size of the quantum dot ($\Omega_e + \Omega_h$) calculated for different Ω_e/Ω_h ratios={1,2,3,4}. Panel (a) shows the main splittings of the XX-Mn GS: δ_2 (black-solid line) and $2 \times \delta_4$ (red-dashed line), while panel (b) shows the splittings between the XX-Mn states with $|M_z| = 5/2$ - δ_1 (black-solid line), $|M_z| = 3/2$ - $\delta_3 \times 5/3$ (green-dashed line) and $|M_z| = 1/2$ - $\delta_5 \times 5$ (red dotted line). Different ratios are differentiated by the symbols: ratio=1 (squares), ratio=2 (stars), ratio=3 (triangles), ratio=4 (circles). (c) The main (δ_2) and (d) $|M_z|$ (δ_1) splittings of XX-Mn GS, calculated for different s-p spacings $\Omega_e + \Omega_h$ and shown as a function of ratio $r = \Omega_e/\Omega_h$.

This can be understood in the following analysis. The splitting between XX-Mn states with $|M_z| = 5/2$ and the $|M_z| = 3/2$, can be approximated by the expression:

$$\delta_2 = 4\frac{\kappa^2}{E_{TS} - E_{SS}}. \tag{8.20}$$

The parameter $\kappa = \frac{3}{\sqrt{2}} A^{SS}_{ss-ss} J^h_{sd}(R)$ is poportional to the $J^h_{sd}(R)$, a scattering-exchange constant of the hole by Mn ion. For the QD with the Mn ion in the center, $R = (0,0)$, the magnitude of the exchange constant $J^h_{sd}(0)$, is equal to $J^h_{ss}(0) = J^h_{00,00}(0) = J^h_{2D}\frac{1}{2\pi}\frac{1}{l^{e\,2}_h}$ - and is inversely proportional to the area of the quantum dot l^e_h [152]. Since the inversion of the hybrid length $(l^e_h)^{-2} \approx \Omega^e_h$, the parameter κ is proportional to the electron intershell spacing Ω^e_h as well. On the other hand, the difference of the energy between the bare XX_{SS} and XX_{TS} levels $E_{TS} - E_{SS}$ is proportional to the s-p energy spacing $\Omega_e + \Omega_h$, while $\Omega_e + \Omega_h = \frac{1+r}{r}\Omega_e$. For a given ratio $r = \Omega_e/\Omega_h$, the main XX-Mn splitting is in fact proportional to the $\Omega_e + \Omega_h$:

$$\delta_2 \sim \frac{\kappa^2}{E_{TS} - E_{SS}} \sim \left(\frac{r}{r+1}\right)^2 (\Omega_e + \Omega_h)\,. \tag{8.21}$$

In Figure 8.9 (b) similar calculations for the spin-flip induced splitting of each of the three groups of XX-Mn levels are presented. The black-solid lines show the splittings between $M_z = \pm 5/2$ biexciton states (δ_1), the green-dashed lines correspond to the splittings between $M_z = \pm 3/2$ biexciton states (δ_3), while the red-dotted lines to splittings between $M_z = \pm 1/2$ (δ_5). The ratios are denoted with the symbols as explained in the caption of Fig. 8.9 (a). The splitting between each of the groups of levels is proportional to Mn spin projection M_z. To simplify the picture, the splitting δ_5 is multiplied by a factor of 5, while δ_3 by a factor 5/3, which alignes the lines corresponding to the same Ω_e/Ω_h ratio. The dependence of the $|M_z|$ splitting on the s-p single-particle shell spacings is also linear.

Since in the experiment it is easier to measure the s-p energy spacing $(\Omega_e + \Omega_h)$ than the ratio $r = \Omega_e/\Omega_h$, the same results as in Figs. 8.9 (a,b) can be presented in a different form. Fig. 8.9 shows the XX-Mn splittings δ_2 (c) and δ_1 (d) calculated for the different s-p energy spacing $\Omega_e + \Omega_h$ as a function of Ω_e/Ω_h ratio. The dependence of the δ_2 agrees with the relation, Eq. 8.21 derived previously.

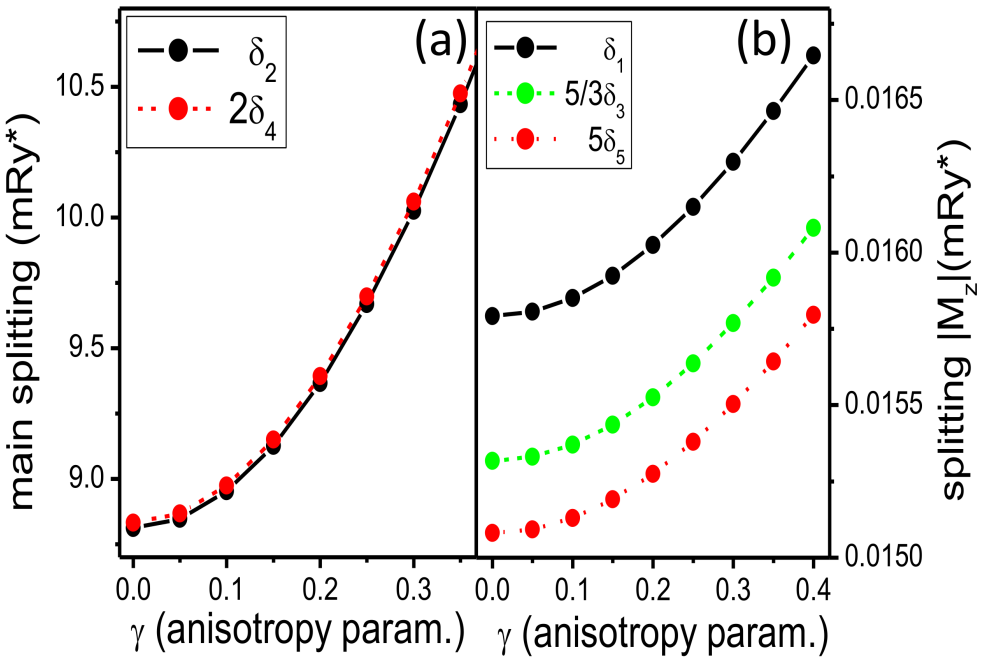

Figure 8.10: (a) The main δ_2 and $2\delta_4$ and (b) $|M_z|$ δ_1, $5/3\delta_3$ and $5\delta_5$ splittings of XX-Mn ground state, as a function of the anisotropy parameter γ.

The splittings δ_{1-5} of the ground state of the XX-Mn are analysed also as a function of the anisotropy of the QD (Fig. 8.10) which is parametrized by the anisotropy parameter γ. Fig. 8.10 (a) shows the main splittings of the XX-Mn GS δ_2 (black-solid line) and $2\delta_4$ (red-dashed line), while 8.10 (b) presents the $|M_z|$ splittings δ_1 (black-solid line), δ_3 (green-dashed line), and δ_5 (red-dotted line). The main splittings grow by approximately 23.5% when the anisotropy parameter changes from $\gamma = 0$ to $\gamma = 0.4$, while the $|M_z|$ splittings exhibit very weak dependence on the anisotropy of the QD, growing by approximately 4.7% in this range.

Figure 8.11 shows a measured (b) and calculated (a) X-Mn and XX-Mn emission spectra. Good agreement between experiment and theory can be seen [189]. Most of the parameters used in the calculations leading to the emission spectra presented in Fig. 8.11 (a) are the same as in the rest of this Chapter. However, the dielectric constant of the barrier (ZnTe) $\varepsilon = 7.4$, is used this time.

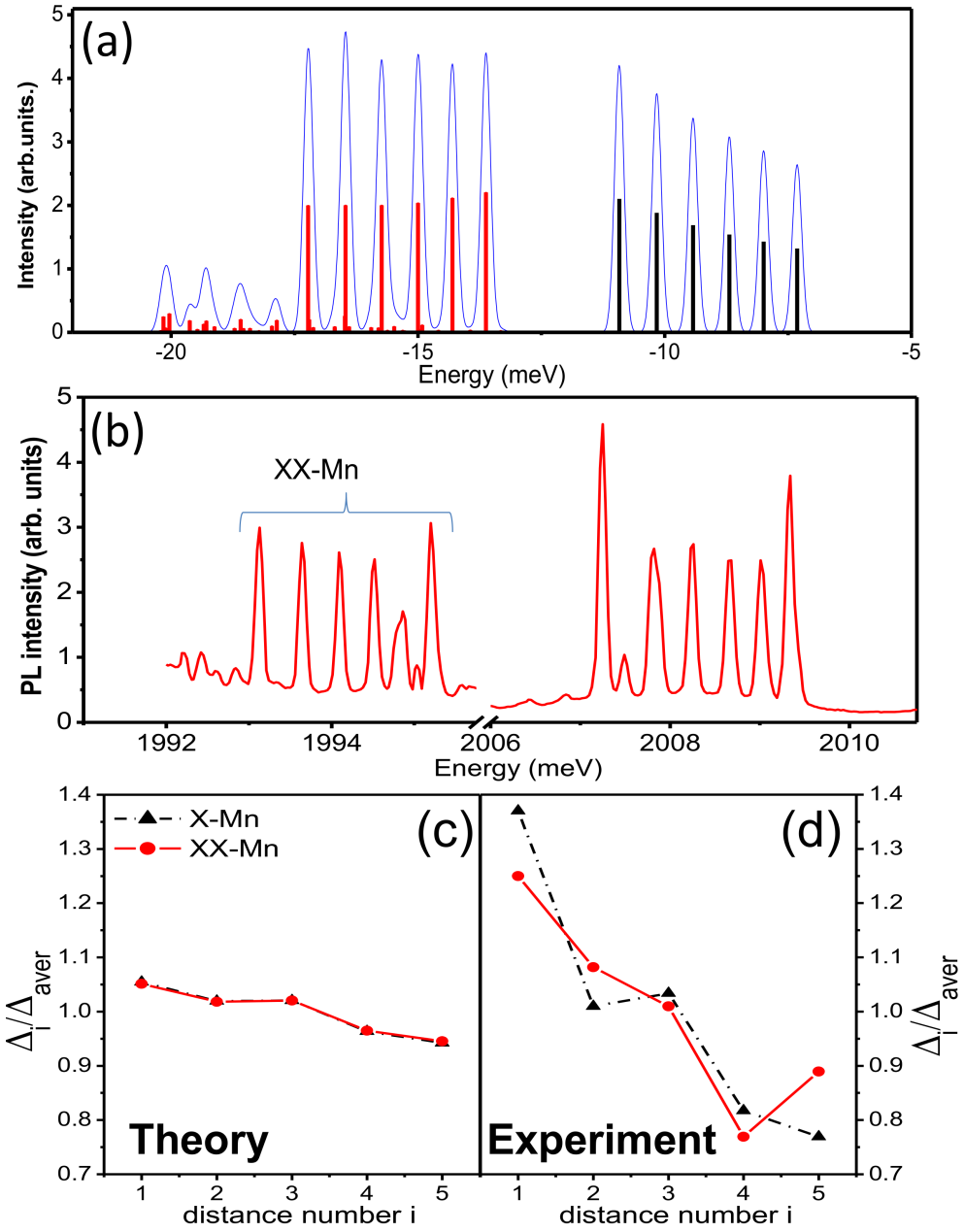

Figure 8.11: Computed (a) and measured (b) emission spectra of the QD, with the emission from X-Mn complex (black) and XX-Mn complex (red) calculated for the temperature $T = 75$ K. The lower panels show the normalized spacings of the emission lines (Δ_i/Δ_{aver}) of the X-Mn (black) and XX-Mn (red) (Δ_{aver} is average spacing) calculated (c), and extracted (d) from measured emission spectra.

Previously the dielectric constant of a CdTe $\varepsilon = 10.6$ was used. With this new dielectric constant the effective Rydberg is $Ry^* = 13.4$ meV. This change was motivated by the fact that screening of Coulomb interactions in mainly due to barrier material. The value of the dielectric constant is probably between 7.4 and 10.6.

The short-range and anisotropic electron-hole exchange exciton fine structure calculated with the bulk exchange parameters (μ^2, and E_{SR}), and the above material parameters, give the bright-dark exciton splitting $\Delta_0 = 0.45$ meV, the bright exciton splitting $\Delta_1 = 0.16$ meV, and the dark exciton splitting $\Delta_2 = 0$. For completenes, all other parameters are also given below. The shell spacing is taken to be $\Omega_h + \Omega_e = 30$ meV, and $\Omega_e/\Omega_h = 4$. The bulk e-Mn and h-Mn couplings are: $J^h_{c2D} = 60$ meV·nm^3 and $J^e_{c2D} = 15$ meV·nm^3. The height of the QD is $d = 2$ nm.

Figs. 8.11 (c) and (d) show the gaps between the calculated and measured maxima Δ_i/Δ_{aver} and $\Delta^{XX}_i/\Delta_{aver}$, respectively. As in Fig. 8.8, the calculated emission peak spacings for both X-Mn (black-dashed line) [151] and XX-Mn (red-solid line) *decrease* with increasing peak separation number i. Deviation from the linear decrease is due to the electron-hole exchange and anisotropy, as explained in Chapter 6. One needs to reemphasize that this tendency is *opposite* to that predicted by the spin model, where the peak spacing of XX-Mn is a mirror image of that of X-Mn (Fig. 8.4 (b)). The experimental results, presented in Fig. 8.11(d), show an identical trend to that predicted by the correlated exciton-Mn model.

In the X-Mn emission spectra one has direct access to all energies E_i, as well as all XX-Mn *emission maxima* L_i, as defined in Fig. 8.4 (b). By extracting these values from the presented experimental spectra one obtains the energy splitting of the XX-Mn complex. The energies E_{XX2}, and E_{XX3}, as well as E_{XX4} and E_{XX5} are separated by: $\delta_2 = E_{XX3} - E_{XX2} = (L_2 - L_1) - (E_6 - E_5) = 0.2$ meV, Eq. 8.18, and $\delta_4 = E_{XX5} - E_{XX4} = (L_3 - L_2) - (E_5 - E_4) = 0.105$ meV, Eq. 8.19. For comparison, the numerically calculated splittings of the XX-Mn are $\delta_2 = 0.079$ meV and $\delta_4 = 0.039$ meV, close to the ones extracted from experiments by Besombes *et al.* [156] ($\delta_2 = 0.075$ meV and $\delta_4 = 0.035$ meV).

The fine structure of the XX-Mn complex can also be detected directly by absorption of microwave radiation due to transistions in the Mn spin system as in NMR. The absorption of a photon requires change of angular momentum by one, with transitions of Mn spin from, e.g., $E_{-}(-5/2)$ to $E_{-}(-3/2)$ energy levels. The predicted absorbed photon energies would hence correspond to the two energy splittings, δ_2 and δ_4.

Chapter 9

Summary

In this Thesis I have presented studies of the electronic and optical properties of the self-assembled CdTe quantum dots containing a single magnetic Mn impurity. The presentation started with a general introduction to quantum dots and a short review of the methods of their fabrication describing two different methods of their fabrication. In the first method the lateral confinement is created by the metalic gates generating electrostatic field that locally depletes the two-dimensional electron gas. These QDs can confine only electrons. The second method uses the Stranski-Krastanow phase transition in the epitaxial growth of heterostructures. The QDs grown this way can confine both types of carriers: electrons and holes. The important experimental techniques used to probe the properties of carriers confined in the QDs have been briefly summarized.

In Chapter 2, the fundamental facts about the non-magnetic quantum dots have been presented, including a short overview of the methods of modeling of the QD confinement with the focus on the two-dimensional parabolic potential model within the effective mass approximation used throughout this Thesis. The methods of the analysis of many interacting particles have been discussed, followed by a detailed analysis of the electronic and optical properties of an exciton (an interacting electron-hole pair) confined in the QD as well as a short presentation of the multi-exciton complexes.

In Chapter 3 the electron-hole exchange in the basis of the harmonic oscillator functions has been derived and analysed. Its influence on the fine structure of the exciton complex has been discussed as a function of model parameters: the

number of confined shells, the anisotropy of the confining potential as well as the external magnetic field.

Next, in Chapter 4 I present an analysis of the electronic structure of the single Mn atom, and of the formation of bonds between Mn and neighbouring atoms in the crystal. The short-range exchange interaction between the Mn and carriers confined in the QD has also been analysed. The introduction of the magnetic moment into semiconductor material can be also achieved by fabrication of a lateral quadruple quantum dot which can confine electrons. It is shown here that one can turn on and off the magnetic moment created by the spin of the electrons confined in such structure by changing the number of confined carriers.

In Chapter 5, the computational approach to the problem of interacting carriers confined in a magnetic dot has been described. For both the exciton and bi-exciton complex the procedure consists of two steps. First, the Hamiltonian of the interacting electrons and holes in the symmetric confining potential of a nonmagnetic dot is diagonalized to obtain the correlated energies and wave functions. In the second step the electron-hole exchange interaction, anisotropy, as well as the electron-Mn and hole-Mn interactions are included, and Hamiltonian matrices are written in the basis of the correlated electron-hole states calculated in the first step of the procedure. This two-step procedure allows to reduce the computational power needed to carry out these calculations.

Chapter 6 begins with the description of the widely used spin-model of the interaction of the spins of electrons an holes with the spin of Mn ion. This model allows for a basic understanding of the exciton-Mn system. However, by comparing it with the fully microscopic, correlated model of the exciton-Mn complex, it is demonstrated that the spin model is an oversimplification. By using the microscopic description of the exciton-Mn interaction, a novel quantum interference effect is predicted, leading to the change of the strength of the interaction between the exciton and Mn ion. This effect originates from the correlated character of the confined excitons, and is therefore not captured by the simple spin model. The quantum interference is reflected in the optical spectra of this complex as a modification of the splitting of the emission/absorption lines as compared to the spin model. Moreover, the splitting between the lines becomes non-uniform as a

result of the Mn-induced interaction between ground and excited exciton states. This second signature of the QI is also reported here.

In Chapter 7 the magnetic-field evolution of the optical properties of the exciton-Mn complex has been analysed. It is compared to previously reported experimental results in which the coupling between the exciton and Mn ion is approximately constant in a wide range of the magntic field. This puzzling result indicates that the coupling between the Mn spin and the confined charge carriers does not depend on the magnetic field, contrary to an intuitively expected increase of the coupling due to the magnetic squeezing of carrier wave functions. The calculations in the fully microscopic model lead to the conclusion that the excitonic correlations are responsible for a near cancellation of the magnetic squeezing effect with increasing magnetic field.

In Chapter 8 the interaction between a bi-exciton and the Mn ion has been discussed. Since the ground state of the bi-exciton is spinless, it is not expected to interact with the magnetic impurity. However, the existence of the fine structe of the ground state of the biexciton-Mn complex has been predicted and its signature in the optical spectra was analysed. The existence of this novel fine structure of a spin-singlet system is again due to correlations, this time brought about by the scattering by the spin impurity from singlet to excited triplet state. The optical signatures of the XX-Mn fine structure are predicted theoretically and compared the experimental emission spectra.

Appendix A

.1 Envelope function and effective mass approximation

In the envelope function approximation (EFA), the state of an electron $\psi(\mathbf{r})$ is approximated by a product of a slowly varying envelope function $F(\mathbf{r})$ and a microscopic function $u(\mathbf{r})$ which varies on the scale of the Wigner-Seitz unit cell (WS): $\psi(\mathbf{r}) = F(\mathbf{r})u(\mathbf{r})$.

The electronic states in a periodic crystal satisfy the Bloch theorem $\phi_{n\mathbf{k}}(\mathbf{r}) = \exp(i\mathbf{kr})u_{n\mathbf{k}}(\mathbf{r})$, while $u_{n\mathbf{k}}(\mathbf{r}) = u_{n\mathbf{k}}(\mathbf{r}+\mathbf{R})$, where $u_{n\mathbf{k}}(\mathbf{r})$ is the periodic part of the Bloch function, $\mathbf{k}$ is the crystal momentum, and $\mathbf{R}$ is the lattice vector. The periodic part of the Bloch function at a crystal momentum $\mathbf{k}$ can be expanded as

$$u_{n\mathbf{k}}(\mathbf{r}) = \sum_{i=1}^{\infty} b_{in}(\mathbf{k})u_{i0}(\mathbf{r}) \tag{1}$$

because all bands at $\mathbf{k}$=0 form a complete set of functions. $b_{in}(\mathbf{k})$ are the expansion coefficients, whose exact form is not cecessary for the following considerations. In practice this expansion is truncated to some subset of bands.

Since the envelope $F(\mathbf{r})$ varies slowly with $\mathbf{r}$, one can further approximate it by the sum: $F(\mathbf{r}) = \sum_i A(\mathbf{R}_i)S(\mathbf{r}-\mathbf{R}_i)$. The discrete function $A(\mathbf{R}_i)$ has one value for each unit cell at the position $\mathbf{R}_i$, while the function $S(\mathbf{r}-\mathbf{R}_i)$ is the continuation of this discrete function and is defined as $S(\mathbf{r}-\mathbf{R}_i) = 1$ within the

unit cell at the position $\mathbf{R}_i$. From this assumption it follows that:

$$\begin{aligned}\int_{BvK} F(\mathbf{r})V(\mathbf{r})d\mathbf{r} &= \sum_i A(\mathbf{R}_i)\int_{BvK} S(\mathbf{r}-\mathbf{R}_i)V(\mathbf{r})d\mathbf{r} \\ &= \sum_i A(\mathbf{R}_i)\int_{WS(\mathbf{R}_i)} V(\mathbf{r})d\mathbf{r} \\ &= \frac{1}{V_{WS}}\int_{BvK} F(\mathbf{r})d\mathbf{r}\int_{WS(\mathbf{R}_i)} V(\mathbf{r})d\mathbf{r}\end{aligned} \tag{2}$$

and the last step follows from the fact that:

$$\int_{BvK} F(\mathbf{r})d\mathbf{r} = \sum_i A(\mathbf{R}_i)\int_{BvK} S(\mathbf{r}-\mathbf{R}_i)d\mathbf{r} = \sum_i A(\mathbf{R}_i)V_{WS(R_i)}. \tag{3}$$

The symbol BvK denotes the QD domain, while $WS(R_i)$ denotes the Wigner-Seitz cell at the position $\mathbf{R}_i$. In general the valence band (VB) and the conduction band (CB) wavefunctions can be written as:

$$\begin{aligned}\phi_v^j(\mathbf{r}) &= \sum_{r,\tau} A_{r\tau}^j F_v^{rj}(\mathbf{r})u_{v\tau}(\mathbf{r}), \quad v\tau \to -3/2, -1/2, 1/2, 3/2 \\ \phi_c^l(\mathbf{r}) &= \sum_{p,\sigma} A_{p\sigma}^l F_c^{pl}(\mathbf{r})u_{c\sigma}(\mathbf{r}), \quad c\sigma \to -1/2(\beta), 1/2(\alpha)\end{aligned}$$

In this work, all calculation are made in the effective mass approximation (EMA), which neglects the coupling between the bands. In EMA, each jth valence band electron (lth conduction band electron) state is labelled by its band index $v\tau$ ($c\sigma$) and the envelope label j (l):

$$\begin{aligned}\phi_{v\tau}^j(\mathbf{r}) &= F_v^j(\mathbf{r})u_{v\tau}(\mathbf{r}), \quad v\tau \to -3/2, -1/2, 1/2, 3/2 \\ \phi_{c\sigma}^l(\mathbf{r}) &= F_c^l(\mathbf{r})u_{c\sigma}(\mathbf{r}), \quad c\sigma \to -1/2(\beta), 1/2(\alpha)\end{aligned} \tag{4}$$

The microscopic part of the conduction and valence states are the periodic part of the Bloch functions at the Γ point. The microscopic functions in the conduction band have s symmetry in T_d crystals. They are labeled as $|c\alpha\rangle$ and $|c\beta\rangle$

for $s_z = 1/2$ and $s_z = -1/2$ electrons, respectively. In the spinor representation:

$$\begin{aligned} u_{c\alpha}(\mathbf{r}) &= \langle \mathbf{r}|c\alpha\rangle = \phi_s(r)\begin{pmatrix} Y_{00}(\hat{r}) \\ 0 \end{pmatrix} \\ u_{c\beta}(\mathbf{r}) &= \langle \mathbf{r}|c\beta\rangle = \phi_s(r)\begin{pmatrix} 0 \\ Y_{00}(\hat{r}) \end{pmatrix} \end{aligned} \tag{5}$$

On the other hand, the microscopic parts of the valence band have p symmetry. They are labeled according to the generalized angular momentum as $|v-3/2\rangle$, $|v-1/2\rangle$, $|v+1/2\rangle$,$|v+3/2\rangle$.

$$\begin{aligned} u_{v-3/2}(\mathbf{r}) = \langle \mathbf{r}|v-3/2\rangle &= \phi_p(r)\frac{|X\rangle - i|Y\rangle}{\sqrt{2}}|\downarrow\rangle = \phi_p(r)\begin{pmatrix} 0 \\ Y_{1-1}(\hat{r}) \end{pmatrix} \\ u_{v-1/2}(\mathbf{r}) = \langle \mathbf{r}|v-1/2\rangle &= \phi_p(r)\left(\frac{|X\rangle - i|Y\rangle}{\sqrt{6}}|\uparrow\rangle + \sqrt{\frac{2}{3}}|Z\rangle|\downarrow\rangle\right) \\ &= \phi_p(r)\begin{pmatrix} \sqrt{\frac{1}{3}}Y_{1-1}(\hat{r}) \\ \sqrt{\frac{2}{3}}Y_{10}(\hat{r}) \end{pmatrix} \\ u_{v+1/2}(\mathbf{r}) = \langle \mathbf{r}|v+1/2\rangle &= \phi_p(r)\left(-\frac{|X\rangle + i|Y\rangle}{\sqrt{6}}|\downarrow\rangle + \sqrt{\frac{2}{3}}|Z\rangle|\uparrow\rangle\right) \\ &= \phi_p(r)\begin{pmatrix} \sqrt{\frac{2}{3}}Y_{10}(\hat{r}) \\ \sqrt{\frac{1}{3}}Y_{11}(\hat{r}) \end{pmatrix} \\ u_{v+3/2}(\mathbf{r}) = \langle \mathbf{r}|v+3/2\rangle &= -\phi_p(r)\frac{|X\rangle + i|Y\rangle}{\sqrt{2}}|\uparrow\rangle = \phi_p(r)\begin{pmatrix} Y_{11}(\hat{r}) \\ 0 \end{pmatrix} \end{aligned} \tag{6}$$

where the spherical harmonics are given by:

$$\begin{aligned} Y_{00}(\theta,\phi) &= \frac{1}{\sqrt{4\pi}} \\ Y_{1-1}(\theta,\phi) &= \sqrt{\frac{3}{8\pi}} sin\theta \exp(-i\phi) \\ Y_{10}(\theta,\phi) &= \sqrt{\frac{3}{4\pi}} cos\theta \\ Y_{11}(\theta,\phi) &= -\sqrt{\frac{3}{8\pi}} sin\theta \exp(i\phi) \end{aligned} \tag{7}$$

The electrons excited to the conduction band leave behind unoccupied states in the valence band. The unoccupied state in the VB is called a hole, and its wave function can be described by taking a transformation of the function of VB electrons. To describe the hole wave function, the wave function of the electron in the VB: $\phi^j_{v\tau}(\mathbf{r}) = F^j_v(\mathbf{r})\, u_{v\tau}(\mathbf{r})$ is transformed into: $\psi^j_{v-\tau}(\mathbf{r}) = H^{j^+}_v(\mathbf{r})\, u_{vh-\tau}(\mathbf{r})$, where $H^j_v(\mathbf{r})$ is the hole envelope function, while $u_{vh-\tau}(\mathbf{r})$ is the microscopic part of the hole wavefunction.

Appendix B

.2 Derivation of the direct Coulomb matrix elements

The electron-electron Coulomb matrix elements in the two-dimensional harmonic oscillator basis have an analytical form derived by Hawrylak [114] and used later on in Refs. [101, 107]. Here the main points of this derivation will be presented (Ref. [53, 115]). The Coulomb potential expressed in the units of the effective Rydberg has the form:

$$v\left(\mathbf{r}_1-\mathbf{r}_2\right)=\frac{2}{\left|\mathbf{r}_1-\mathbf{r}_2\right|}, \tag{8}$$

with position variables in the units of Bohr radii.

The matrix element $V_{ee}(i\sigma, j\sigma'|k\sigma', l\sigma)$ (given by Eq. 2.25) is a matrix element of the Coulomb potential between the single-particle envelope wave functions: $F^{+}_{i\sigma}(\mathbf{r}_1)$,$F^{+}_{j\sigma'}(\mathbf{r}_2)$, $F_{k\sigma'}(\mathbf{r}_2)$ and $F_{l\sigma}(\mathbf{r}_1)$. The composite indices i, j, k and l describe the states in the harmonic-oscillator basis with the quantum numbers: $i=(n^{1i}_{+}, n^{1i}_{-})$, $j=(n^{2j}_{+}, n^{2j}_{-})$, $k=(n^{2k}_{+}, n^{2k}_{+})$, and $l=(n^{1l}_{+}, n^{1l}_{-})$, where the index enumerating the electrons is kept for transparency of the derivation. This matrix element can be symbolicaly written as:

$$V_{ee}(i\sigma, j\sigma'|k\sigma', l\sigma)=\langle i\sigma j\sigma'|v\left(\mathbf{r}_1-\mathbf{r}_2\right)|k\sigma' l\sigma\rangle, \tag{9}$$

while the function $v\left(\mathbf{r}_1-\mathbf{r}_2\right)$ can be expressed in terms of the plane waves. This

allows for the separation of the variables describing each of the particles:

$$\begin{aligned} V_{ee}(i\sigma, j\sigma'|k\sigma', l\sigma) &= \langle i\sigma|\langle j\sigma'|\sum_q \frac{4\pi}{q} e^{i\mathbf{q}(\mathbf{r}_1-\mathbf{r}_2)}|k\sigma'\rangle|l\sigma\rangle \\ &= \sum_q \frac{4\pi}{q}\langle i\sigma|e^{i\mathbf{q}\mathbf{r}_1}|l\sigma\rangle\langle j\sigma'|e^{i\mathbf{q}\mathbf{r}_2}|k\sigma'\rangle \\ &= \sum_q \frac{4\pi}{q}\cdot M_1 \cdot M_2. \end{aligned} \tag{10}$$

The next step is to calculate the single-particle matrix elements M_1 and M_2 of the form: $M_1 = \langle i\sigma|e^{i\mathbf{q}\mathbf{r}_1}|l\sigma\rangle$. To do so, the coordinates x and y for each particle are expressed in the language of the HO operators (Eq. 2.15).

$$e^{i\mathbf{q}\mathbf{r}_1} = e^{i\left[\frac{q_x l}{\sqrt{2}}\left(a_1+a_1^+ +b_1+b_1^+\right)+i\frac{q_y l}{\sqrt{2}}\left(a_1-a_1^+ -b_1+b_1^+\right)\right]} \tag{11}$$

Introducing the notation $Q = \frac{l_h^e}{\sqrt{2}}(q_x + iq_y)$ and using the Trotter-Suzuki formula:

$$e^{\hat{A}+\hat{B}} = e^{\hat{A}}e^{\hat{B}}e^{-\frac{1}{2}[\hat{A},\hat{B}]}, \tag{12}$$

one obtains:

$$\begin{aligned} e^{i\mathbf{q}\mathbf{r}_1} &= e^{-|Q|^2}e^{iQ^*a_1^+}e^{iQa_1}e^{iQb_1^+}e^{iQ^*b_1} \\ e^{-i\mathbf{q}\mathbf{r}_2} &= e^{-|Q|^2}e^{-iQ^*a_2^+}e^{-iQa_2}e^{-iQb_2^+}e^{-iQ^*b_2}. \end{aligned}$$

The matrix element $M_1 = \langle i\sigma|e^{i\mathbf{q}\mathbf{r}_1}|l\sigma\rangle$ does not depend on the spin of the particle, so the spin variables will be dropped in further derivation. Using the expansion of the Fock-Darwin states in terms of the HO operators (Eq.2.8), one can write the unit operator as:

$$\hat{\mathbf{1}} = \sum_{p1=0}^{\infty}\sum_{p2=0}^{\infty}|p1p2\rangle\langle p1p2| = \frac{1}{p1!p2!}\sum_{p1=0}^{\infty}\sum_{p2=0}^{\infty}(a_1^+)^{p_1}(b_1^+)^{p_2}|00\rangle\langle 00|(b_1)^{p_2}(a_1)^{p_1}. \tag{13}$$

Introducing the unit operator in this form, and using the expansion of the exponential operators in the Taylor series:

$$e^{iQa_1} = \sum_{s=0}^{\infty} \frac{(iQ)^s}{s!} a_1^s, \tag{14}$$

the matrix element M_1 will have the form:

$$\begin{aligned} M_1 &= \frac{1}{\sqrt{n_+^{1i}! n_-^{1i}! n_+^{1l}! n_-^{1l}!}} \sum_{p1=0}^{min(n_+^{1i}, n_+^{1l})} \sum_{p2=0}^{min(n_-^{1i}, n_-^{1l})} \frac{e^{-|Q|^2}}{p_1! p_2!} \\ &\times \langle 00 | b_1^{n_-^{1i}} a_1^{n_+^{1i}} \frac{(iQ^*)^{n_+^{1i}-p_1}}{(n_+^{1i}-p_1)!} \left(a_1^+\right)^{n_+^{1i}-p_1} \frac{(iQ)^{n_-^{1i}-p_2}}{(n_-^{1i}-p_2)!} \left(b_1^+\right)^{n_-^{1i}-p_2} \left(a_1^+\right)^{p_1} \left(b_1^+\right)^{p_2} |00\rangle \\ &\times \langle 00 | b_1^{p_2} a_1^{p_1} \frac{(iQ)^{n_+^{1l}-p_1}}{(n_+^{1l}-p_1)!} (a_1)^{n_+^{1l}-p_1} \frac{(iQ^*)^{n_-^{1l}-p_2}}{(n_-^{1l}-p_2)!} (b_1)^{n_-^{1l}-p_2} \left(a_1^+\right)^{n_+^{1l}} \left(b_1^+\right)^{n_-^{1l}} |00\rangle. \end{aligned} \tag{15}$$

This form follows the fact that only one of the terms in the power expansion of each of the exponent opetators results in the non-zero matrix element.

Application of all of the HO operators gives:

$$\begin{aligned} M_1 &= \frac{e^{-|Q|^2}}{\sqrt{n_+^{1i}! n_-^{1i}! n_+^{1l}! n_-^{1l}!}} \sum_{p1=0}^{min(n_+^{1i}, n_+^{1l})} \sum_{p2=0}^{min(n_-^{1i}, n_-^{1l})} p_1! p_2! \binom{n_+^{1i}}{p_1} \binom{n_+^{1l}}{p_1} \binom{n_-^{1i}}{p_2} \binom{n_-^{1l}}{p_2} \\ &\times (iQ^*)^{n_+^{1i}-p_1} (iQ)^{n_-^{1i}-p_2} (iQ)^{n_+^{1l}-p_1} (iQ^*)^{n_-^{1l}-p_2} \end{aligned} \tag{16}$$

The matrix element M_2 for the second particle has an analogous form. Now, the

Coulomb interaction matrix element (Eq. 10) can be calculated as:

$$
\begin{aligned}
V_{ee}(i\sigma, j\sigma'|k\sigma', l\sigma) &= \frac{1}{4\pi^2}\int_0^\infty qdq \int_0^{2\pi} q\phi_q \frac{4\pi}{q} M_1 M_2 \\
= \frac{1}{\pi}\frac{1}{\sqrt{n_+^{1i}!n_-^{1i}!n_+^{1l}!n_-^{1l}!n_+^{2j}!n_-^{2j}!n_+^{2k}!n_-^{2k}!}} &\sum_{p1=0}^{min(n_+^{1i},n_+^{1l})} p_1! \binom{n_+^{1i}}{p_1}\binom{n_+^{1l}}{p_1} \\
\times \sum_{p2=0}^{min(n_-^{1i},n_-^{1l})} p_2! \binom{n_-^{1i}}{p_2}\binom{n_-^{1l}}{p_2} &\sum_{p3=0}^{min(n_+^{2j},n_+^{2k})} p_3! \binom{n_+^{2j}}{p_3}\binom{n_+^{2k}}{p_3} \\
\times \sum_{p4=0}^{min(n_-^{2j},n_-^{2k})} p_4! \binom{n_-^{2j}}{p_4}\binom{n_-^{2k}}{p_4} &\times I_{p_1p_2p_3p_4}
\end{aligned}
\tag{17}
$$

where the integral:

$$
\begin{aligned}
I_{p_1p_2p_3p_4} &= \int_0^\infty qdq \int_0^{2\pi} q\phi_q e^{-2|Q|^2} (iQ^*)^{n_+^{1i}-p_1} (iQ)^{n_-^{1i}-p_2} (iQ)^{n_+^{1l}-p_1} (iQ^*)^{n_-^{1l}-p_2} \\
&\times (-iQ^*)^{n_+^{2j}-p_3} (-iQ)^{n_-^{2j}-p_4} (-iQ)^{n_+^{2k}-p_3} (-iQ^*)^{n_-^{2k}-p_4}.
\end{aligned}
\tag{18}
$$

Since the variable Q is a complex number and $Q = \frac{l_h^e}{\sqrt{2}}(q_x + iq_y)$, the variable q in the integral $I_{p_1p_2p_3p_4}$ can be changed to Q in the following way: $Q = |Q|e^{i\phi_q} = \frac{l_h^e}{\sqrt{2}} q e^{i\phi_q}$, and $dq = d|Q|\frac{\sqrt{2}}{l_h^e}$. The integral can be separated into two integrals - one over Q:

$$
\begin{aligned}
&\frac{\sqrt{2}}{l_h^e}\int_0^\infty d|Q|e^{-2|Q|^2} (iQ)^{n_+^{1i}+n_-^{1i}+n_+^{1l}+n_-^{1l}+n_+^{2j}+n_-^{2j}+n_+^{2k}+n_-^{2k}-2p_1-2p_2-2p_3-2p_4} \\
&\times(-1)^{n_+^{2j}+n_-^{2j}+n_+^{2k}+n_-^{2k}},
\end{aligned}
\tag{19}
$$

and one integral over the angle ϕ_q:

$$
\int_0^{2\pi} d\phi_q e^{i\phi_q\left(-n_+^{1i}+n_-^{1i}+n_+^{1l}-n_-^{1l}-n_+^{2j}+n_-^{2j}+n_+^{2k}-n_-^{2k}\right)} = 2\pi\delta_{L_L,L_R},
\tag{20}
$$

where L_L is the angular momentum of the pair of electrons on the left side of

the Coulomb interaction matrix element (particle i and j), and L_R is the angular momentum of the pair of electrons on the right side of the matrix element (particle k and j). Using the identity that follows from the conservation of the angular momentum: $n_+^{1i}+n_+^{2j}+n_-^{1l}+n_-^{2k}=+n_+^{1l}+n_+^{2k}+n_-^{1i}+n_-^{2j}$, one can rewrite the exponent in the integral over Q: $n_+^{1i}+n_-^{1i}+n_+^{1l}+n_-^{1l}+n_+^{2j}+n_-^{2j}+n_+^{2k}+n_-^{2k}-2p_1-2p_2-2p_3-2p_4=2\left(n_+^{1i}+n_+^{2j}+n_-^{1l}+n_-^{2k}-p_1-p_2-p_3-p_4\right)=2p$. Then the integral $I_{p_1p_2p_3p_4}$ takes the form:

$$I_{p_1p_2p_3p_4}=2\pi\frac{\sqrt{2}}{l_h^e}\int_0^\infty d|Q|e^{-2|Q|^2}\left(Q\right)^{2p}\left(-1\right)^p\left(-1\right)^{n_+^{2j}+n_-^{2j}+n_+^{2k}+n_-^{2k}}\delta_{L_L,L_R}. \quad (21)$$

After changing integration variables one more time to $x=2Q^2$:

$$\begin{aligned} I_{p_1p_2p_3p_4} &= \delta_{L_L,L_R}\frac{\pi}{l_h^e}\left(-\frac{1}{2}\right)^p\left(-1\right)^{n_+^{2j}+n_-^{2j}+n_+^{2k}+n_-^{2k}}\int_0^\infty dxe^{-x}\left(x\right)^{p+1/2-1} \\ &= \delta_{L_L,L_R}\frac{\pi}{l_h^e}\left(-\frac{1}{2}\right)^p\left(-1\right)^{n_+^{2j}+n_-^{2j}+n_+^{2k}+n_-^{2k}}\Gamma\left(p+\frac{1}{2}\right). \end{aligned} \quad (22)$$

Finally, the Coulomb interaction matrix element (Eq.17) attains the form:

$$\begin{aligned} V_{ee}(i\sigma,j\sigma'|k\sigma',l\sigma) &= \frac{1}{l_h^e}\delta_{L_L,L_R}\frac{\left(-1\right)^{n_+^{2j}+n_-^{2j}+n_+^{2k}+n_-^{2k}}}{\sqrt{n_+^{1i}!n_-^{1i}!n_+^{1l}!n_-^{1l}!n_+^{2j}!n_-^{2j}!n_+^{2k}!n_-^{2k}!}} \\ &\times\sum_{p1=0}^{min(n_+^{1i},n_+^{1l})}p_1!\binom{n_+^{1i}}{p_1}\binom{n_+^{1l}}{p_1}\sum_{p2=0}^{min(n_-^{1i},n_-^{1l})}p_2!\binom{n_-^{1i}}{p_2}\binom{n_-^{1l}}{p_2} \\ &\times\sum_{p3=0}^{min(n_+^{2j},n_+^{2k})}p_3!\binom{n_+^{2j}}{p_3}\binom{n_+^{2k}}{p_3}\sum_{p4=0}^{min(n_-^{2j},n_-^{2k})}p_4!\binom{n_-^{2j}}{p_4}\binom{n_-^{2k}}{p_4}\left(-\frac{1}{2}\right)^p\Gamma\left(p+\frac{1}{2}\right) \end{aligned} \quad (23)$$

Appendix C

.3 Definition of the problem

The first step in the description of the electron-hole exchange interaction is the explanation of the terms and notions used. Figure 1 (a) shows the reference state with the valence band filled with electrons and an empty conduction band. The excited state of the system is shown in Figs. 1 (b) and (c). The excited state is created by a transfer of the electron from the valence to the conduction band. In Figs. 1(b) and (c) there is one additional electron in the conduction band with a spin of 1/2. The valence band can be described as a full valence band with one missing electron with a spin of 1/2, Fig. 1(b), or from the point of view of holes - a band with one hole with the spin of $-1/2$ Fig. 1(c) (after removal an electron with a spin of 1/2 the valence band has an uncompensated spin of $-1/2$ which is called the spin of a hole). The origin of the electron-hole exchange Coulomb interaction becomes clear if one uses the language of the missing electrons in the valence band. For that reason, in this Chapter the language of electrons in the valence band will be used and the final result will be translated into the language of the electron in the conduction band and the hole in a the valence band.

The Coulomb interaction Hamiltonian between two electrons has the form:

$$\hat{H}_V = \frac{1}{2}\sum_{i'j'k'l'}\sum_{\sigma,\sigma'\sigma'',\sigma'''} V_{ee}(i'\sigma, j'\sigma'|k'\sigma'', l'\sigma''')c^+_{i'\sigma}c^+_{j'\sigma'}c_{k'\sigma''}c_{l'\sigma'''} \qquad (24)$$

where the matrix element $V_{ee}(i'\sigma, j'\sigma'|k'\sigma'', l'\sigma''')$ is given by the Eq. 2.23, while $c_{i'\sigma}$ and $c^+_{i'\sigma}$ are the anihilation and creation operators of the electron with the

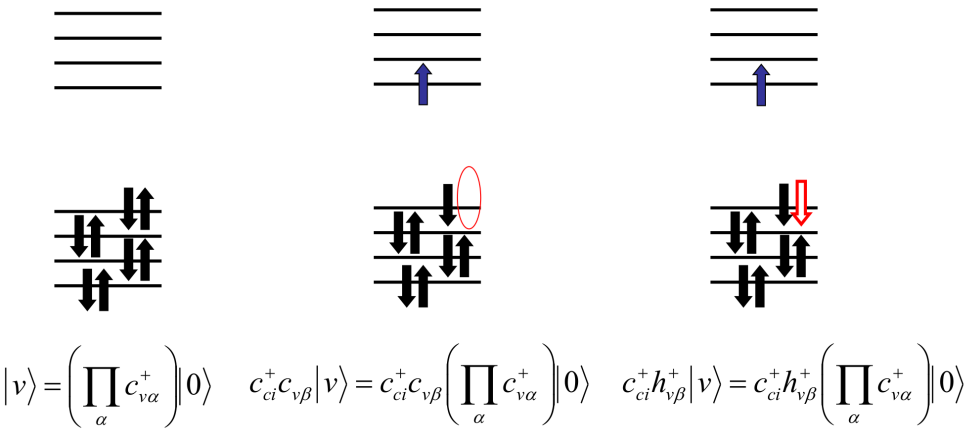

Figure 1: Illustration of two different languages used to describe the simplest excited state of a semiconductor.

spin σ in the state i', where i' denotes the set of the orbital quantum numbers appropriate to describe this state.

The matrix element of the Coulomb interaction between two configurations, $\langle L| = \langle ci\sigma, vj\tau| = \langle 0|c_{i\sigma}c^+_{j\tau}$ and $|R\rangle = |vk\tau', cl\sigma'\rangle = c_{k\tau'}c^+_{l\sigma'}|0\rangle$, will be calculated. The electron with quantum numbers described by $i\sigma$ ($l\sigma'$) is in the conduction band, while the quantum numbers $j\tau$ ($k\tau'$) describe a *missing electron* in the valence band.

The matrix element of the Coulomb intection between these configurations consists of two terms, direct and exchange (in the same way as that between two electrons in the conduction band):

$$\begin{aligned}\langle L|\hat{H}_V|R\rangle &= \sum_{i'j'k'l'}\sum_{\sigma,\sigma'\sigma'',\sigma'''}\langle 0|c_{i\sigma}c^+_{j\tau}\{c^+_{i'\sigma}c^+_{j'\sigma'}c_{k'\sigma''}c_{l'\sigma'''}\}c_{k\tau'}c^+_{l\sigma'}|0\rangle V_{ee}(i'\sigma, j'\sigma'|k'\sigma'', l'\sigma''') \\ &= -V^D_{ee}(ci\sigma, vk\tau'|vj\tau, cl\sigma') + V^X_{ee}(ci\sigma, vk\tau'|cl\sigma', vj\tau). \qquad (25)\end{aligned}$$

Note, that there is no $1/2$ factor in this matrix element, since the indices i' and l' go over the conduction band states, while the indices k' and j' go over the valence band states.

.4 Calculation of Exchange Matrix Elements

.4.1 Division into the short- and long-range electron-hole exchange

The direct part of the Coulomb interaction matrix elements is given by

$$V_{ee}^{D}(ci\sigma, vk\tau'|vj\tau, cl\sigma') = 2\iint\limits_{BvK} d\mathbf{r}_1' d\mathbf{r}_2' \frac{q_1(\mathbf{r}_1')q_2(\mathbf{r}_2')}{|\mathbf{r}_1' - \mathbf{r}_2'|}$$
$$q_1(\mathbf{r}_1') = F_{ci}^{+}(\mathbf{r}_1')u_{c\sigma}^{+}(\mathbf{r}_1')F_{cl}(\mathbf{r}_1')u_{c\sigma'}(\mathbf{r}_1')$$
$$q_2(\mathbf{r}_2') = F_{vk}^{+}(\mathbf{r}_2')u_{v\tau'}^{+}(\mathbf{r}_2')F_{vj}(\mathbf{r}_2')u_{v\tau}(\mathbf{r}_2')$$

where the wave functions of the conduction and valence band electron have been explicitly written as products of a slowly varying envelope $F(\mathbf{r})$ and a microscopic part $u(\mathbf{r})$ (defined by Eq. 4 in the Appendix A.1). This integral is a Coulomb interaction between two *generalized charges*, where each charge is a product of two conduction or valence band wave functions. If the integration over the microscopic part is carried out, as in the case of Eqs. 2.24 and 2.25, this integral is approximated as:

$$\begin{aligned} &V_{ee}^{D}(ci\sigma, vk\tau'|vj\tau, cl\sigma') \\ &= \delta_{\sigma\sigma'}\delta_{\tau\tau'}\iint\limits_{BvK} d\mathbf{r}_1' d\mathbf{r}_2' F_{ci}^{+}(\mathbf{r}_1')F_{vj}(\mathbf{r}_2')\frac{2}{|\mathbf{r}_1' - \mathbf{r}_2'|}F_{vk}^{+}(\mathbf{r}_2')F_{cl}(\mathbf{r}_1') \end{aligned} \tag{26}$$

The exchange matrix element can be compared to the Coulomb interaction of the two charges as well:

$$V_{ee}^{X}(ci\sigma, vk\tau'|cl\sigma', vj\tau) = 2\iint\limits_{BvK} d\mathbf{r}_1' d\mathbf{r}_2' \frac{q_1(\mathbf{r}_1')q_2(\mathbf{r}_2')}{|\mathbf{r}_1' - \mathbf{r}_2'|} \tag{27}$$
$$q_1(\mathbf{r}_1') = F_{ci}^{+}(\mathbf{r}_1')u_{c\sigma}^{+}(\mathbf{r}_1')F_{vj}(\mathbf{r}_1')u_{v\tau}(\mathbf{r}_1')$$
$$q_2(\mathbf{r}_2') = F_{vk}^{+}(\mathbf{r}_2')u_{v\tau'}^{+}(\mathbf{r}_2')F_{cl}(\mathbf{r}_2')u_{c\sigma'}(\mathbf{r}_2').$$

Each of the charges is now a product of the wave function of the electron in the valence band and the electron in the conduction band. The goal now is to integrate out the microscopic part of this integral. It is useful to divide the integration region (the QD domain) into two parts: the short-ranged part, where the electron and the hole can be found in the same Wigner-Seitz unit cell, and the long-range part, where they are in different cells. The full integration region (QD domain) will be refered to as the Born-von Karman cell (BvK) and the individual unit cell within the BvK cell as the Wigner-Seitz cell (WS). The double integration over the BvK cell (which consists of N_{cell} WS cells) is replaced by $N_{cell} \times N_{cell}$ integrals over WS cells. One can write

$$\int_{\mathbf{r}'_1 \in BvK} \int_{\mathbf{r}'_2 \in BvK} d\mathbf{r}'_1 d\mathbf{r}'_2 \longrightarrow \tag{28}$$
$$\sum_{q=1}^{N_{cell}} \int_{\mathbf{r}_1 \in WS(\mathbf{R}_q)} \int_{\mathbf{r}_2 \in WS(\mathbf{R}_q)} d\mathbf{r}_1 d\mathbf{r}_2 + \sum_{q,p=1, q \neq p}^{N_{cell}} \int_{\mathbf{r}_1 \in WS(\mathbf{R}_q)} \int_{\mathbf{r}_2 \in WS(\mathbf{R}_p)} d\mathbf{r}_1 d\mathbf{r}_2,$$

where $\mathbf{R}_q$ and $\mathbf{R}_p$ describe the position of the WS cells as shown in Fig 2. The

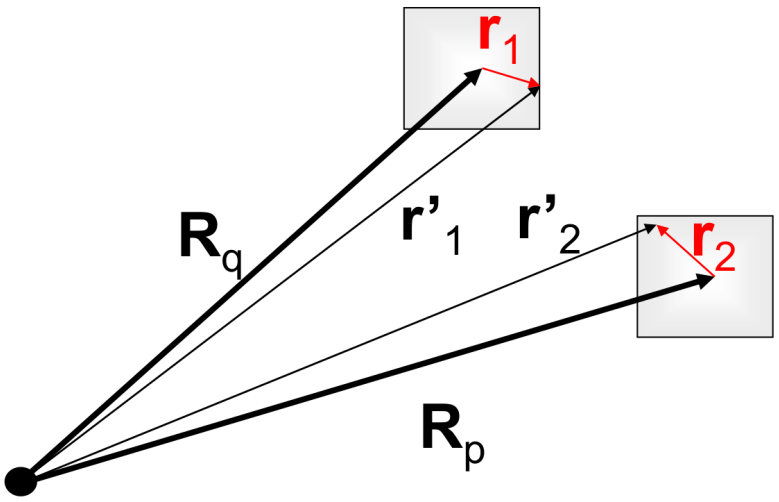

Figure 2: Schematic picture explaining the notation and relations between the integration variables in the BvK cell r'_1 and r'_2, the variables describing the position of the WS cell R_p and R_q, and the variables within a WS cell r_1 and r_2.

first term in the equation (28) consists of N_{cell} integrals, in which $\mathbf{r}_1$ and $\mathbf{r}_2$ go over the same cell (short-range exchange integral), whereas the second term consists of $N_{cell} \times (N_{cell} - 1)$ integrals, in which $\mathbf{r}_1$ and $\mathbf{r}_2$ go over two distinct WS cells (long-range exchange integral). Therefore, the exchange matrix element is decomposed into the short-range exchange V^E_{SR} and long-range exchange V^E_{LR} parts as: $V^E(ci\sigma, vk\tau'|cl\sigma', vj\tau) = V^E_{SR}(ci\sigma, vk\tau'|cl\sigma', vj\tau) + V^E_{LR}(ci\sigma, vk\tau'|cl\sigma', vj\tau)$'.

In more detail,

$$
\begin{aligned}
&V^X_{ee}(ci\sigma, vk\tau'|cl\sigma', vj\tau) = \\
&= 2 \iint\limits_{BvK} d\mathbf{r}'_1 d\mathbf{r}'_2 \frac{F^+_{ci}(\mathbf{r}'_1) u^+_{c\sigma}(\mathbf{r}'_1) F_{vj}(\mathbf{r}'_1) u_{v\tau}(\mathbf{r}'_1) F^+_{vk}(\mathbf{r}'_2) u^+_{v\tau'}(\mathbf{r}'_2) F_{cl}(\mathbf{r}'_2) u_{c\sigma'}(\mathbf{r}'_2)}{|\mathbf{r}'_1 - \mathbf{r}'_2|} \\
&= 2 \sum_q \sum_p \iint\limits_{BvK} d\mathbf{r}'_1 d\mathbf{r}'_2 \frac{u^+_{c\sigma}(\mathbf{r}'_1) u_{v\tau}(\mathbf{r}'_1) u^+_{v\tau'}(\mathbf{r}'_2) u_{c\sigma'}(\mathbf{r}'_2)}{|\mathbf{r}'_1 - \mathbf{r}'_2|} \\
&\times A^+_{ci}(\mathbf{R}_q) A_{vj}(\mathbf{R}_q) A^+_{vk}(\mathbf{R}_p) A_{cl}(\mathbf{R}_p) S(\mathbf{r}'_1 - \mathbf{R}_q) S(\mathbf{r}'_2 - \mathbf{R}_p).
\end{aligned}
$$

The expression for the slowly varying envelope function $F(\mathbf{r}) = \sum_q A(\mathbf{R}_q) S(\mathbf{r} - \mathbf{R}_q)$ described in the Appendix A.1 was used. In the second step the variables $\mathbf{r}'_1 - \mathbf{R}_q = \mathbf{r}_1$ and $\mathbf{r}'_2 - \mathbf{R}_p = \mathbf{r}_2$ will be changed. Since the function $S(\mathbf{r}'_1 - \mathbf{R}_q)$ ($S(\mathbf{r}'_2 - \mathbf{R}_p)$) is equal to 0 outside of the unit cell described by position vector $\mathbf{R}_q$ ($\mathbf{R}_p$), the integration region over $\mathbf{r}_1$ ($\mathbf{r}_2$) can be changed to the unit cell WS($\mathbf{R}_q$)

(WS($\mathbf{R}_p$)).

$$
\begin{aligned}
&V_{ee}^X(ci\sigma, vk\tau'|cl\sigma', vj\tau) = \\
&= 2\sum_q \sum_p \int\limits_{WS(\mathbf{R}_q)} \int\limits_{WS(\mathbf{R}_p)} d\mathbf{r}_1 d\mathbf{r}_2 \frac{u_{c\sigma}^+(\mathbf{r}_1+\mathbf{R}_q)u_{v\tau}(\mathbf{r}_1+\mathbf{R}_q)u_{v\tau'}^+(\mathbf{r}_2+\mathbf{R}_p)u_{c\sigma'}(\mathbf{r}_2+\mathbf{R}_p)}{|\mathbf{r}_1+\mathbf{R}_q-\mathbf{r}_2-\mathbf{R}_p|} \\
&\times A_{ci}^+(\mathbf{R}_q)A_{vj}(\mathbf{R}_q)A_{vk}^+(\mathbf{R}_p)A_{cl}(\mathbf{R}_p) \\
&= 2\sum_q \int\limits_{WS(\mathbf{R}_q)} \int\limits_{WS(\mathbf{R}_i)} d\mathbf{r}_1 d\mathbf{r}_2 \frac{u_{c\sigma}^+(\mathbf{r}_1)u_{v\tau}(\mathbf{r}_1)u_{v\tau'}^+(\mathbf{r}_2)u_{c\sigma'}(\mathbf{r}_2)}{|\mathbf{r}_1-\mathbf{r}_2|} \\
&\times A_{ci}^+(\mathbf{R}_q)A_{vj}(\mathbf{R}_q)A_{vk}^+(\mathbf{R}_q)A_{cl}(\mathbf{R}_q) \\
&+2\sum_q \sum_p \int\limits_{WS(\mathbf{R}_q)} \int\limits_{WS(\mathbf{R}_p)} d\mathbf{r}_1 d\mathbf{r}_2 \frac{u_{c\sigma}^+(\mathbf{r}_1+\mathbf{R}_q)u_{v\tau}(\mathbf{r}_1+\mathbf{R}_q)u_{v\tau'}^+(\mathbf{r}_2+\mathbf{R}_p)u_{c\sigma'}(\mathbf{r}_2+\mathbf{R}_p)}{|\mathbf{r}_1+\mathbf{R}_q-\mathbf{r}_2-\mathbf{R}_p|} \\
&\times A_{ci}^+(\mathbf{R}_q)A_{vj}(\mathbf{R}_q)A_{vk}^+(\mathbf{R}_p)A_{cl}(\mathbf{R}_p) \\
&= V_{SR}^X(ci\sigma, vk\tau'|cl\sigma', vj\tau) + V_{LR}^X(ci\sigma, vk\tau'|cl\sigma', vj\tau).
\end{aligned}
$$

The short-range interaction part is given by:

$$
\begin{aligned}
&V_{SR}^X(ci\sigma, vk\tau'|cl\sigma', vj\tau) \\
&= \sum_q I_{SR}\left(ci\sigma, vk\tau'|cl\sigma', vj\tau\right) \times A_{ci}^+(\mathbf{R}_q)A_{vj}(\mathbf{R}_q)A_{vk}^+(\mathbf{R}_q)A_{cl}(\mathbf{R}_q),
\end{aligned} \tag{29}
$$

while the long-range interaction part is:

$$
\begin{aligned}
&V_{LR}^X(ci\sigma, vk\tau'|cl\sigma', vj\tau) \\
&= \sum_q \sum_p I_{LR}^{qp}(ci\sigma, vk\tau'|cl\sigma', vj\tau) \times A_{ci}^+(\mathbf{R}_q)A_{vj}(\mathbf{R}_q)A_{vk}^+(\mathbf{R}_p)A_{cl}(\mathbf{R}_p).
\end{aligned} \tag{30}
$$

.4.2 Short-range exchange

The microscopic integral of the short-range exchange has the form:

$$I_{SR}\left(ci\sigma, vk\tau'|cl\sigma', vj\tau\right) = 2 \int\limits_{WS(\mathbf{R}_q)} \int\limits_{WS(\mathbf{R}_q)} d\mathbf{r}_1 d\mathbf{r}_2 \frac{u^+_{c\sigma}(\mathbf{r}_1) u_{v\tau}(\mathbf{r}_1) u^+_{v\tau'}(\mathbf{r}_2) u_{c\sigma'}(\mathbf{r}_2)}{|\mathbf{r}_1 - \mathbf{r}_2|}. \tag{31}$$

Using the multipole expansion for $1/|\mathbf{r}_1 - \mathbf{r}_2|$:

$$\frac{1}{|\mathbf{r}_1 - \mathbf{r}_2|} = 4\pi \sum_l \sum_{m=-l}^{l} \frac{1}{2l+1} \frac{r^l_<}{r^{l+1}_>} Y^*_{lm}(\Omega') Y_{lm}(\Omega) \tag{32}$$

and the fact that $u_{c\sigma}(\mathbf{r}) = \phi_s(\mathbf{r}) \times Y_{c\sigma}(\Omega)$, $u_{v\tau}(\mathbf{r}) = \phi_p(\mathbf{r}) \times Y_{v\tau}(\Omega)$, one can obtain the expression for the short-range exchange microscopic integral:

$$\begin{aligned} & I_{SR}\left(ci\sigma, vk\tau'|cl\sigma', vj\tau\right) = \\ = \; & 8\pi \sum_l \sum_{m=-l}^{l} \frac{1}{2l+1} \int_{WS(\mathbf{R}_q)} \int_{WS(\mathbf{R}_q)} dr_1 dr_2 r_1^2 r_2^2 \frac{r^l_<}{r^{l+1}_>} |\phi_s(\mathbf{r}_1)|^2 |\phi_p(\mathbf{r}_2)|^2 \\ \times \; & \int_{WS(\mathbf{R}_q)} \int_{WS(\mathbf{R}_q)} d\Omega_1 d\Omega_2 Y^*_{lm}(\Omega_1) Y_{lm}(\Omega_2) Y^*_{c\sigma}(\Omega_1) Y_{v\tau}(\Omega_1) Y_{c\sigma'}(\Omega_2) Y^*_{v\tau'}(\Omega_2). \end{aligned}$$

This expression can be parameterized by a single numerical parameter

$$E_{SR} = \frac{1}{3} \int_{WS(\mathbf{R}_q)} \int_{WS(\mathbf{R}_q)} dr_1 dr_2 r_1^2 r_2^2 \frac{r^l_<}{r^{l+1}_>} |\phi_s(\mathbf{r_1})|^2 |\phi_p(\mathbf{r_2})|^2 \tag{33}$$

which is the radial part of the short-range exchange microscopic integral. The angular part of this integral can be written as the 8×8 matrix:

$$\begin{aligned} & \langle c\sigma, v\tau|H_{SR}|c\sigma', v\tau'\rangle = 3 \cdot 4\pi \sum_l \sum_{m=-l}^{l} \frac{1}{2l+1} \\ \times \; & \int_{WS(\mathbf{R}_q)} \int_{WS(\mathbf{R}_q)} d\Omega_1 d\Omega_2 Y^*_{lm}(\Omega_1) Y_{lm}(\Omega_2) Y^*_{c\sigma}(\Omega_1) Y_{v\tau}(\Omega_1) Y_{c\sigma'}(\Omega_2) Y^*_{v\tau'}(\Omega_2) \end{aligned} \tag{34}$$

Now $I_{SR}\,(ci\sigma, vk\tau'|cl\sigma', vj\tau)$ has the form:

$$I_{SR}\,(ci\sigma, vk\tau'|cl\sigma', vj\tau) \;=\; 2E_{SR}\langle c\sigma, v\tau|H_{SR}|c\sigma', v\tau'\rangle \tag{35}$$

An example calculation of one of the $\langle c\sigma, v\tau|H_{SR}|c\sigma', v\tau'\rangle$ matrix elements is given below:

$$\begin{aligned}
\langle \alpha, +3/2|H_{SR}|\alpha, +3/2\rangle \quad &= \quad 3\cdot 4\pi \sum_{l}\sum_{m=-l}^{l} \frac{1}{2l+1}\int d\Omega_1 \int d\Omega_2 Y^*_{lm}(\Omega_1)Y_{lm}(\Omega_2) \\
&\times \quad (Y^*_{00}(\Omega_1), 0)\begin{pmatrix} Y_{11}(\Omega_1) \\ 0 \end{pmatrix}(Y_{00}(\Omega_2), 0)\begin{pmatrix} Y^*_{11}(\Omega_2) \\ 0 \end{pmatrix} \\
&=_{\substack{l=1\\ m=-1}} \quad 3\frac{4\pi}{3}\int d\Omega_1 \int d\Omega_2 Y_{11}(\Omega_1)Y_{1-1}(\Omega_2)\frac{1}{4\pi}Y_{11}(\Omega_1)Y_{1-1}(\Omega_2) \\
&= \quad 1,
\end{aligned}$$

where the notation α denoting electron spin $\frac{1}{2}$, and β for electron spin $-\frac{1}{2}$ is used as introduced in Appendix A.1. Analogous calculations have to be done for all other matrix elements and the final form of the matrix H_{SR} is:

$\lvert c\sigma' v\tau'\rangle \rightarrow$ $\langle c\sigma v\tau\rvert \downarrow$	$\lvert\alpha-\frac{3}{2}\rangle$	$\lvert\alpha-\frac{1}{2}\rangle$	$\lvert\alpha+\frac{1}{2}\rangle$	$\lvert\alpha+\frac{3}{2}\rangle$	$\lvert\beta-\frac{3}{2}\rangle$	$\lvert\beta-\frac{1}{2}\rangle$	$\lvert\beta+\frac{1}{2}\rangle$	$\lvert\beta+\frac{3}{2}\rangle$
$\langle\alpha-\frac{3}{2}\rvert$	0	0	0	0	0	0	0	0
$\langle\alpha-\frac{1}{2}\rvert$	0	$\frac{1}{3}$	0	0	$\sqrt{\frac{1}{3}}$	0	0	0
$\langle\alpha+\frac{1}{2}\rvert$	0	0	$\frac{2}{3}$	0	0	$\frac{2}{3}$	0	0
$\langle\alpha+\frac{3}{2}\rvert$	0	0	0	1	0	0	$\sqrt{\frac{1}{3}}$	0
$\langle\beta-\frac{3}{2}\rvert$	0	$\sqrt{\frac{1}{3}}$	0	0	1	0	0	0
$\langle\beta-\frac{1}{2}\rvert$	0	0	$\frac{2}{3}$	0	0	$\frac{2}{3}$	0	0
$\langle\beta+\frac{1}{2}\rvert$	0	0	0	$\sqrt{\frac{1}{3}}$	0	0	$\frac{1}{3}$	0
$\langle\beta+\frac{3}{2}\rvert$	0	0	0	0	0	0	0	0

Using equations Eqs. 29 and 35, the final short-range matrix element has the

form:

$$
\begin{aligned}
&V^X_{SR}(ci\sigma, vk\tau'|cl\sigma', vj\tau q) \qquad (36)\\
&= 2E_{SR}\langle ci\sigma, vj\tau|H_{SR}|cl\sigma', vk\tau'\rangle \sum_q A^+_{ci}(\mathbf{R}_q)A_{vj}(\mathbf{R}_q)A^+_{vk}(\mathbf{R}_q)A_{cl}(\mathbf{R}_q)\\
&= \frac{2}{V_{WS}}E_{SR}\langle c\sigma, v\tau|H_{SR}|c\sigma', v\tau'\rangle \int_{BvK} d\mathbf{r}' F^+_{ci}(\mathbf{r}')F_{vj}(\mathbf{r}')F^+_{vk}(\mathbf{r}')F_{cl}(\mathbf{r}')
\end{aligned}
$$

where the summation over the unit cells WS is replaced by the equivalent integration over the QD domain.

.4.3 Long-range exchange

The microscopic integral in the long-range exchange depends on the orientation of the cells:

$$
\begin{aligned}
&I^{qp}_{LR}(ci\sigma, vk\tau'|cl\sigma', vj\tau) \qquad (37)\\
&= 2\int\limits_{WS(\mathbf{R}_q)}\int\limits_{WS(\mathbf{R}_p)} d\mathbf{r}_1 d\mathbf{r}_2 \frac{u^+_{c\sigma}(\mathbf{r}_1+\mathbf{R}_q)u_{v\tau}(\mathbf{r}_1+\mathbf{R}_q)u^+_{v\tau'}(\mathbf{r}_2+\mathbf{R}_p)u_{c\sigma'}(\mathbf{r}_2+\mathbf{R}_p)}{|\mathbf{r}_1+\mathbf{R}_q-\mathbf{r}_2-\mathbf{R}_p|}
\end{aligned}
$$

In what follows, the shorter notation: $I^{qp}_{LR} = I^{qp}_{LR}(ci\sigma, vk\tau'|cl\sigma', vj\tau)$ will be used. The Coulomb potential is expanded in a power series of $\mathbf{r}_1$ and $\mathbf{r}_2$ (which are defined in the unit cells at the positions $\mathbf{R}_q$ and $\mathbf{R}_p$ respectively):

$$
\frac{1}{|\mathbf{r}_1-\mathbf{r}_2+\mathbf{R}_q-\mathbf{R}_p|} = \frac{1}{|\mathbf{R}|} - \frac{\mathbf{R}}{|\mathbf{R}|^3}(\mathbf{r}_1-\mathbf{r}_2) + \sum_{\lambda,\eta} r^\lambda_1 r^\eta_2 \frac{|\mathbf{R}|^2\delta_{\lambda\eta} - 3R_\lambda R_\eta}{|\mathbf{R}|^5}. \qquad (38)
$$

The notation $\mathbf{R} = \mathbf{R}_q - \mathbf{R}_p$ and $\mathbf{r} = \mathbf{r}_1 - \mathbf{r}_2$ has been used. Equation (37) becames then:

$$
\begin{aligned}
& I_{LR}^{qp} = \\
= \quad & \frac{2}{\mathbf{R}_q - \mathbf{R}_p} \underbrace{\int\limits_{WS(\mathbf{R}_q)} d\mathbf{r}_1 u_{c\sigma}^{+}(\mathbf{r}_1 + \mathbf{R}_q) u_{v\tau}(\mathbf{r}_1 + \mathbf{R}_q)}_{} \underbrace{\int\limits_{WS(\mathbf{R}_p)} d\mathbf{r}_2 u_{v\tau'}^{+}(\mathbf{r}_2 + \mathbf{R}_p) u_{c\sigma'}(\mathbf{r}_2 + \mathbf{R}_p)}_{} \\
+ \quad & 2\frac{\mathbf{R}_q - \mathbf{R}_p}{|\mathbf{R}_q - \mathbf{R}_p|^3} \left(\underbrace{\int\limits_{WS(\mathbf{R}_p)} d\mathbf{r}_2 u_{c\sigma}^{+}(\mathbf{r}_1 + \mathbf{R}_q) u_{v\tau}(\mathbf{r}_1 + \mathbf{R}_q)}_{} \int\limits_{WS(\mathbf{R}_q)} d\mathbf{r}_1 u_{c\sigma'}(\mathbf{r}_2 + \mathbf{R}_p) u_{v\tau'}(\mathbf{r}_2 + \mathbf{R}_p) \mathbf{r}_2 \right. \\
- \quad & \left. \int\limits_{WS(\mathbf{R}_q)} d\mathbf{r}_1 u_{c\sigma}^{+}(\mathbf{r}_1 + \mathbf{R}_q) u_{v\tau}(\mathbf{r}_1 + \mathbf{R}_q) \mathbf{r}_1 \underbrace{\int\limits_{WS(\mathbf{R}_p)} d\mathbf{r}_2 u_{v\tau'}^{+}(\mathbf{r}_2 + \mathbf{R}_p) u_{c\sigma'}(\mathbf{r}_2 + \mathbf{R}_p)}_{} \right) \\
+ \quad & 2 \sum_{\lambda,\eta} \frac{|\mathbf{R}_q - \mathbf{R}_p|^2 \delta_{\lambda\eta} - 3 (\mathbf{R}_q - \mathbf{R}_p)_\lambda (\mathbf{R}_q - \mathbf{R}_p)_\eta}{|\mathbf{R}_q - \mathbf{R}_p|^5} \\
\times \quad & \int\limits_{WS(\mathbf{R}_q)} d\mathbf{r}_1 u_{c\sigma}^{+}(\mathbf{r}_1 + \mathbf{R}_q) u_{v\tau}(\mathbf{r}_1 + \mathbf{R}_q) \mathbf{r}_1^\lambda \int\limits_{WS(\mathbf{R}_p)} d\mathbf{r}_2 u_{c\sigma'}(\mathbf{r}_2 + \mathbf{R}_p) u_{v\tau'}^{+}(\mathbf{r}_2 + \mathbf{R}_p) \mathbf{r}_2^\eta
\end{aligned}
$$

where integrals above the *underbrackets* are equal to 0 due to a difference of symmetry of the conduction and the valence band Bloch functions (radial integrals $\int_{WS} r^2 \phi_s^*(r) \phi_p(r) dr = 0$).

Finally:

$$
\begin{aligned}
I_{LR}^{qp} \quad = \quad & 2 \sum_{\lambda,\eta} \frac{|\mathbf{R}_q - \mathbf{R}_p|^2 \delta_{\lambda\eta} - 3 (\mathbf{R}_q - \mathbf{R}_p)_\lambda (\mathbf{R}_q - \mathbf{R}_p)_\eta}{|\mathbf{R}_q - \mathbf{R}_p|^5} \\
& \times \int\limits_{WS(\mathbf{R}_q)} d\mathbf{r}_1 u_{c\sigma}^{+}(\mathbf{r}_1 + \mathbf{R}_q) u_{v\tau}(\mathbf{r}_1 + \mathbf{R}_q) \mathbf{r}_1^\lambda \int\limits_{WS(\mathbf{R}_p)} d\mathbf{r}_2 u_{c\sigma'}(\mathbf{r}_2 + \mathbf{R}_p) u_{v\tau'}^{+}(\mathbf{r}_2 + \mathbf{R}_p) \mathbf{r}_2^\eta .
\end{aligned}
$$

The definition of the transition dipole moment between the microscopic parts of the electron and hole wavefunctions is:

$$\mathbf{d}_{\alpha\beta} = \int_{WS(\mathbf{R})} d\mathbf{r} u^{+}_{\alpha}(\mathbf{r}) \mathbf{r} u_{\beta}(\mathbf{r}) = \mu \mathbf{d}^{0}_{\alpha\beta}, \tag{39}$$

where $\mathbf{d}^{0}_{\alpha\beta}$ is a *reduced* dipole moment, which is an integral over the angles. It depends on the spherical harmonics involved in the integration. Parameter

$$\mu = \frac{1}{\sqrt{6}} \int_{WS} r^2 \phi^{*}_{s}(r) r \phi_{p}(r) dr \tag{40}$$

is a radial integral within the WS cell and its value is taken from the experiment.

$$I^{qp}_{LR} = 2 \sum_{\lambda,\eta} \left(\mathbf{d}^{0\eta}_{c\sigma' v\tau'}\right)^{+} \frac{|\mathbf{R}_q - \mathbf{R}_p|^2 \delta_{\lambda\eta} - 3 \left(\mathbf{R}_q - \mathbf{R}_p\right)_{\lambda} \left(\mathbf{R}_q - \mathbf{R}_p\right)_{\eta}}{|\mathbf{R}_q - \mathbf{R}_p|^5} \mathbf{d}^{0\lambda}_{c\sigma v\tau} \tag{41}$$

Using the equations Eqs.30 and 41, the long-range exchange interaction can be written in the form:

$$V^{X}_{LR}(ci\sigma, vk\tau'|cl\sigma', vj\tau) = 2\mu^2 \sum_{qp} A^{+}_{ci}(\mathbf{R}_q) A_{vj}(\mathbf{R}_q) A^{+}_{vk}(\mathbf{R}_p) A_{cl}(\mathbf{R}_p)$$
$$\times \sum_{\lambda,\eta} \left(\mathbf{d}^{0\eta}_{c\sigma' v\tau'}\right)^{+} \frac{|\mathbf{R}_q - \mathbf{R}_p|^2 \delta_{\lambda\eta} - 3 \left(\mathbf{R}_q - \mathbf{R}_p\right)_{\lambda} \left(\mathbf{R}_q - \mathbf{R}_p\right)_{\eta}}{|\mathbf{R}_q - \mathbf{R}_p|^5} \mathbf{d}^{0\lambda}_{c\sigma v\tau}$$

The summation over the WS unit cells may be replaced by the integration over the QD domain (BvK) over the variables $\mathbf{r'}_1$ and $\mathbf{r'}_2$. The "primes" can be then dropped:

$$V^{X}_{LR}(ci\sigma, vk\tau'|cl\sigma', vj\tau) = \frac{2\mu^2}{V^2_{WS}} \iint_{BvK} d\mathbf{r}_1 d\mathbf{r}_2 F^{+}_{ci}(\mathbf{r}_1) F_{vj}(\mathbf{r}_1) F^{+}_{vk}(\mathbf{r}_2) F_{cl}(\mathbf{r}_2) \tag{42}$$
$$\times \sum_{\lambda,\eta} \left(\mathbf{d}^{0\eta}_{c\sigma' v\tau'}\right)^{+} \frac{|\mathbf{r}_1 - \mathbf{r}_2|^2 \delta_{\lambda\eta} - 3 \left(\mathbf{r}_1 - \mathbf{r}_2\right)_{\lambda} \left(\mathbf{r}_1 - \mathbf{r}_2\right)_{\eta}}{|\mathbf{r}_1 - \mathbf{r}_2|^5} \mathbf{d}^{0\lambda}_{c\sigma v\tau}$$

The difference $\mathbf{R}_q - \mathbf{R}_p$ in the integral was replaced by $\mathbf{r}_1 - \mathbf{r}_2$, since during integration the regions inside the same unit cell make a negligibly small contribution to the double integral. If the following identity:

$$\frac{|\mathbf{r}_1-\mathbf{r}_2|^2\delta_{\lambda\eta}-3(\mathbf{r}_1-\mathbf{r}_2)_\lambda(\mathbf{r}_1-\mathbf{r}_2)_\eta}{|\mathbf{r}_1-\mathbf{r}_2|^5}=-\frac{\partial^2}{\partial\mathbf{r}_1^\lambda\partial\mathbf{r}_1^\eta}\frac{1}{|\mathbf{r}_1-\mathbf{r}_2|}-\frac{4\pi}{3}\delta_{\lambda\eta}\delta(\mathbf{r}_1-\mathbf{r}_2), \quad (43)$$

is inserted to the expression for the long-range exchange interaction Eq. 42, one obtains:

$$\begin{aligned} V_{LR}^{X}(ci\sigma,vk\tau'|cl\sigma',vj\tau) &= -\frac{8\pi}{3}\frac{\mu^2}{V_{WS}^2}\sum_{\lambda}\left(\mathbf{d}^{0\lambda}_{c\sigma'v\tau'}\right)^{+}\mathbf{d}^{0\lambda}_{c\sigma v\tau} \\ &\times \int_{BvK} d\mathbf{r}_1 F_{ci}^{+}(\mathbf{r}_1)F_{vj}(\mathbf{r}_1)F_{vk}^{+}(\mathbf{r}_1)F_{cl}(\mathbf{r}_1) \quad (44) \\ &- \frac{\mu^2}{V_{WS}^2}\sum_{\lambda,\eta}\left(\mathbf{d}^{0\eta}_{c\sigma'v\tau'}\right)^{+}\mathbf{d}^{0\lambda}_{c\sigma v\tau}\iint_{BvK} d\mathbf{r}_1 d\mathbf{r}_2 \frac{\partial^2}{\partial\mathbf{r}_1^\lambda\partial\mathbf{r}_1^\eta}\frac{2}{|\mathbf{r}_1-\mathbf{r}_2|} \\ &\times F_{ci}^{+}(\mathbf{r}_1)F_{vj}(\mathbf{r}_1)F_{vk}^{+}(\mathbf{r}_2)F_{cl}(\mathbf{r}_2). \end{aligned}$$

The first term in this expresion has exactly the same form as the short-range electron-hole exchange (Eq. 36).

$$\begin{aligned} V_{LR}^{XS}(ci\sigma,vk\tau'|cl\sigma',vj\tau) &= -\frac{8\pi}{3}\frac{\mu^2}{V_{WS}^2}\sum_{\lambda}\left(\mathbf{d}^{0\lambda}_{c\sigma'v\tau'}\right)^{+}\mathbf{d}^{0\lambda}_{c\sigma v\tau} \quad (45) \\ &\times \int_{BvK)} d\mathbf{r}_1 F_{ci}^{+}(\mathbf{r}_1)F_{vj}(\mathbf{r}_1)F_{vk}^{+}(\mathbf{r}_1)F_{cl}(\mathbf{r}_1) \end{aligned}$$

The second integral, after double integration by parts over r_1, takes the form:

$$\begin{aligned} V_{LR}^{XL}(ci\sigma,vk\tau'|cl\sigma',vj\tau) &= -\frac{\mu^2}{V_{WS}^2}\sum_{\lambda,\eta}\left(\mathbf{d}^{0\eta}_{c\sigma'v\tau'}\right)^{+}\mathbf{d}^{0\lambda}_{c\sigma v\tau}\iint_{BvK} d\mathbf{r}_1 d\mathbf{r}_2 \quad (46) \\ &\times \left(\frac{\partial^2}{\partial\mathbf{r}_1^\lambda\partial\mathbf{r}_1^\eta}F_{ci}^{+}(\mathbf{r}_1)F_{vj}(\mathbf{r}_1)\right)\frac{2}{|\mathbf{r}_1-\mathbf{r}_2|}F_{vk}^{+}(\mathbf{r}_2)F_{cl}(\mathbf{r}_2). \end{aligned}$$

Using the notation:

$$R_{\lambda\eta} = \iint\limits_{BvK} d\mathbf{r}_1 d\mathbf{r}_2 \left(\frac{\partial^2}{\partial \mathbf{r}_1^\lambda \partial \mathbf{r}_1^\eta} F_{ci}^+(\mathbf{r}_1) F_{vj}(\mathbf{r}_1) \right) \frac{1}{|\mathbf{r}_1 - \mathbf{r}_2|} F_{vk}^+(\mathbf{r}_2) F_{cl}(\mathbf{r}_2),$$

the long-range exchange integral (46) can be written as:

$$V_{LR}^{XL}(ci\sigma, vk\tau' | cl\sigma', vj\tau) = -\frac{\mu^2}{V_{WS}^2} \sum_{\lambda,\eta} \left(\mathbf{d}_{c\sigma' v\tau'}^{0\eta} \right)^+ \mathbf{d}_{c\sigma v\tau}^{0\lambda} R_{\lambda\eta} \tag{47}$$

The dipole moments $d_{\alpha\beta}$ (Eq. 39) can be written in the form of a table:

	d^x	d^y	d^z	
$\|\alpha - 3/2\rangle$	0	0	0	
$\|\alpha - 1/2\rangle$	$1/\sqrt{3}$	$-i/\sqrt{3}$	0	
$\|\alpha + 1/2\rangle$	0	0	$2/\sqrt{3}$	
$\|\alpha + 3/2\rangle$	-1	$-i$	0	$\times \mu$
$\|\beta - 3/2\rangle$	1	$-i$	0	
$\|\beta - 1/2\rangle$	0	0	$2/\sqrt{3}$	
$\|\beta + 1/2\rangle$	$-1/\sqrt{3}$	$-i/\sqrt{3}$	0	
$\|\beta + 3/2\rangle$	0	0	0	

Here we show an example calculation of the dipole matrix element $\mathbf{d}_{\alpha-1/2}^x$:

$$\begin{aligned}
\mathbf{d}_{\alpha-1/2}^x &= \int_{WS(\mathbf{R})} d\mathbf{r} \phi_s^*(\mathbf{r}) \left(Y_{00}^*(\hat{r}), 0\right) x \phi_p(\mathbf{r}) \left(\frac{\sqrt{\frac{1}{3}} Y_{1-1}(\hat{r})}{\sqrt{\frac{2}{3}} Y_{10}(\hat{r})} \right) \\
&= \underbrace{\int_{WS(\mathbf{R})} d\mathbf{r} \phi_s^*(\mathbf{r}) r \phi_p(\mathbf{r})}_{} \int_0^{2\pi} d\varphi \int_0^{\pi} d\theta \sin\theta \cos\varphi \sin\theta \sqrt{\frac{1}{3}} Y_{00}^*(\hat{r}) Y_{1-1}(\hat{r}) \\
&= \sqrt{6}\mu \underbrace{\int_0^{2\Pi} d\varphi \cos\varphi \exp(-i\varphi)}_{} \underbrace{\int_0^{\Pi} d\theta \sin^3\theta}_{} \sqrt{\frac{1}{3}} \sqrt{\frac{3}{8\pi}} \frac{1}{\sqrt{4\pi}} \\
&= \sqrt{6}\mu \cdot \pi \cdot \frac{4}{3} \cdot \frac{1}{\sqrt{2}} \frac{1}{4\pi} = \frac{\mu}{\sqrt{3}}.
\end{aligned}$$

The matrix $\sum_\lambda \left(\mathbf{d}^{0\lambda}_{c\sigma' v\tau'}\right)^+ \mathbf{d}^{0\lambda}_{c\sigma v\tau}$ corresponding to the short-range-like element in the long-range interaction (Eq. 45) can be written as:

$$\sum_\lambda \mathbf{d}^{0\lambda}_{c\sigma v\tau}\left(\mathbf{d}^{0\lambda}_{c\sigma' v\tau'}\right)^+ = \mathbf{d}^{0x}_{c\sigma v\tau}\left(\mathbf{d}^{0x}_{c\sigma' v\tau'}\right)^+ + \mathbf{d}^{0y}_{c\sigma v\tau}\left(\mathbf{d}^{0y}_{c\sigma' v\tau'}\right)^+ + \mathbf{d}^{0z}_{c\sigma v\tau}\left(\mathbf{d}^{0z}_{c\sigma' v\tau'}\right)^+ = \quad (48)$$

$\lvert c\sigma' v\tau'\rangle$ $\langle c\sigma v\tau\rvert \downarrow$	$\lvert\alpha-\frac{3}{2}\rangle$	$\lvert\alpha-\frac{1}{2}\rangle$	$\lvert\alpha+\frac{1}{2}\rangle$	$\lvert\alpha+\frac{3}{2}\rangle$	$\lvert\beta-\frac{3}{2}\rangle$	$\lvert\beta-\frac{1}{2}\rangle$	$\lvert\beta+\frac{1}{2}\rangle$	$\lvert\beta+\frac{3}{2}\rangle$
$\langle\alpha-\frac{3}{2}\rvert$	0	0	0	0	0	0	0	0
$\langle\alpha-\frac{1}{2}\rvert$	0	$\frac{2}{3}$	0	0	$\sqrt{\frac{2}{3}}$	0	0	0
$\langle\alpha+\frac{1}{2}\rvert$	0	0	$\frac{4}{3}$	0	0	$\frac{4}{3}$	0	0
$\langle\alpha+\frac{3}{2}\rvert$	0	0	0	2	0	0	$\sqrt{\frac{2}{3}}$	0
$\langle\beta-\frac{3}{2}\rvert$	0	$\sqrt{\frac{2}{3}}$	0	0	2	0	0	0
$\langle\beta-\frac{1}{2}\rvert$	0	0	$\frac{4}{3}$	0	0	$\frac{4}{3}$	0	0
$\langle\beta+\frac{1}{2}\rvert$	0	0	0	$\sqrt{\frac{2}{3}}$	0	0	$\frac{2}{3}$	0
$\langle\beta+\frac{3}{2}\rvert$	0	0	0	0	0	0	0	0

On the other hand, the key element in the calculation of the second part of the long-range exchange (Eq. 46) is the matrix

$$\sum_{\lambda,\eta}\left(\mathbf{d}^{0\eta}_{c\sigma' v\tau'}\right)^+ \mathbf{d}^{0\lambda}_{c\sigma v\tau} R_{\lambda\eta} \quad (49)$$

For the two-dimensional system or any system for which $R_{z\alpha} = 0$ (a 3D QD which doesn't have a bound excited state in the z direction) it takes a form:

$$\sum_{\lambda\eta}\left(\mathbf{d}^{0\eta}_{c\sigma' v\tau'}\right)^+ \mathbf{d}^{0\lambda}_{c\sigma v\tau} R_{\lambda\eta} = \quad (50)$$

$\langle ci\sigma vj\tau \vert \downarrow$ / $\vert vk\tau' cl\sigma' \rangle$	$\vert\alpha-\frac{3}{2}\rangle$	$\vert\alpha-\frac{1}{2}\rangle$	$\vert\alpha+\frac{1}{2}\rangle$	$\vert\alpha+\frac{3}{2}\rangle$	$\vert\beta-\frac{3}{2}\rangle$	$\vert\beta-\frac{1}{2}\rangle$	$\vert\beta+\frac{1}{2}\rangle$	$\vert\beta+\frac{3}{2}\rangle$
$\langle\alpha-\frac{3}{2}\vert$	0	0	0	0	0	0	0	0
$\langle\alpha-\frac{1}{2}\vert$	0	$\frac{1}{3}A_{ij}^{kl}$	0	$\frac{1}{\sqrt{3}}B_{ij}^{kl}$	$\frac{1}{\sqrt{3}}A_{ij}^{kl}$	0	$\frac{1}{3}B_{ij}^{kl}$	0
$\langle\alpha+\frac{1}{2}\vert$	0	0	0	0	0	0	0	0
$\langle\alpha+\frac{3}{2}\vert$	0	$\frac{1}{\sqrt{3}}C_{ij}^{kl}$	0	A_{ij}^{kl}	C_{ij}^{kl}	0	$\frac{1}{\sqrt{3}}{}_{ij}^{kl}A_{ij}^{kl}$	0
$\langle\beta-\frac{3}{2}\vert$	0	$\frac{1}{\sqrt{3}}A_{ij}^{kl}$	0	B_{ij}^{kl}	A_{ij}^{kl}	0	$\frac{1}{\sqrt{3}}B_{ij}^{kl}$	0
$\langle\beta-\frac{1}{2}\vert$	0	0	0	0	0	0	0	0
$\langle\beta+\frac{1}{2}\vert$	0	$\frac{1}{3}C_{ij}^{kl}$	0	$\frac{1}{\sqrt{3}}A_{ij}^{kl}$	$\frac{1}{\sqrt{3}}C_{ij}^{kl}$	0	$\frac{1}{3}A_{ij}^{kl}$	0
$\langle\beta+\frac{3}{2}\vert$	0	0	0	0	0	0	0	0

where the following notation is used:

$$\begin{aligned} A_{ij}^{kl} &= R_{xx}^{ijkl} + R_{yy}^{ijkl} \\ B_{ij}^{kl} &= -R_{xx}^{ijkl} + R_{yy}^{ijkl} + 2iR_{xy}^{ijkl} \\ C_{ij}^{kl} &= -R_{xx}^{ijkl} + R_{yy}^{ijkl} - 2iR_{xy}^{ijkl} \end{aligned}$$

.5 Matrix form of the electron-hole exchange

.5.1 Electron-electron language

From the derivation of the short-range exchange (Eq. 36), short-range-like element in the long-range interaction (Eq. 45) as well as the long-range exchange integral (Eqs. 46 and 47), one can notice that the state $|\alpha-\frac{3}{2}\rangle$ and $|\beta+\frac{3}{2}\rangle$ are not coupled with any other state. The full electron-hole exchange matrices written in the basis including both light and heavy valence band are shown below:

$$V_{ee}^{X}(ci\sigma, vk\tau'|cl\sigma', vj\tau) = \tag{51}$$

$\lvert vk\tau' cl\sigma'\rangle$								
$\langle ci\sigma vj\tau\rvert$	$\lvert\alpha-\frac{3}{2}\rangle$	$\lvert\alpha-\frac{1}{2}\rangle$	$\lvert\alpha+\frac{1}{2}\rangle$	$\lvert\alpha+\frac{3}{2}\rangle$	$\lvert\beta-\frac{3}{2}\rangle$	$\lvert\beta-\frac{1}{2}\rangle$	$\lvert\beta+\frac{1}{2}\rangle$	$\lvert\beta+\frac{3}{2}\rangle$
$\langle\alpha-\frac{3}{2}\rvert$	0	0	0	0	0	0	0	0
$\langle\alpha-\frac{1}{2}\rvert$	0	$\frac{1}{3}\delta^{SLL}$	0	$\frac{1}{\sqrt{3}}\delta_{12}$	$\frac{1}{\sqrt{3}}\delta^{SLL}$	0	$\frac{1}{3}\delta_{12}$	0
$\langle\alpha+\frac{1}{2}\rvert$	0	0	$\frac{2}{3}\delta_0^{SL}$	0	0	$\frac{2}{3}\delta_0^{SL}$	0	0
$\langle\alpha+\frac{3}{2}\rvert$	0	$\frac{1}{\sqrt{3}}\delta_{21}$	0	δ^{SLL}	δ_{21}	0	$\frac{1}{\sqrt{3}}\delta^{SLL}$	0
$\langle\beta-\frac{3}{2}\rvert$	0	$\frac{1}{\sqrt{3}}\delta^{SLL}$	0	δ_{12}	δ^{SLL}	0	$\frac{1}{\sqrt{3}}\delta_{12}$	0
$\langle\beta-\frac{1}{2}\rvert$	0	0	$\frac{2}{3}\delta_0^{SL}$	0	0	$\frac{2}{3}\delta_0^{SL}$	0	
$\langle\beta+\frac{1}{2}\rvert$	0	$\frac{1}{3}\delta_{21}$	0	$\frac{1}{\sqrt{3}}\delta^{SLL}$	$\frac{1}{\sqrt{3}}\delta_{21}$	0	$\frac{1}{3}\delta^{SLL}$	0
$\langle\beta+\frac{3}{2}\rvert$	0	0	0	0	0	0	0	0

where, as in the Ref. [123], the following notation was used:

$$\delta_0^{SL}{}_{ij}^{kl} = \delta_0^{SRE}{}_{ij}^{kl} + \delta_0^{LRE}{}_{ij}^{kl} \tag{52}$$

$$\delta_0^{SRE}{}_{ij}^{kl} = \frac{2E_{SR}}{V_{WS}} \int_{BvK} d\mathbf{r}_1 F_{ci}^{+}(\mathbf{r}_1) F_{vj}(\mathbf{r}_1) F_{vk}^{+}(\mathbf{r}_1) F_{cl}(\mathbf{r}_1) \tag{53}$$

$$\delta_0^{LRE}{}_{ij}^{kl} = -\frac{16\pi\mu^2}{3V_{WS}^2} \int_{BvK} d\mathbf{r}_1 F_{ci}^{+}(\mathbf{r}_1) F_{vj}(\mathbf{r}_1) F_{vk}^{+}(\mathbf{r}_1) F_{cl}(\mathbf{r}_1) \tag{54}$$

$$\delta^{L}{}_{ij}^{kl} = -\frac{\mu^2}{V_{WS}^2} \left(R_{xx}^{ijkl} + R_{yy}^{ijkl} \right) \tag{55}$$

$$\delta^{SLL}{}_{ij}^{kl} = \delta_0^{SL}{}_{ij}^{kl} + \delta^{L}{}_{ij}^{kl} \tag{56}$$

$$\delta_{12}{}_{ij}^{kl} = \frac{\mu^2}{V_{WS}^2} \left(R_{xx}^{ijkl} - R_{yy}^{ijkl} - 2iR_{xy}^{ijkl} \right) \tag{57}$$

$$\delta_{21}{}_{ij}^{kl} = \frac{\mu^2}{V_{WS}^2} \left(R_{xx}^{ijkl} - R_{yy}^{ijkl} + 2iR_{xy}^{ijkl} \right) \tag{58}$$

and as previously (Eq. 47):

$$R_{\lambda\eta} = \iint_{BvK} d\mathbf{r}_1 d\mathbf{r}_2 \left(\frac{\partial^2}{\partial \mathbf{r}_1^{\lambda} \partial \mathbf{r}_1^{\eta}} F_{ci}^{+}(\mathbf{r}_1) F_{vj}(\mathbf{r}_1) \right) \frac{2}{|\mathbf{r}_1 - \mathbf{r}_2|} F_{vk}^{+}(\mathbf{r}_2) F_{cl}(\mathbf{r}_2).$$

If the basis is restricted, and the light-hole band is neglected, then the electron-hole exchange matrix takes the form:

$$V_{ee}^{X}(ci\sigma, vk\tau'|cl\sigma', vj\tau) = \tag{59}$$

$$\left(\begin{array}{c|cccc} |vk\tau' cl\sigma'\rangle \rightarrow & & & & \\ \langle ci\sigma vj\tau| \downarrow & |\alpha - \frac{3}{2}\rangle & |\alpha + \frac{3}{2}\rangle & |\beta - \frac{3}{2}\rangle & |\beta + \frac{3}{2}\rangle \\ \hline \langle \alpha - \frac{3}{2}| & 0 & 0 & 0 & 0 \\ \langle \alpha + \frac{3}{2}| & 0 & (\delta_0^{SL} + \delta^{L}) & \delta_{21} & 0 \\ \langle \beta - \frac{3}{2}| & 0 & \delta_{12} & (\delta_0^{SL} + \delta^{L}) & 0 \\ \langle \beta + \frac{3}{2}| & 0 & 0 & 0 & 0 \end{array}\right)$$

. The diagonal matrix elemets $\delta^{SLL^{kl}}_{ij}$ were written explicitely as a sum of the $\delta^{SLL^{kl}}_{ij} = \delta_0^{SL^{kl}}_{ij} + \delta^{L^{kl}}_{ij}$.

.5.2 Electron-hole language

Now one can transfer the obtained result into the language of an electron in the conduction band and a hole in the valence band, remembering that $\phi_h = \phi_e^*$.

Due to this fact, the spin parts of the wave functions are transformed in the following way:

$|\alpha - 3/2\rangle \longrightarrow |\alpha + 3/2\rangle, \quad |\alpha + 3/2\rangle \longrightarrow |\alpha - 3/2\rangle$

$|\beta - 3/2\rangle \longrightarrow |\beta + 3/2\rangle, \quad |\beta + 3/2\rangle \longrightarrow |\beta - 3/2\rangle.$

The electron-hole exchange matrix in this language has the form:

$$V_{eh}^{X}(ci\sigma, vj\tau|cl\sigma', vk\tau') = \tag{60}$$

$$\left(\begin{array}{c|cccc} |vk\tau' cl\sigma'\rangle \rightarrow & & & & \\ \langle ci\sigma vj\tau| \downarrow & |\alpha - \frac{3}{2}\rangle & |\alpha + \frac{3}{2}\rangle & |\beta - \frac{3}{2}\rangle & |\beta + \frac{3}{2}\rangle \\ \hline \langle \alpha - \frac{3}{2}| & (\delta_0^{SL} + \delta^{L}) & 0 & 0 & \delta_{21} \\ \langle \alpha + \frac{3}{2}| & 0 & 0 & 0 & 0 \\ \langle \beta - \frac{3}{2}| & 0 & 0 & 0 & 0 \\ \langle \beta + \frac{3}{2}| & \delta_{12} & 0 & 0 & (\delta_0^{SL} + \delta^{L}) \end{array}\right)$$

with:

$$\delta_0^{SL}{}_{ij}^{kl} = \delta_0^{SRE}{}_{ij}^{kl} + \delta_0^{LRE}{}_{ij}^{kl} \quad (61)$$

$$\delta_0^{SRE}{}_{ij}^{kl} = \frac{2E_{SR}}{V_{WS}} \int_{BvK} d\mathbf{r}_1 F_{ci}^{+}(\mathbf{r}_1) H_{vj}^{+}(\mathbf{r}_1) H_{vk}(\mathbf{r}_1) F_{cl}(\mathbf{r}_1) \quad (62)$$

$$\delta_0^{LRE}{}_{ij}^{kl} = -\frac{16\pi\mu^2}{3V_{WS}^2} \int_{BvK} d\mathbf{r}_1 F_{ci}^{+}(\mathbf{r}_1) H_{vj}^{+}(\mathbf{r}_1) H_{vk}(\mathbf{r}_1) F_{cl}(\mathbf{r}_1) \quad (63)$$

$$\delta^{L}{}_{ij}^{kl} = -\frac{\mu^2}{V_{WS}^2} \left(R_{xx}^{ijkl} + R_{yy}^{ijkl} \right) \quad (64)$$

$$\delta_{12}{}_{ij}^{kl} = \frac{\mu^2}{V_{WS}^2} \left(R_{xx}^{ijkl} - R_{yy}^{ijkl} - 2iR_{xy}^{ijkl} \right) \quad (65)$$

$$\delta_{21}{}_{ij}^{kl} = \frac{\mu^2}{V_{WS}^2} \left(R_{xx}^{ijkl} - R_{yy}^{ijkl} + 2iR_{xy}^{ijkl} \right) \quad (66)$$

where now:

$$R_{\lambda\eta}^{ijkl} = \iint_{BvK} d\mathbf{r}_1 d\mathbf{r}_2 \left(\frac{\partial^2}{\partial \mathbf{r}_1^{\lambda} \partial \mathbf{r}_1^{\eta}} F_{ci}^{+}(\mathbf{r}_1) H_{vj}^{+}(\mathbf{r}_1) \right) \frac{2}{|\mathbf{r}_1 - \mathbf{r}_2|} H_{vk}(\mathbf{r}_2) F_{cl}(\mathbf{r}_2). \quad (67)$$

References

[1] G. Binasch, P. Grunberg, F. Saurenbach, and W. Zinn. Enhanced magnetoresistance in layered magnetic structures with antiferromagnetic interlayer exchange. *Phys. Rev. B*, 39:4828–4830, Mar 1989. doi: 10.1103/PhysRevB.39.4828. URL http://link.aps.org/doi/10.1103/PhysRevB.39.4828. 1

[2] M. N. Baibich, J. M. Broto, A. Fert, F. Nguyen Van Dau, F. Petroff, P. Etienne, G. Creuzet, A. Friederich, and J. Chazelas. Giant magnetoresistance of (001)Fe/(001)Cr magnetic superlattices. *Phys. Rev. Lett.*, 61:2472–2475, Nov 1988. doi: 10.1103/PhysRevLett.61.2472. URL http://link.aps.org/doi/10.1103/PhysRevLett.61.2472. 1

[3] T. Dietl, D. D. Awschalom, M. Kaminska, and H. Ohno. *Spintronics, Volume 82 (Semiconductors and Semimetals), Ed. by E. R. Weber*. Academic Press, USA, 2008. 1

[4] Ed. by T. Shinjo. *Nanomagnetism and Spintronics*. Elsevier, Amsterdam, 2009.

[5] S. A. Wolf, D. D. Awschalom, R. A. Buhrman, J. M. Daughton, S. von Molnr, M. L. Roukes, A. Y. Chtchelkanova, and D. M. Treger. Spintronics: A spin-based electronics vision for the future. *Science*, 294:1488–1495, 2001. doi: 10.1126/science.1065389.

[6] I. Zutic, J. Fabian, and S. Das Sarma. Spintronics: Fundamentals and applications. *Rev. Mod. Phys.*, 76:323–

410, Apr 2004. doi: 10.1103/RevModPhys.76.323. URL http://link.aps.org/doi/10.1103/RevModPhys.76.323.

[7] D. Loss and D. P. DiVincenzo. Quantum computation with quantum dots. *Phys. Rev. A*, 57:120–126, Jan 1998. doi: 10.1103/PhysRevA.57.120. URL http://link.aps.org/doi/10.1103/PhysRevA.57.120. 4

[8] G. Burkard, D. Loss, and D. P. DiVincenzo. Coupled quantum dots as quantum gates. *Phys. Rev. B*, 59:2070–2078, Jan 1999. doi: 10.1103/PhysRevB.59.2070. URL http://link.aps.org/doi/10.1103/PhysRevB.59.2070.

[9] S. Tarucha, D. G. Austing, T. Honda, R. J. van der Hage, and L. P. Kouwenhoven. Shell filling and spin effects in a few electron quantum dot. *Phys. Rev. Lett.*, 77:3613–3616, Oct 1996. doi: 10.1103/PhysRevLett.77.3613. URL http://link.aps.org/doi/10.1103/PhysRevLett.77.3613. 12

[10] J. A. Brum and P. Hawrylak. Coupled quantum dots as quantum exclusive-OR gate. *Superlattices and Microstructures*, 22, 1997. doi: 10.1006/spmi.1996.0263. URL http://dx.doi.org/10.1006/spmi.1996.0263.

[11] M. Ciorga, A. S. Sachrajda, P. Hawrylak, C. Gould, P. Zawadzki, S. Julian, Y. Feng, and Z. Wasilewski. Addition spectrum of a lateral dot from Coulomb and spin-blockade spectroscopy. *Phys. Rev. B*, 61: R16315–R16318, Jun 2000. doi: 10.1103/PhysRevB.61.R16315. URL http://link.aps.org/doi/10.1103/PhysRevB.61.R16315. 6

[12] V. Cerletti, W. A. Coish, O. Gywat, and D. Loss. Recipes for spin-based quantum computing. *Nanotechnology*, 16:R27, 2005. doi: doi:10.1088/0957-4484/16/4/R01. 1

[13] R.T. Delves. HgTe – MnTe alloys II. electrical properties. *J. Phys. Chem. Solids*, 24:885–897, 1963. doi: 10.1016/0022-3697(63)90065-9. URL http://dx.doi.org/10.1016/0022-3697(63)90065-9. 1

[14] J. K. Furdyna. Diluted magnetic semiconductors. *J. Appl. Phys*, 64:R29, 1988. doi: 10.1063/1.341700. URL http://dx.doi.org/10.1063/1.341700. 128

[15] J. A. Gaj, R. Planel, and G. Fishman. Relation of magneto-optical properties of free excitons to spin alignment of Mn^{2+} ions in $Cd_{1-x}Mn_xTe$. *Solid Stat. Communication*, 29:435–438, 1979. doi: 10.1016/0038-1098(79)91211-0. URL http://dx.doi.org/10.1016/0038-1098(79)91211-0.

[16] H. Ohno. Making nonmagnetic semiconductors ferromagnetic. *Science*, 281: 951–956, 1998. doi: 10.1126/science.281.5379.951.

[17] T. Jungwirth, J. Sinova, J. Masek, J. Kucera, and A. H. MacDonald. Theory of ferromagnetic (III, Mn)V semiconductors. *Rev. Mod. Phys.*, 78:809–864, Aug 2006. doi: 10.1103/RevModPhys.78.809. URL http://link.aps.org/doi/10.1103/RevModPhys.78.809. x, 67

[18] T. Dietl. *Diluted Magnetic Semiconductors in Handbook of Semiconductors vol. 3B, Ed. by Mahajan, S.* North Holland,, Amsterdam, 2008. 1

[19] J. Kossut and J. A. Gaj. *Introduction to the Physics of Diluted Magnetic Semiconductors*. Springer, Berlin, 2005. 1, 56

[20] Y. Leger, L. Besombes, J. Fernandez-Rossier, L. Maingault, and H. Mariette. Electrical control of a single mn atom in a quantum dot. *Phys. Rev. Lett.*, 97:107401, Sep 2006. doi: 10.1103/PhysRevLett.97.107401. URL http://link.aps.org/doi/10.1103/PhysRevLett.97.107401. 1, 69

[21] P. Hawrylak, M. Grabowski, and J. J. Quinn. Tunneling in a periodic array of semimagnetic quantum dots. *Phys. Rev. B*, 44: 13082–13084, Dec 1991. doi: 10.1103/PhysRevB.44.13082. URL http://link.aps.org/doi/10.1103/PhysRevB.44.13082. 2

[22] L. Besombes, Léger, L. Y., Maingault, D. Ferrand, H. Mariette, and J. Cibert. Probing the spin state of a single magnetic ion in an individual quantum dot. *Phys. Rev. Lett.*, 93: 207403, Nov 2004. doi: 10.1103/PhysRevLett.93.207403. URL http://link.aps.org/doi/10.1103/PhysRevLett.93.207403. 69, 70, 74, 93, 94, 127

[23] A. Kudelski, A. Lemaitre, A. Miard, P. Voisin, T. C. M. Graham, R. J. Warburton, and O. Krebs. Optically probing the fine structure of a single Mn atom in an InAs quantum dot. *Phys. Rev. Lett.*, 99:247209, Dec 2007. doi: 10.1103/PhysRevLett.99.247209. URL http://link.aps.org/doi/10.1103/PhysRevLett.99.247209. 141

[24] M. Goryca, T. Kazimierczuk, M. Nawrocki, A. Golnik, J. A. Gaj, Kossacki, P. Wojnar, and G. Karczewski. Optical manipulation of a single Mn spin in a CdTe-based quantum dot. *Phys. Rev. Lett.*, 103:087401, Aug 2009. doi: 10.1103/PhysRevLett.103.087401. URL http://link.aps.org/doi/10.1103/PhysRevLett.103.087401. 2, 69, 93, 122

[25] L. Esaki and R. Tsu. Superlattice and negative differential conductivity in semiconductors. *IBM J. Res. Develop.*, 14:61–5, 1970. 3

[26] R. Dingle, W. Wiegmann, and C. H. Henry. Quantum states of confined carriers in very thin $Al_xGa_{1-x}As$-GaAs-$Al_xGa_{1-x}As$ heterostructures. *Phys. Rev. Lett.*, 33:827–830, Sep 1974. doi: 10.1103/PhysRevLett.33.827. URL http://link.aps.org/doi/10.1103/PhysRevLett.33.827.

[27] L.L. Chang, L. Esaki, and R. Tsu. Resonant tunneling in semiconductor double barriers. *Appl. Phys. Lett.*, 24:593, 1974. doi: 10.1063/1.1655067. URL http://dx.doi.org/10.1063/1.1655067. 3

[28] T. Chakraborty. Physics of the artificial atoms: Quantum dots in a magnetic field. *Comments Condens. Matter Phys.*, 16:35, 1992. 3

[29] M.A. Kastner. Artificial atoms. *Physics Today*, 46:23, 1993. doi: 10.1063/1.881393. URL http://dx.doi.org/10.1063/1.881393. 4

[30] L. Jacak, P. Hawrylak, and A. Wojs. *Quantum Dots*. Springer, Berlin, 1997. 9, 44

[31] D. Bimberg, M. Grundmann, and N. N. Ledentsov. *Quantum Dot Heterostructures*. Wiley, New York, 1999.

[32] T. Chakraborty. *Quantum Dots: A Survey of the Properties of Artificial Atoms*. Elsevier Science,, Amsterdam,, 1999.

[33] R. C. Ashoori. Electrons in artificial atoms. *Nature*, pages 413–419, 2006. doi: 10.1038/379413a0. 3, 4

[34] J. Cibert, P. M. Petroff, G. J. Dolan, S. J. Pearton, A. C. Gossard, and J. H. English. Optically detected carrier confinement to one and zero dimension in GaAs quantum well wires and boxes. *Appl. Phys. Lett.*, 49:1275, 1986. doi: 10.1063/1.97384. URL http://dx.doi.org/10.1063/1.97384. 3, 4

[35] H. Temkin, G. J. Dolan, M. B. Panish, and S. N. G. Chu. Low-temperature photoluminescence from InGaAs/InP quantum wires and boxes. *Appl. Phys. Lett.*, 50:413, 1987. doi: 10.1063/1.98159. URL http://dx.doi.org/10.1063/1.98159.

[36] K. Kash, A. Scherer, J. M. Worlock, H. G. Craighead, and M. C. Tamargo. Optical spectroscopy of ultrasmall structures etched from quantum wells. *Appl. Phys. Lett.*, 49:1043, 1986. doi: 10.1063/1.97466. URL http://dx.doi.org/10.1063/1.97466.

[37] M. A. Reed, R. T. Bate, W. M. Duncan, W. R. Frensley, and H. D. Shih. Spatial quantization in GaAs – AlGaAs multiple quantum dots. *J. Vac. Sci. Technol. B*, 4:358, 1986. doi: 10.1116/1.583331. URL http://dx.doi.org/10.1116/1.583331. 3, 4

[38] O. Benson, C. Santori, M. Pelton, , and Y. Yamamoto. Regulated and entangled photons from a single quantum dot. *Phys. Rev. Lett.*, 84:2513–2516, Mar 2000. doi: 10.1103/PhysRevLett.84.2513. URL http://link.aps.org/doi/10.1103/PhysRevLett.84.2513. 4

[39] N. Akopian, N. H. Lindner, E. Poem, Y. Berlatzky, J. Avron, D. Gershoni, B. D. Gerardot, and P. M. Petroff. Entangled photon pairs from semiconductor quantum dots. *Phys. Rev. Lett.*, 96: 130501, Apr 2006. doi: 10.1103/PhysRevLett.96.130501. URL http://link.aps.org/doi/10.1103/PhysRevLett.96.130501. 4

[40] A.J. Shields. Semiconductor quantum light sources. *Nature Phot.*, 1:215–223, 2007. doi: 10.1038/nphoton.2007.46.

[41] A. Schliwa, M. Winkelnkemper, A. Lochmann, E. Stock, and D. Bimberg. In(Ga)As/GaAs quantum dots grown on a (111) surface as ideal sources of entangled photon pairs. *Phys. Rev. B*, 80: 161307, Oct 2009. doi: 10.1103/PhysRevB.80.161307. URL http://link.aps.org/doi/10.1103/PhysRevB.80.161307. 4

[42] F. Sotier, T. Thomay, T. Hanke, J. Korger, S. Mahapatra, A. Frey, K. Brunner, R. Bratschitsch, and A. Leitenstorfer. Femtosecond few-fermion dynamics and deterministic single-photon gain in a quantum dot. *Nature Phys.*, 5:352 – 356, 2009. doi: 10.1038/nphys1229. 4

[43] W. A. Coish and J. M. Gambetta. Entangled photons on demand: Erasing which-path information with sidebands. *Phys. Rev. B*, 80:241303, Dec 2009. doi: 10.1103/PhysRevB.80.241303. URL http://link.aps.org/doi/10.1103/PhysRevB.80.241303.

[44] C. L. Salter, R. M. Stevenson, I. Farrer, C. A. Nicoll, D. A. Ritchie, and A. J. Shields. An entangled-light-emitting diode. *Nature*, 465:594 – 597, 2010. doi: 10.1038/nature09078. 4

[45] J. Phillips, K. Kamath, and P. Bhattacharya. Far-infrared photoconductivity in self-organized InAs quantum dots. *Appl. Phys. Lett.*, 72:2020, 1998. doi: 10.1063/1.121252. URL http://dx.doi.org/10.1063/1.121252. 4

[46] B. Aslan, H. C. Liu, M. Korkusinski, S.-J. Cheng, and P. Hawrylak. Response spectra from mid- to far-infrared, polarization behaviors, and effects of electron numbers in quantum-dot photodetectors. *Appl. Phys. Lett.*, 82:630, 2003. doi: 10.1063/1.1540728. URL http://dx.doi.org/10.1063/1.1540728.

[47] B. Aslan, H. C. Liu, M. Korkusinski, P. Hawrylak, and D. J. Lockwood. Polarons in electron-populated quantum dots revealed by resonant Raman scattering. *Phys. Rev. B*, 73:

233311, Jun 2006. doi: 10.1103/PhysRevB.73.233311. URL http://link.aps.org/doi/10.1103/PhysRevB.73.233311.

[48] H. Lim, S. Tsao, W. Zhang, and M. Razeghi. High-performance InAs quantum-dot infrared photodetectors grown on InP substrate operating at room temperature. *Appl. Phys. Lett.*, 90:131112, 2007. doi: 10.1063/1.2719160. URL http://dx.doi.org/10.1063/1.2719160. 4

[49] P. Michler, A. Kiraz, C. Becher, W. V. Schoenfeld, P. M. Petroff, L. Zhang, E. Hu, and A. Imamoglu. A quantum dot single-photon turnstile device. *Science*, 290:2282–2285, 2000. doi: 10.1126/science.290.5500.2282. 4

[50] V. S. C. Manga Rao and S. Hughes. Single quantum dot spontaneous emission in a finite-size photonic crystal waveguide: Proposal for an efficient "on chip" single photon gun. *Phys. Rev. Lett.*, 99:193901, Nov 2007. doi: 10.1103/PhysRevLett.99.193901. URL http://link.aps.org/doi/10.1103/PhysRevLett.99.193901. 4

[51] S. Fafard, K. Hinzer, S. Raymond, M. Dion, J. McCaffrey, Y. Feng, and S. Charbonneau. Red-emitting semiconductor quantum dot lasers. *Science*, 274:1350–1353, 1996. doi: 10.1126/science.274.5291.1350. 4

[52] L. Gaudreau, S. A. Studenikin, A. S. Sachrajda, P. Zawadzki, A. Kam, J. Lapointe, M. Korkusinski, and P. Hawrylak. Stability diagram of a few-electron triple dot. *Phys. Rev. Lett.*, 97:036807, Jul 2006. doi: 10.1103/PhysRevLett.97.036807. URL http://link.aps.org/doi/10.1103/PhysRevLett.97.036807. viii, 5, 6

[53] M. Korkusinski. *Correlations in semiconductor quantum dots*. PhD Dissertation, University of Ottawa, 2004. viii, 5, 24, 175

[54] P. M. Petroff and S. P. DenBaars. MBE and MOCVD growth and properties of self-assembling quantum dot arrays in III – V semiconductor structures. *Superlattices and Microstructures*, 15:15, 1994. doi: 10.1006/spmi.1994.1004. URL http://dx.doi.org/10.1006/spmi.1994.1004. viii, 5, 7

[55] P. Michler. *Single Quantum Dots: Fundamentals, Applications and new concepts*. Springer, New York, 2003. viii, 5, 9

[56] R. Hanson, L. P. Kouwenhoven, J. R. Petta, S. Tarucha, and L. M. K. Vandersypen. Spins in few-electron quantum dots. *Rev. Mod. Phys.*, 79:1217–1265, Oct 2007. doi: 10.1103/RevModPhys.79.1217. URL http://link.aps.org/doi/10.1103/RevModPhys.79.1217. 4

[57] R. C. Ashoori, H. L. Stormer, J. S. Weiner, L. N. Pfeiffer, S. J. Pearton, K. W. Baldwin, and K. W. West. Single-electron capacitance spectroscopy of discrete quantum levels. *Phys. Rev. Lett.*, 68: 3088–3091, May 1992. doi: 10.1103/PhysRevLett.68.3088. URL http://link.aps.org/doi/10.1103/PhysRevLett.68.3088. 6

[58] R. C. Ashoori, H. L. Stormer, J. S. Weiner, L. N. Pfeiffer, K. W. Baldwin, and K. W. West. N-electron ground state energies of a quantum dot in magnetic field. *Phys. Rev. Lett.*, 71:613–616, Jul 1993. doi: 10.1103/PhysRevLett.71.613. URL http://link.aps.org/doi/10.1103/PhysRevLett.71.613.

[59] P. Hawrylak, C. Gould, A. Sachrajda, Y. Feng, and Z. Wasilewski. Collapse of the Zeeman gap in quantum dots due to electronic correlations. *Phys. Rev. B*, 59:2801–2806, Jan 1999. doi: 10.1103/PhysRevB.59.2801. URL http://link.aps.org/doi/10.1103/PhysRevB.59.2801.

[60] P. Hawrylak. Single-electron capacitance spectroscopy of few-electron artificial atoms in a magnetic field: Theory and experiment. *Phys. Rev. Lett.*, 71:3347–3350, Nov 1993. doi: 10.1103/PhysRevLett.71.3347. URL http://link.aps.org/doi/10.1103/PhysRevLett.71.3347. 6, 12, 14

[61] J. M. Elzerman, R. Hanson, L. H. W. van Beveren, B. Witkamp, L. M. K. Vandersypen, and L. P. Kouwenhoven. Single-shot read-out of an individual electron spin in a quantum dot. *Nature*, 430:431–435, 2004. doi: 10.1038/nature02693. 6

[62] J. Petta, A. Johnson, J. Taylor, E. Laird, A. Yacoby, M. D. Lukin, C. M. Marcus, and M. P. Hanson. Coherent manipulation of coupled electron spins in semiconductor quantum dots. *Science*, 309:2180–2184, 2005. doi: 10.1126/science.1116955.

[63] M. Pioro-Ladriere, M. R. Abolfath, P. Zawadzki, J. Lapointe, S. A. Studenikin, A. S. Sachrajda, and P. Hawrylak. Charge sensing of an artificial H_2^+ molecule in lateral quantum dots. *Phys. Rev. B*, 72:125307, Sep 2005. doi: 10.1103/PhysRevB.72.125307. URL http://link.aps.org/doi/10.1103/PhysRevB.72.125307. 6

[64] D. Schröer, A. D. Greentree, L. Gaudreau, K. Eberl, L. C. L. Hollenberg, J. P. Kotthaus, and S. Ludwig. Electrostatically defined serial triple quantum dot charged with few electrons. *Phys. Rev. B*, 76:075306, Aug 2007. doi: 10.1103/PhysRevB.76.075306. URL http://link.aps.org/doi/10.1103/PhysRevB.76.075306. 6

[65] M. C. Rogge and R. J. Haug. Noninvasive detection of molecular bonds in quantum dots. *Phys. Rev. B*, 78: 153310, Oct 2008. doi: 10.1103/PhysRevB.78.153310. URL http://link.aps.org/doi/10.1103/PhysRevB.78.153310.

[66] E. A. Laird, J. M. Taylor, D. P. DiVincenzo, C. M. Marcus, M. P. Hanson, and A. C. Gossard. Coherent spin manipulation in an exchange-only qubit. *Phys. Rev. B*, 82:075403, Aug 2010. doi: 10.1103/PhysRevB.82.075403. URL http://link.aps.org/doi/10.1103/PhysRevB.82.075403.

[67] S. Amaha, T. Hatano, H. Tamura, S. Teraoka, T. Kubo, Y. Tokura, D. G. Austing, and S. Tarucha. Resonance-hybrid states in a triple quantum dot. *Phys. Rev. B*, 85:081301, Feb 2012. doi: 10.1103/PhysRevB.85.081301. URL http://link.aps.org/doi/10.1103/PhysRevB.85.081301.

[68] C.-Y. Hsieh, Y.-P. Shim, M. Korkusinski, and P. Hawrylak. Physics of lateral triple quantum-dot molecules with controlled electron numbers. *Rep. Progr. Phys.*, 75:114501, 2012. doi: 10.1088/0034-4885/75/11/114501. 6, 79, 81

[69] P. Hawrylak and M. Korkusinski. Voltage-controlled coded qubit based on electron spin. *Solid State Commun.*, 136:508–512, 2005. doi: 10.1016/j.ssc.2005.09.026. URL http://dx.doi.org/10.1016/j.ssc.2005.09.026.

[70] M. Korkusinski, I. Puerto Gimenez, P. Hawrylak, L. Gaudreau, S. A. Studenikin, and A. S. Sachrajda. Topological Hunds rules and the electronic properties of a triple lateral quantum dot molecule. *Phys. Rev. B*, 75:115301, Mar 2007. doi: 10.1103/PhysRevB.75.115301. URL http://link.aps.org/doi/10.1103/PhysRevB.75.115301. 81

[71] I. Puerto Gimenez, M. Korkusinski, and P. Hawrylak. Linear combination of harmonic orbitals and configuration interaction method for the voltage control of exchange interaction in gated lateral quantum dot networks. *Phys. Rev. B*, 76:075336, Aug 2007. doi: 10.1103/PhysRevB.76.075336. URL http://link.aps.org/doi/10.1103/PhysRevB.76.075336. 81

[72] F. Delgado, Y.-P. Shim, M. Korkusinski, L. Gaudreau, S. A. Studenikin, A. S. Sachrajda, and P. Hawrylak. Spin-selective Aharonov-Bohm oscillations in a lateral triple quantum dot. *Phys. Rev. Lett.*, 101:226810, Nov 2008. doi: 10.1103/PhysRevLett.101.226810. URL http://link.aps.org/doi/10.1103/PhysRevLett.101.226810.

[73] I. Puerto Gimenez, C.-Y. Hsieh, M. Korkusinski, and P. Hawrylak. Charged-impurity-induced dephasing of a voltage-controlled coded qubit based on electron spin in a triple quantum dot. *Phys. Rev. B*, 79:205311, May 2009. doi: 10.1103/PhysRevB.79.205311. URL http://link.aps.org/doi/10.1103/PhysRevB.79.205311. 6

[74] W. G. van der Wiel, S. De Franceschi, J. M. Elzerman, T. Fujisawa, S. Tarucha, and L. P. Kouwenhoven. Electron transport through double quantum dots. *Rev. Mod. Phys.*, 75: 1–22, Dec 2002. doi: 10.1103/RevModPhys.75.1. URL http://link.aps.org/doi/10.1103/RevModPhys.75.1. 6

[75] Y.-P. Shim, F. Delgado, and P. Hawrylak. Tunneling spectroscopy of spin-selective Aharonov-Bohm oscillations in a lateral triple quantum dot

molecule. *Phys. Rev. B*, 80:115305, Sep 2009. doi: 10.1103/PhysRevB.80.115305. URL http://link.aps.org/doi/10.1103/PhysRevB.80.115305. 6

[76] M. Field, C. G. Smith, M. Pepper, D. A. Ritchie, J. E. F. Frost, G. A. C. Jones, and D. G. Hasko. Measurements of Coulomb blockade with a noninvasive voltage probe. *Phys. Rev. Lett.*, 70: 1311–1314, Mar 1993. doi: 10.1103/PhysRevLett.70.1311. URL http://link.aps.org/doi/10.1103/PhysRevLett.70.1311. 6, 7

[77] L. Gaudreau, A. Kam, G. Granger, S. A. Studenikin, P. Zawadzki, and A. S. Sachrajda. A tunable few electron triple quantum dot. *Appl. Phys. Lett.*, 95:193101, 2009. doi: 10.1063/1.3258663. URL http://dx.doi.org/10.1063/1.3258663.

[78] D. Sprinzak, Y. Ji, M. Heiblum, D. Mahalu, and H. Shtrikman. Charge distribution in a Kondo-correlated quantum dot. *Phys. Rev. Lett.*, 88:176805, Apr 2002. doi: 10.1103/PhysRevLett.88.176805. URL http://link.aps.org/doi/10.1103/PhysRevLett.88.176805. 7

[79] J. M. Elzerman, R. Hanson, L. H. Willems van Beveren, L. M. K Vandersypen, and L. P. Kouwenhoven. Excited-state spectroscopy on a nearly closed quantum dot via charge detection. *Appl. Phys. Lett.*, 84:4617, 2004. doi: 10.1063/1.1757023. URL http://dx.doi.org/10.1063/1.1757023. 6, 7

[80] E. Bauer. Phnomenologische theorie der kristallabscheidung an oberflchen. *Zeitschrift fr Kristallographie - Crystalline Materials*, 110:372–394, 1958. doi: 10.1524/zkri.1958.110.1-6.372. 7

[81] T. Schwarz-Selinger, Y. L. Foo, D. G. Cahill, and J. E. Greene. Surface mass transport and island nucleation during growth of Ge on laser textured Si(001). *Phys. Rev. B*, 65: 125317, Mar 2002. doi: 10.1103/PhysRevB.65.125317. URL http://link.aps.org/doi/10.1103/PhysRevB.65.125317.

[82] D. J. Eaglesham and M. Cerullo. Dislocation-free Stranski-Krastanow growth of Ge on Si(100). *Phys. Rev. Lett.*, 64: 1943–1946, Apr 1990. doi: 10.1103/PhysRevLett.64.1943. URL http://link.aps.org/doi/10.1103/PhysRevLett.64.1943.

[83] J.-Y. Marzin, J.-M. Gérard, A. Izraël, D. Barrier, and G. Bastard. Photoluminescence of single InAs quantum dots obtained by self-organized growth on GaAs. *Phys. Rev. Lett.*, 73: 716–719, Aug 1994. doi: 10.1103/PhysRevLett.73.716. URL http://link.aps.org/doi/10.1103/PhysRevLett.73.716. 7, 9

[84] I. N. Stranski and L. Krastanow. *Akad. Wiss. Let. Mainz Math Natur K1 IIb*, 146:797–810, 1939. 8

[85] C.-H. Chiu, Z. Huang, and C. T. Poh. Formation of nanostructures by the activated Stranski-Krastanow transition method. *Phys. Rev. Lett.*, 93:136105, Sep 2004. doi: 10.1103/PhysRevLett.93.136105. URL http://link.aps.org/doi/10.1103/PhysRevLett.93.136105. 8

[86] M. E. Reimer, M. Korkusinski, D. Dalacu, J. Lefebvre, J. Lapointe, P. J. Poole, G. C. Aers, W. R. McKinnon, P. Hawrylak, and R. L. Williams. Prepositioned single quantum dot in a lateral electric field. *Phys. Rev. B*, 78:195301, Nov 2008. doi: 10.1103/PhysRevB.78.195301. URL http://link.aps.org/doi/10.1103/PhysRevB.78.195301. 9, 43

[87] M. E. Reimer, W. R. McKinnon, J. Lapointe, D. Dalacu, P. J. Poole, G. C. Aers, D. Kim, M. Korkusinski, P. Hawrylak, and R. L. Williams. Towards scalable gated quantum dots for quantum information applications. *Physica E*, 40:1790–1793, 2008. doi: 10.1016/j.physe.2007.08.131. URL http://dx.doi.org/10.1016/j.physe.2007.08.131. viii, 8, 9

[88] T. Fukui, S. Ando, Y. Tokura, and T. Toriyama. GaAs tetrahedral quantum dot structures fabricated using selective area metalorganic chemical vapor deposition. *Appl. Phys. Lett.*, 58:2018, 1991. doi: 10.1063/1.105026. URL http://dx.doi.org/10.1063/1.105026. 8

[89] R. L. Williams, G. C. Aers, J. Lefebvre, P. J. Poole, and D. Chithrani. Quantum dot site-selection using in situ prepared nano-templates. *Physica E*, 13:1200 – 1203, 2002. doi: 10.1063/1.105026. URL http://dx.doi.org/10.1063/1.105026. 8, 9

[90] J. G. Keizer, M. Bozkurt, J. Bocquel, T. Mano, T. Noda, K. Sakoda, E. C. Clark, M. Bichler, G. Abstreiter, J. J. Finley, W. Lu, T. Rohel, H. Folliot, N. Bertru, and P. M. Koenraad. Shape control of quantum dots studied by cross-sectional scanning tunneling microscopy. *J. Appl. Phys.*, 109:102413–6, 2011. doi: doi:10.1063/1.3577960. URL http://dx.doi.org/10.1063/1.3577960. viii, 11

[91] G. W. Bryant, M. Zielinski, N. Malkova, J. Sims, W. Jaskólski, and J. Aizpurua. Controlling the optics of quantum dots with nanomechanical strain. *Phys. Rev. B*, 84:235412, Dec 2011. doi: 10.1103/PhysRevB.84.235412. URL http://link.aps.org/doi/10.1103/PhysRevB.84.235412. 10

[92] C. Robert, C. Cornet, P. Turban, T. Nguyen Thanh, M. O. Nestoklon, J. Even, J. M. Jancu, M. Perrin, H. Folliot, T. Rohel, S. Tricot, A. Balocchi, D. Lagarde, X. Marie, N. Bertru, O. Durand, and A. Le Corre. Electronic, optical, and structural properties of (In, Ga)As/GaP quantum dots. *Phys. Rev. B*, 86:205316, Nov 2012. doi: 10.1103/PhysRevB.86.205316. URL http://link.aps.org/doi/10.1103/PhysRevB.86.205316.

[93] M. Zielinski. Including strain in atomistic tight-binding hamiltonians: An application to self-assembled InAs/GaAs and InAs/InP quantum dots. *Phys. Rev. B*, 86:115424, Sep 2012. doi: 10.1103/PhysRevB.86.115424. URL http://link.aps.org/doi/10.1103/PhysRevB.86.115424.

[94] M. Zielinski, M. Korkusinski, and P. Hawrylak. Atomistic tight-binding theory of multiexciton complexes in a self-assembled InAs quantum dot. *Phys. Rev. B*, 81:085301, Feb 2010. doi: 10.1103/PhysRevB.81.085301. URL http://link.aps.org/doi/10.1103/PhysRevB.81.085301. 10, 37, 43, 44

[95] A. Wojs, P. Hawrylak, S. Fafard, and L. Jacak. Electronic structure and magneto-optics of self-assembled quantum dots. *Phys. Rev. B*, 54:5604–5608, Aug 1996. doi: 10.1103/PhysRevB.54.5604. URL http://link.aps.org/doi/10.1103/PhysRevB.54.5604. 12, 44

[96] A. Kumar, S. E. Laux, and F. Stern. Electron states in a GaAs quantum dot in a magnetic field. *Phys. Rev. B*, 42: 5166–5175, Sep 1990. doi: 10.1103/PhysRevB.42.5166. URL http://link.aps.org/doi/10.1103/PhysRevB.42.5166.

[97] M. Macucci, K. Hess, and G. J. Iafrate. Electronic energy spectrum and the concept of capacitance in quantum dots. *Phys. Rev. B*, 48:17354–17363, Dec 1993. doi: 10.1103/PhysRevB.48.17354. URL http://link.aps.org/doi/10.1103/PhysRevB.48.17354. 12

[98] T. H. Oosterkamp, J. W. Janssen, L. P. Kouwenhoven, D. G. Austing, T. Honda, and S. Tarucha. Maximum-density droplet and charge redistributions in quantum dots at high magnetic fields. *Phys. Rev. Lett.*, 82:2931–2934, Apr 1999. doi: 10.1103/PhysRevLett.82.2931. URL http://link.aps.org/doi/10.1103/PhysRevLett.82.2931. 12

[99] S. Tarucha, D. G. Austing, Y. Tokura, W. G. van der Wiel, and L. P. Kouwenhoven. Direct Coulomb and exchange interaction in artificial atoms. *Phys. Rev. Lett.*, 84:2485–2488, Mar 2000. doi: 10.1103/PhysRevLett.84.2485. URL http://link.aps.org/doi/10.1103/PhysRevLett.84.2485. 12

[100] A. Wojs and P. Hawrylak. Theory of photoluminescence from modulation-doped self-assembled quantum dots in a magnetic field. *Phys. Rev. B*, 55:13066–13071, May 1997. doi: 10.1103/PhysRevB.55.13066. URL http://link.aps.org/doi/10.1103/PhysRevB.55.13066. 12

[101] S.-J. Cheng, W. Sheng, and P. Hawrylak. Theory of excitonic artificial atoms: InGaAs/GaAs quantum dots in strong magnetic fields. *Phys. Rev. B*, 68:235330, Dec 2003. doi: 10.1103/PhysRevB.68.235330. URL

http://link.aps.org/doi/10.1103/PhysRevB.68.235330. 12, 24, 62, 136, 175

[102] P. Hawrylak. Excitonic artificial atoms: Engineering optical properties of quantum dots. *Phys. Rev. B*, 60:5597–5608, Aug 1999. doi: 10.1103/PhysRevB.60.5597. URL http://link.aps.org/doi/10.1103/PhysRevB.60.5597. 37, 38, 41

[103] P. Hawrylak, G. A. Narvaez, M. Bayer, and A. Forchel. Excitonic absorption in a quantum dot. *Phys. Rev. Lett.*, 85: 389–392, Jul 2000. doi: 10.1103/PhysRevLett.85.389. URL http://link.aps.org/doi/10.1103/PhysRevLett.85.389. 27, 30, 34, 104, 128

[104] A. Wojs and P. Hawrylak. Charging and infrared spectroscopy of self-assembled quantum dots in a magnetic field. *Phys. Rev. B*, 53: 10841–10845, Apr 1996. doi: 10.1103/PhysRevB.53.10841. URL http://link.aps.org/doi/10.1103/PhysRevB.53.10841. 12, 44, 57

[105] K. H. Schmidt, G. Medeiros-Ribeiro, M. Oestreich, P. M. Petroff, and G. H. Döhler. Carrier relaxation and electronic structure in InAs self-assembled quantum dots. *Phys. Rev. B*, 54: 11346–11353, Oct 1996. doi: 10.1103/PhysRevB.54.11346. URL http://link.aps.org/doi/10.1103/PhysRevB.54.11346. 12

[106] H. Drexler, D. Leonard, W. Hansen, J. P. Kotthaus, and P. M. Petroff. Spectroscopy of quantum levels in charge-tunable InGaAs quantum dots. *Phys. Rev. Lett.*, 73:2252–2255, Oct 1994. doi: 10.1103/PhysRevLett.73.2252. URL http://link.aps.org/doi/10.1103/PhysRevLett.73.2252. 12

[107] S. Raymond, S. Studenikin, A. Sachrajda, Z. Wasilewski, S. J. Cheng, W. Sheng, P. Hawrylak, A. Babinski, M. Potemski, G. Ortner, and M. Bayer. Excitonic energy shell structure of self-assembled InGaAs/GaAs quantum dots. *Phys. Rev. Lett.*, 92: 187402, May 2004. doi: 10.1103/PhysRevLett.92.187402. URL

http://link.aps.org/doi/10.1103/PhysRevLett.92.187402. 12, 14, 24, 44, 62, 136, 175

[108] M. Bayer, G. Ortner, O. Stern, A. Kuther, A. A. Gorbunov, A. Forchel, P. Hawrylak, S. Fafard, K. Hinzer, T. L. Reinecke, S. N. Walck, J. P. Reithmaier, F. Klopf, and F. Schäfer. Fine structure of neutral and charged excitons in self-assembled In(Ga)As/(Al)GaAs quantum dots. *Phys. Rev. B*, 65:195315, May 2002. doi: 10.1103/PhysRevB.65.195315. URL http://link.aps.org/doi/10.1103/PhysRevB.65.195315. 12, 27, 28, 57

[109] D. Chithrani, M. Korkusinski, S.-J. Cheng, P. Hawrylak, R.L. Willinams, J. Lefebre, P.J. Poole, and G.C. Aers. Electronic structure of the p-shell in single, site-selected InAs/InP quantum dots. *Physica E*, 26:322, 2005. 12, 27, 35

[110] C. G. Darwin. The diamagnetism of the free electron,. *Math. Proc. Cambridge Phil. Soc.*, 27:86–90, 1931. doi: 10.1017/S0305004100009373. URL http://dx.doi.org/10.1017/S0305004100009373. 13

[111] V. Fock. Bemerkung zur quantelung des harmonischen oszilators in magnetfeld. *Z. Phys.*, 47:446–448, 1928. 13

[112] E. S. Kadantsev, M. Zielinski, M. Korkusinski, and P. Hawrylak. Ab initio calculation of band edges modified by (001) biaxial strain in group IIIAVA and group IIBVIA semiconductors: Application to quasiparticle energy levels of strained InAs/InP quantum dot. *J. Appl. Phys*, 107:104315, 2010. doi: 10.1063/1.3406144. URL http://dx.doi.org/10.1063/1.3406144. 15

[113] A. H. Trojnar, E. S. Kadantsev, M. Korkusinski, and P. Hawrylak. Theory of fine structure of correlated exciton states in self-assembled semiconductor quantum dots in a magnetic field. *Phys. Rev. B*, 84:245314, Dec 2011. doi: 10.1103/PhysRevB.84.245314. URL http://link.aps.org/doi/10.1103/PhysRevB.84.245314. 18, 87

[114] P. Hawrylak. Far infrared absorption by screened d^- states in quantum wells in a strong magnetic field. *Solid State Commun.*, 88:475–479, 1993. doi: 10.1016/0038-1098(93)90617-V. URL http://dx.doi.org/10.1016/0038-1098(93)90617-V. 22, 24, 49, 86, 175

[115] A. Wensauer. *quantenpunkte im Magnetfeld*. PhD Dissertation, Universitat Regensburg, 2003. 24, 175

[116] A. Wojs and P. Hawrylak. Negatively charged magnetoexcitons in quantum dots. *Phys. Rev. B*, 51:10880–10885, Apr 1995. doi: 10.1103/PhysRevB.51.10880. URL http://link.aps.org/doi/10.1103/PhysRevB.51.10880. 25, 44, 49, 86

[117] K. Hinzer, P. Hawrylak, M. Korkusinski, S. Fafard, M. Bayer, O. Stern, A. Gorbunov, and A. Forchel. Optical spectroscopy of a single $Al_{0.36}In_{0.64}As/Al_{0.33}Ga_{0.67}As$ quantum dot. *Phys. Rev. B*, 63:075314, Jan 2001. doi: 10.1103/PhysRevB.63.075314. URL http://link.aps.org/doi/10.1103/PhysRevB.63.075314. 27, 37, 43, 141

[118] M. Grundmann, O. Stier, and D. Bimberg. InAs/GaAs pyramidal quantum dots: Strain distribution, optical phonons, and electronic structure. *Phys. Rev. B*, 52:11969–11981, Oct 1995. doi: 10.1103/PhysRevB.52.11969. URL http://link.aps.org/doi/10.1103/PhysRevB.52.11969.

[119] M. Molas, K. Golasa, K. Kuldova, J. Borysiuk, A. Babinski, J. Lapointe, and Z. R. Wasilewski. The effect of In-flush on the optical anisotropy of InAs/GaAs quantum dots. *J. Appl. Phys.*, 111:033510, 2012. doi: 10.1063/1.3681329. URL http://dx.doi.org/10.1063/1.3681329. 27

[120] T. Takagahara. Effects of dielectric confinement and electron-hole exchange interaction on excitonic states in semiconductor quantum dots. *Phys. Rev. B*, 47:4569–4584, Feb 1993. doi: 10.1103/PhysRevB.47.4569. URL http://link.aps.org/doi/10.1103/PhysRevB.47.4569. 28, 43, 46, 62

[121] T. Takagahara. Theory of exciton doublet structures and polarization relaxation in single quantum dots. *Phys. Rev. B*, 62: 16840–16855, Dec 2000. doi: 10.1103/PhysRevB.62.16840. URL http://link.aps.org/doi/10.1103/PhysRevB.62.16840. 43, 62

[122] S. V. Goupalov and E. L. Ivchenko. A tight-binding representation of electron-hole exchange interaction in semiconductors. *Phys. Solid State*, 43:1867, 2001. doi: 10.1002/(SICI)1521-3951(200104)224:3⟨649::AID-PSSB649⟩3.0.CO;2-Y. 43

[123] E. Kadantsev and P. Hawrylak. Theory of exciton fine structure in semiconductor quantum dots: Quantum dot anisotropy and lateral electric field. *Phys. Rev. B*, 81:045311, Jan 2010. doi: 10.1103/PhysRevB.81.045311. URL http://link.aps.org/doi/10.1103/PhysRevB.81.045311. 43, 45, 46, 50, 62, 195

[124] E. S. Kadantsev and P. Hawrylak. Effective theory of electron-hole exchange in semiconductor quantum dots. *J. of Phys.: Conf. Ser.*, 248:012018, 2010. doi: doi:10.1088/1742-6596/248/1/012018. 28

[125] M. Bayer, O. Stern, P. Hawrylak, S. Fafard, and A. Forchel. Hidden symmetries in the energy levels of excitonic artificial atoms in quantum dots. *Nature*, 405:923, 2000. doi: 10.1038/35016020. URL http://dx.doi.org/10.1038/35016020M3. ix, 37, 39, 104, 141

[126] D. V. Regelman, D. Gershoni, E. Ehrenfreund, W. V. Schoenfeld, and P. M. Petroff. Spectroscopy of single semiconductor quantum dots at negative, neutral, and positive charge states. *phys. stat. sol. (a)*, 190:491–497, 2002. doi: 10.1002/1521-396X(200204)190:2⟨491::AID-PSSA491⟩3.0.CO;2-G. 37, 141

[127] M. Korkusinski and P. Hawrylak. Optical signatures of spin polarization of carriers in quantum dots. *Phys. Rev. Lett.*, 101:027205, Jul 2008. doi: 10.1103/PhysRevLett.101.027205. 37

[128] M. Korkusinski, Hawrylak P., and M. Potemski. A spin-polarized bi-exciton in a semiconductor quantum dot. *J. Phys.: Condens. Matter*, 20:454213, 2008. doi: 10.1088/0953-8984/20/45/454213. 41

[129] A. Wojs and P. Hawrylak. Exciton-exciton interactions in highly excited quantum dots in a magnetic field. *Solid State Commun.*, 100:487–491, 1996. doi: 10.1016/0038-1098(96)00403-6. URL http://dx.doi.org/10.1016/0038-1098(96)00403-6. 37

[130] G. Chen, N. H. Bonadeo, D. G. Steel, D. Gammon, D. S. Katzer, D. Park, and L.J. Sham. Optically induced entanglement of excitons in a single quantum dot. *Science*, 289:1906, 2000. doi: 10.1126/science.289.5486.1906. 42

[131] D. Gammon, E. S. Snow, B. V. Shanabrook, D. S. Katzer, and D. Park. Fine structure splitting in the optical spectra of single GaAs quantum dots. *Phys. Rev. Lett.*, 76:3005–3008, Apr 1996. doi: 10.1103/PhysRevLett.76.3005. URL http://link.aps.org/doi/10.1103/PhysRevLett.76.3005.

[132] J. G. Tischler, A. S. Bracker, D. Gammon, and D. Park. Fine structure of trions and excitons in single GaAs quantum dots. *Phys. Rev. B*, 66:081310, Aug 2002. doi: 10.1103/PhysRevB.66.081310. URL http://link.aps.org/doi/10.1103/PhysRevB.66.081310. 42

[133] M. Bayer, A. Kuther, A. Forchel, A. Gorbunov, V. B. Timofeev, F. Schäfer, J. P. Reithmaier, T. L. Reinecke, and S. N. Walck. Electron and hole g factors and exchange interaction from studies of the exciton fine structure in $In_{0.60}Ga_{0.40}As$ quantum dots. *Phys. Rev. Lett.*, 82:1748–1751, Feb 1999. doi: 10.1103/PhysRevLett.82.1748. URL http://link.aps.org/doi/10.1103/PhysRevLett.82.1748. 42

[134] M. Bayer, G. Ortner, O. Stern, A. Kuther, A. A. Gorbunov, A. Forchel, P. Hawrylak, Fafard S., K. Hinzer, T. L. Reinecke, S. N. Walck, J. P. Reithmaier, F. Klopf, and F. Schäfer. Fine structure of neutral and charged excitons in self-assembled In(Ga)As/(Al)GaAs quantum dots. *Phys. Rev. B*, 65:195315, May 2002. doi: 10.1103/PhysRevB.65.195315.

URL http://link.aps.org/doi/10.1103/PhysRevB.65.195315. 42, 43, 62, 95

[135] R. S. Knox. *Theory of excitons, vol. 5 of Solid State Phys. Suppl.* Academic Press, Berlin, 1963. 42

[136] M. M. Denisov and V. P. Makarov. Longitudinal and transverse excitons in semiconductors. *Phys. Stat. Sol. b*, 56:9–59, 1973. doi: 10.1002/pssb.2220560102.

[137] G.L. Bir and G.E. Pikus. *Symmetry and Strain-Induced Effects in Semiconductors*. Wiley, New York, 1974. 42

[138] S.V. Goupalov, E.L. Ivchenko, and A.V. Kavokin. Fine structure of localized exciton levels in quantum wells. *J. of Exp. and Theor. Phys.*, 86: 388–394, 1998. 43

[139] M. Glazov, E. L. Ivchenko, L. Besombes, Y. Léger, L. Maingault, and H. Mariette. Fine structure of exciton excited levels in a quantum dot with a magnetic ion. *Phys. Rev. B*, 75: 205313, May 2007. doi: 10.1103/PhysRevB.75.205313. URL http://link.aps.org/doi/10.1103/PhysRevB.75.205313. 43, 62, 93

[140] M. Z. Maialle, E. A. de Andrada e Silva, and L. J. Sham. Exciton spin dynamics in quantum wells. *Phys. Rev. B*, 47: 15776–15788, Jun 1993. doi: 10.1103/PhysRevB.47.15776. URL http://link.aps.org/doi/10.1103/PhysRevB.47.15776. 43

[141] Al. L. Efros, M. Rosen, M. Kuno, M. Nirmal, D. J. Norris, and M. Bawendi. Band-edge exciton in quantum dots of semiconductors with a degenerate valence band: Dark and bright exciton states. *Phys. Rev. B*, 54:4843–4856, Aug 1996. doi: 10.1103/PhysRevB.54.4843. URL http://link.aps.org/doi/10.1103/PhysRevB.54.4843. 43

[142] A. Franceschetti, L. W. Wang, H. Fu, and A. Zunger. Short-range versus long-range electron-hole exchange interactions

in semiconductor quantum dots. *Phys. Rev. B*, 58:R13367–R13370, Nov 1998. doi: 10.1103/PhysRevB.58.R13367. URL http://link.aps.org/doi/10.1103/PhysRevB.58.R13367. 43, 44

[143] G. Bester, S. Nair, and A. Zunger. Pseudopotential calculation of the excitonic fine structure of million-atom self-assembled $In_{1-x}Ga_xAs$/GaAs quantum dots. *Phys. Rev. B*, 67: 161306, Apr 2003. doi: 10.1103/PhysRevB.67.161306. URL http://link.aps.org/doi/10.1103/PhysRevB.67.161306.

[144] L. He, M. Gong, C.-F. Li, G.-C. Guo, and A. Zunger. Highly reduced fine-structure splitting in InAs/InP quantum dots offering an efficient on-demand entangled 1.55-μm photon emitter. *Phys. Rev. Lett.*, 101:157405, Oct 2008. doi: 10.1103/PhysRevLett.101.157405. URL http://link.aps.org/doi/10.1103/PhysRevLett.101.157405. 43, 44

[145] A. Greilich, M. Schwab, T. Berstermann, T. Auer, R. Oulton, D. R. Yakovlev, M. Bayer, V. Stavarache, D. Reuter, and A. Wieck. Tailored quantum dots for entangled photon pair creation. *Phys. Rev. B*, 73:045323, Jan 2006. doi: 10.1103/PhysRevB.73.045323. URL http://link.aps.org/doi/10.1103/PhysRevB.73.045323. 43

[146] R. M. Stevenson, R. J. Young, P. Atkinson, K. Cooper, D. A. Ritchie, and A.J. Shields. A semiconductor source of triggered entangled photon pairs. *Nature*, 439:179–182, 2006. doi: 10.1038/nature04446. 43

[147] M. M. Glazov, E. L. Ivchenko, O. Krebs, K. Kowalik, and P. Voisin. Diamagnetic contribution to the effect of in-plane magnetic field on a quantum-dot exciton fine structure. *Phys. Rev. B*, 76:193313, Nov 2007. doi: 10.1103/PhysRevB.76.193313. URL http://link.aps.org/doi/10.1103/PhysRevB.76.193313.

[148] K. Kowalik, O. Krebs, A. Golnik, J. Suffczynski, P. Wojnar, J. Kossut, J. A. Gaj, and P. Voisin. Manipulating the exciton fine structure of single CdTe?ZnTe quantum dots by an in-plane magnetic field. *Phys.*

Rev. B, 75:195340, May 2007. doi: 10.1103/PhysRevB.75.195340. URL http://link.aps.org/doi/10.1103/PhysRevB.75.195340. 43

[149] W. Sheng, S.-J. Cheng, and P. Hawrylak. Multiband theory of multi-exciton complexes in self-assembled quantum dots. *Phys. Rev. B*, 71:035316, Jan 2005. doi: 10.1103/PhysRevB.71.035316. URL http://link.aps.org/doi/10.1103/PhysRevB.71.035316. 44

[150] S.-J. Cheng and P. Hawrylak. Controlling magnetism of semi-magnetic quantum dots with odd-even exciton numbers. *Eur. Phys. Lett.*, 81:37005, 2008. doi: 10.1209/0295-5075/81/37005. 56, 73, 87, 93, 94, 105, 128

[151] A. H. Trojnar, M. Korkusinski, E. S. Kadantsev, P. Hawrylak, M. Goryca, T. Kazimierczuk, P. Kossacki, P. Wojnar, and M. Potemski. Quantum interference in exciton-mn spin interactions in a CdTe semiconductor quantum dot. *Phys. Rev. Lett.*, 107: 207403, Nov 2011. doi: 10.1103/PhysRevLett.107.207403. URL http://link.aps.org/doi/10.1103/PhysRevLett.107.207403. xv, 69, 93, 107, 109, 110, 122, 127, 128, 132, 136, 137, 141, 152, 166

[152] F. Qu and P. Hawrylak. Magnetic exchange interactions in quantum dots containing electrons and magnetic ions. *Phys. Rev. Lett.*, 95:217206, Nov 2005. doi: 10.1103/PhysRevLett.95.217206. URL http://link.aps.org/doi/10.1103/PhysRevLett.95.217206. 56, 72, 73, 100, 105, 128, 130, 163

[153] K. C. Hass and H. Ehrenreich. Electronic and magnetic properties of IIVI diluted magnetic semiconductors. *J. Cryst. Growth*, 86:8–14, 1988. URL http://dx.doi.org/10.1016/0022-0248(90)90691-D. 68

[154] K. Sato, L. Bergqvist, J. Kudrnovsky, P. H. Dederichs, O. Eriksson, I. Turek, B. Sanyal, G. Bouzerar, H. Katayama-Yoshida, V. A. Dinh, T. Fukushima, H. Kizaki, and R. Zeller. First-principles theory of dilute magnetic semiconductors. *Rev. Mod. Phys.*, 82: 1633–1690, May 2010. doi: 10.1103/RevModPhys.82.1633. URL http://link.aps.org/doi/10.1103/RevModPhys.82.1633. xi, 69

[155] Y. Léger, L. Besombes, L. Maingault, D. Ferrand, and H. Mariette. Geometrical effects on the optical properties of quantum dots doped with a single magnetic atom. *Phys. Rev. Lett.*, 95: 047403, Jul 2005. doi: 10.1103/PhysRevLett.95.047403. URL http://link.aps.org/doi/10.1103/PhysRevLett.95.047403. 69, 93, 100, 122, 127, 130

[156] L. Besombes, Y. Leger, L. Maingault, D. Ferrand, H. Mariette, and J. Cibert. Carrier-induced spin splitting of an individual magnetic atom embedded in a quantum dot. *Phys. Rev. B*, 71:161307, Apr 2005. doi: 10.1103/PhysRevB.71.161307. URL http://link.aps.org/doi/10.1103/PhysRevB.71.161307. 69, 70, 93, 141, 142, 152, 166

[157] A. Kudelski, A. Lemaitre, A. Miard, P. Voisin, T. C. M. Graham, R. J. Warburton, and O. Krebs. Optically probing the fine structure of a single Mn atom in an InAs quantum dot. *Phys. Rev. Lett.*, 99:247209, Dec 2007. doi: 10.1103/PhysRevLett.99.247209. URL http://link.aps.org/doi/10.1103/PhysRevLett.99.247209. 69

[158] O. Krebs, E. Benjamin, and A. Lemaitre. Magnetic anisotropy of singly mn-doped InAs/GaAs quantum dots. *Phys. Rev. B*, 80:165315, Oct 2009. doi: 10.1103/PhysRevB.80.165315. URL http://link.aps.org/doi/10.1103/PhysRevB.80.165315. 69

[159] C. Le Gall, L. Besombes, H. Boukari, R. Kolodka, J. Cibert, and H. Mariette. Optical spin orientation of a single manganese atom in a semiconductor quantum dot using quasiresonant photoexcitation. *Phys. Rev. Lett.*, 102:127402, Mar 2009. doi: 10.1103/PhysRevLett.102.127402. URL http://link.aps.org/doi/10.1103/PhysRevLett.102.127402. 69

[160] C. L. Cao, L. Besombes, and J. Fernndez-Rossier. Modelling optical spin pumping of a single Mn atom in a CdTe quantum dot. *J. Phys.:Conf. Ser.*, 210:012046, 2010. doi: 10.1088/1742-6596/210/1/012046.

[161] A. O. Govorov and A. V. Kalameitsev. Optical properties of a semiconductor quantum dot with a single magnetic impurity: photoinduced spin orientation. *Phys. Rev. B*, 71:035338, Jan 2005. doi: 10.1103/PhysRevB.71.035338. URL http://link.aps.org/doi/10.1103/PhysRevB.71.035338. 69, 93

[162] L. Besombes, Y. Leger, L. Maingault, D. Ferrand, J. Cibert, and H. Mariette. Optical probing of the spin state of a single magnetic ion in an individual quantum dot. *Phys. Stat. Sol. (b)*, 242:1237–1241, 2005. doi: 10.1002/pssb.200460780. 69, 93

[163] L. Besombes, Y. Leger, J. Bernos, H. Boukari, H. Mariette, J. P. Poizat, T. Clement, J. Fernández-Rossier, and R. Aguado. Optical probing of spin fluctuations of a single paramagnetic Mn atom in a semiconductor quantum dot. *Phys. Rev. B*, 78:125324, Sep 2008. doi: 10.1103/PhysRevB.78.125324. URL http://link.aps.org/doi/10.1103/PhysRevB.78.125324. 141

[164] C. Le Gall, R. S. Kolodka, C. L. Cao, H. Boukari, H. Mariette, J. Fernández-Rossier, and L. Besombes. Optical initialization, readout, and dynamics of a Mn spin in a quantum dot. *Phys. Rev. B*, 81:245315, Jun 2010. doi: 10.1103/PhysRevB.81.245315. URL http://link.aps.org/doi/10.1103/PhysRevB.81.245315. 69, 70

[165] M. Goryca, P. Plochocka, T. Kazimierczuk, P. Wojnar, Gaj Karczewski, G., M. J. A., Potemski, and P. Kossacki. Brightening of dark excitons in a single CdTe quantum dot containing a single Mn^{2+} ion. *Phys. Rev. B*, 82:165323, Oct 2010. doi: 10.1103/PhysRevB.82.165323. URL http://link.aps.org/doi/10.1103/PhysRevB.82.165323. 69, 74, 93, 94, 127, 130

[166] J. Fernández-Rossier. Single-exciton spectroscopy of semimagnetic quantum dots. *Phys. Rev. B*, 73:045301, Jan 2006. doi: 10.1103/PhysRevB.73.045301. URL http://link.aps.org/doi/10.1103/PhysRevB.73.045301. 69

[167] A. H. Trojnar, M. Korkusinski, M. Potemski, and P. Hawrylak. Theory of optical properties of II − VI semiconductor quantum dots containing a single magnetic ion in a strong magnetic field. *Phys. Rev. B*, 85:165415, Apr 2012. doi: 10.1103/PhysRevB.85.165415. URL http://link.aps.org/doi/10.1103/PhysRevB.85.165415. 69, 91, 93, 127, 128, 130, 134, 141, 152

[168] G. Bacher, A. A. Maksimov, H. Schömig, V. D. Kulakovskii, M. K. Welsch, A. Forchel, P. S. Dorozhkin, A. V. Chernenko, S. Lee, M. Dobrowolska, and J. K. Furdyna. Monitoring statistical magnetic fluctuations on the nanometer scale. *Phys. Rev. Lett.*, 89: 127201, Aug 2002. doi: 10.1103/PhysRevLett.89.127201. URL http://link.aps.org/doi/10.1103/PhysRevLett.89.127201. 70

[169] J. Seufert, G. Bacher, M. Scheibner, A. Forchel, S. Lee, M. Dobrowolska, and J. K. Furdyna. Dynamical spin response in semimagnetic quantum dots. *Phys. Rev. Lett.*, 88: 027402, Dec 2001. doi: 10.1103/PhysRevLett.88.027402. URL http://link.aps.org/doi/10.1103/PhysRevLett.88.027402.

[170] S. Lee, M. Dobrowolska, and J. K. Furdyna. Effect of spin-dependent Mn internal transitions in CdSe magnetic semiconductor quantum dot systems. *Phys. Rev. B*, 72:075320, Aug 2005. doi: 10.1103/PhysRevB.72.075320. URL http://link.aps.org/doi/10.1103/PhysRevB.72.075320. 70

[171] S. Mackowski, H. E. Jackson, L. M. Smith, J. Kossut, G. Karczewski, and W. Heiss. Tuning the properties of magnetic CdMnTe quantum dots. *Appl. Phys. Lett.*, 83:3575, 2003. doi: 10.1063/1.1622438. URL http://dx.doi.org/10.1063/1.1622438. 70

[172] P. Wojnar, J. Suffczynski, K. Kowalik, A. Golnik, G. Karczewski, and J. Kossut. Microluminescence from $Cd_{1-x}Mn_xTe$ magnetic quantum dots containing only a few Mn ions. *Phys. Rev. B*, 75: 155301, Apr 2007. doi: 10.1103/PhysRevB.75.155301. URL http://link.aps.org/doi/10.1103/PhysRevB.75.155301. 71, 122

[173] Y. Léger, L. Besombes, L. Maingault, and H. Mariette. Valence-band mixing in neutral, charged, and Mn-doped self-assembled quantum dots. *Phys. Rev. B*, 76:045331, Jul 2007. doi: 10.1103/PhysRevB.76.045331. URL http://link.aps.org/doi/10.1103/PhysRevB.76.045331. 73, 93, 141

[174] G. Gershon, Yu. Bomze, E. V. Sukhorukov, and M. Reznikov. Detection of non-gaussian fluctuations in a quantum point contact. *Phys. Rev. Lett.*, 101:016803, Jul 2008. doi: 10.1103/PhysRevLett.101.016803. URL http://link.aps.org/doi/10.1103/PhysRevLett.101.016803. 79

[175] Y. Nisikawa and A. Oguri. Numerical renormalization group approach to a quartet quantum-dot array connected to reservoirs: Gate-voltage dependence of the conductance. *Phys. Rev. B*, 73: 125108, Mar 2006. doi: 10.1103/PhysRevB.73.125108. URL http://link.aps.org/doi/10.1103/PhysRevB.73.125108.

[176] A. Sharma and P. Hawrylak. Greenberger-Horne-Zeilinger states in a quantum dot molecule. *Phys. Rev. B*, 83: 125311, Mar 2011. doi: 10.1103/PhysRevB.83.125311. URL http://link.aps.org/doi/10.1103/PhysRevB.83.125311. 79

[177] V. W. Scarola and S. Das Sarma. Exchange gate in solid-state spin-quantum computation: The applicability of the Heisenberg model. *Phys. Rev. A*, 71:032340, Mar 2005. doi: 10.1103/PhysRevA.71.032340. URL http://link.aps.org/doi/10.1103/PhysRevA.71.032340.

[178] A. Mizel and D. A. Lidar. Exchange interaction between three and four coupled quantum dots: theory and applications to quantum computing. *Phys. Rev. B*, 70:115310, Sep 2004. doi: 10.1103/PhysRevB.70.115310. URL http://link.aps.org/doi/10.1103/PhysRevB.70.115310. 79

[179] M. D. Shulman, O. E. Dial, S. P. Harvey, H. Bluhm, V. Umansky, and A. Yacoby. Demonstration of entanglement of electrostatically coupled singlet-triplet qubits. *Science*, 336:202–205, 2012. doi: 10.1126/science.1217692. 79

[180] R. Thalineau, S. Hermalin, A. D. Wieck, C. Bäuerle, L. Saminadayar, and T. Meunier. A few-electron quadruple quantum dot in a closed loop. *Appl. Phys. Lett*, 101:103102, 2012. doi: 10.1063/1.4749811. URL http://dx.doi.org/10.1063/1.4749811. 79

[181] I. Ozfidan, A. H. Trojnar, M. Korkusinski, and P. Hawrylak. Geometry, chirality and electron-electron interactions in the quadruple quantum dot molecule. *Submitted to Sol. St. Comm.*, 2013. 79, 81, 82, 84

[182] Y. Nagaoka. Ferromagnetism in a narrow, almost half-filled s band. *Phys. Rev.*, 147:392–405, Jul 1966. doi: 10.1103/PhysRev.147.392. URL http://link.aps.org/doi/10.1103/PhysRev.147.392. 82

[183] Al. L. Efros, E. I. Rashba, and M. Rosen. Paramagnetic ion-doped nanocrystal as a voltage-controlled spin filter. *Phys. Rev. Lett.*, 87:206601, Oct 2001. doi: 10.1103/PhysRevLett.87.206601. URL http://link.aps.org/doi/10.1103/PhysRevLett.87.206601. 93

[184] C. Le Gall, A. Brunetti, H. Boukari, and L. Besombes. Optical stark effect and dressed exciton states in a Mn-doped CdTe quantum dot. *Phys. Rev. Lett.*, 107:057401, Jul 2011. doi: 10.1103/PhysRevLett.107.057401. URL http://link.aps.org/doi/10.1103/PhysRevLett.107.057401. 93, 141, 152

[185] J. Fernández-Rossier. Single-exciton spectroscopy of semimagnetic quantum dots. *Phys. Rev. B*, 73:045301, Jan 2006. doi: 10.1103/PhysRevB.73.045301. URL http://link.aps.org/doi/10.1103/PhysRevB.73.045301. 93

[186] D. E. Reiter, T. Kuhn, and V. M. Axt. All-optical spin manipulation of a single manganese atom in a quantum dot. *Phys. Rev. Lett.*, 102:177403, Apr 2009. doi: 10.1103/PhysRevLett.102.177403. URL http://link.aps.org/doi/10.1103/PhysRevLett.102.177403. 93

[187] S.-J. Cheng and P. Hawrylak. Controlling magnetism of semi-magnetic quantum dots with odd-even exciton numbers. *Europhys. Lett*, 81:37005, 2008. doi: 10.1209/0295-5075/81/37005. 96, 100, 145

[188] W. Sheng and P. Hawrylak. Spin polarization in self-assembled quantum dots. *Phys. Rev. B*, 73:125331, Mar 2006. doi: 10.1103/PhysRevB.73.125331. URL http://link.aps.org/doi/10.1103/PhysRevB.73.125331. 105

[189] A. H. Trojnar, M. Korkusinski, U. C. Mendes, M. Goryca, M. Koperski, T. Smolenski, P. Kossacki, P. Wojnar, and P. Hawrylak. Fine structure of a biexciton in a single quantum dot with a magnetic impurity. *Phys. Rev. B*, 87:205311, May 2013. doi: 10.1103/PhysRevB.87.205311. URL http://link.aps.org/doi/10.1103/PhysRevB.87.205311. 141, 164

[190] Sørensen, E. S., and I. Affleck. Scaling theory of the kondo screening cloud. *Phys. Rev. B*, 53:9153–9167, Apr 1996. doi: 10.1103/PhysRevB.53.9153. URL http://link.aps.org/doi/10.1103/PhysRevB.53.9153. 145

[191] A. Otte, M. Ternes, K. von Bergmann, S. Loth, H. Brune, C. Lutz, C. Hirjibehedin, and A. Heinrich. The role of magnetic anisotropy in the Kondo effect. *Nature Physics*, 4:847–850, 2008. doi: 10.1038/nphys1072. 146

[192] H. Y. Ramirez, C. H. Lin, C. C. Chao, Y. Hsu, W. T. You, S. Y. Huang, Y. T. Chen, H. C. Tseng, W. H. Chang, S. D. Lin, and S. J. Cheng. Optical fine structures of highly quantized InGaAs/GaAs self-assembled quantum dots. *Phys. Rev. B*, 81:245324, Jun 2010. doi: 10.1103/PhysRevB.81.245324. URL http://link.aps.org/doi/10.1103/PhysRevB.81.245324. 154